

Dynamic response functions of strongly correlated electrons

Results from real-frequency quantum field theory

Nepomuk Ritz



Dynamic response functions of strongly correlated electrons

Results from real-frequency quantum field theory

Nepomuk Ritz

Dissertation

an der Fakultät für Physik

der Ludwig-Maximilians-Universität München

vorgelegt von

Nepomuk Ritz

aus La Jolla, CA, USA



München, den 23. April 2025

Erstgutachter: Prof. Dr. Jan von Delft
Zweitgutachter: Prof. Dr. Lode Pollet
Tag der mündlichen Prüfung: 22. Mai 2025

Zusammenfassung

(Summary in German)

Die quantitative Beschreibung korrelierter Elektronensysteme stellt nach wie vor eine der zentralen Herausforderungen der theoretischen Festkörperphysik dar. Viele faszinierende Phänomene, etwa die Hochtemperatursupraleitung oder die Ausbildung einer „Pseudogap“ in Kupraten und anderen stark korrelierten Materialien, werden durch starke Elektron-Elektron-Wechselwirkungen getrieben, sodass perturbative Methoden in vielen Bereichen versagen. Von besonderer Bedeutung sind dabei dynamische Korrelationsfunktionen, die beschreiben, wie solche Systeme auf zeitabhängige äußere Störungen reagieren, und die entscheidend für das Verständnis zahlreicher experimenteller Messungen sind.

Diese Arbeit widmet sich der präzisen Berechnung dynamischer Antwortfunktionen in wechselwirkenden fermionischen Systemen. Die einleitenden Kapitel beleuchten zunächst die physikalische Relevanz dieser Größen und geben einen Überblick über experimentelle Techniken zu ihrer Messung. Ein besonderer Fokus liegt auf Vierpunktfunktionen, deren Beiträge zu dynamischen Antwortfunktionen für eine qualitativ sowie vor allem quantitativ genaue Beschreibung unerlässlich sind.

Ein zentrales Thema der Arbeit ist die direkte Berechnung dieser Größen in reellen Frequenzen, im Gegensatz zum häufiger verwendeten Zugang über imaginäre Frequenzen. Dieser Ansatz umgeht das notorische Problem der analytischen Fortsetzung, das die Genauigkeit numerischer Studien stark beeinträchtigen kann. Zu diesem Zweck wird der Keldysh-Formalismus verwendet, angewandt hier auf Systeme im thermischen Gleichgewicht. In diesem Rahmen werden zwei zentrale quantenfeldtheoretische Ansätze vorgestellt: die Parquet-Gleichungen, welche selbstkonsistente Beziehungen für die Zweipunkt-Selbstenergie und den Vierpunktvertex auf Zwei-Teilchen-Niveau liefern, sowie die funktionale Renormierungsgruppe (fRG), die eine Renormierungsgruppenperspektive auf der Ebene von Korrelationsfunktionen bietet.

Wir zeigen, dass die vollständige dreidimensionale Struktur des Vierpunktvertex in reellen Frequenzen innerhalb dieses Formalismus kontrollierbar ist. Als konkretes Beispiel lösen wir die Parquet- und fRG-Gleichungen für das Anderson Störstellenmodell („single-impurity Anderson model“, SIAM) und beschreiben die zahlreichen technischen Herausforderungen, die dabei bewältigt werden mussten.

Im abschließenden Teil der Arbeit diskutieren wir Wege zur Erweiterung der vorgestellten Methoden auf ausgedehnte, korrelierte Gittersysteme. Wir argumentieren, dass eine vielversprechende Strategie in der Kombination der genannten diagrammatischen Methoden mit der Dynamischen Mean-Field-Theorie (DMFT) liegt, wobei DMFT als nicht-perturbativer lokaler Ausgangspunkt dient. Hierfür wird jedoch ein DMFT-Störstellenlöser benötigt, der sowohl Zwei- als auch Vierpunktfunktionen berechnen kann. Die neu entwickelte Multipunkt-Erweiterung der Numerischen Renormierungsgruppe (mpNRG) erfüllt diese Anforderung, wenngleich auf Vierpunktniveau gewisse numerische Einschränkungen bestehen. Daher überprüfen wir die Konsistenz der mpNRG-Ergebnisse umfassend, insbesondere die Erfüllung der Parquet-Gleichungen sowie einer Ward-Identität, die wir erstmals in vollständiger Allgemeinheit im Keldysh-Formalismus herleiten. Mit wenigen Ausnahmen erweisen sich diese Relationen als sehr gut erfüllt, was die Eignung von mpNRG als DMFT-Löser für zukünftige diagrammatische Erweiterungen bestätigt. Abschließend heben wir das Potenzial der Quantics Tensor Cross Interpolation (QTCI) Methode hervor, mit deren Hilfe sich kompakte Darstellungen dynamischer Antwortfunktionen effizient finden lassen. Diese Methode verspricht, den Rechenaufwand zukünftiger Berechnungen erheblich zu reduzieren.

Zusammenfassend etabliert diese Arbeit ein robustes Grundgerüst zur Berechnung dynamischer Antwortfunktionen in stark korrelierten Elektronensystemen in reellen Frequenzen. Die vorgestellten quantenfeldtheoretischen Beispielrechnungen für das SIAM sowie die gründlichen Konsistenzprüfungen der mpNRG-Methode legen eine solide Grundlage für zukünftige Erweiterungen auf korrelierte Gittersysteme, die durch Kompressionstechniken wie QTCI numerisch realisierbar erscheinen.

Summary

(Summary in English)

The quantitative description of correlated electron systems remains one of the central challenges in theoretical condensed matter physics. Many fascinating phenomena, such as high-temperature superconductivity or the formation of a pseudogap in cuprates and other correlated materials, are driven by strong electron-electron interactions, rendering perturbative techniques insufficient in many regimes. Of particular importance are dynamical correlation functions, which characterize how such systems respond to time-dependent external perturbations and are key to interpreting a wide range of experimental observations.

This thesis is dedicated to accurately computing dynamic response functions in interacting fermionic systems. The introductory chapters revisit the physical significance of these functions and outline experimental techniques to probe them. Special emphasis is placed on four-point functions, whose contributions to dynamic response functions are essential for both qualitative and, in particular, quantitative accuracy.

The central theme of the thesis is the direct computation of these quantities in real frequencies, as opposed to the more common imaginary-frequency approach. This choice circumvents the notoriously ill-conditioned problem of analytic continuation plaguing the accuracy and reliability of numerical studies. To this end, we adopt the real-frequency Keldysh formalism applied here in thermal equilibrium. Within this framework, two main quantum field-theoretical approaches are presented: the parquet equations, which describe self-consistent relations for the two-point self-energy and four-point vertex at the two-particle level, and the functional renormalization group (fRG), which offers a renormalization-group perspective at the level of correlation functions. We demonstrate that the full three-dimensional real-frequency structure of the four-point vertex can be accurately resolved in this formalism. As a concrete example, we solve the parquet and fRG equations for the single-impurity Anderson model (SIAM) and provide a detailed account of the numerous technical challenges encountered and overcome.

In the final part of the thesis, we discuss pathways toward extending these real-frequency methods to spatially extended, correlated lattice systems. We argue that combining the above diagrammatic approaches with dynamical mean-field theory (DMFT) offers a promising strategy, using DMFT as a non-perturbative local starting point. However, this requires a DMFT impurity solver capable of computing two- and four-point functions. The newly developed multipoint extension to the numerical renormalization group (mpNRG) is a method for this purpose, though some numerical limitations persist at the four-point level. We, therefore, perform extensive consistency checks of mpNRG results, verifying the parquet equations and a Ward identity that we derive in full generality within the Keldysh formalism for the first time. With only a few exceptions, these relations are found to hold with high accuracy, validating the use of mpNRG in future diagrammatic extensions of DMFT. Finally, we highlight the potential of the quantum tensor cross interpolation (QTCI) method to find compressed representations of dynamic response functions efficiently. This technique shows considerable promise in managing the computational demands of future large-scale calculations.

In summary, this thesis establishes a robust framework for computing real-frequency response functions in strongly correlated electron systems. Through proof-of-principle quantum field theory calculations on the SIAM and thorough consistency checks of the mpNRG method, it lays a solid foundation for future extensions to correlated lattice systems, which compression techniques such as the QTCI promise to make computationally feasible.

Publications

This dissertation is based on the following journal articles, listed in order of appearance:

- [P1] *Real-frequency quantum field theory applied to the single-impurity Anderson model*
Anxiang Ge*, **Nepomuk Ritz***, Elias Walter, Santiago Aguirre, Jan von Delft,
and Fabian B. Kugler
Sec. 2.4 / [arXiv:2307.10791](#) Phys. Rev. B, 109, 115128 (2024)

- [P2] *KeldyshQFT: A C++ codebase for real-frequency multiloop functional renormalization
group and parquet computations of the single-impurity Anderson model*
Nepomuk Ritz, Anxiang Ge, Elias Walter, Santiago Aguirre, Jan von Delft, and
Fabian B. Kugler
Sec. 2.6 / [arXiv:2405.20996](#) J. Chem. Phys. 161, 054118 (2024)

- [P3] *MatsubaraFunctions.jl: An equilibrium Green's function library in the Julia
programming language*
Dominik Kiese, Anxiang Ge, **Nepomuk Ritz**, Jan von Delft, and Nils Wentzell
Sec. 2.8 / [arXiv:2309.12511](#) SciPost Phys. Codebases 24 (2024)

- [P4] *Testing the parquet equations and the $U(1)$ Ward identity for real-frequency correla-
tion functions from the multipoint numerical renormalization group*
Nepomuk Ritz, Anxiang Ge, Markus Frankenbach, Mathias Pelz, Jan von Delft,
and Fabian B. Kugler
Sec. 3.4 / [arXiv:2504.05910](#) submitted to Physical Review Research

Acknowledgments

First and foremost, I would like to thank Jan von Delft for his unwavering support in so many ways. Taking me on as a Ph.D. student and endorsing my fellowship application to the *Studienstiftung* during COVID times were by no means guaranteed, and I am deeply grateful for both. His scientific guidance, especially during the more challenging phases of our projects, was invaluable. I am also thankful for the many opportunities he enabled for me to present our work, including trips to the Sherbrooke Summer School in 2022 and the ERG conference in 2024.

A heartfelt thank you goes to Fabian Kugler for co-supervising my projects, even though he just left the group when I began my Ph.D. His expertise and meticulous attention to detail played a crucial role in the success of our research. I learned so much from working with you!

I am grateful to Lode Pollet for kindly agreeing to be the second examiner of my thesis.

A very special thank you to my dear colleague Anxiang Ge, with whom I closely collaborated throughout my Ph.D. Our projects were truly joint efforts; neither of us could have done them alone. Having someone right next to me who knew the intricacies of our work was invaluable for brainstorming new ideas and navigating technical challenges.

Of course, none of our work would have been possible without the pioneering efforts of Elias Walter and Santiago Aguirre, who initiated what started as a Keldysh fRG project and developed the first version of the code base back in 2019. Thank you for laying such a solid foundation!

On the scientific side, I would also like to thank Dominik Kiese and Nils Wentzell for the enjoyable collaboration on their code release paper. The resulting package has since been used in numerous projects, and I hope it continues to benefit future generations!

The NRG data used for benchmarking our real-frequency calculations and in my final project was made possible thanks to the efforts of Andreas Weichselbaum and Seung-Sup Lee, who developed the QSpace library and MuNRG package, respectively. I am also grateful to Jeongmin Shim, Jae-Mo Lihm, Mathias Pelz, and Markus Frankenbach for running NRG calculations and for providing me with the data I needed.

I am deeply thankful to have received a doctoral fellowship from the *Studienstiftung des deutschen Volkes* and a *Marianne-Plehn* fellowship, without which my Ph.D. studies would not have been possible in this form. The *Studienstiftung* also offers invaluable non-material support, from which I benefited immensely.

A significant part of my work involved high-performance numerical computations. I wish to thank the *Rechnerbetriebsgruppe* at the LMU Physics Department and the *Leibniz Rechenzentrum* for providing the essential computational infrastructure.

Discussing physics beyond the confines of the institute has always been a great pleasure, be it at conferences, workshops, or summer schools. In particular, I want to thank André-Marie Tremblay for organizing the inspiring *Sherbrooke Summer School on Computational Quantum Materials* in 2022. I greatly benefited from the exceptional lectures and the connections I formed with fellow junior physicists.

Organizing a scientific workshop myself was a new and rewarding experience. I sincerely thank Marcel Gievers for co-organizing our fRG workshop in Herrsching with me in 2023. I am glad it turned out to be a success, and I have personally gained from the connections I made there. Hopefully, we will get to organize another one in the future. Thanks also to the *Munich Center for Quantum Science and Technology* (MCQST) and the *LMU GraduateCenter* for financially supporting our workshop.

I was fortunate to have been a part of the *International Max Planck Research School for Quantum Science and Technology* (IMPRS-QST) during my Ph.D. The seminars, summer schools, and lectures it offered broadened my scientific perspective greatly. Thank you to Sonya Gzyl for coordinating IMPRS-QST and to Johannes Feldmeier and Rajah Nutakki for co-organizing events in the IMPRS Seminar Series with me.

Teaching was a major, enjoyable, and gratifying aspect of my time at LMU. I am grateful to Jan von Delft, Ivo Sachs, Björn Ladewig, and Hong-Hao Tu for letting me contribute to their courses as a tutor or teaching assistant. I personally learned a great deal as a teaching assistant for *Theoretical Condensed Matter Physics* and *Condensed Matter Many-Body Physics and Field Theory II*, both taught by Hong-Hao. Special thanks to Anxiang Ge and Benedikt Schneider for co-supervising two Bachelor's theses with me.

A huge thank you goes to all my fellow Ph.D. students. In particular, I want to thank Marcel Gievers and Anxiang Ge for thoroughly proofreading this thesis. Thanks also to Marc Ritter for his helpful feedback on the QTCI section. I spent most of my time sharing an office with Andreas Gleis; thank you for the many laughs and insightful discussions, also during the Strange Metal Workshop in Bad Honnef in 2023. I am also grateful to Anxiang Ge, Benedikt Schneider, and Simone Foderà for being my office mates in our "outpost" beyond the emergency fire door. Many thanks to all the other Ph.D. students—Markus Frankenbach, Johannes Halbinger, Ming Huang, Sasha Kovalska, Jheng-Wei Li, Mathias Pelz, Felipe Picoli, Elias Walter, and Changkai Zhang—as well as the many Master's students, for creating such a welcoming and joyful atmosphere at the chair.

Thanks also to the postdocs I overlapped with—Seung-Sup Lee, Björn Sbierski, and Markus Scheb—for many enjoyable conversations, both scientific and otherwise.

A massive thank you goes to Kathrin Higgen, undoubtedly the best secretary in the world!

Every now and then, focusing on something beyond physics is necessary. For me, that has been playing the French horn and making music with others. I am grateful to the Munich international Orchestra for offering a fulfilling balance to academic life. Special thanks to Stefanie Herb and Marlene Grohne for co-chairing the organizational board of the orchestra with me over many years.

Finally, and most importantly, I wish to thank my family. To my parents, Barbara and Raphael, and my little sister, Fidelia: Thank you for your endless and unconditional support over the years and decades. I could not have done this without you.

Contents

Zusammenfassung (Summary in German)	i
Summary (Summary in English)	iii
Publications	v
Acknowledgments	vii
1 Dynamic response functions in many-body physics	1
1.1 Linear response theory	1
1.2 Experimental techniques	3
1.2.1 Inelastic neutron scattering	4
1.2.2 Inelastic electron scattering	5
1.2.3 Reflectivity measurements	5
1.2.4 Angular-resolved photoemission spectroscopy	6
1.3 Fermionic response functions	6
1.3.1 A (very) brief introduction to the Matsubara formalism	7
1.3.2 The problem of analytic continuation	9
2 Real-frequency quantum field theory	11
2.1 Time-dependent expectation values and the Keldysh contour	11
2.2 Electron correlation functions in the Keldysh formalism	15
2.2.1 Keldysh index structure and Keldysh rotation	18
2.2.2 Spin structure and SU(2) symmetry	20
2.2.3 Further symmetries	20
2.3 Diagrammatic methods	21
2.3.1 Parquet formalism	21
2.3.2 Frequency structure of the vertex	23
2.3.3 Asymptotic classes	24
2.3.4 Functional renormalization group	25
2.4 Publication: <i>Real-frequency quantum field theory applied to the single-impurity Anderson model</i>	30
2.5 Technical aspects of real-frequency calculations	55
2.6 Publication: <i>KeldyshQFT: A C++ codebase for real-frequency multiloop functional renormalization group and parquet computations of the single-impurity Anderson model</i>	57
2.7 Digression: Imaginary-frequency QFT in the single boson exchange formalism	79
2.8 Publication: <i>MatsubaraFunctions.jl: An equilibrium Green's function library in the Julia programming language</i>	81
3 The numerical renormalization group and its consistency with quantum field theory	117
3.1 Single-impurity Anderson model	118
3.2 Numerical renormalization group	121
3.3 Ward identities	123

3.4	Publication: <i>Testing the parquet equations and the $U(1)$ Ward identity for real-frequency correlation functions from the multipoint numerical renormalization group</i>	125
4	Outlook	151
4.1	Diagrammatic extensions of dynamical mean field theory	151
4.2	Quantics tensor cross interpolation	154
	Bibliography	157

1 Dynamic response functions in many-body physics

This thesis is dedicated to computations of dynamical correlation functions. To motivate their importance, we begin by taking a step back and discussing how these functions arise in condensed matter systems. We recap basic definitions and results of linear response theory in Sec. 1.1, which naturally gives rise to the concept of dynamic response functions. The coupling between a many-body system and its surroundings is primarily mediated by electromagnetic forces, which can hence be used to probe solid-state system properties in experiments. We review a few relevant experimental measurement techniques in Sec. 1.2, from which we see that the related experimentally measurable quantities can be computed from correlation functions between fermionic operators. We briefly introduce those in Sec. 1.3, before dedicating the remaining parts of this thesis to their explicit computations.

As this chapter is not meant to be a self-contained textbook-style introduction to the subject but rather meant to set the stage for the later parts of this thesis, we only summarize the most important results and concepts and leave out formal derivations and calculations. These can be found in standard textbooks, such as Refs. [Col15] and [AS23], on which this chapter is based.

1.1 Linear response theory

To probe the properties of materials, most experimental techniques apply some perturbation to the system. Such a perturbation could be a beam of laser light, a beam of particles, or some other probe that couples to some degree of freedom of the system of interest. See Sec. 1.2 for important examples. In a second step, the system's response to that perturbation is measured using an appropriate detector. Formally, a time-dependent force term $f(t)$ is coupled to an observable A (which we keep general at this stage) inside the Hamiltonian like $H = H_0 - f(t)A(t)$. Here, H_0 is the unperturbed Hamiltonian, which we assume does not explicitly depend on time. From an expansion of the quantum-mechanical time-evolution operator, one finds that the response of the system to linear order in the force f is given as¹

$$\langle A(t) \rangle = \langle A \rangle + \int_{-\infty}^{\infty} dt' \chi^R(t-t')f(t') + \mathcal{O}(f^2), \quad (1.1)$$

where $\langle A \rangle$ is the expectation value of A in the thermal state of the unperturbed Hamiltonian H_0 .² Formally, a thermal expectation value is defined as $\langle \dots \rangle = \text{Tr} \{ e^{-\beta H_0} \dots \} / \mathcal{Z}$ with the partition function $\mathcal{Z} = \text{Tr} \{ e^{-\beta H_0} \}$ and inverse temperature $\beta = 1/T$, where the trace runs over a complete set of basis states. Here and throughout this thesis, we

¹ In principle, one can also consider the response of another observable A' to the application of a force that couples to the operator A . For this text, we will restrict ourselves to the most relevant special case $A' = A$.

² Often, this expectation value is zero. For instance, in the case of a current that only begins to flow once an external voltage is applied.

use natural units, setting, in particular, $\hbar, k_B = 1$. In Eq. (1.1), the (general) *dynamical susceptibility*, also called *retarded response function*, is given by

$$\chi^R(t-t') = i\langle [A(t), A(t')] \rangle \theta(t-t'), \quad (1.2)$$

where again the expectation value $\langle \dots \rangle$ is meant with respect to a thermal state of the unperturbed Hamiltonian H_0 . Importantly, $\chi^R(t-t')$ is only nonzero for positive values of $t-t'$, which means that the system only shows a response after it was perturbed. In other words, the retarded response function is causal. Since we assumed that H_0 does not explicitly depend on time, all expectation values are time-translational invariant, which lets us perform a Fourier transform of Eq. (1.1), leading to the response

$$\langle A(\omega) \rangle = \langle A \rangle \delta(\omega) + \chi^R(\omega) f(\omega) + \mathcal{O}(f^2) \quad (1.3)$$

in frequency space. This expression is remarkable in several ways: First, it shows that the dynamic response of the system in the observable A to an external perturbation is determined by a dynamical correlation function ($\chi^R(\omega)$), which only depends on the properties of the system itself. Second, a perturbation of a certain frequency ω triggers a response at the same frequency: A maximum of $\langle A(\omega) \rangle$ indicates a maximum of the response function $\chi^R(\omega)$, which in turn indicates that the system has an intrinsic excitation at the frequency ω .³

In addition to the retarded response function, it is useful to define the *correlation function*

$$S(t-t') = \langle A(t)A(t') \rangle - \langle A \rangle^2 = \int_{-\infty}^{\infty} \frac{d\omega}{2\pi} e^{-i\omega(t-t')} S(\omega), \quad (1.4)$$

which describes the fluctuations of the observable A around its equilibrium value. A major result in many-body physics states that this correlation function is related to the retarded response function via

$$S(\omega) = 2[1 + n_B(\omega)] \chi''(\omega), \quad (1.5)$$

where $n_B(\omega) = (e^{\beta\omega} - 1)^{-1}$ is the bosonic distribution function, and $\chi''(\omega) = \text{Im} \chi^R(\omega)$ is the dissipative part of the susceptibility. Hence, Eq. (1.5) is known as the *fluctuation-dissipation theorem* (FDT) [Kub57; Kub66; For18], encompassing both quantum and thermal contributions.⁴ The FDT provides a deep relation between quantum and thermal fluctuations around the equilibrium state and the response of a system to external forces. As a side remark, we note that the dynamic susceptibility, which is defined on the real frequency axis, can be extended to the complex plane employing the *Kramers-Kronig relation*

$$\chi(z \in \mathbb{C}) = \int \frac{d\omega}{\pi} \frac{1}{\omega - z} \chi''(\omega). \quad (1.6)$$

³ Note that this follows directly from the assumption of a linear response. Strictly speaking, this is an approximation, which is justified as long as the force f is sufficiently weak compared to the internal correlations of the system. Often, this is a good approximation. There are, however, exceptions to this, e.g., in laser spectroscopy, where the laser field can become so strong that it triggers a non-linear response. We will not discuss this further.

⁴ Equation (1.5) is most easily derived from a spectral representation of the functions $S(\omega)$ and $\chi^R(\omega)$. We refer to Ref. [Col15] for details.

It follows that from the correlation function in thermal equilibrium, utilizing the FDT, Eq. (1.5), and the Kramers-Kronig relation, Eq. (1.6), the response function of the system can be computed; a highly non-trivial result.

So far, we considered a general observable A , that a general force field couples to and whose response will be measured. Actual experiments, which we will turn to next, use specific observables to probe a system of interest. Below, we list a few common choices for A and the corresponding response functions relevant in the context of electronic systems, of interest in this thesis:

- (i) The response of the spin density operator $\mathbf{S}(t, \mathbf{r}) = c_\alpha^\dagger(t, \mathbf{r}) (\frac{\boldsymbol{\sigma}}{2})_{\alpha\beta} c_\beta(t, \mathbf{r})$ is determined by the *dynamic spin (or magnetic) susceptibility* $\chi_m(\omega)$. It can be measured using inelastic neutron scattering, see Sec. 1.2.1. Here, $\boldsymbol{\sigma}$ is the vector of Pauli matrices, and α and β label spin components. For an extended sample, $\mathbf{S}(t, \mathbf{r})$ not only depends on time but has a spatial dependence, too.
- (ii) Likewise, the response of the charge density operator $\rho(t, \mathbf{r}) = c_\alpha^\dagger(t, \mathbf{r}) c_\alpha(t, \mathbf{r})$ is given by the *dynamic charge (or density) susceptibility* $\chi_d(\omega)$. It can be measured using, e.g., inelastic electron scattering; see Sec. 1.2.2 for details.
- (iii) Another highly relevant material property is the *optical conductivity* $\sigma(\omega)$, which is related to the response of the current density operator $\mathbf{j}(t, \mathbf{r}) = -i \frac{e}{m} c_\alpha^\dagger(t, \mathbf{r}) \overleftrightarrow{\nabla} c_\alpha(t, \mathbf{r})$, where $\overleftrightarrow{\nabla} = \frac{1}{2}(\overrightarrow{\nabla} - \overleftarrow{\nabla})$, and e and m are the electron charge and mass, respectively. It is typically determined from reflectivity measurements; see Sec. 1.2.3 for details. Spatially dependent current-current correlation functions will not be computed in this thesis, which purely focuses on dynamic properties. However, since it is a central goal for future research to generalize the computations laid out later in this thesis to scenarios that include spatially dependent quantities, we briefly discuss these here.
- (iv) Experimentally, it is also possible to couple to the electron field operator $c(t, \mathbf{r})$ itself, which enables the measurement of the electronic spectral function. Such measurements are most famously done using photoemission spectroscopy, see Sec. 1.2.4. Since $c(t, \mathbf{r})$ is a fermionic operator, the previous definitions of response functions valid for bosonic operators A must be modified slightly to account for the fermionic statistics. Fermionic response functions will be defined below in Sec. 1.3.

From the list above, two observations become apparent: First, using second quantization, all operators listed can be expressed using fermionic field operators. Hence, the corresponding response functions can be computed in a purely fermionic theory, which we will restrict ourselves to for the remainder of this thesis. Second, the first three operators listed above are expressed using *two* fermion operators each. The related response functions are given in terms of *four-point* correlation functions in terms of fermionic operators. This general feature highlights the importance of four-point functions in many-body physics, which will also be the main focus of this work.

1.2 Experimental techniques

In the previous section, we argued that experimental measurements of responses of a system of interest to an external perturbation are related to correlation functions. In the following, we will make this relation more explicit for a small but important selection of

commonly used measurement techniques. Here, we will focus on one specific type, namely, *spectroscopy* or scattering experiments. The strategy behind all types of spectroscopy is to first send a beam of particles (photons, neutrons, electrons, ...) onto a sample, which acts as a perturbation. In the spirit of the previous setup, these particles couple to some microscopic variable $A(t, \mathbf{r})$. In a second step, the flux of outgoing particles from the sample, induced by the external perturbation, is measured with a detector. Ideally, the energy *and* momentum transfers ω and \mathbf{q} (compared to the incoming particle beam) are resolved. Such a measurement gives the differential scattering cross section, which, as it turns out, is proportional to the correlation function

$$\frac{d^2\sigma}{d\Omega d\omega}(\omega, \mathbf{q}) \sim \int dt d^3\mathbf{r} \langle A(t, \mathbf{r})A(0) \rangle e^{i(\omega t - \mathbf{q}\cdot\mathbf{r})} = S(\omega, \mathbf{q}). \quad (1.7)$$

The combination of physical constants appropriate to the concrete setup gives the prefactor in Eq. (1.7).

Spectroscopy experiments are, of course, not the only class of experiments performed on condensed matter systems. Of great importance are also measurements of thermodynamic quantities (specific heat, compressibility, ...), which yield insights about universal features. However, they do not give any dynamic properties, which is the focus of this work, so we do not discuss them further.

Another widespread technique is the measurement of *transport* of some physical quantity through a sample. Normally also induced by an external perturbation, linear response theory often applies to this scenario. Indeed, the conductivity discussed below is a transport coefficient, relating the system's response in the form of a current to the application of an external electric field.

In the following, we briefly discuss the setups of some of the most essential spectroscopy experiments, which enable the measurement of the previously discussed dynamic response functions.

1.2.1 Inelastic neutron scattering

In neutron scattering experiments, thermal neutrons are scattered by a sample probe [Lov84; FMS09; Squ12]. Since the neutron is electrically neutral, it interacts only weakly with the sample and can penetrate deep into its bulk. Indeed, it only couples through its magnetic moment (i.e., its spin) to the magnetic fields inside the sample. Besides contributions from the nuclear moments and the dipole field of the electron spins, this is mostly due to the orbital part arising from the motion of unpaired electrons bound to the atoms. Neutron scattering can, therefore, be used to probe the magnetic properties of the atoms that make up the crystal; see Ref. [Ber+17] for a recent study. Concretely, it measures the total neutron scattering amplitude (summation convention implied),

$$S_{\text{tot}}(\omega, \mathbf{q}) = \left(\delta_{i,j} - \frac{q^i q^j}{q^2} \right) S_{\text{spin}}^{i,j}(\omega, \mathbf{q}). \quad (1.8)$$

The dynamic spin-spin correlation function,

$$S_{\text{spin}}^{i,j}(\omega, \mathbf{q}) = \int dt d^3\mathbf{r} \langle S^i(t, \mathbf{r})S^j(0) \rangle e^{i(\omega t - \mathbf{q}\cdot\mathbf{r})}, \quad (1.9)$$

is also called the *spin structure factor*, where in an effective purely electronic theory, the spin density operator reads $\mathbf{S}(t, \mathbf{r}) = c_{\alpha}^{\dagger}(t, \mathbf{r}) \left(\frac{\boldsymbol{\sigma}}{2} \right)_{\alpha\beta} c_{\beta}(t, \mathbf{r})$ in second quantization.

From this correlation function, the dynamical spin susceptibility can be inferred via the FDT, which determines the magnetization $M(\omega, \mathbf{q}) = \chi_m(\omega, \mathbf{q})B(\omega, \mathbf{q})$ that arises when a temporally and spatially variable magnetic field is applied.

1.2.2 Inelastic electron scattering

Directly measuring the dynamic charge or density susceptibility is difficult due to a lack of experimental probes at low energies. Many experiments have measured the consequences of phenomena like the formation of charge-density waves, such as an opening of the associated gap in the spectral function, which is accompanied by a peak in the charge susceptibility, without, however, measuring it directly. Commonly used *inelastic X-ray scattering* (IXS) measurements are often dominated by phonons since the X-ray beam couples to the electron density operator, dominated by valence electrons in real materials. Neutral lattice modes hence easily dominate over the electronic excitations one would want to measure. While valence excitations can, by now, be measured using *resonant inelastic X-ray scattering* (RIXS) [Abb+99; Ame+11], which tunes the X-ray beam energy to the absorption edge, only moderate energy resolutions ~ 40 meV have been achieved so far. Effectively, the actual quantity of interest is not the dynamic electron density response but the charge response, to which the positively charged nuclei in solids contribute as well. Only recently has it become possible to measure the actual charge response at nonzero momentum with meV energy resolution using momentum-resolved *inelastic electron scattering* [Vig+17]. In this study, a monochromatic beam of low-energy electrons (with only 10 – 200 eV) was scattered from the surface of a material in an ultrahigh vacuum, which allowed the measurement of finite-momentum charge excitations in the high-temperature superconductor $\text{Bi}_2\text{Sr}_2\text{CaCu}_2\text{O}_{8+x}$. The experimental details are beyond the scope of this work.

1.2.3 Reflectivity measurements

Measurements of the optical reflectivity coefficient $r(\omega) = (1 - \sqrt{\epsilon(\omega)}) / (1 + \sqrt{\epsilon(\omega)})$ allow the determination of the *dielectric function* $\epsilon(\omega)$, which characterizes the polarization properties of the material in response to an applied electromagnetic field. It is related to the *optical conductivity* $\sigma(\omega)$ via

$$\epsilon(\omega) = 1 + i \frac{\sigma(\omega)}{\omega}, \quad (1.10)$$

which itself is defined as the current response due to the application of an electric field, $\mathbf{j}(\omega) = \sigma(\omega)\mathbf{E}(\omega)$. For isotropic samples, the optical conductivity is a diagonal matrix; in general, it is a 3×3 tensor. In the former case, a given component of the optical conductivity is computed as

$$\sigma(\omega) = \frac{i}{\omega} \left(\frac{ne^2}{m} - \langle j(\omega)j(-\omega) \rangle \right), \quad (1.11)$$

where e and m are the electron charge and mass, respectively, n is the electron density and j labels the corresponding component of the current density operator $\mathbf{j}(t, \mathbf{r}) = -i \frac{e}{m} c_\alpha^\dagger(t, \mathbf{r}) \overleftrightarrow{\nabla} c_\alpha(t, \mathbf{r})$. The first term describes the short-time (high-frequency) response due to the ballistic motion of the electrons in the electric field and, in the spirit of semi-classical transport theory, could be called the ‘‘Drude’’ term. The second term describes the slow relaxation of the current to the equilibrium state and is a short-hand

notation for

$$\langle j(\omega)j(-\omega) \rangle = i \int_0^\infty dt d^3\mathbf{r} \langle [j(t, \mathbf{r}), j(0)] \rangle e^{i\omega t}, \quad (1.12)$$

and hence encapsulates all the effects due to thermal and quantum fluctuations.

1.2.4 Angular-resolved photoemission spectroscopy

Angular-resolved photoemission spectroscopy (ARPES) is slightly different from the experiments discussed before since it uses the coupling of light to the electron field $c(t, \mathbf{r})$ directly. It targets a sample with incoming X-ray radiation that ejects core electrons from the probe. ARPES then measures the spatially and energetically resolved intensity of the outgoing electrons to determine the electron-electron correlation function,

$$I(\omega, \mathbf{q}) \sim \int dt d^3\mathbf{r} \langle c^\dagger(t, \mathbf{r})c(0) \rangle e^{i(\omega t - \mathbf{q} \cdot \mathbf{r})}. \quad (1.13)$$

Via a fermionic version of the FDT, which will be discussed later, this quantity is related to the frequency- and momentum-resolved electron spectral function. This way, ARPES can probe the full dispersion relation, i.e., the interacting band structure of a material of interest such as cuprate superconductors studied in Ref. [DHS03].

Since X-ray radiation interacts much more strongly with matter than electrically neutral neutrons, ARPES can only probe the sample's surface. In addition, the momenta of the spectral function perpendicular to the sample's surface cannot be probed. Furthermore, ARPES is unavailable when an external magnetic field is present since this would disturb the X-ray beam. Nevertheless, it has been and still is a highly valuable tool used to gain insights into the properties of correlated materials. One recent highlight is the unprecedentedly accurate measurement of the spectral function of the correlated material Sr_2RuO_4 , which used improved techniques even to probe the bulk of the material [Tam+19].

1.3 Fermionic response functions

For the remainder of this work, we will restrict ourselves to a purely electronic formulation of the many-body problem in the solid state. In particular, we express all observables of interest in terms of fermionic operators in second quantization, as exemplified at the end of Sec. 1.1. Analogous to the response functions defined there, we now introduce the corresponding fermionic response functions, which are customarily also called *Green's functions*.

Particularly important is the analogue of Eq. (1.2), which defines the *retarded electron Green's function*,

$$G^R(t) = -i \langle \{c(t), c^\dagger(0)\} \rangle \theta(t) = \int \frac{d\nu}{2\pi} G^R(\nu) e^{-i\nu t}. \quad (1.14)$$

Note that in contrast to Eq. (1.2), there now appears an anti-commutator instead of a commutator, and we have added a minus sign for later convenience. In addition, w.l.o.g., we have taken the second time argument to be $t' = 0$ and named the frequency in the Fourier transform ν instead of ω , as is customary for fermionic operators. Usually, the Green's function will have more dependencies, such as an additional momentum

dependence or dependencies on spin or orbital indices. For ease of notation and because we will primarily focus on the dynamical properties of correlation functions in the following, we suppress those additional dependencies here. Again, an important observation is that the retarded Green's function is causal, since it is only finite for positive times $t > 0$. Analogous to the Kramers-Kronig relation for dynamic susceptibilities, Eq. (1.6), the electron Green's function can also be extended to the complex plane,

$$G(z) = \int d\nu' \frac{A(\nu')}{z - \nu'}, \quad (1.15)$$

with the *spectral function* $A(\nu) = -\text{Im } G^R(\nu)/\pi$. The retarded function is recovered as

$$G^R(\nu) = G(\nu + i0^+) = \int d\nu' \frac{A(\nu')}{\nu - \nu' + i0^+}. \quad (1.16)$$

The retarded function has singularities slightly below the real axis, but is analytic in the entire upper complex half plane. Using a spectral, i.e., ‘‘Lehmann–Källén’’ representation of the Green's function [Käl52; Leh54], one can show that the spectral function is the Fourier transform of the expectation value of the anti-commutator,

$$\langle \{c(t), c^\dagger(0)\} \rangle = \int d\nu A(\nu) e^{-i\nu t}. \quad (1.17)$$

Since $\{c, c^\dagger\} = 1$ at equal times, the spectral function is normalized,

$$\int d\nu A(\nu) = 1. \quad (1.18)$$

Physically, this property ensures that the probability of finding an electron in any of all possible states is conserved and equal to one.

In this thesis, we will go into much more detail on fermionic correlation functions. We will introduce four-point correlation functions, which, as we have already seen, are instrumental for the computation of dynamic response functions. Also, we will explicitly lay out how those functions can be computed using quantum field theory methods. Before doing that, however, we will quickly explain how these functions are traditionally calculated in thermal equilibrium by briefly introducing the imaginary-frequency Matsubara formalism. Lastly, we will sketch why this formalism can become problematic in practice, which motivates the next chapter devoted to the direct computation of fermionic correlation functions in real frequencies.

1.3.1 A (very) brief introduction to the Matsubara formalism

The classic imaginary-frequency approach to thermal quantum field theory goes back to Bloch, who first noticed a link between inverse temperature and imaginary time [Blo32]. This idea was formalized by Matsubara [Mat55] and extended by Kubo, Martin, and Schwinger [Kub57; MS59], who developed what is nowadays taught as the *Matsubara formalism* to many-body physics in modern textbooks [AS23; Col15; NO19].

While the Matsubara formalism is the most popular framework for computing correlation functions in many-body physics to this day, it is not the main focus of this work. The main reason for this is the *analytic continuation*, see Sec. 1.3.2, of correlation functions computed in imaginary frequencies to the real axis, which is required to obtain dynamical

correlation functions. It turns out that this operation is numerically ill-conditioned. This problem is the primary motivation to pursue an alternative approach that enables the direct computation of those functions in real frequencies, which will be introduced in the subsequent chapter. Still, we use the Matsubara formalism from time to time for comparisons of numerical results for static quantities (i.e., dynamic response functions in the limit $\omega \rightarrow 0$ or $t \rightarrow 0$), which do not require analytic continuation. Also, later in this thesis, we reprint a paper detailing a numerical code designed to compute Matsubara functions. We, therefore, provide a brief introduction to the main ideas of the formalism here.

In thermal equilibrium, the basic quantity of interest is the quantum partition function $\mathcal{Z} = \text{Tr} \{e^{-\beta H}\}$ with inverse temperature $\beta = 1/T$ and the Hamiltonian H . The basic insight underlying the Matsubara formalism is that the exponential factor is reminiscent of the quantum-mechanical time-evolution operator, only in imaginary time. Making the trace explicit by choosing an overcomplete basis of the fermionic analogue of coherent states using Grassmann variables, the partition function is written as⁵

$$\mathcal{Z} = \int d\bar{c} dc e^{-\bar{c}c} \langle -c | e^{-\beta \hat{H}} | c \rangle. \quad (1.19)$$

Performing a Trotter-decomposition of the exponential and inserting an overcomplete set of states at every imaginary time step, the partition function can be expressed as a functional integral,

$$\mathcal{Z} = \int \mathcal{D}[\bar{c}, c] e^{-S} \quad \text{with the action} \quad S = \int_0^\beta d\tau \{ \bar{c}(\tau) \partial_\tau c(\tau) + H[\bar{c}, c] \}. \quad (1.20)$$

Here, $\tau = it$ is an *imaginary time* defined on the interval $\tau \in [0, \beta)$ and $H[\bar{c}, c]$ is the normal-ordered Hamiltonian, in which all fermionic operators c and c^\dagger have been replaced by the corresponding Grassmann variables $c(\tau)$ and $\bar{c}(\tau)$, respectively. The Grassmann variables are anti-periodic in this interval, $c(\beta) = -c(0)$, which motivates a Fourier series representation,

$$c(\tau) = \frac{1}{\beta} \sum_{\nu_n} c_n e^{-i\nu_n \tau}, \quad (1.21)$$

with the discrete (fermionic) *Matsubara frequencies*

$$\nu_n = \frac{(2n+1)\pi}{\beta}, \quad n \in \mathbb{Z}. \quad (1.22)$$

Introducing proper source fields added to the partition function yields a generating functional, which can be used to generate correlation functions through functional differentiation. Evaluating these explicitly usually requires some approximation, such as a perturbation expansion in the interaction term of the Hamiltonian and subsequent evaluations of Gaussian functional integrals. Importantly, dynamic correlation functions, such as the two-point Green's function, are defined on a set of discrete points on the imaginary frequency axis. This description is convenient in multiple ways: First, most elementary analytical operations, such as summations over Matsubara frequencies, can be carried out using complex analysis. Of course, advanced approximation methods such as those discussed later in this thesis cannot be carried out analytically anymore; they

⁵ Again, for ease of notation, we suppress additional dependencies of the Grassmann variables.

require numerical methods. However, their application is comparatively convenient in the Matsubara formalism, too: All correlation functions only have to be computed on the set of discrete Matsubara frequencies and contractions between electron fields that would, for continuous variables, require numerical integrations, instead only require summations over the discrete Matsubara frequencies.

1.3.2 The problem of analytic continuation

Computing a correlation function for those imaginary discrete Matsubara frequencies is, however, only one step. To obtain a retarded dynamic Green's function, according to Eq. (1.16), one in addition has to perform an *analytic continuation* of the result to the real, continuous frequency axis [BM61]. If a closed analytic expression for the Matsubara Green's function $G(i\nu_n)$ is available, this can easily be achieved by simply replacing $i\nu_n \rightarrow \nu + i0^+$. However, this prescription only applies to two-point functions. Analytic continuation of four-point functions, which, as we have seen, are ubiquitous in many-body physics, is much more complicated. It was only figured out very recently how this can be achieved in full generality [Ge+24].

Still, major problems can arise if there is no analytic expression, but only a numerical result for $G(i\nu_n)$. In this case, analytic continuation is a numerically ill-conditioned inverse problem. That is because it is impossible to numerically compute the full Matsubara correlator for all Matsubara frequencies. All computational methods only work with a finite set of points on the imaginary axis, making it challenging to accurately reconstruct the spectral function when trying to invert Eq. (1.15). Crucially, the integrand kernel on the right-hand side of Eq. (1.15) for imaginary z along the Matsubara axis turns out to have super-exponentially decreasing singular values. Consequently, given a Matsubara Green's function, there is an enormous number of plausible real-frequency spectral functions that satisfy Eq. (1.15) within a given accuracy. Selecting the “correct” spectral function is hence sensitive to even tiny potential noise, gaps, or errors in the numerical data [Shi+17; Ots+17]. In addition, Matsubara Green's functions often turn out to be comparatively smooth, while the corresponding real-frequency spectral functions might show a rich structure that is difficult to recover, especially at high frequencies. One concrete example of such an issue will be seen in Ref. [P1]. This issue is particularly problematic since there is no unique solution to the analytic continuation problem for numerical data, and even small numerical inaccuracies can lead to large errors in the result.

To remedy this problem, a multitude of strategies based on stochastic methods [San98], fitting techniques [JG96; HGL23; ZYG24; ZG24], interpolation methods [BG96; FYG21] and even machine learning [Fou+20] have been developed over the years and progress on the problem is being made to this day. Still, every method has limitations, such as noise sensitivity, cutoff effects, or sometimes not preserving causality by producing negative spectral weight [FYG21]. This fact reflects that none of the methods can rigorously overcome the issue that the problem is mathematically ill-conditioned.

The analytic continuation problem, therefore, is one of the primary motivations for this thesis, in which we lay out a strategy for computing real-frequency dynamical correlation functions *directly*. This goal will be achieved using a more general thermal quantum field theory formulation called the Keldysh formalism, which we will introduce next.

2 Real-frequency quantum field theory

This chapter is the primary introduction to the formalism employed in this thesis. After providing some historical context, we recap the main idea behind the Keldysh formalism, which enables the direct computation of real-frequency correlation functions. We introduce these in more formal detail, mainly focusing on the four-point correlation function and the associated vertex, which is one of this thesis' main objects of interest. We discuss some of its properties before mentioning the main diagrammatic methods employed in this work for its concrete computation: the parquet equations and the functional renormalization group.

2.1 Time-dependent expectation values and the Keldysh contour

The Keldysh formalism is a theoretical framework originally intended to study systems out of equilibrium with quantum field theory. Building on earlier work by Schwinger, Kadanoff, and Baym [Sch61; Kad18; BM61], it was invented by Keldysh [Kel64]. Since then, it has become the main framework for studying the quantum dynamics of systems out of equilibrium. However, it can be applied to systems in thermal equilibrium, too. In this case, its main selling point lies in its formulation in real time (or frequency); hence, no analytic continuation from imaginary to real frequencies is required. Therein lies its use for the studies presented in this work.

As in the preceding chapter, we are interested in computing the time-dependence of the expectation value of some observable A . In the most general setting, this is given by

$$\langle A \rangle(t) = \text{Tr} \{ A(t) \rho(t) \}. \quad (2.1)$$

Here, the trace runs over some complete set of basis states and the time-dependent density matrix $\rho(t) = U(t, t_0) \rho_0 U(t_0, t)$ describes the state of the quantum system of interest, where $\rho_0 \equiv \rho(t_0)$ is the density matrix at some initial time t_0 . Furthermore, the operator $A(t)$ might be explicitly time-dependent. $U(t, t_0)$ is the quantum-mechanical time evolution operator, which evolves a quantum state from t_0 to $t > t_0$. Conversely, $U(t_0, t)$ evolves the state from t back to the initial time t_0 .¹ The time evolution of the density matrix is determined by the *von Neumann equation*,

$$\partial_t \rho(t) = -i[H(t), \rho(t)], \quad (2.2)$$

¹ When restricting ourselves to the case of thermal equilibrium and employing the adiabatic assumption, we will later take the limit $t_0 \rightarrow -\infty$, which will result in significant simplifications. For now, we keep the initial time t_0 general.

where $H(t)$ is the Hamiltonian of the system, which might also be explicitly time dependent.² Formally, the von Neumann equation is solved by

$$U(t, t_0) = \mathcal{T} \exp \left[-i \int_{t_0}^t dt' H(t') \right], \quad (2.3)$$

where \mathcal{T} is the time-ordering operator, which places operators evaluated at *later* times to the *left* of operators evaluated at *earlier* times. The time evolution of the density matrix also requires the operator for backwards time evolution. The Hermitian conjugate gives this backwards time evolution,

$$U(t_0, t) = [U(t, t_0)]^\dagger = \tilde{\mathcal{T}} \exp \left[i \int_{t_0}^t dt' H(t') \right] = \tilde{\mathcal{T}} \exp \left[-i \int_t^{t_0} dt' H(t') \right], \quad (2.4)$$

where $\tilde{\mathcal{T}}$ now is the anti-time-ordering operator, which places operators evaluated at *earlier* times to the *left* of operators evaluated at *later* times. Using the cyclicity of the trace, the time-dependent expectation value, Eq. (2.1), is written as

$$\langle A \rangle(t) = \text{Tr} \{ U(t_0, t) A(t) U(t, t_0) \rho_0 \}. \quad (2.5)$$

This expression has an intuitive physical interpretation: First, the system of interest is prepared in some initial state ρ_0 at time t_0 . Then, it is evolved forwards in time until the time t , where the operator of interest $A(t)$ is evaluated. Afterwards, it is evolved backwards in time, until the initial time t_0 again. Historically, the idea of using two time evolutions to compute expectation values goes back to Schwinger [Sch61]. For later convenience, we can extend the time evolution from t to ∞ and back to t , using the unitarity property of the time evolution operator, $U(t, t) = U(t, \infty)U(\infty, t) = U(t, \infty)[U(t, \infty)]^\dagger = \mathbb{1}$. This property allows us to write

$$\langle A \rangle(t) = \text{Tr} \{ U(t_0, \infty)U(\infty, t)A(t)U(t, t_0)\rho_0 \} \quad (2.6a)$$

$$= \text{Tr} \{ U(t_0, t)A(t)U(t, \infty)U(\infty, t_0)\rho_0 \}. \quad (2.6b)$$

We see that it makes no difference whether the operator $A(t)$ is evaluated during the forwards or the backwards time evolution.³ To simplify the notation, the two time evolutions inside the trace motivate the *contour-time-ordering operator*, which formally lets us write the expectation value as

$$\langle A \rangle(t) = \text{Tr} \left\{ \mathcal{T}_{\mathcal{C}} \left(\exp \left[-i \int_{\mathcal{C}_{t_0}} dt' H(t') \right] A(t) \right) \rho_0 \right\}. \quad (2.7)$$

Here, \mathcal{C}_{t_0} denotes the *Keldysh contour* pictorially shown at the very left in Fig. 2.1, which starts at initial time t_0 and $\mathcal{T}_{\mathcal{C}}$ orders all following operators such that operators evaluated on later parts of the contour are placed to the left of the others. Making the

² We use the von Neumann equation, as it can be seen as the generalization of the *Schrödinger equation* for the time evolution of pure quantum states. As we will later be primarily interested in systems characterized by a mixed state (a thermal state, to be precise), we use a description with a density matrix throughout.

³ This will be different when evaluating expectation values of operator products, see below.

contour-time-ordering explicit, the integral inside the exponent reads

$$\begin{aligned} \int_{\mathcal{C}_{t_0}} dt' H(t') &= \int_{t_0}^{\infty} dt' H^-(t') + \int_{\infty}^{t_0} dt' H^+(t') = \int_{t_0}^{\infty} dt' H^-(t') - \int_{t_0}^{\infty} dt' H^+(t') \\ &= \sum_{j \in \{-, +\}} (-j) \int_{t_0}^{\infty} dt' H^j(t'). \end{aligned} \quad (2.8)$$

Here, we introduced a contour index $j \in \{-, +\}$ to label the contour branch onto which the operator H is placed. This index is useful because each time now appears twice, once on the contour's forward and once on the backward branch. For Hamiltonians that are local in time (meaning that they only depend on one time argument, if at all), the distinction between the two branches is not essential since they evaluate to the same expression on both branches. However, the distinction is important when evaluating products of operators evaluated at different times: Along the $-$ branch of the contour, they are time-ordered; along the $+$ branch of the contour, they are anti-time-ordered. Explicitly, for a product of two (bosonic) operators A_1 and A_2 , evaluated at times t_1 and $t_2 < t_1$, respectively, the contour-time-ordering operator acts as

$$\mathcal{T}_{\mathcal{C}} A_1^j(t_1) A_2^j(t_2) = \begin{cases} A_1^-(t_1) A_2^-(t_2) \\ A_2^+(t_2) A_1^+(t_1), \end{cases} \quad (2.9)$$

depending on the contour index j . If the contour indices differ, the operator on the backward contour ($j = +$) is placed to the left of the operator on the forward contour ($j = -$). This prescription holds for bosonic observables A ; note that the contour ordering implies a minus sign if applied to fermionic operators when two are swapped. Important examples for such operator products will appear later when we introduce electron Green's functions in this formalism.

So far, we have kept our discussion very general. It could be applied to a setting where (i) the Hamiltonian is explicitly time dependent and (ii) the initial density matrix ρ_0 is arbitrary. Therein lies the power of the Keldysh formalism: It can be applied in circumstances that arise, e.g., when describing non-equilibrium or explicitly time-dependent phenomena. For the rest of this thesis, we will be more modest. We restrict ourselves to the case of thermal equilibrium, where the Hamiltonian is time-independent and the initial density matrix is just given by the thermal density matrix, $\rho_0 \stackrel{\text{th.eq.}}{=} e^{-\beta H} / \mathcal{Z}$ with the partition function $\mathcal{Z} = \text{Tr} \{e^{-\beta H}\}$ and H is time independent. In this case, Eq. (2.3) for the time evolution operator simplifies to $U(t, t_0) = e^{-i(t-t_0)H}$. By simple inspection, one notices that one can write $e^{-\beta H} = U(t_0 - i\beta, t_0)$. Again, using the cyclicity of the trace, the time-dependent expectation value, Eq. (2.5), is then written as

$$\langle A \rangle(t) = \frac{1}{\mathcal{Z}} \text{Tr} \{U(t_0 - i\beta, t_0) U(t_0, t) A(t) U(t, t_0)\}. \quad (2.10)$$

This type of time evolution can be visualized by attaching another branch to the time contour at the end of the contour \mathcal{C}_{t_0} , along the imaginary axis in vertical direction from t_0 to $t_0 - i\beta$. Along this part of the contour, all operators (including the Hamiltonian) are defined to be equal to the same operator evaluated at initial time t_0 : $A(t_0 - i\tau) = A(t_0) \equiv A$. Here, τ is an *imaginary time* $\tau \equiv it \in [0, \beta)$. We could now compute expectation

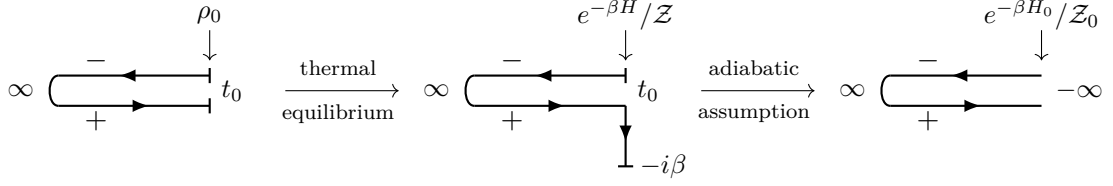


Figure 2.1 Keldysh contours for three different settings. The one on the left corresponds to the most general scenario, applicable in particular to non-equilibrium problems, in which an initial state, described by the initial density matrix ρ_0 , is prepared at the initial time t_0 , followed by the time evolution along the two branches of the contour. The second contour arises when the initial density matrix is chosen to be the one of the canonical ensemble in thermal equilibrium. The contribution to thermal expectation values from the density matrix can be treated as an additional time evolution in imaginary time from 0 to $-\beta$. The third form arises in the case of thermal equilibrium when, additionally, the adiabatic assumption can be employed. Then, the thermal density matrix can be formally prepared from the non-interacting one by adiabatically turning on the interactions, starting from negative infinite time.

values of operators on this part of the contour as

$$\begin{aligned} \langle A \rangle(t_0 - i\tau) &= \frac{1}{\mathcal{Z}} \text{Tr} \{ U(t_0 - i\beta, t_0 - i\tau) A(t_0 - i\tau) U(t_0 - i\tau, t_0) \} \\ &= \frac{1}{\mathcal{Z}} \text{Tr} \{ e^{-(\beta-\tau)H} A e^{-\tau H} \} = \frac{1}{\mathcal{Z}} \text{Tr} \{ e^{-\beta H} A \}, \end{aligned} \quad (2.11)$$

where we used the cyclicity of the trace again in the last step. Equation (2.11) gives nothing but the thermal expectation value of the operator A and is the basis of the Matsubara formalism discussed before in Sec. 1.3.1. Since it is formulated entirely in imaginary time (the real initial time t_0 drops out), this brings along the problem of analytic continuation, see Sec. 1.3.2.

Since we want to avoid that issue, we will stick with Eq. (2.10) for the time-dependent expectation value. However, it is unclear from the start how one should deal with the time evolution along the imaginary part of the contour. It turns out that this issue is solved by utilizing the *adiabatic assumption* [BF28]: Assume that the system was non-interacting at the very beginning of time ($t \rightarrow -\infty$) and that interactions were switched on adiabatically to prepare the system in the initial interacting state at initial time t_0 . In thermal equilibrium, this state is characterized by the thermal density matrix w.r.t. the full Hamiltonian H . The word “adiabatically” means in this context that the eigenstates of the non-interacting system directly evolve into the eigenstates of the interacting system without any level crossings. As t_0 drops out if H is not explicitly time-dependent, we can let $t_0 \rightarrow -\infty$. Then, we can replace the thermal density matrix by the thermal density matrix w.r.t. the *non-interacting* Hamiltonian H_0 .⁴ That is because the interaction vanishes on the vertical branch of the contour for $t_0 \rightarrow -\infty$, since $H(-\infty - i\tau) \equiv H(-\infty) = H_0$, see above. Since the non-interacting density matrix only includes quadratic terms of fermion operators, it can be used to apply Wick’s theorem [Wic50]. In other words, this replacement now enables a conventional perturbation expansion of the time evolution operator in the interacting part of the Hamiltonian, which is the basis of diagrammatic quantum field theory calculations. A formal derivation

⁴ H_0 now labels the quadratic part of the Hamiltonian, not the full interacting Hamiltonian without an external perturbation as in Ch.1.

of this result is provided in Sec. 2.2.3 of Ref. [Jak10]. Also, since we set $t_0 \rightarrow -\infty$, all time integrations naturally run across the entire real axis from $-\infty$ to ∞ , which is convenient and enables easy Fourier transformations. Note, however, that the adiabatic assumption is far from trivial, and there are many important examples of interesting physical systems for which it does not hold. For example, systems that undergo quantum phase transitions as the interaction increases or that form bound states violate the adiabatic assumption. As the adiabatic assumption lies at the heart of any perturbation theory in the interaction, this strongly limits the applicability of diagrammatic methods in general [And00].

2.2 Electron correlation functions in the Keldysh formalism

Next, we introduce the correlation functions in the Keldysh formalism of concrete interest for this work. We will almost exclusively be concerned with electron Green's functions and higher-order, particularly four-point, correlation functions for the correlated electron problem, as briefly introduced in Sec. 1.3. The main theoretical framework of this thesis will be a quantum field theory description, for which we introduce some basic definitions and notation in the following. We will closely follow the conventions in Ref. [Wal22] since those were used in the publications reprinted later in this thesis.

The basic starting point for our field theory is the quantum partition function \mathcal{Z} . In a purely electronic (and thus fermionic) theory, the trace is made explicit using an overcomplete set of fermionic Grassmann variables c and \bar{c} . \mathcal{Z} is then given in terms of a *functional integral*,

$$\mathcal{Z} = \int \mathcal{D}[\bar{c}, c] e^{iS[\bar{c}, c]}, \quad (2.12)$$

with the action

$$S[\bar{c}, c] = S_0[\bar{c}, c] + S_{\text{int}}[\bar{c}, c] = \bar{c}_{1'} [G_0^{-1}]_{1'|1} c_1 + \frac{1}{4} \bar{c}_{1'} \bar{c}_{2'} [\Gamma_0]_{1'2'|12} c_2 c_1, \quad (2.13)$$

which has a non-interacting (quadratic) and an interacting (quartic) part. The multi-indices in Eq. (2.13) comprise all dependencies of the Grassmann variables, i.e., time, Keldysh contour index, spin, and all other dependencies and quantum numbers there might be. We use the Einstein summation convention, meaning all repeated indices are summed or integrated. Contracting time and Keldysh indices thus means an integration along the Keldysh contour as explicitly specified in Eq. (2.8).⁵ The first term of the action includes the inverse bare propagator,

$$[G_0^{-1}]_{1'|1} = \delta_{1'|1} i\partial_{t_1} - h_{1'|1}, \quad (2.14)$$

which is given by two terms: a diagonal dynamical term and the single-particle Hamiltonian in the form of the non-interacting Hamiltonian matrix elements in terms of the Grassmann variables, i.e., $H_0[\bar{c}, c] = \bar{c}_{1'} h_{1'|1} c_1$. The second term of the action is the interacting part of the Hamiltonian, multiplied by a minus sign. It includes the *bare vertex* Γ_0 . From this point forward, we will assume that the interaction is instantaneous, i.e., local in

⁵ This time, the Keldysh contour runs twice over the full real-time axis, however. See our discussion in the last paragraph of Sec. 2.1.

time.⁶ This assumption reflects the general view of the theory as an *effective* description of electrons in condensed matter systems: Microscopically, the electron-electron interaction is, of course, mediated by three-point direct and exchange processes of photons as described by quantum electrodynamics. In the effective description of interest here, the photon fields have been integrated out, yielding only a quartic interaction of the electrons. In a standard diagrammatic visualization, the usual *Feynman diagrams* are thus replaced by the *Hugenholtz* notation [Hug57], which exclusively involves electron fields,

$$[\Gamma_0]_{1'2'|12} = \begin{array}{c} 2 \\ \swarrow \quad \searrow \\ \bullet \\ \swarrow \quad \searrow \\ 1' \quad 1 \end{array} \quad 2' \quad = \quad \begin{array}{c} \swarrow \quad \searrow \\ \text{---} \\ \swarrow \quad \searrow \end{array} - \begin{array}{c} \swarrow \quad \searrow \\ \text{---} \\ \swarrow \quad \searrow \end{array}. \quad (2.15)$$

Concretely, in the case of an instantaneous interaction, all time arguments and contour indices have to be equal in the bare vertex for it to be non-vanishing. Also, Pauli's exclusion principle restricts the possible combinations of spin arguments because only electrons with opposite spins can interact at the same point in space and time. Making the dependence on Keldysh contour indices j , spin indices σ , and time indices t explicit, where the indices q shall label all other indices there might be, the bare interaction then reads [Jak10; Wal22]

$$[\Gamma_0]_{\sigma_1 \sigma_2' | \sigma_1 \sigma_2}^{j_1 j_2' | j_1 j_2} (t_1', t_2' | t_1, t_2; q_1', q_2' | q_1 q_2) = -j_1 \delta_{j_1' = j_2' = j_1 = j_2} \delta(t_1' = t_2' = t_1 = t_2) \\ \times (\delta_{\sigma_1', \sigma_2} \delta_{\sigma_2', \sigma_1} - \delta_{\sigma_1', \sigma_1} \delta_{\sigma_2', \sigma_2}) [\Gamma_0](q_1', q_2' | q_1 q_2), \quad (2.16)$$

where the minus sign in the second spin-delta term is due to the fermionic statistics of electrons, leading to a sign change when two electrons are swapped.

We now define the correlation functions of interest from the functional integral and introduce the customary diagrammatic notation. First, the *bare propagator*, whose inverse defines the non-interacting part of the action, is given by

$$[G_0]_{1|1'} = -i \langle \mathcal{T}_C c_1 \bar{c}_{1'} \rangle_0 = \frac{-i}{\mathcal{Z}_0} \int \mathcal{D}[\bar{c}, c] c_1 \bar{c}_{1'} e^{iS_0[\bar{c}, c]} \equiv \begin{array}{c} 1 \\ \longleftarrow \\ 1' \end{array} \quad (2.17a)$$

$$\text{with } \mathcal{Z}_0 = \int \mathcal{D}[\bar{c}, c] e^{iS_0[\bar{c}, c]} \quad \text{the non-interacting partition function,} \quad (2.17b)$$

i.e., the two-point Green's function of the non-interacting theory. Eqs. (2.17) can easily be verified from the action using the standard Gaussian integral for functional integrals with Grassmann variables [NO19]. The functional integral automatically ensures time-ordering along the Keldysh contour of the fields inside the expectation value. While the bare Green's function is known exactly, the two-point electron Green's function of the full interacting theory is of greater interest, which cannot be computed as easily. It is,

⁶ We also demand that it is local in space, although this will not be relevant to our discussion later, focusing on zero-dimensional problems. Physically, the assumption of a spatially local bare interaction of electrons is motivated by the fact that, due to the mobility of the conduction electrons in a metal, the long-range Coulomb interactions are screened, such that electrons can be modeled to interact when they meet on the same lattice site only. The relevance of non-local interactions in models of correlated materials is the subject of very current research [Pad+25; Sch+25].

analogously, defined as

$$G_{1|1'} = -i\langle \mathcal{T}_C c_1 \bar{c}_{1'} \rangle = \frac{-i}{\mathcal{Z}} \int \mathcal{D}[\bar{c}, c] c_1 \bar{c}_{1'} e^{iS[\bar{c}, c]} \equiv 1 \longleftarrow 1' , \quad (2.18)$$

now using the full action S . One famous result of quantum field theory is the relation between the bare and the full Green's function called the *Dyson equation* [Dys49], introducing the *self-energy* Σ ,

$$G_{1|1'} = [G_0]_{1|1'} + [G_0]_{1|2'} \Sigma_{2'|2} G_{2|1'} = 1 \longleftarrow 1' + 1 \longleftarrow 2' \textcircled{\Sigma} 2 \longleftarrow 1' \quad (2.19a)$$

$$\Leftrightarrow G_{1'|1}^{-1} = [G_0^{-1}]_{1'|1} - \Sigma_{1'|1} . \quad (2.19b)$$

It can be shown that, in terms of Hugenholtz diagrams, the self-energy is the sum of amputated *one-particle irreducible* two-point diagrams [NO19]. As it comprises all effects of the electron-electron interaction on the two-point level, it is one of the main quantities of interest in many-body physics. It will show up many times in the following.

The four-point correlation function is similarly defined as

$$G_{12|1'2'}^{(4)} = i\langle \mathcal{T}_C c_1 c_2 \bar{c}_{2'} \bar{c}_{1'} \rangle = \begin{array}{c} \xrightarrow{2'} \quad \xrightarrow{2} \\ | \quad | \\ \text{---} G^{(4)} \text{---} \\ | \quad | \\ \xleftarrow{1} \quad \xleftarrow{1'} \end{array} . \quad (2.20)$$

Employing its tree expansion [KBS10], the four-point function is decomposed into two disconnected terms and one connected term,

$$\begin{aligned} iG_{12|1'2'}^{(4)} &= G_{1|1'} G_{2|2'} - G_{1|2'} G_{2|1'} + iG_{c;12|1'2'}^{(4)} \\ &= \begin{array}{c} \xrightarrow{2'} \quad \xrightarrow{2} \\ | \quad | \\ \text{---} \quad \text{---} \\ | \quad | \\ \xleftarrow{1} \quad \xleftarrow{1'} \end{array} - \begin{array}{c} \xrightarrow{2'} \\ | \\ \text{---} \\ | \\ \xleftarrow{1} \end{array} \begin{array}{c} \xrightarrow{2} \\ | \\ \text{---} \\ | \\ \xleftarrow{1'} \end{array} + i \begin{array}{c} \xrightarrow{2'} \quad \xrightarrow{2} \\ | \quad | \\ \text{---} G_c^{(4)} \text{---} \\ | \quad | \\ \xleftarrow{1} \quad \xleftarrow{1'} \end{array} , \end{aligned} \quad (2.21)$$

where the connected contribution is given in terms of the four-point vertex Γ ,

$$G_{c;12|1'2'}^{(4)} = -G_{1|3'} G_{2|4'} \Gamma_{3'4'|34} G_{3|1'} G_{4|2'} = - \begin{array}{c} \xrightarrow{2'} \quad \xrightarrow{4} \quad \xrightarrow{4'} \quad \xrightarrow{2} \\ | \quad | \quad | \quad | \\ \text{---} \Gamma \text{---} \\ | \quad | \quad | \quad | \\ \xleftarrow{1} \quad \xleftarrow{3'} \quad \xleftarrow{3} \quad \xleftarrow{1'} \end{array} . \quad (2.22)$$

Thus, the vertex is the amputated part of the connected contribution to the four-point electron Green's function. As is the case for the self-energy, all diagrams contributing to the vertex are one-particle irreducible. Referring back to the end of our discussion of linear response theory in Sec. 1.1, we see that the four-point correlation function shows up in dynamic response functions, particularly susceptibilities, that involve pairs of electron fields. Using Eq. (2.21), there are thus contributions to the susceptibilities from pairs of two-point functions, but also from the connected term that involves the four-point vertex, Eq. (2.22). Therefore, the latter are sometimes called *vertex corrections* or *vertex contributions*.

2.2.1 Keldysh index structure and Keldysh rotation

After introducing the primary quantities of interest, we now focus on the structure of the two-point and four-point functions regarding their dependence on Keldysh indices. Since a general n -point function is given via an expectation value of a product of n fermion fields, which can each be placed on either of the two branches of the Keldysh contour, it will have 2^n Keldysh components in total. The resulting additional “Keldysh” index is already one of the main complications of the Keldysh formalism compared to the Matsubara formalism.

Starting with the two-point Green’s function G , we explicitly write down all its four Keldysh components. Making only their dependence on time arguments and Keldysh indices explicit, we have

$$G^{-|+}(t_1|t_2) = -i\langle\mathcal{T}_{\mathcal{C}} c^-(t_1)\bar{c}^+(t_2)\rangle = i\langle\bar{c}(t_2)c(t_1)\rangle \equiv G^<(t_1, t_2) \quad (2.23a)$$

$$G^{+|-}(t_1|t_2) = -i\langle\mathcal{T}_{\mathcal{C}} c^+(t_1)\bar{c}^-(t_2)\rangle = -i\langle c(t_1)\bar{c}(t_2)\rangle \equiv G^>(t_1, t_2) \quad (2.23b)$$

$$G^{-|-}(t_1|t_2) = -i\langle\mathcal{T}_{\mathcal{C}} c^-(t_1)\bar{c}^-(t_2)\rangle = G^>(t_1, t_2)\theta(t_1 - t_2) + G^<(t_1, t_2)\theta(t_2 - t_1) \quad (2.23c)$$

$$G^{+|+}(t_1|t_2) = -i\langle\mathcal{T}_{\mathcal{C}} c^+(t_1)\bar{c}^+(t_2)\rangle = G^<(t_1, t_2)\theta(t_1 - t_2) + G^>(t_1, t_2)\theta(t_2 - t_1) \quad (2.23d)$$

where we defined the “greater” and “lesser” Green’s functions $G^>$ and $G^<$, and made the effect of the contour-time-ordering operator $\mathcal{T}_{\mathcal{C}}$ explicit. As can be confirmed easily from those definitions, the components of the Green’s function are not independent. Concretely, one component can be eliminated by making use of the equation

$$G^{-|+} + G^{+|-} - G^{-|-} - G^{+|+} = 0. \quad (2.24)$$

This redundancy motivates the *Keldysh rotation* [Kel64], defined as (summation convention implied)

$$G^{\alpha|\alpha'} = D^{\alpha|j} G^{jj'} (D^{-1})^{j'|\alpha'}, \quad (2.25)$$

with the matrix D and its inverse D^{-1} given by

$$D = \frac{1}{\sqrt{2}} \begin{pmatrix} 1 & -1 \\ 1 & 1 \end{pmatrix} \quad D^{-1} = \frac{1}{\sqrt{2}} \begin{pmatrix} 1 & 1 \\ -1 & 1 \end{pmatrix}. \quad (2.26)$$

Carrying out the transformation explicitly and employing Eq. (2.24), the Keldysh structure of the Green’s function reads

$$(G^{\alpha|\alpha'}) = \begin{pmatrix} 0 & G^A \\ G^R & G^K \end{pmatrix}, \quad (2.27)$$

where the component $G^{1|1}$ now vanishes by construction. Indeed, G^R labels the physically important *retarded* component of G , which was already introduced in Eq. (1.14). $G^A(t_1, t_2) = [G^R(t_2, t_1)]^*$ is the *advanced* component, which is related to the retarded component by complex conjugation, and $G^K(t_1, t_2) = G^>(t_1, t_2) + G^<(t_1, t_2) = -[G^K(t_2, t_1)]^*$ is called the *Keldysh* component.

The same transformation can be done for the self-energy Σ , whose Keldysh structure reads

$$(\Sigma^{\alpha'|\alpha}) = \begin{pmatrix} \Sigma^{1|1} & \Sigma^{1|2} \\ \Sigma^{2|1} & \Sigma^{2|2} \end{pmatrix} = \begin{pmatrix} \Sigma^K & \Sigma^R \\ \Sigma^A & 0 \end{pmatrix} \quad (2.28)$$

Compared to G , the Keldysh indices $\alpha', \alpha \in \{1, 2\}$ are interchanged, which is inferred from the structure of the Dyson equation, Eq. (2.19a). Likewise, the vertex is transformed into the Keldysh basis as

$$\Gamma^{\alpha_1' \alpha_2' | \alpha_1 \alpha_2} = D^{\alpha_1' | j_1'} D^{\alpha_2' | j_2'} \Gamma^{j_1' j_2' | j_1 j_2} (D^{-1})^{j_1 | \alpha_1} (D^{-1})^{j_2 | \alpha_2}. \quad (2.29)$$

Evidently, Γ is a $2^4 = 16$ -component matrix in Keldysh space. As for Σ , the Keldysh component that vanishes due to causality is the component where all Keldysh indices are equal to 2, i.e. $\Gamma^{22|22} = 0$. Furthermore, the bare interaction simplifies since the instantaneous interaction considered in this work is only finite if all contour indices are equal, see Eq. (2.16). Explicitly, this means in Keldysh space that

$$[\Gamma_0]^{\alpha_1' \alpha_2' | \alpha_1 \alpha_2} = \begin{cases} \Gamma_0/2 & \text{if } \alpha_1' + \alpha_2' + \alpha_1 + \alpha_2 \text{ odd} \\ 0 & \text{otherwise.} \end{cases} \quad (2.30)$$

In thermal equilibrium, the number of independent Keldysh components of all correlation functions is reduced to a single one through the now fermionic version of the fluctuation dissipation theorem, whose bosonic form was already given in Eq. (1.5). After performing a Fourier transform, possible in the steady state of thermal equilibrium, the FDT for G reads

$$G^K(\nu) = [1 - 2n_F(\nu)][G^R(\nu) - G^A(\nu)] = 2i \tanh\left(\frac{\beta\nu}{2}\right) \text{Im } G^R(\nu), \quad (2.31)$$

with the Fermi-Dirac distribution function $n_F(\nu) = [e^{\beta\nu} + 1]^{-1}$. The same equation holds for the Keldysh components of Σ . As the bosonic version, this equation is best proven using a spectral representation of G , which goes beyond the scope of this work (see, for example, Ref. [Ge+24]). Similar, though much more involved equations relate the Keldysh components of the vertex Γ in thermal equilibrium. They are also called ‘‘Kubo-Martin-Schwinger’’ (KMS) relations [Kub57; MS59]. Since we do not employ them in this work (the exception being one specific relation studied in the Appendix of Ref. [P4]), we refrain from discussing them here. For general KMS relations, see Refs. [WH02; JPS10; Ge+24].

Before closing this section, we comment on one subtlety regarding equal-time correlators, which is relevant to parts of the first publication reprinted in this thesis, Ref. [P1]. The definitions of $G^{-|-}$ and G^{++} in Eqs. (2.23) are ambiguous for the case $t_1 = t_2 \equiv t$, due to the non-unique definition of the Heaviside function for equal times. Therefore, when both Grassmann fields of the two-point function sit on the same point of the Keldysh contour, one must impose a particular ordering. Commonly, one demands *normal ordering* of the fields, meaning that all \bar{c} fields must be placed to the left of the c fields, which is required anyway for the construction of the functional integral, Eq. (2.12). Then, $G^{-|-}(t, t) = G^<(t, t) = G^{++}(t, t)$. In that case, Eq. (2.24) is not valid, so the result of the Keldysh rotation is different. For a detailed discussion of the consequences related to our work, see App. E of Ref. [P1]. Mostly, this subtlety is irrelevant when doing a Fourier transform to frequency space because the point $t_1 = t_2$ is of measure zero in time

integrals. It only becomes important in the case of propagator loops that begin and end at the same bare vertex because, due to its instantaneous nature, both Grassmann fields are evaluated on the same point of the contour in this case. In frequency space, this amounts to frequency integrals over only a single propagator.

2.2.2 Spin structure and SU(2) symmetry

After discussing the Keldysh index dependence of the two- and four-point correlation functions, we now turn to their spin dependence. A priori, it is similar to the Keldysh structure, since a general n -point function also has n spin indices, each of which can take two values, either spin up or spin down, $\sigma_i \in \{\uparrow, \downarrow\}$. An n -point correlation function thus has 2^n spin components. However, their spin structure strongly simplifies once SU(2) spin symmetry is imposed, which is, e.g., valid when no external magnetic field is applied.⁷ From this point on, and throughout this thesis, we will assume SU(2) spin symmetry. As a first consequence, all correlation functions conserve the total spin. For two-point functions, this means that they are diagonal in their spin arguments, e.g., $\Sigma_{\sigma_1'|\sigma_1} \sim \delta_{\sigma_1',\sigma_1}$. Furthermore, the two-point functions are invariant under global spin flips, $\Sigma_{\uparrow\uparrow} = \Sigma_{\downarrow\downarrow}$. In summary, there is hence just one independent spin component; therefore, the spin index for two-point functions can be dropped entirely.

For four-point functions, spin conservation due to SU(2) symmetry implies $\Gamma_{\sigma_1'\sigma_2'|\sigma_1\sigma_2} \sim \delta_{\sigma_1'+\sigma_2',\sigma_1+\sigma_2}$. As shown explicitly in Refs. [RVT12; Roh13], the non-zero spin components of the vertex are

$$\Gamma_{\sigma\bar{\sigma}|\sigma\bar{\sigma}} \equiv \Gamma_{\uparrow\downarrow}; \quad \Gamma_{\sigma\bar{\sigma}|\bar{\sigma}\sigma} \equiv \Gamma_{\uparrow\downarrow}^{\bar{}}; \quad \Gamma_{\sigma\sigma|\sigma\sigma} \equiv \Gamma_{\uparrow\uparrow}, \quad (2.32)$$

where a bar over a spin index indicates its inversion ($\bar{\uparrow} = \downarrow$ and vice versa). The notation in Eq. (2.32) signals that invariance under global spin flips was already exploited. Furthermore, SU(2) spin symmetry leads to another relation between the three components,

$$\Gamma_{\uparrow\uparrow} = \Gamma_{\uparrow\downarrow} + \Gamma_{\uparrow\downarrow}^{\bar{}}, \quad (2.33)$$

which leaves only two independent spin components.⁸

2.2.3 Further symmetries

Before closing this section, we comment that the vertex has numerous other symmetries that could be exploited in a numerical treatment. Among those is, in particular, crossing symmetry, which is a direct manifestation of the fermionic statistics of electrons. According to crossing symmetry, pairs of external fermionic indices can be swapped, yielding a minus sign but leaving the vertex otherwise unchanged,

$$\Gamma_{1'2'|12} = -\Gamma_{2'1'|12} = -\Gamma_{1'2'|21} = +\Gamma_{2'1'|21}. \quad (2.34)$$

⁷ In the sense of Sec. 1.1, this means that the undisturbed Hamiltonian should not include a magnetic field term. An external magnetic field can still be applied as an external perturbation to probe the magnetic susceptibility of the system. Remember that linear response determines this from the properties of the undisturbed system!

⁸ The number of independent spin components can be further reduced to just one also for the vertex using crossing symmetry $\Gamma_{1'2'|12} = -\Gamma_{1'2'|21}$ (see next subsection) to relate $\Gamma_{\uparrow\downarrow}$ and $\Gamma_{\uparrow\downarrow}^{\bar{}}$ [Roh13]. This relation is more intricate in practice, as it swaps different Keldysh components and two-particle channels when employing the parquet decomposition, which will be introduced in the next section. This relation is not used in this work.

Furthermore, ingoing at outgoing fermion lines can be interchanged by complex conjugation,

$$\Gamma_{1'2'|12} = (-1)^{1+\alpha_{1'}+\alpha_{2'}+\alpha_1+\alpha_2} \left[\Gamma_{12|1'2'} \right]^* , \quad (2.35)$$

which yields a minus sign depending on the combination of Keldysh indices. For details on the derivation of these symmetries and their concrete application, see Refs. [Jak10; JPS10; Wal22].

In addition to crossing symmetry and complex conjugation, which can be applied generally, the vertex might have even more symmetries depending on the physical problem of interest. For systems in thermal equilibrium, there is, in particular, time-translation invariance, which directly translates into frequency conservation after a Fourier transform of the time dependencies of the vertex. Time-translation invariance hence eliminates one of the four frequencies of the vertex and enables flexible and efficient parametrizations of the remaining three frequencies of the vertex, which will be discussed in the next section. Furthermore, time-reversal symmetry and/or particle-hole symmetry lead to symmetries in the frequency domain. These will not be discussed here; for details on this subject, see Ref. [Ge25].

2.3 Diagrammatic methods

In the previous section, we introduced the self-energy Σ and the vertex Γ , the primary quantities of interest in a quantum field theory treatment of correlated electronic systems, and discussed their generic properties in the Keldysh formalism. In this section, we summarize two (related) frameworks that can be used to compute these functions, namely the *parquet formalism* and the *functional renormalization group* in a vertex expansion. At their core, both frameworks provide exact relations for the quantities involved; however, some approximation always has to be employed to apply them in practice. Still, they stand out from other commonly used quantum field theory methods, because *(i)* they take contributions from all orders of perturbation theory in Γ_0 into account and *(ii)* they are both unbiased in the three two-particle channels of the vertex (see below), hence not singling out any kind of two-particle quantum fluctuation. The latter property is of great importance in modern condensed matter physics since, in many models of interest, such as the Hubbard model, different kinds of fluctuations compete on very similar energy scales, such that an unbiased treatment of them is paramount.

2.3.1 Parquet formalism

The parquet formalism is a framework for organizing the diagrammatic contributions to the four-point vertex Γ . It was developed in the mid-20th century [LAK54; DM64b; DM64a] and was soon applied to various problems in both high-energy physics [DST57] and solid-state physics [Abr65; NGR69; RGN69]. In the early 1990s, it was further formalized and used for the first time in numerical studies of condensed matter systems [BSW89; BW91]. In its modern formulation [Bic04], the starting point of the parquet formalism is the *parquet decomposition* of the two-particle vertex Γ , which classifies all connected, one-particle irreducible, and amputated four-point diagrams concerning their two-particle reducibility. A diagram is *two-particle reducible* (2PR) if it can be disconnected by cutting a *pair* of internal propagators. It turns out that there are three distinct types of two-particle reducible diagrams, depending on the orientation of the internal propagators to be cut: There exist three so-called *two-particle channels* a (for

“antiparallel”, sometimes called \overline{ph} for “particle-hole-crossed”), p (for “parallel”, sometimes called pp for “particle-particle”) and t (for “transversal antiparallel”, sometimes called ph for “particle-hole”). These three channels are mutually exclusive, meaning that any diagram that is 2PR in one channel cannot be 2PR in any of the other channels. All 2PR diagrams are thus part of one of the three 2PR vertices $\gamma_{r \in \{a,p,t\}}$. In addition, there exist diagrams that are not 2PR in any of the three channels. These diagrams are thus called *two-particle irreducible* (2PI) and are part of the 2PI vertex R . The parquet decomposition of the vertex Γ thus reads

$$\Gamma = R + \sum_{r \in \{a,p,t\}} \gamma_r \quad (2.36a)$$

$$= \begin{array}{c} \text{[Diagram: } R \text{]} \\ + \text{[Diagram: } \gamma_a \text{]} \\ + \text{[Diagram: } \gamma_p \text{]} \\ + \text{[Diagram: } \gamma_t \text{]} \end{array} \quad (2.36b)$$

$$= \begin{array}{c} \text{[Diagram: } R \text{]} \\ + \text{[Diagram: } \gamma_a \text{]} \\ + \frac{1}{2} \text{[Diagram: } \gamma_p \text{]} \\ - \text{[Diagram: } \gamma_t \text{]} \\ + O[(\Gamma_0)^3], \end{array} \quad (2.36c)$$

where we show the first diagrammatic contributions in perturbation theory in Eq. (2.36c) and indicate two-particle reducibility of the three two-particle channels.

At the heart of the parquet formalism lies a set of self-consistent equations for the self-energy Σ and the three two-particle reducible vertices γ_r . The latter are called *Bethe–Salpeter equations* (BSEs) [SB51],

$$\gamma_r = I_r \circ \Pi_r \circ \Gamma = \Gamma \circ \Pi_r \circ I_r. \quad (2.37)$$

Here, $I_r = \Gamma - \gamma_r$ labels the two-particle irreducible vertices in channel r . Π_r is the so-called “bubble”; a pair of propagators used to connect two vertices in channel r , and the symbol \circ is a shorthand notation for contractions over all quantum numbers and time or frequency integrations. The BSEs are symmetric under the exchange $\Gamma \leftrightarrow I_r$ on the right-hand side. Diagrammatically, the BSEs are depicted as

$$\begin{array}{c} \text{[Diagram: } \gamma_a \text{]} \\ = \text{[Diagram: } I_a \text{ and } \Gamma \text{ connected by a bubble]} \\ = \text{[Diagram: } \Gamma \text{ and } I_a \text{ connected by a bubble]} \end{array}, \quad (2.38a)$$

$$\begin{array}{c} \text{[Diagram: } \gamma_p \text{]} \\ = \frac{1}{2} \text{[Diagram: } I_p \text{ and } \Gamma \text{ connected by a bubble]} \\ = \frac{1}{2} \text{[Diagram: } \Gamma \text{ and } I_p \text{ connected by a bubble]} \end{array}, \quad (2.38b)$$

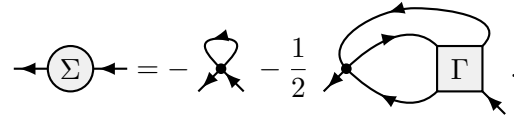
$$\begin{array}{c} \text{[Diagram: } \gamma_t \text{]} \\ = - \text{[Diagram: } I_t \text{ and } \Gamma \text{ connected by a bubble]} \\ = - \text{[Diagram: } \Gamma \text{ and } I_t \text{ connected by a bubble]} \end{array}, \quad (2.38c)$$

where we made the channel-specific numerical prefactors explicit. These are absorbed in the definitions of the propagator pairs Π_r . An explicit parametrization of these equations in the KF can be found in App. C of Ref. [P1].

In addition to the BSEs, the parquet formalism provides a relation between the vertex and the self-energy. This is an equation of motion called *Schwinger–Dyson equation* (SDE) [Dys49; Sch51],

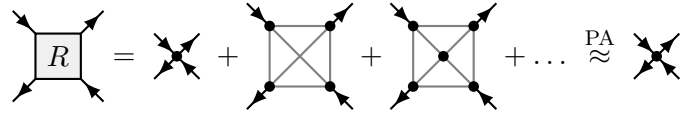
$$\Sigma = - \left[\Gamma_0 + \frac{1}{2} \Gamma_0 \circ \Pi_a \circ \Gamma \right] \cdot G. \quad (2.39)$$

Here, the symbol \cdot denotes the contraction of a four-point object with a single propagator. Note that the second term can be parametrized in terms of any of the three two-particle channels, the only differences being the prefactors (see, e.g., App. C of Ref. [P1]). Here, we chose the a channel parametrization exemplarily. Diagrammatically, the SDE is depicted as



$$\text{Diagrammatic SDE: } \Sigma \text{ (circle)} = - \text{tadpole} - \frac{1}{2} \text{two-vertex diagram} - \text{two-vertex diagram with } \Gamma \text{ box}. \quad (2.40)$$

Since the BSEs involve only full Green's functions G , into which Σ enters via the Dyson equation, Eq. (2.19a), the SDE and the three BSEs, together called the *parquet equations*, provide exact self-consistent relations for both the self-energy Σ and the 2PR vertices γ_r . For a formal derivation of these equations, see, e.g., Refs. [Kug19; Eck+23]. However, they cannot be solved without external input since the parquet formalism does not provide an equation for the 2PI vertex R . In practice, some expression for R must be provided to close the parquet equations and enable their self-consistent solution. At this point, some approximation typically has to be made since finding the exact result for R is usually impossible. The simplest possible approximation is called the *parquet approximation* (PA) and uses only the very first contribution to R in perturbation theory, which is the bare vertex,



$$R \text{ (square)} = \text{bare vertex} + \text{cross diagram} + \text{square diagram} + \dots \stackrel{\text{PA}}{\approx} \text{bare vertex}. \quad (2.41)$$

The next term contributing to R is of fourth order in perturbation theory. Hence, the PA can be justified if the bare coupling is small. However, it fails beyond intermediate coupling strengths for the same reason. While the PA is employed in two publications reprinted in this thesis [P1; P2], in the last one, Ref. [P4], we go beyond the PA and investigate the parquet equations at large interaction.

2.3.2 Frequency structure of the vertex

After introducing the parquet decomposition of the vertex, we now provide details on one of the technically most important parts regarding practical calculations: the parametrization of the vertex in frequency space. Since we are, in the context of this work, only interested in the steady state of thermal equilibrium, after a Fourier transform, all correlation functions satisfy (real) frequency conservation. Hence, three instead of four frequencies are sufficient for a complete parametrization for the vertex. It turns out that different choices for these three frequencies are preferential in practice, depending on the two-particle channel in question. For each of those, a bosonic transfer frequency

ω_r and two fermionic frequencies ν_r and ν'_r are used⁹:

$$\begin{array}{c}
 \begin{array}{ccc}
 \nu_2 & \nu_2' & \\
 \swarrow & \nearrow & \\
 \Gamma & & \\
 \nwarrow & \searrow & \\
 \nu_1' & \nu_1 &
 \end{array}
 & = &
 \begin{array}{ccc}
 \nu_2 & \nu_2' & \\
 \swarrow & \nearrow & \\
 R & & \\
 \nwarrow & \searrow & \\
 \nu_1' & \nu_1 &
 \end{array}
 +
 \begin{array}{ccc}
 \nu_a + \frac{\omega_a}{2} & \nu'_a + \frac{\omega_a}{2} & \\
 \swarrow & \nearrow & \\
 \gamma_a & & \\
 \nwarrow & \searrow & \\
 \nu_a - \frac{\omega_a}{2} & \nu'_a - \frac{\omega_a}{2} &
 \end{array}
 +
 \begin{array}{ccc}
 \frac{\omega_p}{2} - \nu'_p & \frac{\omega_p}{2} - \nu_p & \\
 \swarrow & \nearrow & \\
 \gamma_p & & \\
 \nwarrow & \searrow & \\
 \frac{\omega_p}{2} + \nu_p & \frac{\omega_p}{2} + \nu'_p &
 \end{array}
 +
 \begin{array}{ccc}
 \nu_t + \frac{\omega_t}{2} & \nu_t - \frac{\omega_t}{2} & \\
 \swarrow & \nearrow & \\
 \gamma_t & & \\
 \nwarrow & \searrow & \\
 \nu'_t + \frac{\omega_t}{2} & \nu'_t - \frac{\omega_t}{2} &
 \end{array}
 \end{array}
 \quad (2.42)$$

The definitions of the frequency sets $\{\omega_r, \nu_r, \nu'_r\}$ can be inferred from Eq. (2.42). They are explicitly written down in App. A of Ref. [Wal22], together with the linear transformations between the three parametrizations. The main practical advantages of the channel-dependent frequency parametrization are that (i) the structures of the vertices are centered around $\omega_r = 0$ due to the symmetric parametrization and that (ii) the contributions to the 2PR vertices can be decomposed further into *asymptotic classes*, depending on their asymptotic behavior in the limit of large frequencies.

2.3.3 Asymptotic classes

The decomposition of each of the three two-particle channels into four *asymptotic classes*, respectively, was introduced in Ref. [Wen+20]. It uses the fact that the instantaneous bare vertex Γ_0 is frequency independent. Consequently, diagrams in which external fermion propagator lines meet at the same bare vertex do not depend on all three frequencies when using the channel-dependent frequency parametrization. Hence, their numerical parametrization is simplified significantly. Also, those diagrams yield a finite contribution in the limit, in which the frequencies they do not depend on are taken to infinity. Hence the name “asymptotic classes”. Concretely, in each two-particle channel r , one defines

- (i) the $K_{1,r}$ class, where both pairs of external fermion lines meet at the same bare vertex, respectively. In the frequency parametrization native to channel r , these diagrams only depend on the bosonic transfer frequency ω_r . They can hence be extracted from γ_r by taking the limit of both fermionic frequencies to infinity,

$$K_{1,r}(\omega_r) = \lim_{\nu_r \rightarrow \infty} \lim_{\nu'_r \rightarrow \infty} \gamma_r(\omega_r, \nu_r, \nu'_r) \stackrel{r=a}{=} \nu_a \left(\begin{array}{c} \xrightarrow{\omega_a} \\ \swarrow \quad \nearrow \\ K_{1,a} \\ \nwarrow \quad \searrow \\ \nu'_a \end{array} \right), \quad (2.43a)$$

- (ii) the $K_{2,r}$ class, where the right pair of external fermion lines meets at the same bare vertex, but the left external lines attach to different bare vertices. Those diagrams do not depend on the fermionic frequency ν_r and can hence be extracted by taking the limit $\nu_r \rightarrow \infty$ and subtracting the $K_{1,r}$ class,

$$K_{2,r}(\omega_r, \nu_r) = \lim_{\nu'_r \rightarrow \infty} \gamma_r(\omega_r, \nu_r, \nu'_r) - K_{1,r}(\omega_r) \stackrel{r=a}{=} \nu_a \left(\begin{array}{c} \xrightarrow{\omega_a} \\ \swarrow \quad \nearrow \\ K_{2,a} \\ \nwarrow \quad \searrow \\ \nu'_a \end{array} \right), \quad (2.43b)$$

- (iii) the $K_{2',r}$ class, which is similar to the $K_{2,r}$ class, the difference being that the role of the left and right pair of external fermion lines is interchanged. Hence, it does

⁹ The nomenclature of “bosonic” and “fermionic” frequencies is due to the Matsubara formalism, which distinguishes between even (“bosonic”) and odd (“fermionic”) Matsubara frequencies. For real-frequency calculations, there is no practical difference between these two types.

not depend on the fermionic frequency ν_r and can be extracted as

$$K_{2',r}(\omega_r, \nu_r') = \lim_{\nu_r \rightarrow \infty} \gamma_r(\omega_r, \nu_r, \nu_r') - K_{1,r}(\omega_r) \stackrel{r \equiv a}{=} \nu_a \left(\begin{array}{c} \omega_a \\ \swarrow \quad \searrow \\ K_{2',a} \\ \nwarrow \quad \nearrow \\ \nu_a \end{array} \right) \nu_a', \quad (2.43c)$$

- (iv) and the $K_{3,r}$ class, which consists of all diagrams in channel r that genuinely depend on all three frequencies independently. It can thus easily be extracted by subtracting the other three diagrammatic classes from the reducible vertex,

$$K_{3,r}(\omega_r, \nu_r, \nu_r') = \gamma_r(\omega_r, \nu_r, \nu_r') - K_{1,r}(\omega_r) - K_{2,r}(\omega_r, \nu_r) - K_{2',r}(\omega_r, \nu_r')$$

$$\stackrel{r \equiv a}{=} \nu_a \left(\begin{array}{c} \omega_a \\ \swarrow \quad \searrow \\ K_{3,a} \\ \nwarrow \quad \nearrow \\ \nu_a \end{array} \right) \nu_a'. \quad (2.43d)$$

To fully exploit the simplifications the asymptotic decomposition entails, the BSEs, Eq. (2.37), can likewise be formulated for the individual asymptotic contributions [Gie+22]. For a detailed numerical study of those, see in particular Ref. [P4].

2.3.4 Functional renormalization group

The functional renormalization group (fRG) [KBS10; Met+12; Dup+21] is a general quantum field theoretical framework inspired by the traditional “Wilsonian” renormalization group (RG) [Wil75; Sha94]. There, high-energy fluctuations are successively integrated out to identify the relevant parameters in a corresponding low-energy (i.e., large length scale) effective theory. The fRG generalizes this concept to correlation functions, starting from an exact functional flow equation for the generating functional, called the “Wetterich equation” [Wet93]. A subsequent “vertex expansion” of the Wetterich equation yields an infinite hierarchy of flow equations for 1PI vertices [Mor94], which is the starting point of the following discussion. Mathematically, the flow equations are a set of coupled ordinary differential equations, which describe the evolution of the 1PI vertices with respect to a flow parameter Λ . In the Wilsonian sense, Λ would represent an energy scale, such as an energy or momentum cutoff, to be incrementally lowered throughout the RG flow. It turns out, however, that the fRG is more general in that regard, in that Λ could, in principle, represent any single-particle parameter of the theory. In this sense, the fRG can be used to interpolate between two points in an abstract “theory space”. In practice, an fRG flow is started at some initial value Λ_i of the flow parameter, at which the theory is under control, in the sense that the self-energy and vertex are known, at least to a good enough approximation. The flow equations are then integrated up to a final value Λ_f ,

$$\Sigma^f = \int_{\Lambda_i}^{\Lambda_f} d\Lambda \dot{\Sigma}^\Lambda \quad \Gamma^f = \int_{\Lambda_i}^{\Lambda_f} d\Lambda \dot{\Gamma}^\Lambda, \quad (2.44)$$

which should represent the actual theory of interest.

The first two fRG flow equations of the hierarchy for a fermionic theory with a quartic interaction read

$$\dot{\Sigma} = -\Gamma \cdot S = - \text{[Diagram: A square box labeled } \Gamma \text{ with a loop on top and two external legs on the bottom]}, \quad (2.45a)$$

$$\begin{aligned} \dot{\Gamma} &= \sum_{r \in \{a,p,t\}} \Gamma \circ \dot{\Pi}_r^S \circ \Gamma + \Gamma^{(6)} \cdot S \\ &= \text{[Diagram: Two squares labeled } \Gamma \text{ connected by a loop]} + \frac{1}{2} \text{[Diagram: Two squares labeled } \Gamma \text{ connected by two loops]} - \text{[Diagram: Two squares labeled } \Gamma \text{ connected by a loop with a diagonal line]} + \text{[Diagram: A hexagon labeled } \Gamma^{(6)} \text{ with two external legs]}, \end{aligned} \quad (2.45b)$$

and can be compactly represented diagrammatically. Here, $S = \partial_\Lambda G|_{\Sigma=\text{const.}}$ is called the *single scale propagator*.¹⁰ The crossed out “bubble terms” are a shorthand notation for the sum of two terms, $\dot{\Pi}_r^S = (GS + SG)_r$, parametrized in the corresponding channel r . One notable feature of the fRG compared to many other diagrammatic methods in many-body theory is that it is unbiased in the three two-particle channels a , p , and t since all three of them are included equitably inside the flow equations. It can hence be used to compare the magnitude of quantum fluctuations in the three channels without singling out any of them from the beginning as, e.g., done in the “random phase approximation” (RPA), which sums a ladder series in a given channel [NO19]. However, the flow equation for the n -point vertex requires the $(n+2)$ -point vertex as an input to the right-hand side. In practice, this turns out to be problematic since the six-point vertex $\Gamma^{(6)}$, required in the flow equation for the four-point vertex, is a high-dimensional object that depends on six arguments (or at least five, if energy-momentum conservation can be exploited). In most cases, this makes the six-point vertex numerically intractable. For this reason, in most concrete applications of the vertex expansion of fRG, the contribution from $\Gamma^{(6)}$ is neglected altogether. Due to the diagrammatic structure of the flow equation, this is called the “one-loop” truncation of the fRG flow hierarchy. This truncation can be argued to be justified in the weak interaction regime, since there is no bare contribution to $\Gamma^{(6)}$, but it only starts at third order in the bare four-point interaction. However, as has been argued at length in Refs. [KD18c; KD18b; KD18a; Kug19], this truncation introduces several issues: First, the one-loop truncation cannot be expected to be quantitatively reliable beyond weak interaction, since this assumption was used to neglect the contribution from the six-point vertex in the first place. Second, while still being unbiased in the three two-particle channels a , p , and t , the one-loop truncation places a bias on ladder diagrams. As a consequence, it predicts ordering tendencies too strongly, ultimately leading to a violation of the Mermin–Wagner theorem [MW66; Kat09; MH12]. Third, the flow equation for the four-point vertex Γ ceases to be a total derivative with respect to the flow parameter Λ when the contribution from the six-point vertex is neglected. Consequently, the solution of the flow equation depends on the regulator that was chosen, i.e. on the “path” that was taken through the abstract “theory space”

¹⁰ So-called because in a regulator scheme with a sharp cutoff, S becomes a delta function in frequency space, singling out a particular energy scale.

during the integration of the differential equation, Eq. (2.44). This regulator dependence is unphysical since the choice of regulator is arbitrary and seriously limits the predictive power of fRG in the one-loop truncation. We will see an explicit example of this regulator dependence later in Ref. [P1].

As laid out in Refs. [KD18c; KD18b; KD18a; Kug19], all of the before-mentioned shortcomings of the one-loop truncation in fRG can be improved or even cured by iteratively adding higher loop-order contributions to the flow equations. Formally, these contributions can be organized as

$$\dot{\Gamma} = \sum_{r \in \{a,p,t\}} \dot{\gamma}_r; \quad \dot{\gamma}_r = \sum_{\ell=1}^{\infty} \dot{\gamma}_r^{(\ell)}, \quad (2.46)$$

where the flow equations at any given loop order ℓ depend on the vertices at lower loop orders. Concretely, these *multiloop flow-equations* for the 2PR vertices read

$$\dot{\gamma}_r^{(1)} = \Gamma \circ \dot{\Pi}_r \circ \Gamma \stackrel{r=a}{\equiv} \text{Diagram}, \quad (2.47a)$$

$$\dot{\gamma}_r^{(2)} = \dot{\gamma}_r^{(1)} \circ \Pi_r \circ \Gamma + \Gamma \circ \Pi_r \circ \dot{\gamma}_r^{(1)} \stackrel{r=a}{\equiv} \underbrace{\text{Diagram}}_{\dot{\gamma}_{a,L}^{(2)}} + \underbrace{\text{Diagram}}_{\dot{\gamma}_{a,R}^{(2)}}, \quad (2.47b)$$

$$\dot{\gamma}_a^{(\ell>2)} = \dot{\gamma}_r^{(\ell-1)} \circ \Pi_r \circ \Gamma + \Gamma \circ \Pi_r \circ \dot{\gamma}_r^{(\ell-2)} \circ \Pi_r \circ \Gamma + \Gamma \circ \Pi_r \circ \dot{\gamma}_r^{(\ell-1)} \stackrel{r=a}{\equiv} \underbrace{\text{Diagram}}_{\dot{\gamma}_{a,L}^{(\ell>2)}} + \underbrace{\text{Diagram}}_{\dot{\gamma}_{a,C}^{(\ell>2)}} + \underbrace{\text{Diagram}}_{\dot{\gamma}_{a,R}^{(\ell>2)}}, \quad (2.47c)$$

In these equations, the single-scale propagator S has been replaced by the full derivative of the propagator,¹¹ $\partial_\Lambda G = S + G\Sigma G$. Starting at third loop order, the flow equations for the self-energy Σ also has to be modified,

$$\dot{\Sigma} \leftarrow = - \text{Diagram} - \underbrace{\text{Diagram}}_{\dot{\Sigma}_{\bar{t}}} - \underbrace{\text{Diagram}}_{\dot{\Sigma}_t}. \quad (2.48)$$

¹¹ It was already proposed in Ref. [Kat04] to replace S by $\partial_\Lambda G$. This replacement was argued to improve the fulfillment of Ward identities, which we will discuss later in the thesis, in fRG. It has since been commonly adopted and called “Katanin substitution”.

Notably, the multiloop flow equation for the vertex feeds into the multiloop flow equation for self-energy and vice versa. Starting at the third loop order, a self-consistent treatment of the flow equations is required, which is not the case in the one-loop truncation.

It can be shown that, if converged in the number of loop orders ℓ , the multiloop hierarchy of fRG flow equations adds precisely the 2PR contributions from the six-point vertex required to reinstate the property of the flow equation for the four-point vertex being a full derivative. This way, the one-loop truncation's unphysical property of regulator dependence is cured. Indeed, a converged solution of the multiloop flow exactly yields a solution of the self-consistent parquet equations, which is inherently independent of any regulator. It was shown in Ref. [KD18a] that the multiloop flow equations can even be derived by introducing a regulator into the parquet equations via the bare propagator $G_0 \rightarrow G_0^\Lambda$ and taking the derivative w.r.t. Λ . Self-consistently solving the parquet equations is, therefore, equivalent to solving the multiloop flow equations. Furthermore, the bias on ladder diagrams of the one-loop truncation is cured, such that the multiloop fRG (mfRG) satisfies the Mermin-Wagner theorem. Still, as the mfRG uses the parquet decomposition of the vertex and does not provide a flow equation for its 2PI part R , some expression for R has to be supplied, or an approximation has to be made. The PA is the easiest choice, rendering the mfRG accurate only in the weak interaction regime. However, since the PA for Γ is exact up to (not including) fourth order in the bare interaction Γ_0 , this is still an improvement over the one-loop truncation, which is exact only up to third order.

By now, the mfRG has been applied to various problems in the field of correlated many-body systems such as electronic systems like the Anderson impurity model [Cha+22], the 2D Hubbard model [Tag+19; Fra+22], or quantum spin systems [Tho+20; Kie+22; Rit+22]. However, these studies used mfRG in either the finite- or zero-temperature Matsubara formalism. Building upon work already started in Ref. [Wal22], mfRG calculations are now also possible in the KF. While results from mfRG are not included in Ref. [P1], the codebase presented in Ref. [P2] can perform mfRG calculations for the Anderson impurity model using various regulators.

However, it is unclear whether there are circumstances in which solving the mfRG flow equations is numerically preferential over directly solving the parquet equations in the Keldysh formalism. This assertion was one of the main motivations for developing the framework since solving ordinary differential equations in general is numerically easier than solving self-consistent equations. In mfRG, however, requiring convergence in the loop order ℓ may necessitate a large number of calculations at each step, and the iterations of the flow equations for the self-energy and the vertex starting at $\ell = 3$ re-introduces a self-consistency to be satisfied, which is not present in the one-loop fRG. While this is already an issue for mfRG calculations in the Matsubara formalism, in the Keldysh formalism, it seems that on top of that, the contributions to the vertex flow acquire increasingly sharp structures in higher loop orders; see the appendix of Ref. [Ge25]. Such sharp structures require ever denser frequency grids, far beyond what is needed to resolve the full vertex. It has therefore been concluded that there currently is no practical advantage of the mfRG flow equations over the parquet equations themselves.

This point marks the end of our introduction to real-frequency quantum field theory in the Keldysh formalism. In the following, we reprint two publications in which these methods are applied. The first one, Ref. [P1], performs extensive fRG and parquet computations on the single-impurity Anderson model, benchmarking these methods against the numerical

renormalization group later introduced in Secs. 3.1 and 3.2. In the second publication, Ref. [P2], many technical details regarding the implementation of the codebase written to perform these calculations are presented, including a detailed discussion of the mRG algorithm.

Real-frequency quantum field theory applied to the single-impurity Anderson model

by

A. Ge*¹, N. Ritz*¹, E. Walter¹, S. Aguirre¹, J. von Delft¹, and
F.B. Kugler^{2,3}

¹ Arnold Sommerfeld Center for Theoretical Physics, Center for NanoScience, and
Munich Center for Quantum Science and Technology,
Ludwig-Maximilians-Universität München, 80333 Munich, Germany

² Center for Computational Quantum Physics, Flatiron Institute,
162 5th Avenue, New York, New York 10010, USA

³ Department of Physics and Astronomy and Center for Materials Theory,
Rutgers University, Piscataway, New Jersey 08854, USA

reprinted on pages **31–54**

with permission from

Phys. Rev. B **109**, 115128 (2024),

<https://doi.org/10.1103/PhysRevB.109.115128>

American Physical Society, 2024.

Real-frequency quantum field theory applied to the single-impurity Anderson model

Anxiang Ge ^{1,*}, Nepomuk Ritz ^{1,*}, Elias Walter ¹, Santiago Aguirre,¹ Jan von Delft ¹ and Fabian B. Kugler ^{2,3}

¹*Arnold Sommerfeld Center for Theoretical Physics, Center for NanoScience, and Munich Center for Quantum Science and Technology, Ludwig-Maximilians-Universität München, 80333 Munich, Germany*

²*Center for Computational Quantum Physics, Flatiron Institute, 162 5th Avenue, New York, New York 10010, USA*

³*Department of Physics and Astronomy and Center for Materials Theory, Rutgers University, Piscataway, New Jersey 08854, USA*

 (Received 2 November 2023; revised 6 February 2024; accepted 6 February 2024; published 15 March 2024)

A major challenge in the field of correlated electrons is the computation of dynamical correlation functions. For comparisons with experiment, one is interested in their real-frequency dependence. This is difficult to compute because imaginary-frequency data from the Matsubara formalism require analytic continuation, a numerically ill-posed problem. Here, we apply quantum field theory to the single-impurity Anderson model using the Keldysh instead of the Matsubara formalism with direct access to the self-energy and dynamical susceptibilities on the real-frequency axis. We present results from the functional renormalization group (fRG) at the one-loop level and from solving the self-consistent parquet equations in the parquet approximation. In contrast with previous Keldysh fRG works, we employ a parametrization of the four-point vertex which captures its full dependence on three real-frequency arguments. We compare our results to benchmark data obtained with the numerical renormalization group and to second-order perturbation theory. We find that capturing the full frequency dependence of the four-point vertex significantly improves the fRG results compared with previous implementations, and that solving the parquet equations yields the best agreement with the numerical renormalization group benchmark data but is only feasible up to moderate interaction strengths. Our methodical advances pave the way for treating more complicated models in the future.

DOI: [10.1103/PhysRevB.109.115128](https://doi.org/10.1103/PhysRevB.109.115128)

I. INTRODUCTION

Strongly correlated electrons are of central interest in condensed-matter physics and a prime application for quantum field theory (QFT). Two current frontiers in this context are (i) dealing with two-particle correlations on top of the familiar one-particle correlations, and (ii) obtaining real-frequency information relevant to experiments, as opposed to imaginary-frequency information popular in theoretical analyses. Indeed, much attention has recently been devoted to the two-particle—or four-point (4p)—vertex of correlated systems, e.g., regarding efficient representations [1–7] or the divergences of two-particle irreducible vertices [8–22]. Moreover, new algorithms have emerged, such as diagrammatic Monte Carlo for real-frequency 2p functions (one frequency argument) working with analytic Matsubara summation [23–29] or real-time integration [30–33], as well as numerical renormalization group (NRG) computations of real-frequency 4p functions (three frequency arguments) [34,35].

Here, we combine aspects (i) and (ii) and study real-frequency two-particle correlations in a QFT framework within the Keldysh formalism (KF) [36–38]. We employ two related methods: functional renormalization group (fRG) flows at one-loop level [39] and solutions of the self-consistent parquet equations [40]. These approaches are promising candidates for real-frequency diagrammatic extensions [41] of

dynamical mean-field theory [42], where the self-consistently determined impurity model is solved with NRG [43]. In practice, this means using the NRG 4p vertex [34,35] as input for fRG [44,45] or the parquet equations [46,47]. Fully exploiting this nonperturbative input requires taking the full frequency dependence of the 4p vertex into account. The present work is a proof-of-principle study showing that it is indeed possible to track the three-dimensional *real-frequency* dependence of the 4p vertex with fRG and parquet methods.

To demonstrate our capability of handling 4p vertices in real frequencies, we choose the well-known [48] single-impurity Anderson model (AM) [49] as a test case. Its 4p vertex depends only on frequency and spin arguments, orbital or momentum degrees of freedom are not involved. Moreover, we can benchmark our results against numerically exact data obtained with NRG [43].

On a historical note, we mention some early pioneering works on the AM where multipoint functions depending on multiple real frequencies were computed using various diagrammatic methods [50–53]. Anders and Grewe [50,51] computed the finite-temperature impurity density of states and spin-fluctuation spectra up to order $O(1/N^2)$ in a large- N expansion using a resummation that included skeleton diagrams of the crossing variety up to infinite order. This approach involved the analytic continuation of 2p and 3p functions from imaginary to real frequencies. Kroha, Wölfle, and Costi [52,53] studied the AM in the strong-coupling limit using a slave-boson treatment of local fermions and a conserving T -matrix approximation. They computed the auxiliary (pseudofermion and slave boson) spectral functions in the

*These authors contributed equally to this work.

Kondo regime. Their approach involved the analytic continuation of T matrices (4p objects depending on three frequencies) from imaginary to real frequencies. This was possible due to two simplifications arising in their approach. First, the Bethe–Salpeter equations for the T matrices were simplified via ladder approximations that neglect interchannel feedback but are sufficient to capture the leading and subleading infrared singularities. Second, the auxiliary propagators involve projection factors that cause their contributions to vanish along the branch cuts encountered during the analytic continuation of the T matrices. As a result, only integrations along branch cuts of the conduction-electron propagators contribute to the auxiliary-particle self-energies. In particular, only one of the fifteen Keldysh components of the T matrices were involved in these computations.

In the present paper, we consider a more general setting. We compute the full 4p (impurity-electron) vertex, which requires a treatment of the complete Keldysh structure. Furthermore, the diagrammatic methods considered here—the fRG and the parquet equations—treat all three channels of two-particle fluctuations (density, magnetic, pairing) in an equitable manner, fully including interchannel feedback. The latter causes severe technical complications: each channel has its own frequency parametrization; hence, interchannel feedback involves interpolations between different frequency parametrizations, which in turn demand great care when working with discrete frequency grids. One of our goals is to develop numerical strategies for conquering these complications in a general, robust manner, as a first step toward studying more complicated models in future work.

Keldysh fRG flows with dynamic 2p and 4p functions were pioneered by Jakobs and collaborators [54–56] and subsequently used in Refs. [57–59]. In all of these works, the dependence of the 4p vertex on three frequencies was approximated by a sum of three functions, each depending on only one (bosonic) frequency. Here, we present Keldysh one-loop fRG flows with the full, three-dimensional frequency dependence of the vertex, finding remarkable improvement compared with previous implementations [54,55]. We also solve the parquet equations in the parquet approximation (PA) in this setting, yielding results closest to NRG in the regime where the parquet self-consistency iteration converges. This regime corresponds rather accurately to the condition $u < 1$, where $u = U/(\pi\Delta)$ is the dimensionless coupling constant that controls the (convergent bare) zero-temperature perturbation series [60]. For completeness, we also discuss second-order perturbation theory (PT2). Although the PT2 self-energy in the particle-hole symmetric AM (sAM) yields strikingly good results (for known reasons, see Sec. II E), the susceptibilities or the results in the asymmetric AM (aAM) clearly show the benefits of the infinite diagrammatic resummations provided by fRG and the PA.

A conceptual equivalence between truncated fRG flows and solutions of the parquet equations has been established via the multiloop fRG [61–63]. For the AM treated in imaginary frequencies, this equivalence was analyzed numerically in Ref. [64], and multiloop convergence was demonstrated up to moderate interaction strengths. We refrain from presenting a similar study in real frequencies here, leaving that for future work.

The rest of the paper is organized as follows: In Sec. II, we give a minimal introduction to the KF (Sec. II A) and summarize the methodical background for fRG and the PA (Secs. II B and II C). The AM is briefly introduced in Sec. II D, followed by a concise description of our benchmark methods for this model (Sec. II E). In Sec. III, we present our results, beginning with dynamical correlation functions computed directly on the real-frequency axis (Sec. III A). We then turn to various static properties in Sec. III B and check the fulfillment of zero-temperature identities between them (Sec. III C). The frequency-dependent two-particle vertex is shown in Sec. III D. We conclude in Sec. IV and give a brief outlook on possibilities for future work.

Nine Appendixes are devoted to technical matters. Appendix A summarizes our parametrization of the 4p vertex and its symmetry relations. Appendix B shows the frequency dependence of all vertex components, as obtained in the PA. The fully parametrized parquet and fRG flow equations are stated in Appendix C, and Appendix D discusses a channel-adapted evaluation of the Schwinger–Dyson equation for the self-energy in the PA. Appendix E deals with a known equal-time subtlety in the KF, relevant for computing, e.g., the Hartree self-energy in the aAM. In Appendix F, we give a concise definition of all diagrammatic contributions to PT2. We provide more details on the actual fRG and PA implementation in Appendix G and comment on the numerical costs in Appendix H. Finally, Appendix I scrutinizes the fRG static magnetic susceptibility at $u \gtrsim 1$ for different settings of the frequency resolution.

II. BACKGROUND

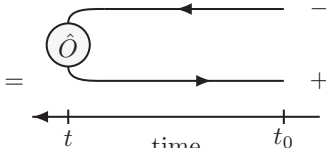
A. Keldysh formalism

The Keldysh formalism [36–38] is a suitable framework for studying systems out of equilibrium, as well as systems in thermal equilibrium if aiming for a finite-temperature real-frequency description. An extensive introduction can be found in Ref. [65]; more compact introductions in the context of fRG are also given in related Ph.D. theses [54,57,66,67]. Here, we only give a short summary of the concepts needed in this paper.

Consider a (potentially time-dependent) Hamiltonian $H(t)$ and a density matrix known at time t_0 , $\rho_0 = \rho(t_0)$. The expectation value of an operator \hat{O} at time t reads

$$\langle \hat{O}(t) \rangle = \text{Tr} \left[\tilde{\mathcal{T}} e^{-i \int_{t_0}^t dt' H(t')} \hat{O} \mathcal{T} e^{-i \int_{t_0}^t dt' H(t')} \rho_0 \right]. \quad (1)$$

Here, \mathcal{T} is the time-ordering operator, and $\tilde{\mathcal{T}}$ denotes antitime ordering. In the KF, one rewrites Eq. (1) as

$$\langle \hat{O}(t) \rangle = \text{Tr} \left[\mathcal{T}_C \left\{ e^{-i \int_t^{t_0} dt' H^+(t')} \hat{O} e^{-i \int_{t_0}^t dt' H^-(t')} \rho_0 \right\} \right]$$


$$= \quad (2)$$

The Hamiltonian, and all operators in it, acquire an additional contour index $c = \mp$, indicating whether they sit on the

forward (−) or backward (+) branch of the Keldysh double-time contour. The contour-ordering operator \mathcal{T}_C puts all operators on the backward branch left of those on the forward branch, and antitime orders (time orders) them on the backward (forward) branch.

In the above equation, \hat{O} , inserted at time t , can be placed on either branch. However, if \hat{O} is a product of multiple operators, they also come with contour indices to ensure the correct ordering. It follows that an n -point correlator generically has 2^n Keldysh components. For example, the two-point correlator in terms of the creation (ψ^\dagger) and the annihilation operator (ψ) reads

$$G^{c|c'}(t, t') = -i\langle \mathcal{T}_C \psi^c(t) \psi^{\dagger c'}(t') \rangle. \quad (3)$$

Resolving the contour indices c, c' yields the matrix

$$G^{c|c'} = \begin{pmatrix} G^{-| -} & G^{-| +} \\ G^{+| -} & G^{+| +} \end{pmatrix} = \begin{pmatrix} G^T & G^< \\ G^> & G^{\bar{T}} \end{pmatrix}. \quad (4)$$

Using the redundancy $G^< + G^> - G^T - G^{\bar{T}} = 0$, which holds as long as $t \neq t'$ (see Appendix E for the case $t = t'$), the Keldysh structure of G can be simplified. The Keldysh rotation invokes the Keldysh indices $k = 1$ and 2 , where

$$\psi^1 = \frac{1}{\sqrt{2}}(\psi^- - \psi^+), \quad \psi^2 = \frac{1}{\sqrt{2}}(\psi^- + \psi^+), \quad (5)$$

and equivalently for ψ^\dagger . We can thus define a basis transformation matrix D via $\psi^k = D^{kc} \psi^c$:

$$D = \frac{1}{\sqrt{2}} \begin{pmatrix} 1 & -1 \\ 1 & 1 \end{pmatrix}, \quad D^{-1} = \frac{1}{\sqrt{2}} \begin{pmatrix} 1 & 1 \\ -1 & 1 \end{pmatrix}. \quad (6)$$

Rotating G as $G^{k|k'} = D^{kc} G^{c|c'} (D^{-1})^{c'k'}$ yields

$$G^{k|k'} = \begin{pmatrix} G^{1|1} & G^{1|2} \\ G^{2|1} & G^{2|2} \end{pmatrix} = \begin{pmatrix} 0 & G^A \\ G^R & G^K \end{pmatrix}, \quad (7)$$

where $G^{1|1} = 0$ follows from the redundancy mentioned above. We find the retarded propagator

$$G^R(t_1, t_2) = -i\Theta(t_1 - t_2) \langle \{c(t_1), c^\dagger(t_2)\} \rangle, \quad (8)$$

where $\{\cdot, \cdot\}$ denotes the anticommutator, and its advanced counterpart $G^A(t_1, t_2) = [G^R(t_2, t_1)]^*$, as well as the Keldysh propagator $G^K(t_1, t_2) = -[G^K(t_2, t_1)]^*$ [54].

For a time-independent problem, we have $G(t_1, t_2) = G(t_1 - t_2)$ and frequency conservation with

$$G(\nu) = \int dt e^{i\nu t} G(t), \quad G(t) = \int \frac{d\nu}{2\pi} e^{-i\nu t} G(\nu). \quad (9)$$

In the following, we consider thermal equilibrium at temperature T and chemical potential μ , set to zero. Then, the density matrix is $\rho_0 = e^{-H/T}/\mathcal{Z}$ (with $k_B = 1$ and $\mathcal{Z} = \text{Tr} e^{-H/T}$), and the Keldysh components of G fulfill the fluctuation-dissipation theorem (FDT) [54,65]

$$G^K(\nu) = 2i \tanh\left(\frac{\nu}{2T}\right) \text{Im} G^R(\nu). \quad (10)$$

B. Diagrammatic framework

The one-particle propagator can be expressed through the bare propagator G_0 and the self-energy Σ via the Dyson

equation. Using multi-indices $1, 1'$, etc., we have

$$G_{1|1'} = \overleftarrow{1} \overleftarrow{1'} = \overleftarrow{1} \overleftarrow{1'}_{G_0} + \overleftarrow{1} \overleftarrow{2'} \overrightarrow{2} \overleftarrow{1'}_G, \quad (11)$$

where the internal arguments $2, 2'$ are summed over. This equation is solved by $G = (G_0^{-1} - \Sigma)^{-1}$. The self-energy has a Keldysh structure similar to Eq. (7),

$$\Sigma^{k'|k_1} = \begin{pmatrix} \Sigma^{1|1} & \Sigma^{1|2} \\ \Sigma^{2|1} & \Sigma^{2|2} \end{pmatrix} = \begin{pmatrix} \Sigma^K & \Sigma^R \\ \Sigma^A & 0 \end{pmatrix}, \quad (12)$$

and $\Sigma^K(\nu) = 2i \tanh(\frac{\nu}{2T}) \text{Im} \Sigma^R(\nu)$, cf. Eq. (10).

The two-particle (or four-point) correlation function $G^{(4)}$ can be expressed through the four-point vertex Γ ,

$$\begin{aligned} G_{12|1'2'}^{(4)} &= \overleftarrow{1} \overleftarrow{1'} \overleftarrow{2'} \overleftarrow{2} \overrightarrow{2} \overrightarrow{1'} \overrightarrow{1} \\ &= \overleftarrow{1} \overleftarrow{1'} \overleftarrow{2'} \overleftarrow{2} \overrightarrow{2} \overrightarrow{1'} \overrightarrow{1} + \overleftarrow{1} \overleftarrow{1'} \overleftarrow{3'} \overleftarrow{3} \overrightarrow{4} \overrightarrow{4'} \overrightarrow{2} \overrightarrow{1'} \end{aligned}, \quad (13)$$

where the internal arguments $(3, 3', 4, 4')$ are again summed over. From $G^{(4)}$, one obtains susceptibilities by contracting pairs of external legs (see Appendix C for details).

The bare vertex, as the full vertex, is fully antisymmetric in its indices. Thus, a purely local and instantaneous interaction is of the type

$$\begin{aligned} (\Gamma_0)_{\sigma'_1 \sigma'_2 | \sigma_1 \sigma_2}(t'_1, t'_2 | t_1, t_2) \\ = -U \delta(t'_1 = t'_2 = t_1 = t_2) \delta_{\sigma_1, \sigma'_2} (\delta_{\sigma'_1, \sigma_2} \delta_{\sigma'_2, \sigma_1} - \delta_{\sigma'_1, \sigma_1} \delta_{\sigma'_2, \sigma_2}), \end{aligned} \quad (14)$$

with $U > 0$ for a repulsive interaction. This corresponds to a Hugenholtz diagram (single dot) [68]

$$(\Gamma_0)_{1'2'|12} = \begin{array}{c} \overleftarrow{2} \overleftarrow{2'} \\ \swarrow \searrow \\ \overleftarrow{1'} \overleftarrow{1} \end{array} = \begin{array}{c} \sigma \swarrow \searrow \\ \text{---} \\ \sigma \swarrow \searrow \end{array} \begin{array}{c} \overrightarrow{\sigma} \overrightarrow{\sigma} \\ \swarrow \searrow \\ \overrightarrow{\sigma} \overrightarrow{\sigma} \end{array} - \begin{array}{c} \overrightarrow{\sigma} \overrightarrow{\sigma} \\ \swarrow \searrow \\ \overrightarrow{\sigma} \overrightarrow{\sigma} \end{array}. \quad (15)$$

As the bare vertex is part of either H^+ or H^- in Eq. (2), all its contour indices must be equal [54],

$$(\Gamma_0)_{1'2'|12} = -c_1 \delta_{c'_1=c'_2=c_1=c_2} (\Gamma_0)_{\sigma'_1 \sigma'_2 | \sigma_1 \sigma_2}(t'_1, t'_2 | t_1, t_2). \quad (16)$$

It acquires a minus sign when moved from the forward ($c_1 = -$) to the backward ($c_1 = +$) branch of the Keldysh contour. After Keldysh rotation, one obtains

$$(\Gamma_0)_{\sigma'_1 \sigma'_2 | \sigma_1 \sigma_2}^{k'_1 k'_2 | k_1 k_2} = \begin{cases} \frac{1}{2} (\Gamma_0)_{\sigma'_1 \sigma'_2 | \sigma_1 \sigma_2}, & \sum_i k_i \text{ odd} \\ 0, & \text{else,} \end{cases} \quad (17)$$

where $\sum_i k_i$ is short for $k'_1 + k'_2 + k_1 + k_2$.

D. Single-impurity Anderson model

The formalism introduced above is completely general and can be applied, e.g., to lattice or impurity models alike. Comparing Keldysh to Matsubara approaches, the spatial or momentum degrees of freedom of lattice models are treated similarly in both cases. By contrast, the temporal or frequency dynamics are naturally very different. In impurity models, the frequency dynamics are isolated, saving the cost of including momentum variables. Hence, we consider in this paper the AM [49] in thermal equilibrium. Its physical behavior is well understood [48], and NRG [43] can be used to obtain highly accurate real-frequency benchmark data.

The model is defined by the Hamiltonian

$$H = \sum_{\epsilon\sigma} \epsilon c_{\epsilon\sigma}^\dagger c_{\epsilon\sigma} + (\epsilon_d + h)n_\uparrow + (\epsilon_d - h)n_\downarrow + U n_\uparrow n_\downarrow + \sum_{\epsilon\sigma} (V_\epsilon d_\sigma^\dagger c_{\epsilon\sigma} + \text{H.c.}), \quad (22)$$

with spinful bath electrons, created by $c_{\epsilon\sigma}^\dagger$, and a local level (d_σ^\dagger). The latter has an on-site energy ϵ_d and Coulomb repulsion U acting on $n_\sigma = d_\sigma^\dagger d_\sigma$. Although we consider $h = 0$, we include the magnetic field in Eq. (22) for a simple definition of the magnetic susceptibility. The bath electrons are integrated out, yielding the frequency-dependent retarded hybridization function $-\text{Im}\Delta^R(\nu) = \sum_\epsilon \pi |V_\epsilon|^2 \delta(\nu - \epsilon)$. We consider a flat hybridization in the wide-band limit, $\Delta_\nu^R = -i\Delta$, so that the bare impurity propagator reads

$$G_0^R(\nu) = \frac{1}{\nu - \epsilon_d + i\Delta}. \quad (23)$$

We use the dimensionless parameter $u = U/(\pi\Delta)$ for the interaction strength on the impurity in units of the hybridization strength to the bath. We focus on two choices of the on-site energy: one with particle-hole symmetry, $\epsilon_d = -U/2$, and one without, $\epsilon_d = 0$. We refer to these as the symmetric AM (sAM) and asymmetric AM (aAM), respectively.

For the sAM, $\Sigma_H = U/2$ is conveniently absorbed into the bare propagator,

$$G_0^R \rightarrow G_H^R = \frac{1}{\nu - \epsilon_d + i\Delta - \Sigma_H} = \frac{1}{\nu + i\Delta}. \quad (24)$$

For perturbative calculations in the aAM (as in PT2 or to initialize the parquet iterations), we also replace G_0 by G_H (see Appendix E for details).

For the fRG treatment, we use the hybridization flow [54], where Δ acts as the flow parameter and is decreased from a very large value to the actual value of interest. This is convenient because every point of the flow describes a physical system, at the given values of Δ , U , T . In other words, the fRG flow provides a complete parameter sweep in Δ , while the other parameters (U , T) remain fixed. Then, the fRG single-scale propagator is

$$S^R(\nu) = \partial_\Delta G^R(\nu)|_{\Sigma=\text{const}} = -i[G^R(\nu)]^2. \quad (25)$$

In the limit $\Delta \rightarrow \infty$, the values of Γ and Σ are [54]

$$\Gamma|_{\Delta=\infty} = \Gamma_0, \quad \Sigma^R|_{\Delta=\infty} = \Sigma_H = U \langle n_\sigma \rangle. \quad (26)$$

Note that while all vertex diagrams of second order or higher vanish as $\Delta \rightarrow \infty$, the first-order contribution of $\Sigma^{R/A}$ (the Hartree term Σ_H) is finite. As discussed in Appendix E, Σ_H is given by an integral over $G^<$, which gives a finite value $U \langle n_\sigma \rangle$ even in the limit $\Delta \rightarrow \infty$. In practice, we start the flow at a large but finite value of Δ , and use the self-consistent solution of the parquet equations as the initial conditions for Σ and Γ , as they can be easily obtained for sufficiently large Δ .

E. Benchmark methods

As a real-frequency benchmark method, we use NRG in a state-of-the-art implementation based on the QSpace tensor library [78–80]. We employ a discretization parameter of $\Lambda = 2$, average over $n_z = 6$ shifts of the logarithmic discretization grid [81], and keep up to 5000 SU(2) multiplets during the iterative diagonalization. Dynamical correlators are obtained via the full density-matrix NRG [82,83], using adaptive broadening [84,85] and a symmetric improved estimator for the self-energy [86]. We also extract zero-temperature quasiparticle parameters from the NRG low-energy spectrum [87–93]. Dividing the quasiparticle interaction \tilde{U} by the square of the quasiparticle weight Z^2 yields the 4p vertex at vanishing frequencies $\Gamma_{\uparrow\downarrow}(\mathbf{0})$. Thereby, we obtain $\Gamma_{\uparrow\downarrow}(\mathbf{0}) = -\tilde{U}/Z^2$ at $T = 0$ very efficiently and accurately. For a finite-temperature estimate, we divide \tilde{U} by the finite-temperature Z deduced from the dynamic self-energy as opposed to the zero-temperature Z following from the low-energy spectrum. We also compute the dynamical 4p vertex in the Keldysh formalism, exploiting the recent advances described in Refs. [34,35].

For completeness, we also compare our results to PT2. Perturbation theory of the AM is known to work well when expanding around the nonmagnetic Hartree–Fock solution [60,94–97]. PT2 famously and fortuitously (cf. the iterated perturbation theory in the DMFT context [42]) gives very good results for the self-energy of the sAM, where $\epsilon_d = -U/2$ and Σ_H cancel exactly. The reason is that Σ_{PT2} is correct in the limits $u \rightarrow 0$ and $u \rightarrow \infty$. In the latter case, the spectrum $-\frac{1}{\pi}\text{Im}G^R$ consists of two discrete peaks, and, in the sAM, the resulting expression for $\Sigma^R = 1/G_0^R - 1/G^R$ is $(U/2)^2/(\nu + i0^+)$, coinciding with PT2. One may further note that corrections to Σ_{PT2} start at order u^4 , as only even powers contribute to the expansion of Σ for the sAM, and that the expansion converges very quickly (see Figs. 3.6 and 3.7 in Ref. [95]). Additionally, the high-frequency asymptote $\lim_{\nu \rightarrow \infty} \nu(\Sigma^R - \Sigma_H)$ is fully captured by PT2, as the general expression $U^2 \langle n_\sigma \rangle (1 - \langle n_\sigma \rangle)$ reduces to $(U/2)^2$ (with $\langle n_\sigma \rangle = 1/2$ in the sAM), i.e., the second-order result.

For the aAM, Σ_H must first be determined in a self-consistent way. This is crucial because $\langle n_\sigma \rangle$ is not well approximated by a few orders in u [recall the Friedel sum rule at $T = 0$ [98], $\langle n_\sigma \rangle = \frac{1}{2} - \frac{1}{\pi} \arctan\{[\epsilon_d + \Sigma(0)]/\Delta\}$]. The self-consistent Hartree propagator fulfills the Friedel sum rule at $T = 0$, but the resulting $\langle n_\sigma \rangle$ for given ϵ_d is of course not exact. When using PT2, we compute quantities of interest, such as Σ_{PT2} , using the Hartree propagator (see Appendix F for details). However, in contrast with the sAM, Σ_{PT2} is not exact at $u \rightarrow \infty$ (cf. Ref. [99]), odd powers in u contribute to Σ , and the high-frequency asymptote of Σ_{PT2} , involving $\langle n_\sigma \rangle$, is not reproduced exactly.

Finally, we also compare our fRG and PA results to “KISF calculations” mimicking the previous state of the art in Keldysh fRG. References [54,55,58] used a scheme where the full vertex is decomposed into the three channels [cf. Eq. (20e)] and, for each two-particle reducible vertex γ_r , only the dependence on the bosonic transfer frequency is retained [see Eq. (76) in Ref. [55]]:

$$\Gamma \approx \Gamma_0 + \sum_{r=a,p,t} \gamma_r(\omega_r). \quad (27)$$

Note that, within Matsubara fRG, Ref. [100] compared this simplification (called “Appr. 1” therein) to the full parametrization. When inserting the vertex parametrized according to Eq. (27) into the self-energy flow (19a), no further approximations are needed. However, when inserting the vertex on the right of the vertex flow equation (19b), the interchannel contributions are approximated by their static values [in thermal equilibrium with $\mu = 0$, see Eq. (83) in Ref. [55]]:

$$\Gamma|_{\text{RHS}(\gamma_r)} \approx \Gamma_0 + \gamma_r(\omega_r) + \sum_{r' \neq r} \gamma_{r'}(\omega_{r'})|_{\omega_{r'}=0}. \quad (28)$$

With this approximation the only frequency dependence of the integrands lies in the propagator pair. By contrast, an exact decomposition of each γ_r has the form [2]

$$\begin{aligned} \gamma_r(\omega_r, \nu_r, \nu'_r) = & K_{1r}(\omega_r) + K_{2r}(\omega_r, \nu_r) \\ & + K_{2r}(\omega_r, \nu'_r) + K_{3r}(\omega_r, \nu_r, \nu'_r). \end{aligned} \quad (29)$$

(The frequency arguments ω_r, ν_r, ν'_r are defined in Appendix A, Fig. 12.) Thus, the above approximation can be understood by retaining only the K_{1r} contributions while ensuring a static feedback (SF) between the different channels—hence the abbreviation KISF. Within KISF, there are different ways of treating the feedback from the self-energy. Previous works found better results at $T = 0$ by inserting only the static rather than full dynamic Σ into the propagator [56]. We confirm this finding at $T = 0$ but observed that the static Σ feedback has problems at $T \neq 0$, failing, e.g., the requirement $\text{Im}\Sigma < 0$. Instead, we obtained much better results (particularly fulfilling $\text{Im}\Sigma < 0$) by using the full dynamic Σ feedback together with the Katanin substitution [70].

F. Note on the numerical implementation

Compared with the more common Matsubara formalism (MF), the KF entails notable differences in the numerical implementation that we summarize here (see Appendix G for details). Most importantly, while finite-temperature Matsubara computations employ a discrete set of (imaginary) frequencies, Keldysh functions depend on continuous (real) frequencies. Furthermore, the Keldysh index structure increases the number of components of the correlators (to be computed and stored) by a factor of 4 and 16 for 2p and 4p objects, respectively. Hence, working in the KF requires considerably higher effort in terms of implementational complexity and numerical resources.

To minimize systematic numerical errors, a faithful representation of the vertex functions is essential. The de-

composition (29) of the reducible vertices [2] is beneficial for capturing the high-frequency asymptotics. Indeed, the lower-dimensional asymptotic functions, K_1 and $K_{2(\nu)}$, allow for a good resolution at comparably low numerical cost. A good resolution of the continuous Keldysh functions further necessitates a suitable choice of sampling points. We use a frequency grid with high resolution at small frequencies, where the vertices show sharp features, and fewer points at higher frequencies. In fRG with the hybridization flow, the frequency grids also have to be rescaled to account for changes scaling with Δ ; for fully adaptive grids (which were not required in this work, cf. Appendix G) see also Refs. [73,74,76].

Continuous-frequency computations also require efficient integration routines. We use an adaptive quadrature routine to capture the essential features of sharply peaked functions (cf. Appendix G). The additional numerical costs due to the Keldysh index structure can be mitigated by vectorization, i.e., by exploiting the matrix structure of the summation over Keldysh components. Storing all Keldysh components contiguously in memory allows for efficient access to matrix-valued vertex data, which can be combined to matrix-valued integrands via linear algebra operations. (Note that vectorization over Keldysh components requires a quadrature routine that accepts matrix-valued integrands.) Symmetries are used to reduce the data points that are computed directly, and most resulting symmetry relations are compatible with vectorization over Keldysh indices (see Appendix A).

Lastly, the fRG and the parquet solver generally have the advantage that computations can be parallelized efficiently over all combinations of external arguments. We use OMP and MPI libraries to parallelize execution across multiple CPUs and compute nodes.

III. RESULTS

In the results, we focus on retarded correlation functions like G^R, Σ^R , and χ^R . For brevity, we denote the real and imaginary parts of, say, G^R by G' and G'' , respectively, i.e., $G^R = G' + iG''$. Since the fRG flow varies Δ at fixed U and T , we consider a temperature of $T/U = 0.01$. Most plots show results both for the sAM ($\epsilon_d = -U/2$) and aAM ($\epsilon_d = 0$). Recall that $u = U/(\pi\Delta)$.

A. Dynamical correlation functions

As a first quantity that is directly measurable in experiment, we show in Fig. 1 the spectral function $\tilde{A}(\nu) \equiv \pi\Delta A(\nu) = -\Delta G''(\nu)$. The absorbed factor of $\pi\Delta$ ensures $\tilde{A}(0) = 1$ for the sAM and $T \rightarrow 0$. We consider three values of $u \in \{0.75, 1, 1.5\}$, referred to as “small,” “intermediate,” and “large” in the following (although truly large interactions in the AM rather are $u \gtrsim 2$ [60]). There are no PA results for large u , as we could not converge the real-frequency self-consistent parquet solver there.

At small u , the curves produced by all methods are almost indistinguishable. Small but noticeable deviations occur for the aAM at intermediate u , and pronounced deviations are found at large u . At $u = 1.5$ in the sAM, only the methods exact in the $u \rightarrow \infty$ limit (cf. Sec. II E), NRG and PT2, produce notable Hubbard bands centered at $\nu = \pm U/2$, while fRG also

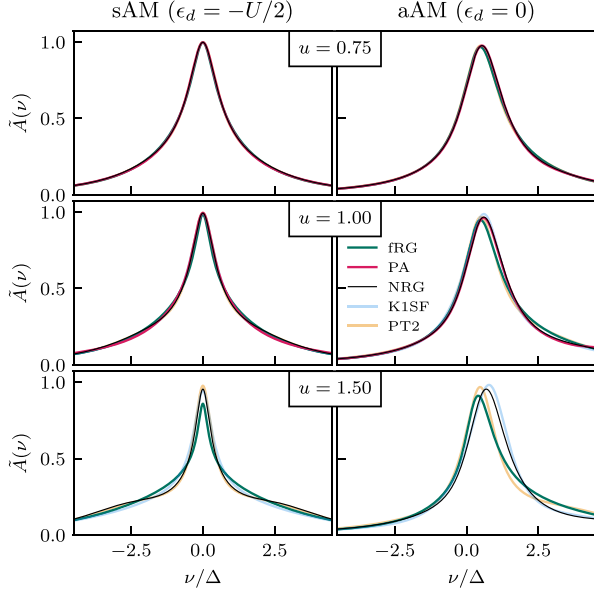


FIG. 1. Spectral functions $\tilde{A}(v) \equiv \pi \Delta A(v)$ for three interaction values u in the symmetric AM (sAM, left) and the asymmetric AM (aAM, right). Deviations between the methods appear with increasing u . Here and in all subsequent figures, we consider a temperature of fixed $T/U = 0.01$. At $u = 1.5$ in the sAM, the onset of Hubbard bands centered at $v = \pm U/2$ is only captured by NRG and (for reasons explained in Sec. II E) PT2. At this interaction strength, fRG underestimates the quasiparticle peak, and we were unable to converge the PA results.

underestimates the height of the quasiparticle peak. Nevertheless, one may come to the conclusion that all methods agree to a reasonable degree of accuracy. Note, although, that at small u , where Σ is small, $G^R = 1/([G_0^R]^{-1} - \Sigma^R)$ and thus also $A(v)$ are dominated by the bare propagator. As all nontrivial features of

$$A(v) = \frac{1}{\pi} \frac{\Delta - \Sigma''(v)}{[v - \epsilon_d - \Sigma'(v)]^2 + [\Delta - \Sigma''(v)]^2}$$

come from Σ , we can gain more insight by looking at Σ directly.

In Fig. 2, we plot the negative imaginary part of the retarded self-energy $-\Sigma''(v)$ in units of the hybridization strength Δ . This quantity is strictly non-negative [86], which is a useful and nontrivial consistency check for all our methods. Here, deviations between the methods are visible at each value of u . At small u , the results mostly agree, albeit better for the sAM than for the aAM. At small and intermediate u in the aAM, the PA matches NRG most closely and also captures the peak position correctly, in contrast with fRG, KISF, and PT2. Strikingly, though, for intermediate u in the sAM (which is the more strongly correlated setting with lower quasiparticle weight Z , see Fig. 7), the PA shows considerable deviations from NRG: Σ'' has a “deformation” in that its maxima are misplaced outward. We performed a separate PA calculation in the MF to confirm that the corresponding MF result per-

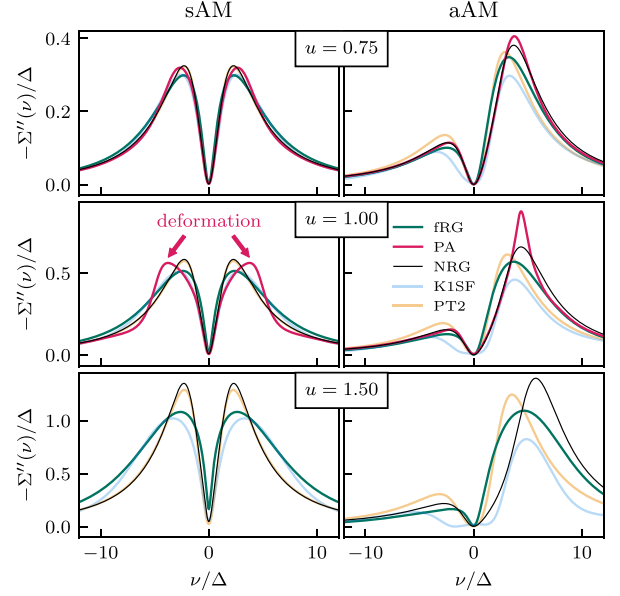


FIG. 2. Imaginary part of the retarded self-energy, organized as in Fig. 1. The limitations of PT2 in the aAM are clearly exposed. The PA results are closest to NRG at $u = 0.75$ for both sAM and aAM, and at $u = 1$ for the aAM (this corresponds to the regime of not too strong correlation, $Z \gtrsim 0.8$, see Fig. 7). Artifacts appear at $u = 1$ in the sAM (where $Z \approx 0.65$, see Fig. 7). Throughout, the fRG results with full frequency dependence match NRG better than those in the KISF simplification.

fectly matches the “trivial” analytic continuation from KF to MF, $-\frac{1}{\pi} \int dv' \frac{\Sigma''(v')}{iv - v'}$, see Fig. 3. Hence, we conclude that the Keldysh self-energy did not acquire artifacts during the real-frequency self-consistent parquet iteration. Instead, the deformations are a deficiency of the PA solution at $u = 1$,

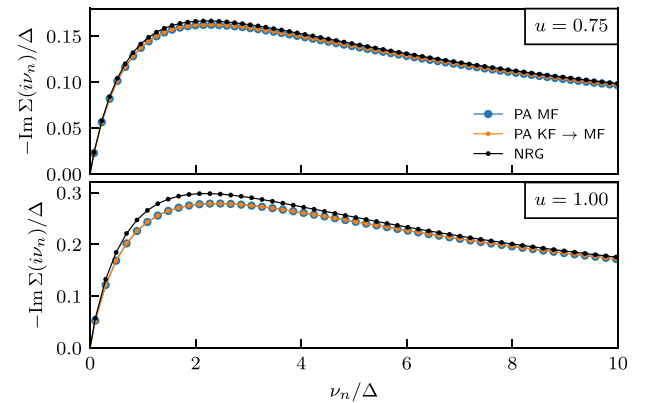


FIG. 3. Imaginary part of the Matsubara self-energy in NRG and the PA. The PA results stem from an independent solver implemented in the MF and from the “trivial” analytic continuation of Σ'' obtained in the KF. The *qualitative* difference between NRG and PA observed in the real-frequency results of Fig. 2 at $u = 1$ can hardly be guessed from these imaginary-frequency results.

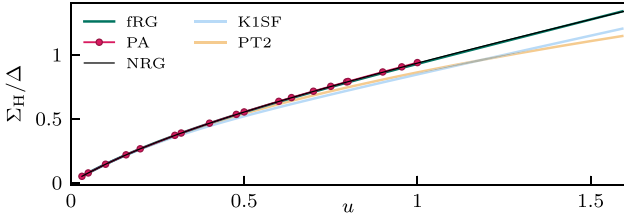


FIG. 4. Hartree self-energy $\Sigma_H = U\langle n_\sigma \rangle$ in the aAM. PT2 corresponds to self-consistent solutions of the Hartree term. Only fRG and PA agree well with NRG.

which are obvious in our Keldysh results, but could not have been guessed from the more benign Matsubara self-energy (Fig. 3).

We also observe from Fig. 2 that the PT2 results become much worse as soon as one leaves the special case of particle-hole symmetry (see Sec. II E). The results from fRG with full frequency dependence are better than those from K1SF, showing that the frequency dependence of Σ is only generated correctly if the dependence of the 4p vertex on its three frequencies is kept [39]. In fact, for large u in the aAM, the K1SF result becomes *negative* (with values on the order of 10^{-5}) at around $\nu/\Delta \simeq \pm 2$, thus failing the previously mentioned consistency check.

The inadequacies of a constant vertex manifest themselves even in the constant Hartree part of the self-energy, $\Sigma_H = U\langle n_\sigma \rangle$, shown in Fig. 4. The fRG and PA calculations produce the NRG value almost exactly, but the K1SF curve starts to deviate early. We attribute this to the fact that diagrammatic contributions beyond the K_1 level are neglected, introducing an error of $O(U^3)$ into the flow of Σ , including Σ_H , see Eq. (E5). The PT2 curve shows the converged values obtained from self-consistent evaluations of the Hartree diagram (see Appendix E), which enters the Hartree propagator used in all PT2 computations. The self-consistency is likely the reason why PT2 performs better than K1SF (which does not obey such a self-consistency) for small and intermediate u .

Apart from \tilde{A} and Σ , other dynamical quantities of interest are susceptibilities. In the diagrammatic methods, these are derived directly from the 4p vertex (see Appendix C). We consider the imaginary part of the retarded magnetic and density dynamical susceptibilities $\tilde{\chi}_{m/d}(\omega) \equiv \pi \Delta \chi_{m/d}(\omega)$, paying special attention to the peak position and height. The peak position of $\tilde{\chi}_m$ shown in Fig. 5 is proportional to the Kondo temperature and decreases with increasing u in the sAM. All methods apart from K1SF produce good results at small u with only minor deviations from NRG. The deviations are smallest in PA from small to intermediate u , until the PA results are no longer available at large u . fRG produces reasonable curves but, at large u , under- or overestimates the peak in the sAM and aAM, respectively. K1SF does not produce sensible results for any u considered, while PT2 performs well for the aAM but yields worse results than fRG in the sAM.

The density susceptibility shown in Fig. 6 is centered at larger frequencies and has smaller magnitude than its magnetic counterpart. Indeed, while $\tilde{\chi}_m$ and $\tilde{\chi}_d$ are equal at $u = 0$, increasing interaction values discriminate between spin fluc-

tuations (enhanced) and charge fluctuations (reduced). Here, fRG and the PA both produce acceptable results. However, the PA data at intermediate u and in the sAM show a deformation around $\omega/\Delta \simeq 5$, reminiscent of the deformation in Σ'' (cf. Fig. 2). The K1SF curve for $\tilde{\chi}_d$ (as for $\tilde{\chi}_m$) is not sensible, this time lying far above (rather than below) the NRG curve. PT2 for $\tilde{\chi}_d$, differently from $\tilde{\chi}_m$, is unreliable, yielding a qualitatively wrong double-peak structure.

In summary, we find that the PA results generically reproduce the NRG benchmark best, but are available only up to intermediate u . Our new fRG computations with the full frequency dependence of the vertex drastically improve upon the K1SF results in almost every case, but become quantitatively off with increasing u .

B. Static properties

We now turn to static quantities, obtained from Σ and Γ by setting all frequency arguments to zero. Although these can also be obtained using the imaginary-frequency MF (see Ref. [100] for an early MF fRG treatment of the AM), they serve as important consistency checks for our Keldysh computations. The zero-frequency fermion objects can be used for an effective low-energy description, and, by rescaling, converted to quasiparticle parameters as in Hewson's renormalized perturbation theory [101]. For the AM in the wide-band limit at $T = 0$, the static fermionic quantities can also be deduced from the static susceptibilities. We hence consider the static magnetic and charge susceptibilities as well, before analyzing the zero-temperature identities in the next section.

By virtue of the Δ flow, see Sec. II D, a single fRG computation suffices to obtain the *entire* dependence of, e.g., $Z(u)$ (at fixed T/U). By contrast, the PA requires separate computations for every value of u , resulting in a significantly bigger numerical effort. The top row of Fig. 7 shows the quasiparticle weight

$$Z = (1 - \partial_\nu \Sigma'|_{\nu=0})^{-1}, \quad (30)$$

as extracted from the slope at $\nu = 0$ of the real part of the retarded self-energy, Σ' . In all cases, the PA reproduces the NRG benchmark best, but is again only available up to $u \lesssim 1$. The fRG curve follows NRG for small u but starts to deviate already at intermediate u . K1SF performs very well in the sAM, but deviates from NRG in the aAM earlier than fRG. Since PT2 reproduces the NRG full self-energy very well for the sAM (cf. Fig. 2), the same applies to Z . In the aAM, PT2 also produces reasonable results for Z , in contrast with $\Sigma''(\nu)$ in Fig. 2.

The second row of Fig. 7 displays the scattering rate $-\Sigma''(0)$ on a logarithmic scale. In the sAM, all methods agree reasonably well up to intermediate u . Beyond that, fRG significantly overestimates $-\Sigma''(0)$ (cf. Fig. 2). In the aAM, the fRG results are slightly better. The PA yields the best agreement with NRG, except for $u \simeq 1$ in the aAM where numerical artifacts appear. K1SF shows large deviations early on, matching the observations in Fig. 2. PT2 reproduces NRG almost exactly, even though this is not the case for $\Sigma''(\nu)$ (Fig. 2) in the aAM.

The last row of Fig. 7 shows the effective interaction. The PA accurately reproduces the NRG results. In strik-

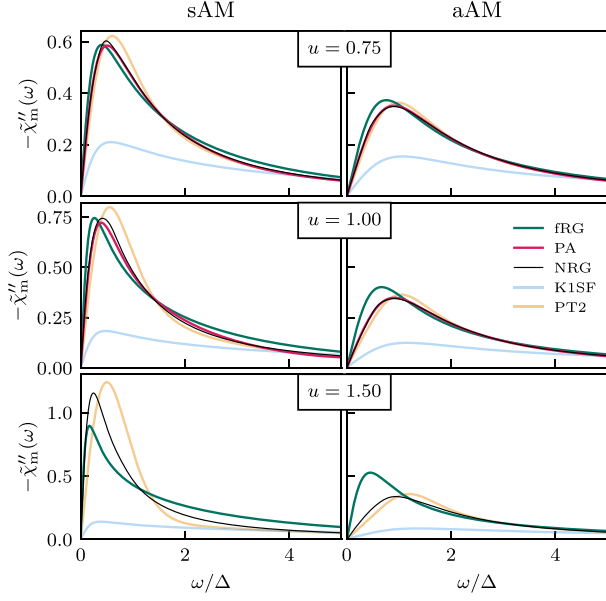


FIG. 5. Imaginary part of the dynamical magnetic susceptibility, $\tilde{\chi}_m(\omega) \equiv \pi \Delta \chi_m(\omega)$. At small to intermediate u , all methods (except K1SF) produce good results, while PA matches NRG best. Toward large u , fRG does not capture the peak correctly. PT2 performs well for the aAM but not the sAM; K1SF is off in all cases.

ing contrast, fRG overestimates the effective interaction very strongly. (This can also be seen in Fig. 11 below, third row, columns four to six, where the frequency-dependent vertex is plotted.) PT2 and K1SF yield only very weak renormalizations of the bare vertex (none at all in PT2 in the sAM).

Figure 8 shows the static magnetic and density susceptibilities,

$$\chi_m = \frac{1}{4} \partial_h \langle \tilde{n}_\uparrow - \tilde{n}_\downarrow \rangle|_{h=0}, \quad \chi_d = \frac{1}{4} \partial_{\epsilon_d} \langle \tilde{n}_\uparrow + \tilde{n}_\downarrow \rangle, \quad (31)$$

where $\tilde{n}_\sigma = n_\sigma - \langle n_\sigma \rangle$. Again, the PA results, where available, reproduce the NRG benchmark best. The fRG results are reasonable up to intermediate u for $\tilde{\chi}'_{m/d}(0) = \pi \Delta \chi_{m/d}$. A comparison with the results obtained by an independent MF computation (dashed lines in Fig. 8) reveals that the KF data at the largest u values is not fully converged in the size of the frequency grid (see Appendix I for details). As for the dynamical susceptibilities, K1SF does not produce sensible results at all. PT2 gives fairly good results, in particular for $\tilde{\chi}'_m$ in the aAM (see also Fig. 5), but $\tilde{\chi}'_d$ in the sAM quickly deviates from NRG rather strongly (as it did in Fig. 6).

In summary, for all the static properties shown in Figs. 7 and 8, the PA results agree very well with NRG for all u for which the parquet solver converged, i.e., up to $u \lesssim 1$. By contrast, fRG results begin to deviate from NRG somewhat earlier than PA, sometimes even much earlier. This difference is most striking for the effective interaction in the bottom panels of Figs. 7, where the performance of fRG is surprisingly (even shockingly) poor.

This comparatively poor performance of fRG may be due in part to the well-known fact that one-loop fRG results de-

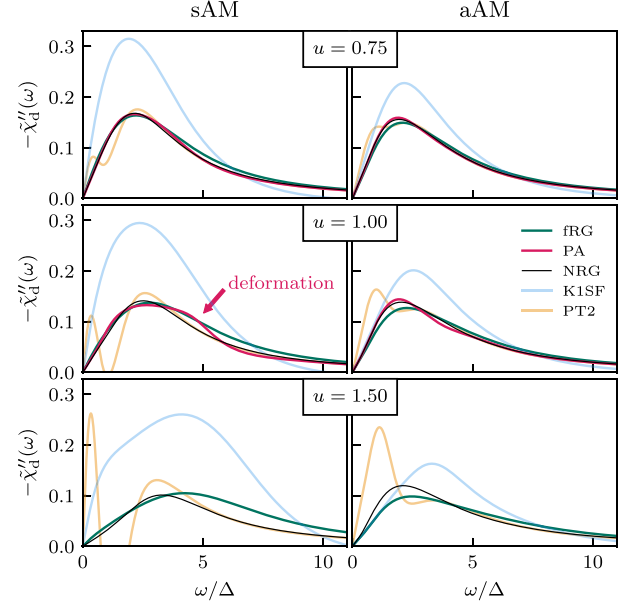


FIG. 6. Imaginary part of the dynamical density susceptibility, $\tilde{\chi}_d(\omega) \equiv \pi \Delta \chi_d(\omega)$. Both fRG and the PA produce good results. The artifact in the PA solution at $u = 1$ in the sAM observed in Fig. 2 is also seen here, while it was not apparent in Fig. 5. Neither PT2 nor K1SF produce sensible results for $\tilde{\chi}_d$.

pend on the choice of the fRG regulator. Figure 9 illustrates this in the present context by comparing our KF results with independent calculations in the MF. For the latter, we used

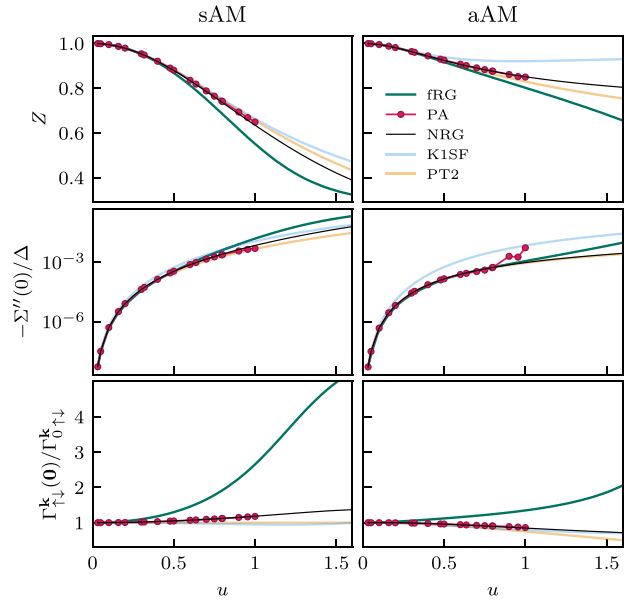


FIG. 7. Static fermionic properties as a function of u : quasiparticle weight Z , scattering rate $-\Sigma''(0)$ on a logarithmic scale, and effective interaction ($k = 12|22$) in units of the bare interaction. Overall, the PA (available for $u \lesssim 1$) matches NRG best, except for $\Sigma''(0)$ at $u \simeq 1$ in the aAM. All other methods agree reasonably well (except for Z and $\Sigma''(0)$ in the aAM in K1SF). Strikingly, fRG strongly overestimates the effective interaction.

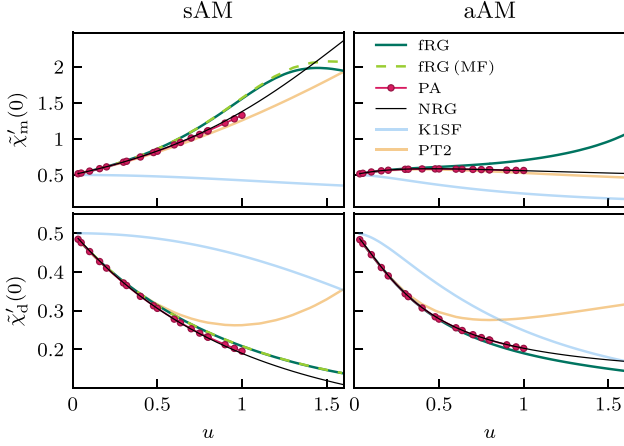


FIG. 8. Static susceptibilities as a function of u . fRG yields sensible results until $\tilde{\chi}_m'$ has a maximum at $u \approx 1.3$. PA data are available only for $u \lesssim 1$, but show excellent agreement with NRG there. Results from K1SF and PT2 (for $\tilde{\chi}_d$) are rather bad.

three different regulators, called Δ flow (same as for our KF computations), U flow, and ω flow. [See Eqs. (3) and (4) in Ref. [64] for definitions of the U and ω flow. The ω and U flows require many more separate computations than the Δ flow, since the former two hold T/Δ fixed (the ω flow also T/U), while the latter holds T/U fixed.] From Fig. 9, we note three salient points. First, the MF and KF results for the Δ flow match. This is expected for numerically converged calculations and serves as a useful consistency check. Second, the U flow deviates from the NRG benchmark very early. Third, the best MF result is obtained from the ω flow (similarly as observed in Ref. [64]). Regrettably, though, this advantage of the MF ω flow is not relevant for the KF: there, the ω flow would violate causality [54] and hence cannot be used. This, and the poor performance of the U flow, is the reason why we chose the Δ flow for all our KF computations.

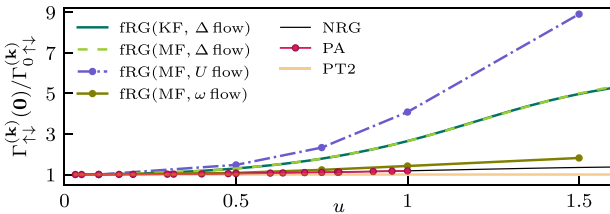


FIG. 9. Effective interaction ($k=12|22$) of the sAM in units of the bare interaction, including fRG results in the MF obtained with three different regulators. The MF result in the Δ flow perfectly matches its KF counterpart. The U flow performs considerably worse, as it quickly deviates from NRG. By far the best result is obtained using the ω flow, which can however not be used in the KF (see the main text for details). In the MF, we approximate vanishing frequencies by averaging over the lowest Matsubara frequencies, $\gamma_r(\mathbf{0}) \approx \frac{1}{4} \sum_{v,v'=\pm\pi T} \gamma_r(\mathbf{0}, v, v')$.

C. Zero-temperature identities

As an internal consistency check for each method, we consider four Fermi-liquid identities. These hold $T = 0$ and, more generally, at $T \ll T_K$, where T_K is the Kondo temperature. We deduce T_K as $T_K = 1/[4\chi_m'(0)]|_{T=0}$ [see, e.g., Eq. (20) in Ref. [102]] from zero-temperature NRG calculations. The resulting values for $u \in \{0.75, 1, 1.5\}$ are $T_K/U \in \{0.31, 0.18, 0.07\}$ for the sAM and $T_K/U \in \{0.58, 0.45, 0.32\}$ for the aAM. Note that the Kondo regime of the sAM corresponds to $u \gtrsim 2$ [101].

First, for a constant hybridization function in the wide-band limit, we have the following two ‘‘Yamada–Yosida (YY) identities’’ generalized to arbitrary ϵ_d [see Eq. (6.1) in Ref. [95] and Eq. (7) in Ref. [97], Eqs. (24)–(25) in Ref. [101], or Eqs. (4.30)–(4.33) in Ref. [103]]:

$$Z^{-1} = [\chi_m(0) + \chi_d(0)]/\rho(0), \quad (32a)$$

$$-\rho(0)\Gamma_{\uparrow\downarrow}(\mathbf{0}) = [\chi_m(0) - \chi_d(0)]/\rho(0). \quad (32b)$$

Here, $\rho(0) \equiv A(0)|_{T=0}$ is the spectral function evaluated at $\nu = 0$ and $T = 0$,

$$\begin{aligned} \rho(0) &= \frac{1}{\pi} \frac{\Delta}{[\epsilon_d + \Sigma'(0)]^2 + \Delta^2} \\ &= \frac{1}{\pi \Delta} \begin{cases} 1 & \text{for } \epsilon_d = -U/2 \\ \frac{1}{1 + [\Sigma'(0)/\Delta]^2} & \text{for } \epsilon_d = 0. \end{cases} \end{aligned} \quad (33)$$

Next, $\Gamma_{\uparrow\downarrow}(\mathbf{0})$ is the full Matsubara 4p vertex evaluated at vanishing frequencies (in the zero-temperature limit). The minus sign in Eq. (32b) stems from our convention of identifying, e.g., the bare Matsubara vertex $\Gamma_{0,\uparrow\downarrow}$ with $-U$. The analytic continuation of ℓ p functions between Matsubara and retarded Keldysh components involves a factor $2^{\ell/2-1}$ [see Eq. (69) in Ref. [34]]. Hence,

$$\Gamma_{\uparrow\downarrow}(\mathbf{0}) = 2\Gamma_{\uparrow\downarrow}^k(\mathbf{0}),$$

$$\mathbf{k} \in \{(12|22), (21|22), (22|12), (22|21)\}. \quad (34)$$

Another identity derived by YY [see Eqs. (13)–(15) and (18) in Ref. [97], Eqs. (31) and (34) in Ref. [101], or Eq. (4.37) in Ref. [103]] implies

$$-\Sigma''(\nu) = \frac{1}{2}\pi\rho(0)^3[\Gamma_{\uparrow\downarrow}(\mathbf{0})]^2(\nu^2 + \pi^2T^2) \quad (35)$$

for $|\nu|, T \ll T_K$. We check this relation by fitting $\Sigma'' \propto (\nu^2 + \pi^2T^2)$. Finally, the Korringa–Shiba (KS) identity [see Eq. (1.4) in Ref. [104]] reads

$$\lim_{\omega \rightarrow 0} \chi_m''(\omega)/\omega = 2\pi[\chi_m'(0)]^2. \quad (36)$$

To check the fulfillment of these identities, we analyze the relative difference $2(\text{LHS} - \text{RHS})/(\text{LHS} + \text{RHS})$ [LHS (RHS) = left- (right-) hand side] of Eqs. (32a), (32b), (35), (36), referred to as YY1, YY2, YY3, KS, respectively. These zero-temperature identities of the AM only hold if $T \ll T_K$. As we keep $T/U = 0.01$ constant, the temperatures increase with u , and $T \ll T_K$ is no longer fulfilled for $u \gtrsim 1$ in the sAM. Accordingly, there, the identities are violated even in NRG.

As can be seen in Fig. 10, the PA fulfills most identities very well (below 8% throughout), but is again available only up to $u \simeq 1$. The fRG results obey YY1 up to $u \lesssim 1$, but show clear deviations in all other identities, setting in already for

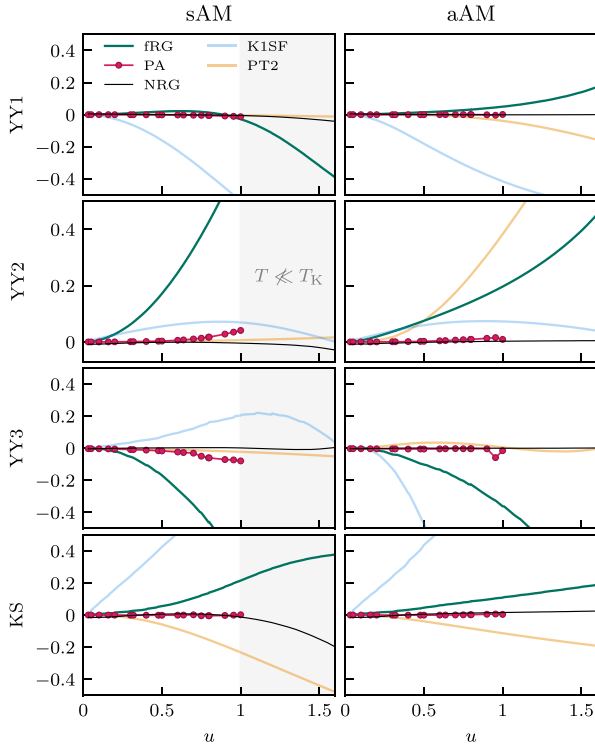


FIG. 10. Relative difference between the left- and right-hand sides of the four zero-temperature identities as a function of u . All calculations have finite $T/U = 0.01$; thus, even NRG violates the identities if $T \ll T_K$ is no longer fulfilled. Apart from NRG, the PA shows the smallest violations of these identities (below 8% throughout), but is only available for $u \lesssim 1$. The fRG data fulfill YY1 relatively well, but show clear deviations otherwise, setting in already for very small values of u . For YY2, e.g., the deviations become significant already at $u \gtrsim 0.25$. PT2 obeys the identities (except KS) in the sAM but not the aAM. K1SF shows major deviations throughout.

very small values of u . Except for the KS relation in the fourth row, PT2 mostly fulfills the identities for the sAM but less so for the aAM, while K1SF shows major deviations, even for small u .

D. Frequency dependence of the 4p vertex

Finally, we show fRG and PA results for the frequency dependence of the 4p vertex in the sAM and compare them to corresponding results from NRG. We restrict ourselves to a fully retarded Keldysh component [34] and show both the same-spin ($\uparrow\uparrow$) and the opposite-spin ($\uparrow\downarrow$) components. We plot the vertex in the two-dimensional frequency plane ($\omega_t = 0$, $v_t = v$, $v'_t = v'$) in the natural parametrization of the t channel for zero transfer frequency. Physically, this corresponds to the effective interaction of two electrons on the impurity with equal or opposite spins, respectively, and energies v , v' without energy transfer [69]. The NRG 4p results are computed with the scheme introduced in Refs. [34,35], utilizing the symmetric improved estimator of Ref. [105].

In Fig. 11, we compare results from fRG, the PA, and NRG for two values of the interaction $u \in \{0.5, 1\}$. We observe good

qualitative agreement throughout, as all methods capture all nontrivial features. At $u = 1$, however, we observe a qualitative discrepancy in the data: $\text{Re}\Gamma_{\uparrow\downarrow}^k$ is strictly positive in fRG and slightly negative in NRG (bottom part, top row, first panel from the right in Fig. 11). The PA result reaches even larger negative values and retains them for a large range of v values. This strong negative signal appears to be an artifact of the PA; it would likely be canceled by additional contributions missed in the PA.

IV. CONCLUSIONS AND OUTLOOK

In this work, we have shown that real-frequency QFT calculations with full frequency resolution of the 4p vertex are feasible. We chose the AM for a proof-of-principle study and employed one-loop fRG flows and solutions of the parquet equations in the PA, benchmarked against NRG. We compared dynamical correlation functions as well as characteristic static quantities and performed a detailed numerical check of zero-temperature identities. We found that keeping the full frequency dependence of the 4p vertex in fRG strongly improves the accuracy compared with previous implementations using functions with at most one-dimensional frequency dependencies. Note that the present study is performed at finite temperature, $T/U = 0.01$, in contrast with previous work on spectral functions at $T = 0$ [55].

The numerical challenges imposed by the fully parametrized real-frequency 4p vertex were overcome via a suitably adapted frequency grid, vectorization over the Keldysh matrix structure, and a parallelized evaluation of the fRG or parquet equations (see Appendix G). We employed frequency grids with up to 125^3 data points, and our most expensive calculation consumed about 25 000 CPU hours for a single data point in the PA.

The PA results could be converged only for $u = U/(\pi\Delta)$ in the range $u \lesssim 1$, but there gave the best agreement with NRG (except at the boundary of the accessible u range). The PA also gave very good results for the effective interaction. However, by looking at $\Gamma_{\uparrow\downarrow}^k$ in a frequency range around the origin, it appears that the mechanism by which the PA achieves low values of $|\Gamma_{\uparrow\downarrow}^k(\mathbf{0})|$ (compared with, say, fRG) is different from that of NRG, as the PA data have a spuriously large regime of strongly negative values in $\text{Re}\Gamma_{\uparrow\downarrow}^k$.

The fRG calculations in the present context were comparatively economical, since a single run with the “ Δ flow” yields an entire parameter sweep in Δ . The flow could be followed to large values of u , well beyond 1, i.e., far beyond the regime where we could converge the PA. However, for $u \gtrsim 0.5$ these one-loop fRG results are significantly less accurate than the PA (as compared with NRG). Strikingly, fRG strongly overestimates the effective interaction $\Gamma_{\uparrow\downarrow}^k(\mathbf{0})$ by factors of three to four for u in the range 1 to 1.5. We compared the Keldysh to Matsubara fRG data obtained using three different regulators, and we found that, for $u > 0.5$, the latter strongly depend on the choice of regulator: For the Δ flow, the Matsubara results agree with the Keldysh results, while performing better than the U flow but worse than the ω flow. Regrettably, the ω flow is not available in the KF, where it violates causality. It would hence be worthwhile to find Keldysh fRG regulators akin to the ω flow but compatible with the KF requirements regarding causality and FDTs [54].

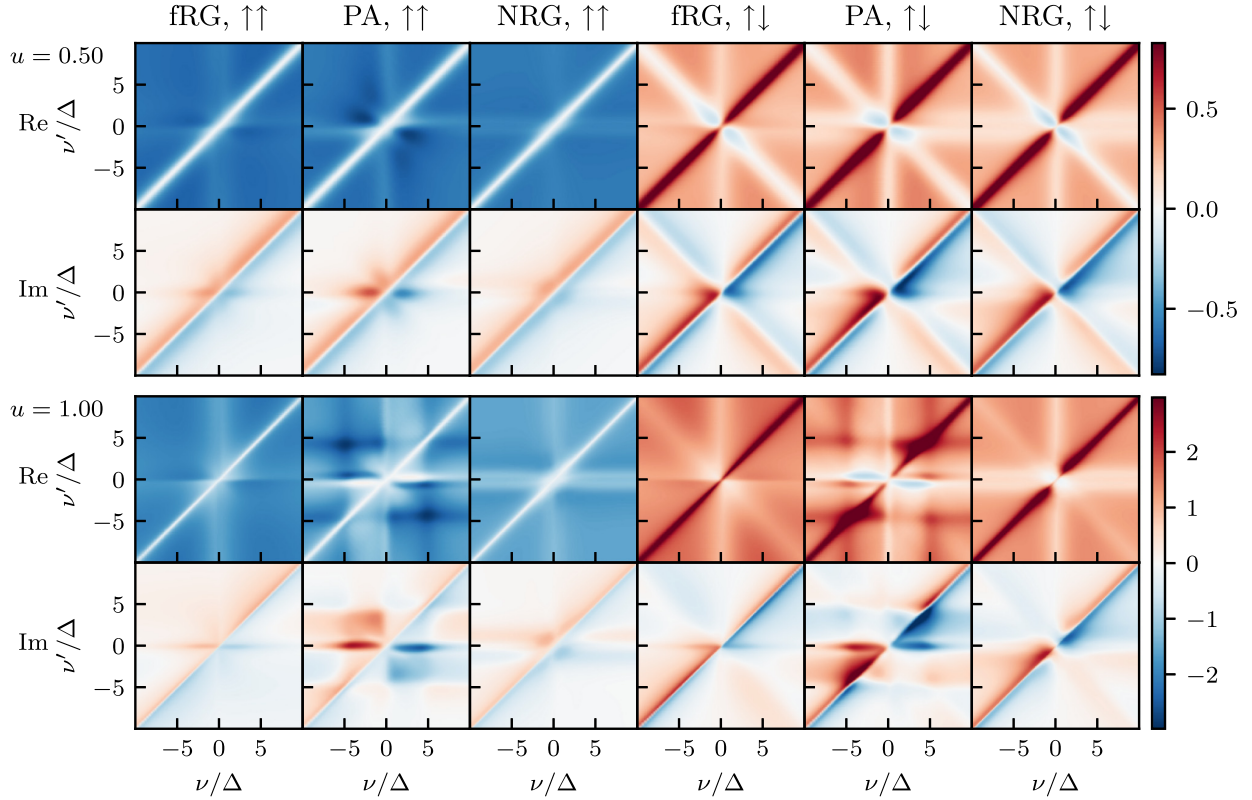


FIG. 11. Fully retarded ($k = 12|22$) Keldysh component of the full vertex, $[\Gamma_{\sigma\sigma'}^k(\omega_r = 0, \nu_i = \nu, \nu'_i = \nu') - \Gamma_{0,\sigma\sigma'}^k]/\Gamma_{0\uparrow\downarrow}^k$, for $u = 0.5$ (top panel) and $u = 1$ (bottom), computed using fRG, PA, and NRG (following Refs. [34,35]). We observe very good agreement for $u = 0.5$, which, qualitatively, mostly persists for higher interaction. However, $\text{Re}\Gamma_{\uparrow\downarrow}$ at $u = 1$ and low frequencies differs significantly between the methods: it is strictly positive in fRG, slightly negative in NRG, but much more strongly negative up to fairly large values of ν in the PA. Generally, the PA shows more complicated features than NRG for larger u , despite being numerically converged, indicating the breakdown of the PA.

The regulator dependence in fRG can be eliminated in the multiloop fRG framework, yielding results equivalent to the PA upon convergence in the number of loops [61–63]. This has been demonstrated numerically in imaginary frequencies for the AM [64] (and in Refs. [71,72] for the Hubbard model). Yet, using a multiloop extension of our Keldysh fRG code, we found the computation of multiloop contributions considerably harder for Keldysh vertices than for Matsubara vertices. The reason seems to be that, for real-frequency Keldysh vertices, the higher-loop contributions for increasing u show a considerably more complicated frequency structure than the original fRG vertex itself (similarly to how the PA vertex has more structure than its fRG counterpart in the bottom panel of Fig. 11). A more detailed analysis along these lines is, however, left for future work.

Our work paves the way for many follow-up studies. For instance, one can exploit the power of the KF to study nonequilibrium phenomena, and the AM with a finite bias voltage is tractable with only minor increase in the numerical costs [55,106]. Furthermore, we here considered moderate interaction strengths $u \lesssim 1.5$ because it is known that fRG and the PA are unable to access the nonperturbative regime of the AM [20,64] or, e.g., the Hubbard model [72,107]. An important future direction is, therefore, to use these methods

in a more indirect manner, as real-frequency diagrammatic extensions [41] of dynamical mean-field theory [42]. The first, established building block for this is the nonperturbative input, namely, 2p and 4p vertices, from NRG [34,35]. The present work presents another building block: real-frequency QFT with full frequency resolution of the 4p vertex. An important next step will be to use our diagrammatic framework to study the consistency of the NRG results for the 2p and 4p vertices, e.g., by checking whether they fulfill the SDE. The final building block will then be to include momentum degrees of freedom in real-frequency QFT approaches built on top of NRG.

Keeping track of the momentum dependence will lead to a major increase in numerical complexity. This can be addressed using economical implementations and compression algorithms such as truncated-unity approaches [108–111] or the new quantics tensor cross interpolation scheme [7,33,77]. The latter can be used to obtain highly compressed tensor network representations of multidimensional functions, potentially leading to exponential reductions in computational costs. First investigations have shown that the objects encountered in diagrammatic many-body approaches may indeed have strongly compressible quantics representations [7].

All raw data required to reproduce the plots as well as the full data analysis and the plotting scripts are available online

[112]. A separate publication of the fully documented source code used to generate the raw data is in preparation.

ACKNOWLEDGMENTS

We thank Jeongmin Shim and Seung-Sup B. Lee for providing data of the NRG 4p vertex as well as Severin Jakobs for a careful reading of the paper. The numerical simulations were performed on the Linux clusters and the SuperMUC cluster (project 23769) at the Leibniz Supercomputing Center in Munich. N.R. acknowledges funding from a graduate scholarship from the German Academic Scholarship Foundation (Studienstiftung des deutschen Volkes) and additional support from the ‘‘Marianne-Plehn-Programm’’ of the state of Bavaria. A.G. and J.v.D. were supported by the Deutsche Forschungsgemeinschaft under Germany’s Excellence Strategy EXC-2111 (Project No. 390814868), and the Munich Quantum Valley, supported by the Bavarian state government with funds from the Hightech Agenda Bayern Plus. F.B.K. acknowledges support by the Alexander von Humboldt Foundation through the Feodor Lynen Fellowship. The Flatiron Institute is a division of the Simons Foundation.

APPENDIX A: THE TWO-PARTICLE VERTEX

In compact notation, we denote the vertex by $\Gamma_{1'2'|12}$ where each leg carries a multi-index $i = (k_i, \sigma_i, v_i)$ with Keldysh index k_i , spin σ_i , and fermionic frequency v_i . Generic symmetries of the full Keldysh vertex are derived in Ref. [56] and other symmetries (such as spin or particle-hole symmetry) are given in Ref. [113]. In the following, we recap these symmetries and detail the parametrization in our implementation. First, we work with Keldysh indices rather than contour indices. In this basis, the $11 \cdots 1$ ($22 \cdots 2$) component of a multipoint correlator (vertex) vanishes [56]. This simplifies, e.g., the Dyson equation, $G^R = [(G_0^R)^{-1} - \Sigma^R]^{-1}$ and implies $\Gamma^{22|22} = 0$. Furthermore, crossing symmetry gives

$$\Gamma_{1'2'|12} = -\Gamma_{2'1'|12} = -\Gamma_{1'2'|21} = \Gamma_{2'1'|21}, \quad (\text{A1})$$

and complex conjugation

$$\Gamma_{1'2'|12} = (-1)^{1+\sum_i k_i} \Gamma_{12|1'2'}^* \quad (\text{A2})$$

Thermal equilibrium entails (generalized) fluctuation-dissipation relations between different Keldysh components. However, we choose to vectorize the code over Keldysh components and thus do not use these relations (see Appendix G for details on the vectorization). For a comprehensive list of multipoint fluctuation-dissipation relations, we refer to Refs. [56,114,115]. They are very well fulfilled (percent level) by our numerical results.

In the absence of a magnetic field, spin conservation and the invariance under a global spin flip reduce the number of independent spin components. The remaining components are related by the SU(2) relation [113]

$$\Gamma_{\sigma\sigma|\sigma\sigma} = \Gamma_{\sigma\bar{\sigma}|\sigma\bar{\sigma}} + \Gamma_{\sigma\bar{\sigma}|\bar{\sigma}\sigma}, \quad (\text{A3})$$

where $\bar{\uparrow} = \downarrow$ and vice versa. Hence, the spin dependence of the vertex can be parametrized by

$$\Gamma_{\sigma'_1\sigma'_2|\sigma_1\sigma_2} = \Gamma_{\uparrow\downarrow}\delta_{\sigma'_1,\sigma_1}\delta_{\sigma'_2,\sigma_2} + \Gamma_{\uparrow\downarrow}\delta_{\sigma'_1,\sigma_2}\delta_{\sigma'_2,\sigma_1}. \quad (\text{A4})$$

The components on the right-hand side are related by crossing symmetry. It thus suffices to compute a single one of them. At particle-hole symmetry, we further have

$$\begin{aligned} \Gamma_{1'2'|12}(v'_1, v'_2|v_1, v_2) &= \Gamma_{12|1'2'}(-v_1, -v_2|-v'_1, -v'_2) \\ &\stackrel{(\text{A2})}{=} (-1)^{1+\sum_i k_i} \Gamma_{1'2'|12}(-v'_1, -v'_2|-v_1, -v_2)^*, \end{aligned} \quad (\text{A5})$$

with the multi-indices $i = (k_i, \sigma_i)$, reducing the number of independent frequency components even more.

By frequency conservation, $v'_1 + v'_2 = v_1 + v_2$, the vertex depends on only three independent frequencies. These are chosen differently for each two-particle reducible vertex γ_r (see Fig. 12), with the bosonic transfer frequency ω_r and the fermionic frequencies v_r and v'_r . The vertices γ_r have nontrivial asymptotics in the limits $v_r^{(\prime)} \rightarrow \infty$. One can decompose the reducible vertex γ_r in asymptotic classes, see Eq. (29) [2]. Since the bare interaction is frequency independent, the asymptotic classes K_{ir} can be identified with certain diagrams that are reducible in channel r [2,73]. Connecting two external legs to the same bare interaction vertex reduces the dependence by one external frequency argument. $K_{1r}(\omega_r)$ consists of all diagrams where the two external legs carrying frequency v_r connect to the same bare vertex and the external legs carrying v'_r connect to another one. Hence, K_{1r} only depends on ω_r . $K_{2r}(\omega_r, v_r)$ consists of all diagrams where the v'_r legs connect to the same bare vertex while each of the other two legs connect to different bare vertices. $K_{2'r}(\omega_r, v'_r)$ is analogous to K_{2r} with the roles of v_r and v'_r interchanged. For $K_{3r}(\omega_r, v_r, v'_r)$ all external legs connect to different bare vertices. The bare vertices simplify not only the dependence of K_1, K_2 , and K_2' on frequencies but also on Keldysh indices. If a bare vertex connects to two external legs, flipping their Keldysh indices, $\bar{1} = 2$ ($\bar{2} = 1$), leaves the function invariant, see Eq. (17). This gives, e.g.,

$$\begin{aligned} K_{1p}^{k_1 k_2 | k_1 k_2} &= K_{1p}^{\bar{k}_1 \bar{k}_2 | k_1 k_2} = K_{1p}^{k_1 k_2 | \bar{k}_1 \bar{k}_2} \\ &= K_{1p}^{\bar{k}_1 \bar{k}_2 | \bar{k}_1 \bar{k}_2}, \end{aligned} \quad (\text{A6a})$$

$$K_{2p, \sigma_1 \sigma_2 | \sigma_1 \sigma_2}^{k_1 k_2} = K_{2p, \sigma_1 \sigma_2 | \sigma_1 \sigma_2}^{k_1 \bar{k}_2}. \quad (\text{A6b})$$

Note that the diagrammatic channels a and t flip under crossing symmetry, i.e., $\gamma_{a,1'2'|12} = -\gamma_{t,1'2'|21}$, while channel p is crossing symmetric itself. The symmetry relations in Eqs. (A1)–(A5) are formulated for full vertices. They can be adapted to the asymptotic classes K_{ir} by inserting the decomposition on both sides of each relation and taking the appropriate limits $v_r^{(\prime)} \rightarrow \infty$. For instance, $K_{\uparrow\downarrow,2p}$ is related to $K_{\uparrow\downarrow,2p}$ by

$$K_{\uparrow\downarrow,2p}^{k_1 k_2 | k_1 k_2}(\omega_p, v_p) \stackrel{(\text{A2})}{=} (-1)^{1+\sum_i k_i} K_{\uparrow\downarrow,2p}^{k_1 k_2 | k_1 k_2}(\omega_p, v_p). \quad (\text{A7})$$

For a formulation of the parquet and fRG equations in terms of asymptotic classes, we refer to Ref. [2] and to Eqs. (75) in Ref. [75].

As we vectorize over Keldysh indices, we explicitly keep track of all Keldysh components. The symmetry relations are then used to reduce the spin and frequency components [Eqs. (A1), (A2), and (A5) for $\Gamma_{\uparrow\downarrow}$]. To implement these symmetries for the K_{3r} class, it is convenient to express the

$$\Gamma(\nu'_1 \nu'_2 | \nu_1 \nu_2) = \text{Diagram} = \text{Diagram} + \text{Diagram} + \text{Diagram} + \text{Diagram}.$$

FIG. 12. We show the frequency conventions for the two-particle reducible vertices γ_r with $r = a, p, t$. Symmetric parametrizations with $\pm \frac{\omega}{2}$ ensure that vertex structures are centered around the frequency axis. The irreducible vertex R is shown in bosonic frequencies for completeness.

relations in terms of the three bosonic frequencies [100], giving

$$\begin{aligned} \Gamma_{\uparrow\downarrow; \omega_a, \omega_p, \omega_t}^{k_1 k_2' | k_1 k_2} &\stackrel{(A2)}{=} [\Gamma_{\uparrow\downarrow; \omega_a, \omega_p, -\omega_t}^{k_1 k_2 | k_1' k_2'}]^* (-1)^{1+\sum_i k_i}, \\ &\stackrel{(A1)}{=} \Gamma_{\uparrow\downarrow; -\omega_a, \omega_p, -\omega_t}^{k_2' k_1' | k_2 k_1} \stackrel{(A5)}{=} [\Gamma_{\uparrow\downarrow; -\omega_a, -\omega_p, -\omega_t}^{k_1' k_2' | k_1 k_2}]^* (-1)^{1+\sum_i k_i}, \end{aligned} \quad (A8)$$

such that the sign of the bosonic frequencies define sectors that are related by symmetry.

APPENDIX B: FREQUENCY DEPENDENCE OF VERTEX COMPONENTS

Figures 13 and 14 show plots for the frequency dependence of the asymptotic classes K_2 and K_3 for each of the three two-particle channels $r \in \{a, p, t\}$, computed in the PA for $u = 0.5$ and $u = 1$, respectively. We use the natural frequency parametrization for each channel r and set the bosonic transfer frequency $\omega_r = 0$ in the plots for K_3 . The figures instructively show what types of nontrivial structures emerge during such calculations. In particular, one can clearly see that the frequency resolution needs to be very high throughout to resolve all sharp features (many occurring on scales much smaller than Δ). Moreover, the weak-coupling results may serve as benchmarks for future computations of Keldysh vertices using other methods, such as NRG or QMC.

APPENDIX C: FULLY PARAMETRIZED EQUATIONS

We can write the parquet equations (20) and one-loop fRG flow equations (19) entirely in terms of two functions, bubbles and loops. A bubble B_r in channel $r = a, p, t$ combines two vertices via a propagator pair

$$\Pi_{a, \omega_a \nu_a}^{34|3'4'} = G_{\nu_a - \omega_a/2}^{3|3'} G_{\nu_a + \omega_a/2}^{4|4'}, \quad (C1a)$$

$$\Pi_{p, \omega_p \nu_p}^{34|3'4'} = G_{\omega_p/2 + \nu_p}^{3|3'} G_{\omega_p/2 - \nu_p}^{4|4'}, \quad (C1b)$$

$$\Pi_{t, \omega_t \nu_t}^{43|3'4'} = G_{\nu_t - \omega_t/2}^{3|3'} G_{\nu_t + \omega_t/2}^{4|4'}, \quad (C1c)$$

where we use the natural frequency parametrization for each channel (see Fig. 15) and superscripts indicate Keldysh indices ($34|3'4'$) = ($k_3 k_4 | k_3' k_4'$). In the following, we give explicit formulas for the $\uparrow\downarrow$ -spin component of bubble diagrams that combine vertices V and W :

$$B_a[V, W]_{\uparrow\downarrow; \omega_a \nu_a \nu'_a}^{1'2'|12} = \int_{\bar{\nu}} V_{\uparrow\downarrow; \omega_a \nu_a \bar{\nu}}^{1'4'|32} \Pi_{a, \omega_a \bar{\nu}}^{34|3'4'} W_{\uparrow\downarrow; \omega_a \bar{\nu} \nu'_a}^{3'2'|14}, \quad (C2a)$$

$$B_p[V, W]_{\uparrow\downarrow; \omega_p \nu_p \nu'_p}^{1'2'|12} = \int_{\bar{\nu}} V_{\uparrow\downarrow; \omega_p \nu_p \bar{\nu}}^{1'2'|34} \Pi_{p, \omega_p \bar{\nu}}^{34|3'4'} W_{\uparrow\downarrow; \omega_p \bar{\nu} \nu'_p}^{3'4'|12}, \quad (C2b)$$

with $\int_{\bar{\nu}} = \int_{-\infty}^{\infty} d\bar{\nu}/2\pi i$ (the internal spin sum and crossing symmetry in B_p cancel the prefactor of $1/2$), and

$$\begin{aligned} B_r[V, W]_{\uparrow\downarrow; \omega_r \nu_r \nu'_r}^{1'2'|12} &= - \int_{\bar{\nu}} \Pi_{t, \omega_t \bar{\nu}}^{43|3'4'} [V_{\uparrow\downarrow; \omega_t, \nu_t, \bar{\nu}}^{4'2'|32} W_{\uparrow\downarrow; \omega_t \bar{\nu} \nu'_t}^{1'3'|14} + V_{\uparrow\downarrow; \omega_t \nu_t \bar{\nu}}^{4'2'|32} W_{\uparrow\downarrow; \omega_t \bar{\nu} \nu'_t}^{1'3'|14}], \end{aligned} \quad (C2c)$$

where the $\uparrow\uparrow$ -spin component is obtained via Eq. (A4).

For the loop, we parametrize the vertex in the t -channel convention with $\omega_t = 0$ and write

$$L[\Gamma, G]_{\nu}^{1'|1} = - \int_{\bar{\nu}} G_{\bar{\nu}}^{2|2'} [\Gamma_{\uparrow\downarrow} + \Gamma_{\uparrow\uparrow, 0\nu, \bar{\nu}}^{1'2'|12}]. \quad (C3)$$

Using the loop L and bubbles B_r , the parquet equations (20) read

$$\gamma_r = B_r[I_r, \Gamma], \quad (C4a)$$

$$\Sigma = L[\Gamma_0, G] + \frac{1}{2} L[B_a[\Gamma_0, \Gamma], G]. \quad (C4b)$$

In the SDE, the internal spin sum can be performed, canceling the factor of $1/2$ in Eq. (C4b) by crossing symmetry to give

$$\Sigma_{\text{SDE}\nu}^{1'|1} = - \int_{\nu_t} G_{\nu_t}^{2|2'} [\Gamma_{0, \uparrow\downarrow} + B_a[\Gamma_0, \Gamma]_{\uparrow\downarrow, 0\nu, \nu}^{1'2'|12}]. \quad (C5)$$

The one-loop fRG flow equations [cf. Eq. (19)] are

$$\dot{\Sigma} = L(\Gamma, S), \quad \dot{\gamma}_r = \dot{B}_r(\Gamma, \Gamma), \quad (C6)$$

where the dot on \dot{B}_r denotes a differentiated propagator pair, $\partial_{\Lambda} \Pi_r = \dot{G}G + G\dot{G}$, including the Katanin substitution $S \rightarrow \dot{G} = S + G\dot{\Sigma}G$ [70].

Susceptibilities are obtained from $G^{(4)}$, Eq. (13), by contracting pairs of external legs and subtracting the disconnected parts [116, 117]. For the spin- $\uparrow\downarrow$ and spin- $\uparrow\uparrow$ components, we get

$$\chi_{a, \sigma\sigma', \omega_a}^{12|1'2'} = \int_{\nu} \Pi_{a, \omega_a \nu}^{12|1'2'} + \int_{\nu} \int_{\nu'} \Pi_{a, \omega_a \nu}^{14|1'4'} \Gamma_{\sigma\sigma', \omega_a \nu \nu'}^{34|3'4'} \Pi_{a, \omega_a \nu'}^{32|3'2'}, \quad (C7a)$$

$$\begin{aligned} \chi_{p, \sigma\sigma', \omega_p}^{12|1'2'} &= \int_{\nu} \Pi_{p, \omega_p \nu}^{12|1'2'} (1 - \delta_{\sigma, \sigma'}) \\ &+ \int_{\nu} \int_{\nu'} \Pi_{p, \omega_p \nu}^{12|3'4'} \Gamma_{\sigma\sigma', \omega_p \nu \nu'}^{34|3'4'} \Pi_{p, \omega_p \nu'}^{34|1'2'}, \end{aligned} \quad (C7b)$$

$$\begin{aligned} \chi_{t, \sigma\sigma', \omega_t}^{12|1'2'} &= - \int_{\nu} \Pi_{t, \omega_t \nu}^{12|1'2'} \delta_{\sigma, \sigma'} \\ &+ \int_{\nu} \int_{\nu'} \Pi_{t, \omega_t \nu}^{12|3'4'} \Gamma_{\sigma\sigma', \omega_t \nu \nu'}^{34|3'4'} \Pi_{t, \omega_t \nu'}^{34|1'2'}. \end{aligned} \quad (C7c)$$

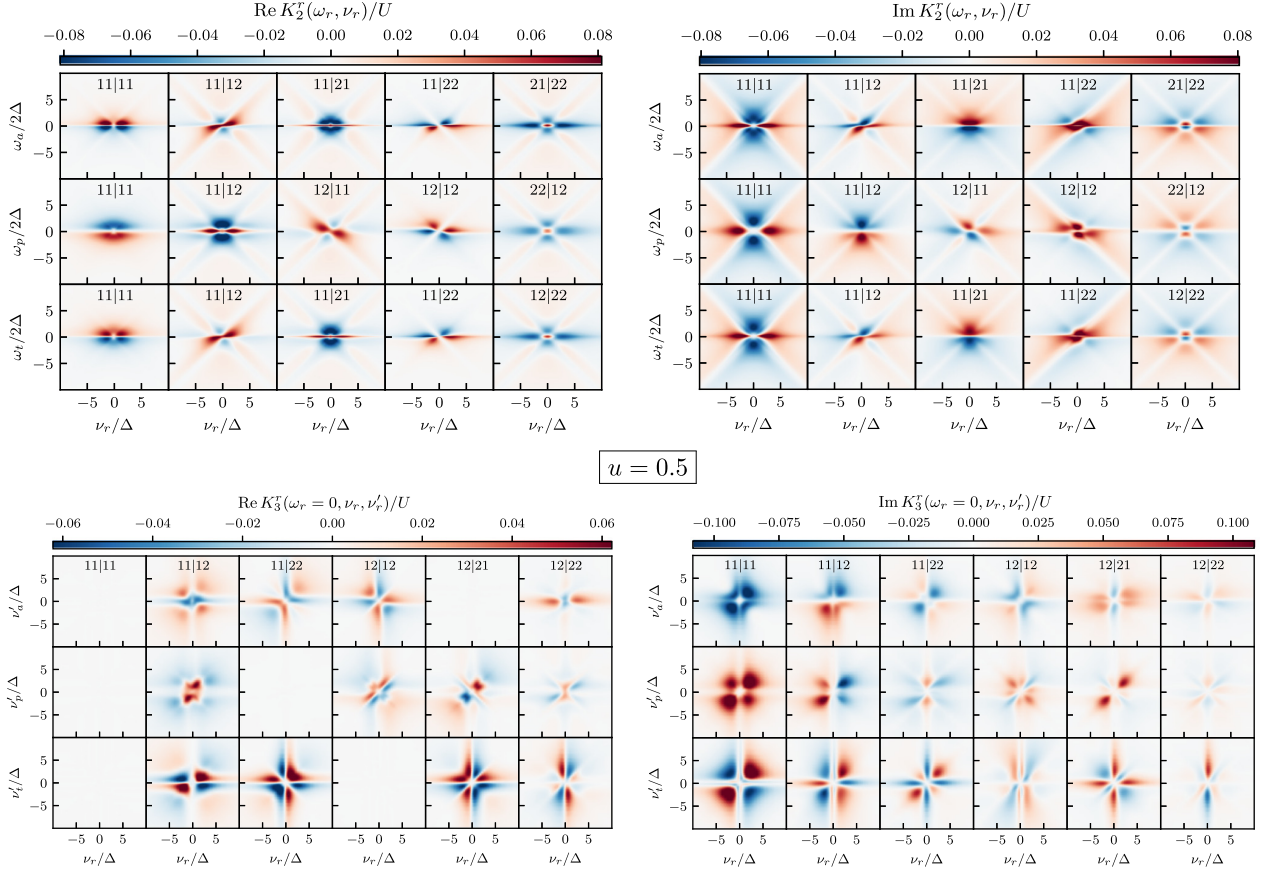


FIG. 13. Real (left) and imaginary (right) parts of K_2 (top) and K_3 (bottom) vertex components in the PA for $u = 0.5$. The three rows of each subfigure show results for the three two-particle channels $r \in \{a, p, t\}$. The columns show all independent Keldysh components. Natural frequency parametrizations were used and for K_3 the bosonic transfer frequency ω_r was set to zero. Consequently, some components of $\text{Re}K_3$ vanish.

From these functions, we obtain physical susceptibilities as $\chi_{d/m} = \chi_{r,\uparrow\uparrow} \pm \chi_{r,\uparrow\downarrow}$, or after exploiting spin and crossing symmetry, Eqs. (A1) and (A3),

$$\chi_d^{12|1'2'} = 2\chi_{t,\uparrow\downarrow}^{12|1'2'} - \chi_{a,\uparrow\downarrow}^{21|1'2'}, \quad (\text{C8a})$$

$$\chi_m^{12|1'2'} = -\chi_{a,\uparrow\downarrow}^{21|1'2'}. \quad (\text{C8b})$$

These functions have the Keldysh structure of 4p functions. To identify the retarded susceptibilities $\chi^R(\omega)$ in terms of 2p functions [analogous to the propagator, Eq. (7)], we use the bare three-leg Hedin vertex $\lambda_0^{(k_1 k_2) k_3}$ [118] where the Keldysh indices k_1, k_2 belong to $\chi^{12|1'2'}$ and k_3 to χ^R . In terms of contour indices, it reads $\lambda_0^{(c_1 c_2) c_3} = -c_1 \delta_{c_1=c_2=c_3}$; in Keldysh indices, the nonzero components are

$$\lambda_0^{(kk)2} = \frac{1}{\sqrt{2}} = \lambda_0^{(k\bar{k})1}. \quad (\text{C9})$$

Hence, two (un-)equal fermionic Keldysh indices translate to a “2” (“1”) for the bosonic line. We thus identify

$$\chi_r^R = \chi_r^{2|1} = 2\chi_r^{1|12}, \quad r = a, p, t. \quad (\text{C10})$$

In the parquet formalism, it was shown that the susceptibilities χ_r ($r \in \{a, p, t\}$) are related to asymptotic functions via [2]

$$(K_{1a})_{1'2'|12} = -(\Gamma_0)_{1'4'|32}(\chi_a)_{34|3'4'}(\Gamma_0)_{3'2'|14}, \quad (\text{C11a})$$

$$(K_{1p})_{1'2'|12} = -(\Gamma_0)_{1'2'|34}(\chi_p)_{34|3'4'}(\Gamma_0)_{3'4'|12}, \quad (\text{C11b})$$

$$(K_{1t})_{1'2'|12} = -(\Gamma_0)_{4'2'|42}(\chi_t)_{34|3'4'}(\Gamma_0)_{1'3'|13}. \quad (\text{C11c})$$

For the retarded spin- $\uparrow\downarrow$ -component, we have

$$K_{1r\uparrow\downarrow}^R = -U^2 \chi_{r\uparrow\downarrow}^R. \quad (\text{C12})$$

Although one-loop fRG does not fulfill the BSEs (20b)–(20d), Eq. (C12) can still be used as an estimate for susceptibilities. In the present context, these are often called “flowing” susceptibilities, while Eq. (C7) defines the “postprocessed” susceptibilities. The PA, fRG, and K1SF results for χ_m and χ_d shown in the main text were computed using Eqs. (C11).

APPENDIX D: CHANNEL-ADAPTED SCHWINGER-DYSON EQUATION

In the parquet formalism, the frequency dependence of the self-energy $\Sigma(\nu)$ enters via the second term in the SDE (20a).

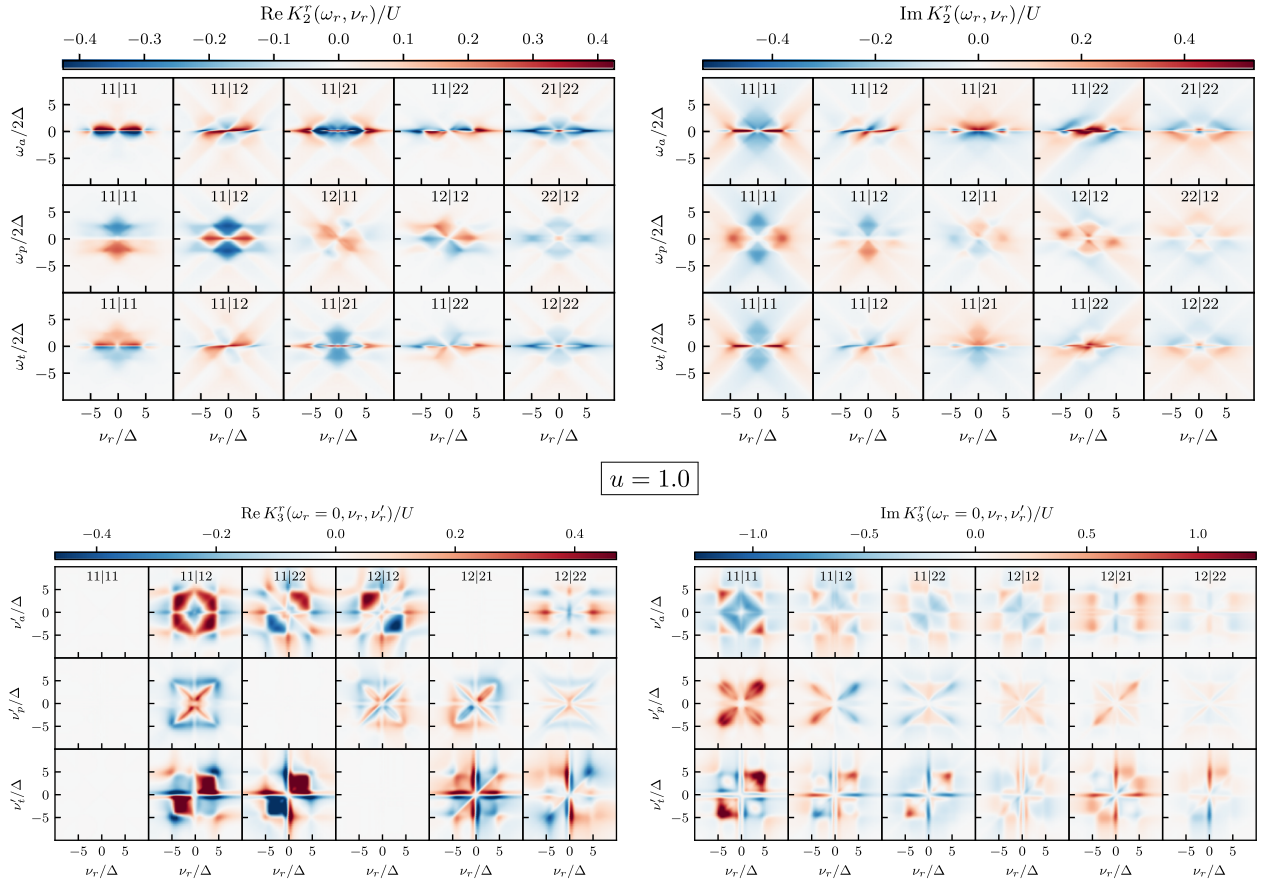
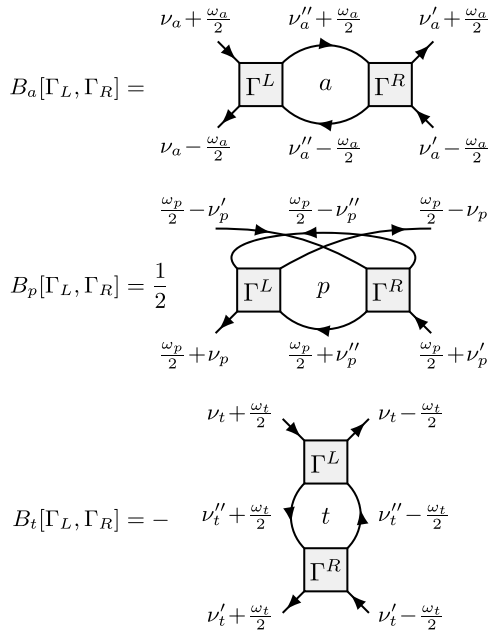

 FIG. 14. Same vertex components as in Fig. 13, computed in the PA for $u = 1$.


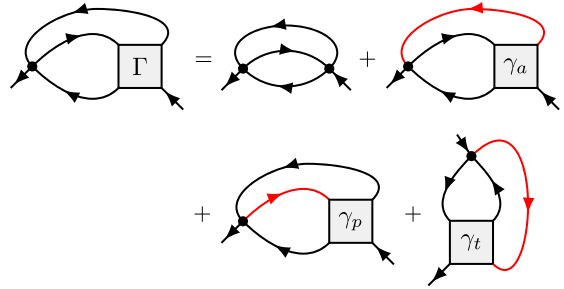
FIG. 15. Diagrammatic representation of the bubble functions in Eq. (C2).

In the following, we discuss three options for the numerical evaluation of this diagram.

First, using the parquet decomposition [Eq. (20e)], the second term of the SDE can be written in terms of bubbles B_r and loop L as (see Fig. 16) [72,107]

$$\Sigma^{\text{SDE1}} = L(B_a(\Gamma_0, \Gamma_0), G) + \sum_r L(B_r(\Gamma_0, \gamma_r), G). \quad (\text{D1})$$

Here and below, a loop, L , acting on a t bubble, B_t , contracts the two right legs, as opposed to the two top legs for all other vertex types (cf. Fig. 16).


 FIG. 16. Rewriting of the SDE, where crossing symmetry was used for the γ_t part. The red line indicates which propagator enters the loop L in Eq. (D1).

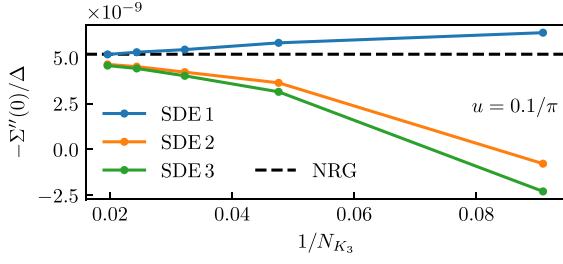


FIG. 17. Imaginary part of the retarded self-energy at $\nu = 0$, computed with the parquet solver and different versions of the SDE, shown as a function of N_{K_3} ($u = 0.1/\pi$, $T/U = 0.01$). The dashed line is the NRG result. For low N_{K_3} , SDE2 and SDE3 give the wrong sign. With increasing resolution, all results approach the correct value.

Second, the SDE in Eq. (20a), without further manipulation, reads

$$\Sigma^{\text{SDE2}} = L(B_r(\Gamma_0, \Gamma), G), \quad r \in \{a, p, t\}, \quad (\text{D2})$$

where the channel r can be freely chosen. Third, using $B_r(\Gamma_0, \gamma_r) = K_{1r} + K_{2r}$ [2], the SDE equivalently reads

$$\Sigma^{\text{SDE3}} = L(K_{1r} + K_{2r}, G). \quad (\text{D3})$$

Even though the above versions of the SDE are analytically equivalent, they vary in numerical accuracy and cost. Evaluating Σ^{SDE3} is cheaper than the others since it skips the computation of bubbles B_r . However, we found that Eq. (D1) is most accurate, since the γ_r are inserted into bubbles B_r of the same channel r . Using the natural frequency parametrization for the reducible vertices $\gamma_r(\omega_r, \nu_r, \nu'_r)$, Σ^{SDE1} also has the benefit that one only needs to interpolate along the ν_r direction.

To illustrate this point, we consider a third-order contribution to the self-energy:

$$L(B_t(\Gamma_0, K_{1t}), G) = L(B_a(\Gamma_0, K_{1t}), G), \quad (\text{D4})$$

$$(\text{D5})$$

Inserting K_{1t} into B_a as done on the right results in diagrams that belong to the asymptotic class $K_{2'a}$. However, on the left, K_{1t} is inserted into B_t , resulting in diagrams belonging to K_{1t} . The latter can be treated with higher resolution and thus lead to better results for Σ , see Fig. 17. Note that the question how to best parametrize the SDE also arises in the context of the truncated-unity formalism for momentum-dependent models, where this choice was found to affect the quality of the results even more strongly due to the additional approximation from the truncation of the form-factor expansion [72,107].

APPENDIX E: EQUAL-TIME CORRELATORS AND HARTREE SELF-ENERGY

Parts of the following discussion can be found in previous works, see Refs. [54,59,66]. We reiterate some of the points made there and extend on them to the context of this work.

The definitions of G^{++} and G^{--} , Eqs. (3) and (4), are ambiguous at $t_1 = t_2$ because $\Theta(t_1 - t_2 = 0)$ is not uniquely defined. If two operators ψ, ψ^\dagger are placed at the same point on the Keldysh contour, it is *a priori* not clear how to order them. The ambiguity is resolved by demanding that ψ^\dagger be put left of ψ (“normal ordering”), which implies $G^{-}(t, t) = G^<(t, t) = G^{++}(t, t)$. Then, $G^< + G^> - G^T - G^{\bar{T}} = 0$ does actually *not* hold, and care is due with Keldysh-rotated quantities. Since the point $t_1 = t_2$ is of zero measure in time integrals, which occur when computing diagrams in frequency space, this subtlety is irrelevant for most practical purposes. However, there is one important exception of equal-time nature, namely, diagrams with loops that begin and end at the *same* bare vertex. With an instantaneous bare interaction, both incoming and outgoing legs have the same time argument, so that these diagrams involve the frequency-integrated (i.e., equal-time) propagator.

The equal-time propagator determines the Hartree self-energy of the AM (e.g., in PT2 calculations),

$$\Sigma_{\text{H}} = - \text{diagram} \quad (\text{E1})$$

Recall that, for the sAM ($\epsilon_d = -U/2$), the Hartree term is constant, $\Sigma_{\text{H}} = U/2$, and can be absorbed into the bare propagator $G_0^R \rightarrow G_{\text{H}}^R$, see Eq. (24). Subsequently, G_{H}^R is used for all computations involving bare propagators. In analogy, in the aAM, the bare propagator is replaced by the Hartree propagator, too. However, here, Σ_{H} is not constant and must be computed self-consistently (using, e.g., a simple bracketing algorithm), as it enters both sides of Eq. (E1). Now, a naive computation of the retarded component of this diagram after the Keldysh rotation (and in the frequency domain) would yield

$$\begin{aligned} \Sigma_{\text{H}}^R &= \Sigma_{\text{H}}^{1|2} = - \text{diagram} = - \underbrace{\text{diagram}}_{G^{1|1} \stackrel{?}{=} 0} - \text{diagram} \\ &\stackrel{?}{=} \frac{U}{2} \int \frac{d\nu'}{2\pi i} G^K(\nu'). \end{aligned} \quad (\text{E2})$$

This is, however, incorrect since $G^{1|1}(t|t) \neq 0$ after Keldysh rotation. The correct result can be found by staying in the contour basis, using that, at equal times, only $\Sigma_{\text{H}}^{-}(t, t) = -\Sigma_{\text{H}}^{++}(t, t)$ is nonzero. Keldysh rotation yields $\Sigma_{\text{H}}^R(t, t) = \Sigma_{\text{H}}^{-}(t, t)$, for which one has

$$\Sigma_{\text{H}}^R = \Sigma_{\text{H}}^{-} = - \text{diagram} = U \int \frac{d\nu'}{2\pi i} G^<(\nu'). \quad (\text{E3})$$

To compute Eq. (E3) in thermal equilibrium, one can relate $G^<$ to G^R using the inverse Keldysh rotation and the FDT

[Eq. (10)]:

$$\begin{aligned} G^<(v) &= \frac{1}{2}[-G^R(v) + G^A(v) + G^K(v)] \\ &= -2in_F(v)\text{Im}G^R(v), \end{aligned} \quad (\text{E4})$$

with the Fermi function $n_F(v) = 1/(1 + e^{v/T})$. This discussion of Σ_H also applies to the PA via the first term of the SDE (20a) (the second vanishes for $|\nu| \rightarrow \infty$).

In fRG, Σ_H is generally renormalized throughout the flow, according to Eq. (19a) for $\dot{\Sigma}$. In the limit $|\nu| \rightarrow \infty$, relevant for extracting the Hartree contribution, only those diagrams survive for which the in- and outgoing lines are attached to the same bare vertex:

$$\dot{\Sigma}_H = - \lim_{\nu \rightarrow \pm\infty} \left[\text{Diagram 1} \right] = - \left[\text{Diagram 2} \right] - \left[\text{Diagram 3} \right] - \left[\text{Diagram 4} \right]. \quad (\text{E5})$$

In practice, the Hartree contribution $\dot{\Sigma}_H$ is not computed separately but is part of the full self-energy flow. There, equal-time propagators are single-scale propagators, occurring in the following contributions:

$$\dot{\Sigma} = - \left[\text{Diagram 1} \right] - \left[\text{Diagram 2} \right] - \left[\text{Diagram 3} \right] - \left[\text{Diagram 4} \right]. \quad (\text{E6})$$

However, in the context of this work, it turns out that these specific equal-time loops *can* be computed from just the Keldysh-component of the single-scale propagator, as in the naive calculation Eq. (E2). The reason is that, in the hybridization flow, the retarded component of the single-scale propagator asymptotically scales as $\approx 1/\nu^2$ for $\nu \rightarrow \pm\infty$, see Eq. (25). Using the FDT in the forms of Eqs. (E4) and (10), we can write

$$\begin{aligned} S^K(v) &= 2i[1 - 2n_F(v)]\text{Im}S^R(v) \\ &= 2i\text{Im}S^R(v) + 2S^<(v). \end{aligned} \quad (\text{E7})$$

When computing $\int d\nu S^K(\nu)$, one can apply Cauchy's theorem to the first term, using its asymptotic behavior (see above). Closing the integration contour by an infinite semicircle in the upper half plane, avoiding the pole in the lower half plane, gives zero. Hence, in the hybridization flow, we have $\int d\nu S^K(\nu) = 2 \int d\nu S^<(\nu)$, and the subtlety discussed previously is irrelevant. Note that this argument may not apply to other regulators, where S has a different expression.

APPENDIX F: DIAGRAMMATIC DEFINITION OF SECOND-ORDER PERTURBATION THEORY

Following the previous discussion, the Hartree term in PT2 is determined self-consistently. The resulting Hartree propa-

gator G_H then fulfills the Dyson equation

$$G_H = G_0 + G_0 \Sigma G_H. \quad (\text{F1})$$

In these and the following diagrams, the Hartree propagator G_H is represented by a black line, whereas the light gray line denotes the bare propagator G_0 . The dynamical part of the self-energy is computed from the first nontrivial term of the SDE, using G_H ,

$$\Sigma - \Sigma_H = -\frac{1}{2} \left[\text{Diagram 1} \right]. \quad (\text{F2})$$

The vertex in PT2 is given by the three diagrams

$$\Gamma - \Gamma_0 = \left[\text{Diagram 1} \right] + \frac{1}{2} \left[\text{Diagram 2} \right] - \left[\text{Diagram 3} \right], \quad (\text{F3})$$

again evaluated with G_H in the internal lines. Susceptibilities are then computed from this vertex via the standard formula; for χ_a , e.g., (again using G_H throughout)

$$\begin{aligned} \chi_a &= \left[\text{Diagram 1} \right] + \left[\text{Diagram 2} \right] + \left[\text{Diagram 3} \right] \\ &+ \left[\text{Diagram 4} \right]. \end{aligned} \quad (\text{F4})$$

To obtain exactly the second-order contribution to the susceptibility, one insertion of the dynamical part of the self-energy into each line of the bubble term is required, which gives rise to the second and third diagrams shown.

We checked that, in the sAM at sufficiently low temperatures, our numerical PT2 solution matches the analytic $T = 0$ results of Ref. [95] [Eqs. (3.14) and (3.6)–(3.8) therein]

$$Z = 1 - (3 - \frac{1}{4}\pi^2)u^2, \quad (\text{F5a})$$

$$-\Sigma''(v)/\Delta = \frac{1}{2}u^2(v^2 + \pi^2 T^2)/\Delta^2, \quad |\nu|, T \ll \Delta, \quad (\text{F5b})$$

$$\tilde{\chi}_{m/d} = \frac{1}{2}[1 \pm u + (3 - \frac{1}{4}\pi^2)u^2]. \quad (\text{F5c})$$

APPENDIX G: IMPLEMENTATION DETAILS

Below, we describe our choices for the implementation of the parquet and fRG solver, the sampling of continuous functions, and the performance-critical quadrature routine. In the process, we also discuss the numerical accuracy of our results.

The evaluation of bubble diagrams, Eq. (C2), is a major bottleneck in our methods. However, computations for different external arguments can be distributed efficiently over multiple threads and compute nodes. It also proved beneficial to vectorize the sum over internal Keldysh indices by reordering and combining Keldysh indices k_i to Keldysh

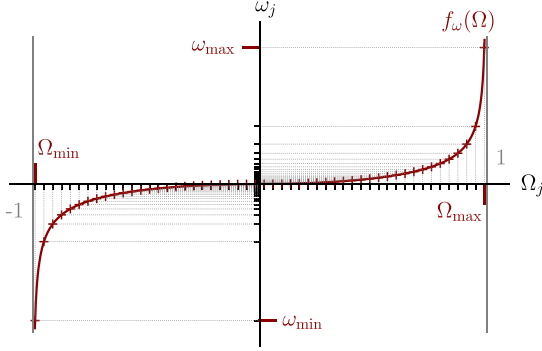


FIG. 18. Nonlinear frequency grid $\{\omega_j\}_{j=1}^N$ obtained via a transformation $f_A(\Omega)$, Eq. (G2), from an auxiliary linear grid $\{\Omega_j\}_{j=1}^N$ of size N .

multi-indices (k_m, k_n)

$$\Gamma^{k_1, k_2, k_1, k_2} \mapsto \begin{cases} \Gamma^{(k_1, k_2), (k_2, k_1)} & \text{for } a \text{ channel} \\ \Gamma^{(k_1, k_2), (k_1, k_2)} & \text{for } p \text{ channel} \\ \Gamma^{(k_2, k_2), (k_1, k_1)} & \text{for } t \text{ channel,} \end{cases} \quad (\text{G1})$$

turning the Keldysh sum into an ordinary matrix product (which is optimized in common linear algebra libraries). This preprocessing step enables us to efficiently fetch matrix-valued integrands and to perform sums over Keldysh indices and spins in an optimized manner. It requires all Keldysh components to be present in the data, and, therefore, all of them are included in our computations. Consequently, FDTs could not be exploited to gain performance benefits as they merely relate different Keldysh components.

For the integrals over internal frequencies in Eqs. (C2) and (C3), we implemented an adaptive quadrature algorithm which picks sampling points based on a local error estimate and tolerance ($\epsilon_{\text{rel}} = 10^{-5}$). With various vertex components, the evaluation of a vertex at a certain frequency is rather expensive. Therefore, we choose a quadrature algorithm that reuses the previous function evaluations when it refines the quadrature value on a subinterval (4-point Gauss–Lobatto rule with 7-point Kronrod extension) [119]. Due to fine structures in the integrands, we found a higher-order quadrature rule to be beneficial for the convergence of the routine. To help the algorithm find the structure in the integrand, we subdivide the integration interval at the expected positions of structure in the vertices or the propagators. Quadrature of the integrand’s tails at high frequency is performed numerically by means of a suitable substitution of the integration variable [120]. For matrix-valued integrands, we use the sup norm $\|\cdot\|_\infty$ to compute the error estimate for the quadrature.

Since Keldysh functions depend on continuous frequencies, a reliable and efficient representation is vital. We choose a nonuniform set of sampling points and obtain function values by (multi-)linear interpolation. The overall behavior of our functions is known: The self-energy and the asymptotic functions K_{ir} can have sharp structures at smaller frequencies while, at large frequencies, they decay to a constant value with an approximate ω^{-k} with $k \in \mathbb{N}$. To capture this behavior, we map an equidistant grid of an auxiliary variable $\Omega \in [-1, 1]$

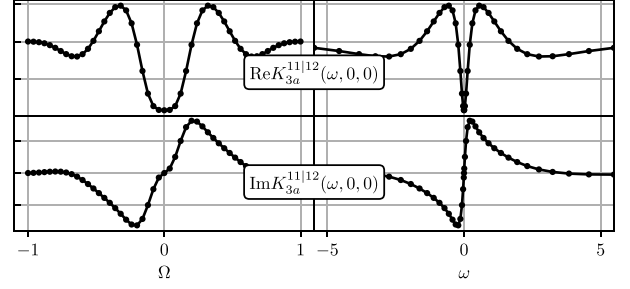


FIG. 19. Illustration of the resolution of vertex data for a slice through $\text{Re}K_{3a}^{11|12}$ and $\text{Im}K_{3a}^{11|12}$. The left panels show the data on the equidistant auxiliary grid, the right panels show the data on real frequencies. Many sampling points are placed around the center where structures are peaked, while the tails are treated with very few points. Here, we also see an artifact due to our choice of the grid function (G2): since the grid function has a discontinuity at second order, we see a saddle point in the bottom left panel even though the function is linear there. The good resolution of the central peak in the real part comes at the cost of a saddle point in the imaginary part.

to a nonuniform one via the function

$$\omega = f_A(\Omega) = \frac{A\Omega|\Omega|}{\sqrt{1-\Omega^2}}, \quad (\text{G2})$$

with constant $A > 0$, see Figs. 18 and 19. The resulting sampling points are dense around $\omega = 0$. At large frequencies, the function $f_A(\Omega)$ captures a $1/\omega^2$ decay effectively for $|\Omega| \lesssim 1$. Furthermore, the structures in the AM scale approximately with the hybridization Δ . Therefore, we choose the frequency-grid parameter A as multiples of Δ and $\omega_{\max} = 100A$. With a fixed maximal frequency ω_{\max} , the variable A determines the interval $[-\Omega_{\max}, \Omega_{\max}]$ used to construct the frequency grid via Eq. (G2). Our choices for A are given in Table I.

It is also possible to adapt the frequency-grid parameter A automatically. Interpolating the vertex linearly, we can approximate the error by the maximal curvature in the space of the linearly sampled auxiliary variable Ω . Hence, we can use the curvature as an error function to optimize the parameter A in Eq. (G2). The direction-dependent curvature of a multivariate function f is encoded in the Hessian, $H_{ij} = \partial_i \partial_j f(\mathbf{x})$. We can efficiently compute a scalar measure for the curvature via the Frobenius norm of the Hessian, giving

$$\|H\|_F^2 = \sum_{i,j} |H_{i,j}|^2 = \text{Tr}H^2 = \sum_i |\lambda_i|^2, \quad (\text{G3})$$

where λ_i are the eigenvalues of H . An approximation of the partial derivatives can be obtained with the finite differences method. However, for the studied parameter regime of the AM, we found (using Brent’s method [121] as the minimizer) that optimizing the grid parameters A did not make a big difference compared with a simple rescaling according to Table I.

TABLE I. Frequency-grid parameter A for Eq. (G2).

	Σ	K_1	$K_{2,\omega}$	$K_{2,v}$	$K_{3,\omega}$	$K_{3,v}$
A/Δ	10	5	15	20	10	10

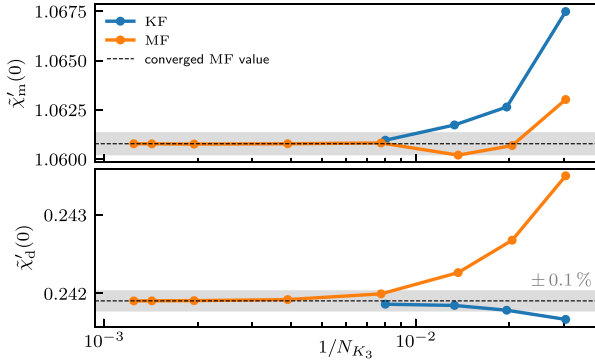


FIG. 20. Convergence with respect to frequency resolution for the static susceptibilities as in Fig. 8 from parquet solvers in the KF and the MF for $u = 0.75$ (a setting where K_2 and K_3 are relevant). The numbers of frequency points for K_1 and K_2 are chosen proportional to N_{K_3} . In the MF, we used $N_{K_3} = 33, 49, 73, 129, 257, 513, 701, 801$, in the KF $N_{K_3} = 33, 51, 75, 125$. The KF and MF results agree very well; the shaded region marks 0.1% deviation.

To verify convergence in the number of sampling points, we compared the static susceptibilities between implementations in the KF and the MF and found agreement up to 1%, see Fig. 20.

To solve the fRG equations (19) we employ a Runge–Kutta solver with adaptive step size control (Cash–Carp). The step size is chosen according to an error estimate and tolerance (here: relative error $\epsilon_{\text{rel}} = 10^{-6}$). Furthermore, we reparametrize the flow parameter $\Lambda(t) = f_{A=5}(t)$ to provide a good first guess for the step sizes, using the same function $f_A(t)$ as for frequencies ω , Eq. (G2), with $A = 5$. It provides large steps for high Λ and small steps for small Λ for equidistant t . As initial condition of Σ^{Λ_i} and Γ^{Λ_i} at large Λ_i , we use the converged parquet solution. As discussed in Sec. III, the PA gives good results in the perturbative regime.

To solve the self-consistent parquet equations f_{PA} in Eqs. (20), which constitute a fixed-point equation for the state $\Psi = (\Sigma, \Gamma)$, i.e., $\Psi = f_{\text{PA}}(\Psi)$, we perform fixed-point iterations until the result meets a tolerance criterion, here $\|\Psi - f_{\text{PA}}(\Psi)\|_{\infty} < 10^{-6} \|\Psi\|_{\infty}$. For intermediate to higher $u \gtrsim 1$, it proves beneficial to stabilize the algorithm with a partial update scheme, i.e.,

$$\Psi \leftarrow (1 - m)\Psi + m f_{\text{PA}}(\Psi), \quad (\text{G4})$$

with mixing factor $0 < m \leq 1$ (here typically $m = 0.5$). For faster convergence in the vicinity of the fixed point, we use Anderson acceleration [122,123].

APPENDIX H: NUMERICAL COSTS

The numerically most complex objects in all calculations are the K_3 components of the two-particle reducible vertices, as they depend on three continuous frequency arguments independently. The numerical cost of a parquet or fRG computation is therefore $O(N_{K_3}^3)$, where N_{K_3} is the number of grid points per frequency used for K_3 . This applies to memory (as all this data has to be stored) and to computation time (as BSEs or fRG flow equations are evaluated for all external

TABLE II. Number of frequency points for different diagrammatic classes and methods. We use the same number of points for Σ as for K_1 . In most PA computations, $N_{K_3} = 51$, except for the largest values of u , which required $N_{K_3} = 101$ for converging the parquet solver.

	N_{K_1}	N_{K_2}	N_{K_3}
fRG	401	201	101
PA	401	201	51–101
PT2	801	0	0
K1SF	401	0	0

arguments). We give in Table II the number of frequency points used for each diagrammatic class. The self-energy was resolved on a grid with the same number of points as the K_1 class.

The numerical cost is further determined by the accuracy (or the convergence criteria) chosen for the iterative parquet solver or the Runge–Kutta solver in fRG flow (see Appendix G). Finally, the accuracy of the integrator also affects the numerical cost strongly (see again Appendix G). Our most costly computations were 150 iterations of the parquet solver with $N_{K_3} = 101$ (required for convergence in the region $u \lesssim 1$). On the KCS cluster at the Leibniz-Rechenzentrum der Bayerischen Akademie der Wissenschaften (LRZ), equipped with chips of the type *Intel® Xeon® Gold 6130 CPU @ 2.10 GHz* capable of hyperthreading, one such computation took about two days on 32 nodes, running 32 threads each.

APPENDIX I: CONVERGENCE OF $\tilde{\chi}_m(0)$

Figure 21 shows the static magnetic susceptibility of the sAM obtained with fRG, zooming into the regime $u \gtrsim 1$ (where deviations between MF and KF results become noticeable) and scrutinizing convergence with respect to frequency resolution. Compared with Fig. 8, there is an additional KF (MF) line with higher (lower) resolution, as determined by the number of frequency points used to resolve the K_3 class, N_{K_3} (cf. Fig. 20). The MF result appears converged in N_{K_3} , whereas the KF result is slightly improved by increasing N_{K_3} . The improvement is minor, however, and does not justify the additional numerical cost: The computation for $N_{K_3} = 125$ consumed roughly 30 000 CPU h, while the computation for $N_{K_3} = 101$ took only half that time. Nevertheless, one should keep in mind that these computations yield a full parameter sweep in u and are thus more economical than individual PA

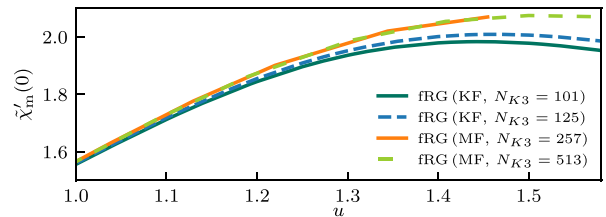


FIG. 21. Static magnetic susceptibility of the sAM obtained with fRG. Compared with Fig. 8, there is an additional KF (MF) line with higher (lower) resolution. The MF result appears converged in N_{K_3} ; the KF result is slightly improved by increasing N_{K_3} from 101 to 125.

computations. Further analysis, including line plots through all vertex components and asymptotic classes, is provided in the dataset attached to this paper. This analysis shows that the

resolution of fine structures in some Keldysh components of the K_3 class could still be improved using even higher values of N_{K_3} .

-
- [1] G. Li, N. Wentzell, P. Pudleiner, P. Thunström, and K. Held, Efficient implementation of the parquet equations: Role of the reducible vertex function and its kernel approximation, *Phys. Rev. B* **93**, 165103 (2016).
- [2] N. Wentzell, G. Li, A. Tagliavini, C. Taranto, G. Rohringer, K. Held, A. Toschi, and S. Andergassen, High-frequency asymptotics of the vertex function: diagrammatic parametrization and algorithmic implementation, *Phys. Rev. B* **102**, 085106 (2020).
- [3] H. Shinaoka, J. Otsuki, K. Haule, M. Wallerberger, E. Gull, K. Yoshimi, and M. Ohzeki, Overcomplete compact representation of two-particle Green's functions, *Phys. Rev. B* **97**, 205111 (2018).
- [4] F. Krien, A. Valli, and M. Capone, Single-boson exchange decomposition of the vertex function, *Phys. Rev. B* **100**, 155149 (2019).
- [5] H. Shinaoka, D. Geffroy, M. Wallerberger, J. Otsuki, K. Yoshimi, E. Gull, and J. Kuneš, Sparse sampling and tensor network representation of two-particle Green's functions, *SciPost Phys.* **8**, 012 (2020).
- [6] M. Wallerberger, H. Shinaoka, and A. Kauch, Solving the Bethe-Salpeter equation with exponential convergence, *Phys. Rev. Res.* **3**, 033168 (2021).
- [7] H. Shinaoka, M. Wallerberger, Y. Murakami, K. Nogaki, R. Sakurai, P. Werner, and A. Kauch, Multiscale space-time ansatz for correlation functions of quantum systems based on quantum tensor trains, *Phys. Rev. X* **13**, 021015 (2023).
- [8] T. Schäfer, G. Rohringer, O. Gunnarsson, S. Ciuchi, G. Sangiovanni, and A. Toschi, Divergent precursors of the Mott-Hubbard transition at the two-particle level, *Phys. Rev. Lett.* **110**, 246405 (2013).
- [9] V. Janiš and V. Pokorný, Critical metal-insulator transition and divergence in a two-particle irreducible vertex in disordered and interacting electron systems, *Phys. Rev. B* **90**, 045143 (2014).
- [10] E. Kozik, M. Ferrero, and A. Georges, Nonexistence of the Luttinger-Ward functional and misleading convergence of skeleton diagrammatic series for Hubbard-like models, *Phys. Rev. Lett.* **114**, 156402 (2015).
- [11] T. Ribic, G. Rohringer, and K. Held, Nonlocal correlations and spectral properties of the Falicov-Kimball model, *Phys. Rev. B* **93**, 195105 (2016).
- [12] T. Schäfer, S. Ciuchi, M. Wallerberger, P. Thunström, O. Gunnarsson, G. Sangiovanni, G. Rohringer, and A. Toschi, Non-perturbative landscape of the Mott-Hubbard transition: Multiple divergence lines around the critical endpoint, *Phys. Rev. B* **94**, 235108 (2016).
- [13] O. Gunnarsson, G. Rohringer, T. Schäfer, G. Sangiovanni, and A. Toschi, Breakdown of traditional many-body theories for correlated electrons, *Phys. Rev. Lett.* **119**, 056402 (2017).
- [14] J. Vučićević, N. Wentzell, M. Ferrero, and O. Parcollet, Practical consequences of the Luttinger-Ward functional multivaluedness for cluster DMFT methods, *Phys. Rev. B* **97**, 125141 (2018).
- [15] P. Thunström, O. Gunnarsson, S. Ciuchi, and G. Rohringer, Analytical investigation of singularities in two-particle irreducible vertex functions of the Hubbard atom, *Phys. Rev. B* **98**, 235107 (2018).
- [16] P. Chalupa, P. Gunacker, T. Schäfer, K. Held, and A. Toschi, Divergences of the irreducible vertex functions in correlated metallic systems: Insights from the Anderson impurity model, *Phys. Rev. B* **97**, 245136 (2018).
- [17] D. Springer, P. Chalupa, S. Ciuchi, G. Sangiovanni, and A. Toschi, Interplay between local response and vertex divergences in many-fermion systems with on-site attraction, *Phys. Rev. B* **101**, 155148 (2020).
- [18] C. Melnick and G. Kotliar, Fermi-liquid theory and divergences of the two-particle irreducible vertex in the periodic Anderson lattice, *Phys. Rev. B* **101**, 165105 (2020).
- [19] M. Reitner, P. Chalupa, L. Del Re, D. Springer, S. Ciuchi, G. Sangiovanni, and A. Toschi, Attractive effect of a strong electronic repulsion: The physics of vertex divergences, *Phys. Rev. Lett.* **125**, 196403 (2020).
- [20] P. Chalupa, T. Schäfer, M. Reitner, D. Springer, S. Andergassen, and A. Toschi, Fingerprints of the local moment formation and its Kondo screening in the generalized susceptibilities of many-electron problems, *Phys. Rev. Lett.* **126**, 056403 (2021).
- [21] S. Adler, F. Krien, P. Chalupa-Gantner, G. Sangiovanni, and A. Toschi, Non-perturbative intertwining between spin and charge correlations: A "smoking gun" single-boson-exchange result, *SciPost Phys.* **16**, 054 (2024).
- [22] M. Pelz, S. Adler, M. Reitner, and A. Toschi, Highly non-perturbative nature of the Mott metal-insulator transition: Two-particle vertex divergences in the coexistence region, *Phys. Rev. B* **108**, 155101 (2023).
- [23] A. Taheridehkordi, S. H. Curnoe, and J. P. F. LeBlanc, Algorithmic Matsubara integration for Hubbard-like models, *Phys. Rev. B* **99**, 035120 (2019).
- [24] A. Taheridehkordi, S. H. Curnoe, and J. P. F. LeBlanc, Algorithmic approach to diagrammatic expansions for real-frequency evaluation of susceptibility functions, *Phys. Rev. B* **102**, 045115 (2020).
- [25] B. D. E. McNiven, G. T. Andrews, and J. P. F. LeBlanc, Single particle properties of the two-dimensional Hubbard model for real frequencies at weak coupling: Breakdown of the Dyson series for partial self-energy expansions, *Phys. Rev. B* **104**, 125114 (2021).
- [26] B. D. E. McNiven, H. Terletska, G. T. Andrews, and J. P. F. LeBlanc, One- and two-particle properties of the weakly interacting two-dimensional Hubbard model in proximity to the van Hove singularity, *Phys. Rev. B* **106**, 035145 (2022).
- [27] J. P. F. LeBlanc, K. Chen, K. Haule, N. V. Prokof'ev, and I. S. Tupitsyn, Dynamic response of an electron gas: Towards the exact exchange-correlation kernel, *Phys. Rev. Lett.* **129**, 246401 (2022).
- [28] M. D. Burke, M. Grandadam, and J. P. F. LeBlanc, Renormalized perturbation theory for fast evaluation of Feynman

- diagrams on the real frequency axis, *Phys. Rev. B* **107**, 115151 (2023).
- [29] M. Grandadam and J. P. F. LeBlanc, Planckian behaviour in the optical conductivity of the weakly coupled Hubbard model, [arXiv:2303.04964](https://arxiv.org/abs/2303.04964).
- [30] C. Bertrand, S. Florens, O. Parcollet, and X. Waintal, Reconstructing nonequilibrium regimes of quantum many-body systems from the analytical structure of perturbative expansions, *Phys. Rev. X* **9**, 041008 (2019).
- [31] C. Bertrand, O. Parcollet, A. Maillard, and X. Waintal, Quantum Monte Carlo algorithm for out-of-equilibrium Green's functions at long times, *Phys. Rev. B* **100**, 125129 (2019).
- [32] C. Bertrand, D. Bauernfeind, P. T. Dumitrescu, M. Maćek, X. Waintal, and O. Parcollet, Quantum quasi Monte Carlo algorithm for out-of-equilibrium Green functions at long times, *Phys. Rev. B* **103**, 155104 (2021).
- [33] Y. Núñez Fernández, M. Jeannin, P. T. Dumitrescu, T. Kloss, J. Kaye, O. Parcollet, and X. Waintal, Learning Feynman diagrams with tensor trains, *Phys. Rev. X* **12**, 041018 (2022).
- [34] F. B. Kugler, S.-S. B. Lee, and J. von Delft, Multipoint correlation functions: Spectral representation and numerical evaluation, *Phys. Rev. X* **11**, 041006 (2021).
- [35] S.-S. B. Lee, F. B. Kugler, and J. von Delft, Computing local multipoint correlators using the numerical renormalization group, *Phys. Rev. X* **11**, 041007 (2021).
- [36] L. V. Keldysh, Diagram technique for nonequilibrium processes, *Sov. Phys. JETP* **20**, 1018 (1965).
- [37] J. Schwinger, Brownian motion of a quantum oscillator, *J. Math. Phys.* **2**, 407 (1961).
- [38] L. P. Kadanoff and G. A. Baym, *Quantum Statistical Mechanics* (Benjamin, New York, 1962).
- [39] W. Metzner, M. Salmhofer, C. Honerkamp, V. Meden, and K. Schönhammer, Functional renormalization group approach to correlated fermion systems, *Rev. Mod. Phys.* **84**, 299 (2012).
- [40] N. E. Bickers, Self-consistent many-body theory for condensed matter systems, in *Theoretical Methods for Strongly Correlated Electrons*, CRM Series in Mathematical Physics, edited by D. Sénéchal, A.-M. Tremblay, and C. Bourbonnais (Springer, New York, 2004).
- [41] G. Rohringer, H. Hafermann, A. Toschi, A. A. Katanin, A. E. Antipov, M. I. Katsnelson, A. I. Lichtenstein, A. N. Rubtsov, and K. Held, Diagrammatic routes to nonlocal correlations beyond dynamical mean field theory, *Rev. Mod. Phys.* **90**, 025003 (2018).
- [42] A. Georges, G. Kotliar, W. Krauth, and M. J. Rozenberg, Dynamical mean-field theory of strongly correlated fermion systems and the limit of infinite dimensions, *Rev. Mod. Phys.* **68**, 13 (1996).
- [43] R. Bulla, T. A. Costi, and T. Pruschke, Numerical renormalization group method for quantum impurity systems, *Rev. Mod. Phys.* **80**, 395 (2008).
- [44] C. Taranto, S. Andergassen, J. Bauer, K. Held, A. Katanin, W. Metzner, G. Rohringer, and A. Toschi, From infinite to two dimensions through the functional renormalization group, *Phys. Rev. Lett.* **112**, 196402 (2014).
- [45] D. Vilardi, C. Taranto, and W. Metzner, Antiferromagnetic and *d*-wave pairing correlations in the strongly interacting two-dimensional Hubbard model from the functional renormalization group, *Phys. Rev. B* **99**, 104501 (2019).
- [46] A. Toschi, A. A. Katanin, and K. Held, Dynamical vertex approximation: A step beyond dynamical mean-field theory, *Phys. Rev. B* **75**, 045118 (2007).
- [47] K. Held, A. A. Katanin, and A. Toschi, Dynamical vertex approximation: An introduction, *Prog. Theor. Phys. Suppl.* **176**, 117 (2008).
- [48] A. C. Hewson, *The Kondo Problem to Heavy Fermions* (Cambridge University Press, Cambridge, 1993).
- [49] P. W. Anderson, Localized magnetic states in metals, *Phys. Rev.* **124**, 41 (1961).
- [50] F. B. Anders and N. Grewe, Perturbational approach to the Anderson model: New results from a post-NCA treatment, *Europhys. Lett.* **26**, 551 (1994).
- [51] F. B. Anders, An enhanced perturbational study on spectral properties of the Anderson model, *J. Phys.: Condens. Matter* **7**, 2801 (1995).
- [52] J. Kroha, P. Wölfle, and T. A. Costi, Unified description of Fermi and non-Fermi liquid behavior in a conserving slave boson approximation for strongly correlated impurity models, *Phys. Rev. Lett.* **79**, 261 (1997).
- [53] J. Kroha and P. Wölfle, Fermi and non-Fermi liquid behavior of local moment systems within a conserving slave boson theory, *Acta Phys. Pol. B* **29**, 3781 (1998).
- [54] S. G. Jakobs, Functional renormalization group studies of quantum transport through mesoscopic systems, Ph.D. thesis, RWTH Aachen University, 2010.
- [55] S. G. Jakobs, M. Pletyukhov, and H. Schoeller, Nonequilibrium functional renormalization group with frequency-dependent vertex function: A study of the single-impurity Anderson model, *Phys. Rev. B* **81**, 195109 (2010).
- [56] S. G. Jakobs, M. Pletyukhov, and H. Schoeller, Properties of multi-particle Green's and vertex functions within Keldysh formalism, *J. Phys. A: Math. Theor.* **43**, 103001 (2010).
- [57] D. Schimmel, Transport through inhomogeneous interacting low-dimensional systems, Ph.D. thesis, Ludwig-Maximilians-Universität München, 2017.
- [58] D. H. Schimmel, B. Bruognolo, and J. von Delft, Spin fluctuations in the 0.7 anomaly in quantum point contacts, *Phys. Rev. Lett.* **119**, 196401 (2017).
- [59] L. Weidinger and J. von Delft, Keldysh functional renormalization group treatment of finite-ranged interactions in quantum point contacts, [arXiv:1912.02700](https://arxiv.org/abs/1912.02700).
- [60] V. Zlatić and B. Horvatić, Series expansion for the symmetric Anderson Hamiltonian, *Phys. Rev. B* **28**, 6904 (1983).
- [61] F. B. Kugler and J. von Delft, Multiloop functional renormalization group for general models, *Phys. Rev. B* **97**, 035162 (2018).
- [62] F. B. Kugler and J. von Delft, Multiloop functional renormalization group that sums up all parquet diagrams, *Phys. Rev. Lett.* **120**, 057403 (2018).
- [63] F. B. Kugler and J. von Delft, Derivation of exact flow equations from the self-consistent parquet relations, *New J. Phys.* **20**, 123029 (2018).
- [64] P. Chalupa-Gantner, F. B. Kugler, C. Hille, J. von Delft, S. Andergassen, and A. Toschi, Fulfillment of sum rules and Ward identities in the multiloop functional renormalization group solution of the Anderson impurity model, *Phys. Rev. Res.* **4**, 023050 (2022).
- [65] A. Kamenev, *Field Theory of Non-Equilibrium Systems* (Cambridge University Press, Cambridge, 2014).

- [66] C. F. Klöckner, Functional renormalization group approach to correlated quantum systems far from equilibrium, Ph.D. thesis, Freie Universität Berlin, 2019.
- [67] E. Walter, Real-frequency dynamics of quantum impurity models studied with fRG, NRG, CFT, Ph.D. thesis, Ludwig-Maximilians-Universität München, 2021.
- [68] J. W. Negele and H. Orland, *Quantum Many-Particle Systems* (CRC Press, Boca Raton, FL, 1998).
- [69] P. Kopietz, L. Bartosch, and F. Schütz, *Introduction to the Functional Renormalization Group* (Springer, Berlin, Heidelberg, 2010).
- [70] A. A. Katanin, Fulfillment of Ward identities in the functional renormalization group approach, *Phys. Rev. B* **70**, 115109 (2004).
- [71] A. Tagliavini, C. Hille, F. Kugler, S. Andergassen, A. Toschi, and C. Honerkamp, Multiloop functional renormalization group for the two-dimensional Hubbard model: Loop convergence of the response functions, *SciPost Phys.* **6**, 009 (2019).
- [72] C. Hille, F. B. Kugler, C. J. Eckhardt, Y.-Y. He, A. Kauch, C. Honerkamp, A. Toschi, and S. Andergassen, Quantitative functional renormalization group description of the two-dimensional Hubbard model, *Phys. Rev. Res.* **2**, 033372 (2020).
- [73] J. Thoenniss, M. K. Ritter, F. B. Kugler, J. von Delft, and M. Punk, Multiloop pseudofermion functional renormalization for quantum spin systems: Application to the spin-1/2 Kagome Heisenberg model, [arXiv:2011.01268](https://arxiv.org/abs/2011.01268).
- [74] D. Kiese, T. Müller, Y. Iqbal, R. Thomale, and S. Trebst, Multiloop functional renormalization group approach to quantum spin systems, *Phys. Rev. Res.* **4**, 023185 (2022).
- [75] M. Gievers, E. Walter, A. Ge, J. von Delft, and F. B. Kugler, Multiloop flow equations for single-boson exchange fRG, *Eur. Phys. J. B* **95**, 108 (2022).
- [76] M. K. Ritter, D. Kiese, T. Müller, F. B. Kugler, R. Thomale, S. Trebst, and J. von Delft, Benchmark calculations of multiloop pseudofermion fRG, *Eur. Phys. J. B* **95**, 102 (2022).
- [77] M. K. Ritter, Y. Núñez Fernández, M. Wallerberger, J. von Delft, H. Shinaoka, and X. Waintal, Quantics tensor cross interpolation for high-resolution parsimonious representations of multivariate functions, *Phys. Rev. Lett.* **132**, 056501 (2024).
- [78] A. Weichselbaum, Non-Abelian symmetries in tensor networks: A quantum symmetry space approach, *Ann. Phys. (NY)* **327**, 2972 (2012).
- [79] A. Weichselbaum, Tensor networks and the numerical renormalization group, *Phys. Rev. B* **86**, 245124 (2012).
- [80] A. Weichselbaum, X-symbols for non-Abelian symmetries in tensor networks, *Phys. Rev. Res.* **2**, 023385 (2020).
- [81] R. Žitko and T. Pruschke, Energy resolution and discretization artifacts in the numerical renormalization group, *Phys. Rev. B* **79**, 085106 (2009).
- [82] A. Weichselbaum and J. von Delft, Sum-rule conserving spectral functions from the numerical renormalization group, *Phys. Rev. Lett.* **99**, 076402 (2007).
- [83] R. Peters, T. Pruschke, and F. B. Anders, Numerical renormalization group approach to Green's functions for quantum impurity models, *Phys. Rev. B* **74**, 245114 (2006).
- [84] S.-S. B. Lee and A. Weichselbaum, Adaptive broadening to improve spectral resolution in the numerical renormalization group, *Phys. Rev. B* **94**, 235127 (2016).
- [85] S.-S. B. Lee, J. von Delft, and A. Weichselbaum, Double-holon origin of the subpeaks at the Hubbard band edges, *Phys. Rev. Lett.* **119**, 236402 (2017).
- [86] F. B. Kugler, Improved estimator for numerical renormalization group calculations of the self-energy, *Phys. Rev. B* **105**, 245132 (2022).
- [87] A. C. Hewson, A. Oguri, and D. Meyer, Renormalized parameters for impurity models, *Eur. Phys. J. B* **40**, 177 (2004).
- [88] J. Bauer and A. C. Hewson, Field-dependent quasiparticles in the infinite-dimensional Hubbard model, *Phys. Rev. B* **76**, 035118 (2007).
- [89] Y. Nishikawa, D. J. G. Crow, and A. C. Hewson, Renormalized parameters and perturbation theory for an n -channel Anderson model with Hund's rule coupling: Symmetric case, *Phys. Rev. B* **82**, 115123 (2010).
- [90] Y. Nishikawa, D. J. G. Crow, and A. C. Hewson, Renormalized parameters and perturbation theory for an n -channel Anderson model with Hund's rule coupling: Asymmetric case, *Phys. Rev. B* **82**, 245109 (2010).
- [91] A. Oguri, R. Sakano, and T. Fujii, $1/(N-1)$ expansion based on a perturbation theory in u for the Anderson model with N -fold degeneracy, *Phys. Rev. B* **84**, 113301 (2011).
- [92] F. B. Kugler, M. Zingl, H. U. R. Strand, S.-S. B. Lee, J. von Delft, and A. Georges, Strongly correlated materials from a numerical renormalization group perspective: How the Fermi-liquid state of Sr_2RuO_4 emerges, *Phys. Rev. Lett.* **124**, 016401 (2020).
- [93] K. Tsutsumi, Y. Teratani, K. Motoyama, R. Sakano, and A. Oguri, Role of bias and tunneling asymmetries in nonlinear Fermi-liquid transport through an $\text{SU}(n)$ quantum dot, *Phys. Rev. B* **108**, 045109 (2023).
- [94] K. Yosida and K. Yamada, Perturbation expansion for the Anderson Hamiltonian, *Prog. Theor. Phys. Suppl.* **46**, 244 (1970).
- [95] K. Yamada, Perturbation expansion for the Anderson Hamiltonian. II, *Prog. Theor. Phys.* **53**, 970 (1975).
- [96] K. Yosida and K. Yamada, Perturbation expansion for the Anderson Hamiltonian. III, *Prog. Theor. Phys.* **53**, 1286 (1975).
- [97] K. Yamada, Perturbation expansion for the Anderson Hamiltonian. IV, *Prog. Theor. Phys.* **54**, 316 (1975).
- [98] D. C. Langreth, Friedel sum rule for Anderson's model of localized impurity states, *Phys. Rev.* **150**, 516 (1966).
- [99] H. Kajueter and G. Kotliar, New iterative perturbation scheme for lattice models with arbitrary filling, *Phys. Rev. Lett.* **77**, 131 (1996).
- [100] C. Karrasch, R. Hedden, R. Peters, T. Pruschke, K. Schönhammer, and V. Meden, A finite-frequency functional renormalization group approach to the single impurity Anderson model, *J. Phys.: Condens. Matter* **20**, 345205 (2008).
- [101] A. C. Hewson, Renormalized perturbation calculations for the single-impurity Anderson model, *J. Phys.: Condens. Matter* **13**, 10011 (2001).
- [102] M. Filippone, C. P. Moca, A. Weichselbaum, J. von Delft, and C. Mora, At which magnetic field, exactly, does the Kondo resonance begin to split? A Fermi liquid description of the low-energy properties of the Anderson model, *Phys. Rev. B* **98**, 075404 (2018).
- [103] P. Kopietz, L. Bartosch, L. Costa, A. Isidori, and A. Ferraz, Ward identities for the Anderson impurity model: Derivation via functional methods and the exact renormalization group, *J. Phys. A: Math. Theor.* **43**, 385004 (2010).

- [104] H. Shiba, The Korringa relation for the impurity nuclear spin-lattice relaxation in dilute Kondo alloys, *Prog. Theor. Phys.* **54**, 967 (1975).
- [105] J.-M. Lihm, J. Halbinger, J. Shim, J. von Delft, F. B. Kugler, and S.-S. B. Lee, Symmetric improved estimators for multipoint vertex functions, [arXiv:2310.12098](https://arxiv.org/abs/2310.12098) [Phys. Rev. B (to be published)].
- [106] T. Fujii and K. Ueda, Perturbative approach to the nonequilibrium Kondo effect in a quantum dot, *Phys. Rev. B* **68**, 155310 (2003).
- [107] C. J. Eckhardt, C. Honerkamp, K. Held, and A. Kauch, Truncated unity parquet solver, *Phys. Rev. B* **101**, 155104 (2020).
- [108] C. Husemann and M. Salmhofer, Efficient parametrization of the vertex function, Ω scheme, and the (t, t') Hubbard model at van Hove filling, *Phys. Rev. B* **79**, 195125 (2009).
- [109] W.-S. Wang, Y.-Y. Xiang, Q.-H. Wang, F. Wang, F. Yang, and D.-H. Lee, Functional renormalization group and variational Monte Carlo studies of the electronic instabilities in graphene near 1/4 doping, *Phys. Rev. B* **85**, 035414 (2012).
- [110] J. Lichtenstein, D. S. d. l. Peña, D. Rohe, E. D. Napoli, C. Honerkamp, and S. A. Maier, High-performance functional renormalization group calculations for interacting fermions, *Comput. Phys. Commun.* **213**, 100 (2017).
- [111] C. J. Eckhardt, G. A. H. Schober, J. Ehrlich, and C. Honerkamp, Truncated-unity parquet equations: application to the repulsive Hubbard model, *Phys. Rev. B* **98**, 075143 (2018).
- [112] A. Ge, N. Ritz, E. Walter, S. Aguirre, J. von Delft, and F. Kugler, Data for: Real-frequency quantum field theory applied to the single-impurity Anderson model (2023), doi:[10.57970/xeqvs-w3p49](https://doi.org/10.57970/xeqvs-w3p49).
- [113] G. Rohringer, A. Valli, and A. Toschi, Local electronic correlation at the two-particle level, *Phys. Rev. B* **86**, 125114 (2012).
- [114] E. Wang and U. Heinz, Generalized fluctuation-dissipation theorem for nonlinear response functions, *Phys. Rev. D: Part. Fields* **66**, 025008 (2002).
- [115] A. Ge, J. Halbinger, S.-S. B. Lee, J. von Delft, and F. B. Kugler, Analytic continuation of multipoint correlation functions, [arXiv:2311.11389](https://arxiv.org/abs/2311.11389) [Ann. Phys. (to be published)].
- [116] G. Rohringer, New routes towards a theoretical treatment of nonlocal electronic correlations, Ph.D. thesis, Vienna University of Technology, 2013.
- [117] G. Eliashberg, Transport equation for a degenerate system of Fermi particles, *Sov. Phys. JETP* **14**, 886 (1962).
- [118] L. Hedin, New method for calculating the one-particle Green's function with application to the electron-gas problem, *Phys. Rev.* **139**, A796 (1965).
- [119] W. H. Press, S. A. Teukolsky, W. T. Vetterling, and B. P. Flannery, *Numerical Recipes: The Art of Scientific Computing*, 3rd ed. (Cambridge University Press, Cambridge, 2007).
- [120] M. Galassi (ed.), *GNU Scientific Library Reference Manual: for GSL version 1.12*, 3rd ed. (Network Theory, Bristol, 2009).
- [121] R. P. Brent, *Algorithms for Minimization without Derivatives* (Prentice-Hall, Inc., Englewood Cliffs, NJ, 1973).
- [122] D. G. Anderson, Iterative procedures for nonlinear integral equations, *J. Assoc. Comput. Mach.* **12**, 547 (1965).
- [123] H. F. Walker and P. Ni, Anderson acceleration for fixed-point iterations, *SIAM J. Numer. Anal.* **49**, 1715 (2011).

2.5 Technical aspects of real-frequency calculations

Numerical quantum field theory calculations in real frequencies are technically demanding, particularly when computing the four-point vertex. While this was mentioned at several points before and in Ref. [P1], that paper focused more on the results of those calculations and their implications for further development of the methodology. Building on a significant amount of preliminary work already done and presented in Refs. [Agu20; Wal22], it was therefore deemed worthwhile to write another paper that focuses more on the technical aspects of the calculations done for Ref. [P1], focusing primarily on the parts that are required for real-frequency calculations.

Among those are, first and foremost, the challenges that relate to the continuous instead of discrete frequency dependence of all functions involved. Numerically, the continuous frequency axes have to be discretized by choosing an appropriate frequency grid. This step requires fine tuning already, as a tradeoff between accuracy and performance has to be made very carefully: On the one hand, the frequency grid must be chosen such that all features of the vertex are resolved correctly, which can be tricky, since the vertex can have sharply peaked structures, especially at low temperature. On the other hand, one cannot afford an arbitrary resolution of the frequency grid since the numerical effort quickly becomes overwhelming as it roughly scales with the third power of the number of frequency grid points (in thermal equilibrium, the vertex has three frequency arguments). Furthermore, contractions over frequency arguments, ubiquitous in the parquet and (m)fRG equations, amount to integrations instead of summations over discrete Matsubara frequencies. These integrations require efficient interpolation routines to read out the vertex at arbitrary frequency values and a performant but still accurate integration algorithm.

While the above points on continuous frequency dependencies are also relevant to computations in the Matsubara formalism at zero temperature (indeed, similar issues have been discussed, e.g., in Ref. [Rit+22]), another challenge arises in the Keldysh formalism due to the additional index structure from the Keldysh indices of all functions. For the vertex, this concretely means that one has to keep track of its 16 Keldysh components. While symmetries can be used to relate many Keldysh components of the vertex, it was found that it is preferential to instead exploit the matrix structure of the Keldysh index dependence of the vertex by vectorizing all computations across the Keldysh indices.

A crucial issue in all parquet and (m)fRG calculations is that at each step, the right-hand sides of the equations have to be evaluated for every possible combination of external arguments of the functions on the left-hand side. Especially for the vertex, this necessitates a vast number of individual calculations at each step. Fortunately, these calculations are all independent, provided each calculation has access to the objects required on the right-hand side. The computations can hence be easily parallelized across multiple threads on a single compute node and across multiple nodes (the latter resulting in an overhead in memory since all required objects have to be copied to every node). The parallelization enables using a high-performance computing cluster for the numerics, which turned out to be crucial to the success of the calculations, since especially the required number of frequency grid points could not have been afforded otherwise.

In addition to all these technical issues, writing the code for parquet and (m)fRG calculations and properly structuring the resulting comprehensive codebase is a formidable challenge. Building on past experiences and countless discussions with many like-minded

peers, Ref. [P2] lays out how the resulting codebase is structured and which possible pitfalls one should look out for if setting up a new code.

Lastly, Ref. [P2] explains in detail how to implement the mfRG algorithm and provides the code that does so. This part was missing in Ref. [P1], showing only results from the one-loop fRG.

**KeldyshQFT: A C++ codebase for real-frequency multiloop
functional renormalization group and parquet computations
of the single-impurity Anderson model**

by

N. Ritz¹, A. Ge¹, E. Walter¹, S. Aguirre¹, J. von Delft¹, and F.B. Kugler²

¹ Arnold Sommerfeld Center for Theoretical Physics, Center for NanoScience, and
Munich Center for Quantum Science and Technology,
Ludwig-Maximilians-Universität München, 80333 Munich, Germany

² Center for Computational Quantum Physics, Flatiron Institute,
162 5th Avenue, New York, New York 10010, USA

reprinted on pages **58–78**

with permission from

***J. Chem. Phys.* 161, 054118 (2024),**

<https://doi.org/10.1063/5.0221340>

2024 AIP Publishing.

KeldyshQFT: A C++ codebase for real-frequency multiloop functional renormalization group and parquet computations of the single-impurity Anderson model

Cite as: J. Chem. Phys. **161**, 054118 (2024); doi: 10.1063/5.0221340

Submitted: 31 May 2024 • Accepted: 3 July 2024 •

Published Online: 7 August 2024



View Online



Export Citation



CrossMark

Nepomuk Ritz,^{1,a)}  Anxiang Ge,¹  Elias Walter,¹  Santiago Aguirre,¹ Jan von Delft,¹ 
and Fabian B. Kugler² 

AFFILIATIONS

¹Arnold Sommerfeld Center for Theoretical Physics, Center for NanoScience, and Munich Center for Quantum Science and Technology, Ludwig-Maximilians-Universität München, 80333 Munich, Germany

²Center for Computational Quantum Physics, Flatiron Institute, 162 5th Avenue, New York, New York 10010, USA

Note: This paper is part of the JCP Special Topic on Algorithms and Software for Open Quantum System Dynamics.

^{a)}Author to whom correspondence should be addressed: nepomuk.ritz@physik.uni-muenchen.de

ABSTRACT

We provide a detailed exposition of our computational framework designed for the accurate calculation of real-frequency dynamical correlation functions of the single-impurity Anderson model in the regime of weak to intermediate coupling. Using quantum field theory within the Keldysh formalism to directly access the self-energy and dynamical susceptibilities in real frequencies, as detailed in our recent publication [Ge *et al.*, Phys. Rev. B **109**, 115128 (2024)], the primary computational challenge is the full three-dimensional real-frequency dependence of the four-point vertex. Our codebase provides a fully MPI+OpenMP parallelized implementation of the functional renormalization group (fRG) and the self-consistent parquet equations within the parquet approximation. It leverages vectorization to handle the additional complexity imposed by the Keldysh formalism, using optimized data structures and highly performant integration routines. Going beyond the results shown in the previous publication, the code includes functionality to perform fRG calculations in the multiloop framework, up to arbitrary loop order, including self-consistent self-energy iterations. Moreover, implementations of various regulators, such as hybridization, interaction, frequency, and temperature, are supplied.

© 2024 Author(s). All article content, except where otherwise noted, is licensed under a Creative Commons Attribution (CC BY) license (<https://creativecommons.org/licenses/by/4.0/>). <https://doi.org/10.1063/5.0221340>

I. INTRODUCTION

In the study of strongly correlated electrons, dynamical correlation functions are quantities of major interest, as they provide insights into the collective behavior and emergent phenomena arising from electronic interactions. Capturing the effects of two-particle (or four-point) correlations is one of the current major frontiers in the field. Their dynamical properties are inherently difficult to compute, as they involve three independent frequency arguments.

While most previous works on this subject focused on four-point functions in imaginary frequencies in the Matsubara

formalism^{2,3} (MaF), obtaining real-frequency information is crucial for direct comparisons to experiments. The extraction of real-frequency data from the results of a calculation in the MaF is, in principle, possible via analytic continuation.⁴ However, it is hard to do so reliably in practice, as the conditions for the procedure outlined in Ref. 4 are not met by finite amounts of numerical data. This renders analytic continuation an ill-defined problem, despite numerous attempts.⁵⁻⁷ Furthermore, it had not been worked out in full detail until very recently⁸ how analytic continuation of four-point functions could be achieved even under the assumption of analytically available results.

Pioneering attempts to directly compute real-frequency dynamical four-point correlation functions using simplified approaches made use of diagrammatic ladder approximations^{9,10} or were restricted to a simplified frequency dependence.^{11–13} The first fully unbiased treatment of the fluctuations contributing to the four-point vertex was achieved only a few years ago using a multipoint extension of the numerical renormalization group (NRG).^{14,15}

Even more recently, we presented a similarly unbiased treatment of the four-point vertex of the single-impurity Anderson model using a QFT framework within the Keldysh formalism (KF), employing two related diagrammatic methods: the functional renormalization group (fRG) and the self-consistent parquet equations in the parquet approximation.¹ While we focused on the conceptual aspects and discussed the performance of the methods in great detail in the previous publication, here we wish to provide a detailed exposition of the computational framework for the numerical calculations of self-energies and vertex functions. In addition to what was shown in Ref. 1, the code discussed in this paper is capable of performing fRG calculations in the multiloop framework up to an arbitrary loop order, which connects the fRG to the parquet formalism.^{16–18}

This paper aims to serve as a reference for future extensions or revisions of the code. The codebase discussed here was developed by several people over the course of multiple years, during which some goals and priorities changed and the code had to be adapted accordingly. This paper will document how the code works and what was learned during its development.

Some general design choices made during development resulted in convenient features of the code and are recommended for future projects. In the following, we briefly discuss the most important features:

a. *Modularity.* Every main building block of the code and each functionality is implemented individually, using classes and functions that serve one purpose only. As a consequence, a developer can keep an overview of the functionality. It is also comparatively easy to reuse existing features and combine them into new functionality. For example, for both the computation of the Schwinger–Dyson equation during parquet computations and the evaluation of the flow equation for the self-energy during the solution of an mFRG flow, the same classes for vertices, propagators, self-energies, and the same function for contracting a loop are used, as described in Secs. II C and II D. In addition, modularity enables unit-testing of each functionality, something too often ignored during research software development. Modularity is probably the most important feature that should be prioritized in developing any research software.

b. *Flexibility.* A modular design makes the code flexible, too. Some additional choices were made to improve its flexibility even further. Most importantly, the code enables computations in three different formalisms: the finite-temperature Matsubara formalism (MaF), the zero-temperature Matsubara formalism, and the Keldysh formalism (KF), which works at any temperature and generalizes to systems out of thermal equilibrium. Consequently, some functionality had to be implemented multiple times, such as contractions, which require summations over discrete Matsubara frequencies in the finite-temperature MaF but integrations over continuous frequencies in the zero-temperature MaF and the KF. Additionally,

in the KF, all quantities are complex-valued, whereas they are real-valued in the MaF for particle–hole symmetry. Template parameters were introduced to enable the same functions to work with objects of different types. Despite the resulting additional complexity, this conveniently enables computations in each of these three formalisms in the same codebase, still using much of the same functionality.

c. *Performance.* Computing dynamical correlation functions is a computationally demanding task, especially for four-point functions that depend on three frequency arguments. Depending on the desired resolution, this requires both excessive memory to store these functions during computations and central processing unit (CPU) power to perform computations for each combination of arguments. Concerning the latter, using optimized data structures for efficient readouts of data as well as an efficient but still precise algorithm for integrating over frequencies (the numerical bottleneck) improved matters significantly. In addition, using a compiled programming language is basically a must, and keeping track of constant variables and member functions helps the compiler optimize the code.

d. *Scalability.* Apart from the simplest calculations, most diagrammatic calculations would not be feasible without parallelization. This is because practically all calculations in parquet formalism, or mFRG, require computations for all possible combinations of external arguments of the correlation functions. As those are independent from each other, it is possible and advisable to parallelize the demanding computations of bubbles and loops (see Sec. II D) in the external arguments. Using the OpenMP and MPI interfaces, this can easily be achieved for parallelization across different threads on the same node and across multiple nodes, respectively (for more details, see Sec. II G 1). As long as the memory requirements are met, the performance of the code scales almost perfectly with the computational resources.

At this point, we disclose that the present code also has a number of weaknesses that evolved over the course of development. If the reader intends to set up a new codebase for the purpose discussed here, we recommend considering the following points:

a. *Too many preprocessor macros (“flags”).* The code contains far too many preprocessor macros, used to specify different parameters and settings before compilation (see Sec. II I). This not only hampers readability but also increases the risk of errors, as it is never possible to test the full functionality of the code because one would have to compile and test all possible configurations independently. With simple combinatorics, this quickly becomes an overwhelming task. Using preprocessor macros is, however, useful for quick implementations of new functionality, which is why they accumulate over time.

b. *Too many overly complicated structures.* The code contains several classes that are way more complicated than they need to be, such as the different vertex classes or the data buffer (see Secs. II C 1 and II G 8). When they were set up, the goal was to keep them as general as possible, such that they could be used for all kinds of models in all kinds of formalisms. For this purpose, templates are used excessively as well. As a consequence, they are indeed flexible, but they are cumbersome to use in any specific context, and their implementations are difficult to grasp. In addition, the code takes a long time to compile and link, which is inconvenient for everyday

development. Ultimately, as a developer, one has to find the right trade-off between flexibility and simplicity.

c. *Too little use of existing implementations.* Several textbook algorithms, such as the Gauß-Lobatto routine for frequency integrations or the Cash–Karp routine for solving ODEs (see Secs. II G 5 and III C 1), were implemented by hand. The reason for this was the desire to comprehend and track the inner workings of the algorithms at every point during a calculation. In hindsight, much time and effort could have been saved if existing implementations of these algorithms had been used as “black boxes.”

d. *Language.* C++ is a very versatile language that runs on essentially any computer and can produce very fast code. However, a codebase written in C++ requires a lot of work to write and maintain. Initially, C++ was chosen for performance reasons. By now, however, there are established alternative programming languages that are easier to use, less error-prone, and (almost) as fast, such as Julia,¹⁹ Rust,²⁰ or Mojo.²¹

e. *Priorities.* Driven by the desire to obtain data with maximal resolution and precision, the top priority has always been performance. While this is very typical for codes written by physicists, it is not in line with the typical recommendation in software engineering, which would prioritize correctness and maintainability over performance.²² While we are confident that the code produces correct results after extensive benchmarks,¹ the code is not written in the simplest way and is not easily readable and maintainable. While we acknowledge that generating results quickly is deemed to be the most important aspect of research at present, we advocate for reconsidering the priorities during research software development for future projects.

The rest of the paper is structured as follows: In Sec. I A, we briefly introduce the single-impurity Anderson model (AM). In Sec. I B, we briefly recapitulate the main concepts of diagrammatic many-body theory. In Sec. I C, we comment on the complications that arise by performing computations in the very general Keldysh formalism, which is the main selling point of the present codebase.

In the second part of the paper, we give details on the code itself, introducing the main objects in Sec. II C and explaining the main functionality in Sec. II D. We list several options for postprocessing the raw data obtained after a completed calculation in Sec. II E and briefly explain how the data are organized in Sec. II F. Special emphasis is placed on performance-critical aspects of the code in Sec. II G. We comment on how the code is tested in Sec. II H. Finally, we provide an overview of the most important options for parameter choices that can be performed in Sec. II I, illustrating the versatility of the codebase.

In the third main part of the paper, we elaborate on how three different diagrammatic algorithms, perturbation theory, the parquet equations, and the mfRG, are implemented. In particular, we list the different flow schemes that are available in mfRG. Finally, Sec. IV presents a conclusion.

Before the end of this introduction, a disclaimer is in order: This paper does not mention every single class or function in the code but focuses on the most important aspects and functionalities. In addition, while the code enables computations in the KF and the MaF at both finite and zero temperatures, we focus our specific descriptions mainly on the KF functionality, as this is a unique feature of our codebase.

A. Model

We consider the single-impurity Anderson model (AM) in thermal equilibrium, one of the most studied models in all of condensed matter physics. Its physical behavior is well understood, and numerically exact benchmark data for single-particle correlation functions is available from NRG,²³ as are exact analytical results for static quantities at zero temperature from the Bethe ansatz.^{24,25} This makes it an ideal candidate for studies focused on reliable method development.

The AM is a minimal model for localized magnetic impurities in metals introduced by Anderson to explain the physics behind the Kondo effect.²⁶ It is defined by the Hamiltonian

$$H = \sum_{c\sigma} \varepsilon_c^\dagger c_{c\sigma} + \sum_{\sigma} \varepsilon_d n_{\sigma} + U n_{\uparrow} n_{\downarrow} + \sum_{c\sigma} (V_{c\sigma} d_{\sigma}^\dagger c_{c\sigma} + \text{H.c.}), \quad (1)$$

describing a local impurity d level with on-site energy ε_d , hybridized with spinful conduction electrons, created by $c_{c\sigma}^\dagger$, of the metal via a matrix element $V_{c\sigma}$. Hence, it qualifies as an open quantum system. The electrons in the localized d state, where $n_{\sigma} = d_{\sigma}^\dagger d_{\sigma}$, interact according to the interaction strength U , whereas the c electrons of the bath are non-interacting. The bath electrons are hence formally integrated out, yielding the frequency-dependent retarded hybridization function $-\text{Im} \Delta^R(\nu) = \sum_{\varepsilon} \pi |V_{\varepsilon}|^2 \delta(\nu - \varepsilon)$. We consider a flat hybridization in the wideband limit, $\Delta^R(\nu) = -i\Delta$, so that the bare impurity propagator reads $G_0^R(\nu) = (\nu - \varepsilon_d + i\Delta)^{-1}$.

The code can treat all choices for the on-site energy ε_d . For the special choice $\varepsilon_d = -U/2$, the model has particle–hole symmetry and is referred to as the symmetric Anderson model (sAM). This setting simplifies the calculations somewhat. For instance, in this case, the Hartree-term of the self-energy is constant $\Sigma_H = U/2$ (see also Sec. III A 1). In addition, in the MaF, all quantities become real-valued, whereas they are complex-valued otherwise. Hence, the code supplies a parameter flag to make use of these properties (see Sec. II I). For general $\varepsilon_d \neq -U/2$, we speak of the asymmetric Anderson model (aAM).

Some physical applications require an additional external magnetic field h , described by an additional term $h(n_{\uparrow} - n_{\downarrow})$ in the Hamiltonian. At present, the codebase is, however, not applicable in this setting, as this would break SU(2) symmetry, which is heavily used and hard-coded into the codebase (see Sec. II G 3). A generalization to $h \neq 0$ is possible but would require major effort.

While the present implementation is restricted to the AM, the code in principle can also treat other models: all data structures possess an additional internal index suitable for encoding additional dependencies and quantum numbers of more complicated models, such as a momentum dependence or multiple orbitals. Indeed, the first attempts to study the 2D Hubbard model had been started; however, the simplest KF perturbation theory calculations turned out to be too demanding at the time. The corresponding functionality is, therefore, not included in this release.

B. Diagrammatic many-body theory

The basic objects of interest in all our calculations are one- and two-particle correlation functions. Their non-trivial contributions due to interaction effects are contained in the self-energy Σ and the four-point vertex Γ ,

$$\Sigma = \text{---} \circlearrowleft \Sigma \text{---}, \quad \Gamma = \text{---} \square \Gamma \text{---} \quad (2)$$

The self-energy is used together with the bare propagator G_0 to express the one-particle propagator G via the Dyson equation

$$G = \text{---} = \text{---} \text{---} G_0 + \text{---} \text{---} \circlearrowleft \Sigma \text{---} \text{---} G \quad (3)$$

which is formally solved by $G = 1/(G_0^{-1} - \Sigma)$. The vertex is the connected and amputated part of the two-particle correlation function $G^{(4)}$,

$$G^{(4)} = \text{---} \text{---} \text{---} \text{---} - \text{---} \downarrow \uparrow \text{---} + \text{---} \text{---} \square \Gamma \text{---} \text{---} \quad (4)$$

from which physical susceptibilities can be obtained by contracting pairs of external legs (see Appendix C of Ref. 1 for details). The first-order contribution to the vertex is given by the fully antisymmetric, local, and instantaneous bare vertex, represented as a single dot,

$$\Gamma_0 = \text{---} \times \text{---} \sim U > 0, \quad (5)$$

in standard Hugenholtz notation. Using the bare vertex and the bare propagator G_0 , diagrammatic perturbation series for both the self-energy and the vertex can be derived, which will be the subject of Sec. III A. A perturbation series up to finite order in Γ_0 is, however, only appropriate for weak coupling strengths. In order to reach larger couplings, an infinite number of diagrams have to be summed. This is the purpose of two related formalisms, the parquet formalism and the multiloop functional renormalization group, to be discussed in Secs. III B and III C, respectively. Both formalisms employ the parquet decomposition to organize all diagrammatic contributions to Γ into one of four distinct categories: Two-particle reducible diagrams in one of the three two-particle channels a , p , and t , included in the three two-particle reducible vertices $\gamma_{r \in \{a,p,t\}}$ or two-particle irreducible diagrams, included in the fully irreducible vertex R ,

$$\Gamma = \text{---} \square R \text{---} + \text{---} \square \gamma_a \text{---} + \text{---} \square \gamma_p \text{---} + \text{---} \square \gamma_t \text{---} \quad (6a)$$

$$= \text{---} \times \text{---} + \text{---} \text{---} \text{---} \text{---} + \frac{1}{2} \text{---} \text{---} \text{---} \text{---} - \text{---} \text{---} \text{---} \text{---} + O[(\Gamma_0)^3]. \quad (6b)$$

Any specific diagram is said to be two-particle reducible if it can be disconnected by splitting a propagator pair. Otherwise, it is said to be two-particle irreducible. The parquet decomposition is exact, as it in essence just provides a classification of all diagrams that contribute to Γ . However, neither the parquet formalism nor the mFRG provide equations for R . In practice, some approximation is required. The simplest one is the parquet approximation (PA)

$$R = \Gamma_0 + O[(\Gamma_0)^4] \approx \Gamma_0, \quad (7)$$

which approximates the fully irreducible vertex R by the bare vertex Γ_0 . As it introduces an error in the fourth order in perturbation theory, it fails for large coupling strengths and is hence applicable only up to intermediate couplings. The PA was applied throughout in Ref. 1 and is the only one so far implemented in the codebase (see Sec. II C 1 for a comment on other possibilities).

C. Keldysh formalism

The following section assumes familiarity with the KF and describes challenges arising for computations with the KF rather than the more widespread MaF (for a more extensive discussion of the KF, see Refs. 27 and 28).

The KF²⁹⁻³¹ works both out of equilibrium and in thermal equilibrium at arbitrary temperature, in a real-frequency description. This is an advantage over the more popular MaF, which works at imaginary (“Matsubara”) frequencies, requiring analytical continuation, a mathematically ill-defined problem if one works with a finite amount of imperfect numerical data. Still, the KF is seldomly used because practical calculations are more complicated for two main reasons.

In the KF, all operators acquire an additional contour index, which specifies whether they sit on the forward or backward branch of the Keldysh double-time contour. It follows that the four-point vertex, for example, has $2^4 = 16$ different components. While some of these components can be eliminated by causality or related to other components by fluctuation–dissipation relations in thermal equilibrium or symmetries, this additional index structure complicates the implementation and the numerics.

In thermal equilibrium, energy conservation can be leveraged by Fourier-transforming all correlation functions into frequency space. In contrast to the MaF at finite temperatures, this dependence is continuous. Hence, contractions over frequency arguments require numerically more expensive integrations instead of summations. The integrations become more costly at lower temperatures as the frequency dependence of the correlation functions becomes more sharply peaked. The four-point functions, which depend on three continuous frequency arguments, are the numerical bottleneck for which arbitrarily high resolutions are out of reach due to both computation and memory demands. Discretizing the frequency dependence in a clever way and using adaptive integration routines is, therefore, key, as discussed in Secs. II G 4 and II G 5.

Finally, the KF also allows for computations outside of thermal equilibrium. However, the present discussion is restricted to thermal equilibrium. Extending the code out of equilibrium is possible with moderate effort.

II. THE CODE

In part II of the paper, we describe the main building blocks of the code—the classes representing correlation functions and other functions for combining them in diagrammatic computations. Furthermore, we describe post-processing schemes and emphasize aspects important for performance. More information on the technical details of individual code pieces can be found in the documentation attached to the source code (see the code availability statement at the end of this paper).

A. Prerequisites

The code itself is written in C++17³² and is built using CMake,³³ demanding at least version 3.10. It requires the GSL,³⁴ boost,³⁵ and Eigen3³⁶ libraries, as well as the HDF5³⁷ library for input and output. For parallelization, the OpenMP³⁸ and MPI³⁹ interfaces are used. Notably, we do not supply precompiled executables that could be run directly, for several reasons: First, the code makes heavy use of preprocessor flags that must be set *before* compilation and that are in part used to specify the concrete problem at hand (see Sec. II I). Second, special compilers for the particular architecture at hand might be available, which could optimize the code during compilation and linking, improving the performance. The user should hence adapt the file CMakeLists.txt accordingly, such that the required libraries are included and linked properly and all compiler settings are as desired.

The technical documentation supplied with the code is generated automatically using the tools Doxygen,⁴⁰ Sphinx,⁴¹ Breathe,⁴² and CMake.

B. Basic structure

The structure of the main part of the codebase is depicted in Fig. 1. The main objects of interest are the SelfEnergy Σ and the four-point Vertex Γ . Separate classes have been implemented for both, discussed in detail below. Both classes use instances of the class that defines suitably chosen FrequencyGrids, to be discussed in Sec. II G 4, for discretizing the continuous frequency dependence. A self-energy and a vertex always come together in any practical calculation, representing data for a step of an mFRG flow or an iteration of the parquet solver. The self-energy and vertex classes are hence combined in a State class $\Psi = (\Sigma, \Gamma)$. The algorithms discussed in Sec. III require computing bubble- and loop-type diagrams, the main functionality of the codebase. As detailed in Sec. II D 1 below, the bubble_function contracts two input vertices with a pair of propagators in one of the three two-particle channels to yield a new four-point vertex, which is stored as an instance of the Vertex class. For example, contracting two vertices Γ_1 and Γ_2 in the *a* channel is denoted as

$$B_a(\Gamma_1, \Gamma_2) = \Gamma_1 \circ \Pi_a \circ \Gamma_2 = \text{Diagram}, \quad (8)$$

see also Appendix C in Ref. 1 for a fully parametrized version. The required propagator pair Π belongs to a separate Bubble

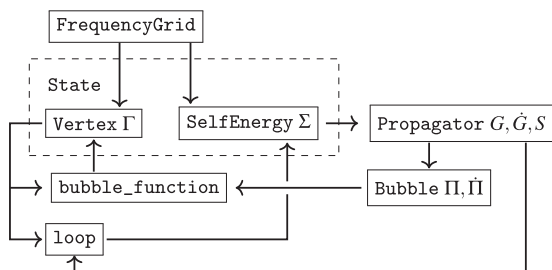


FIG. 1. Schematic depiction of the main parts of the codebase.

class, ensuring the correct combination of propagators and their parametrization. The propagators themselves are defined in the Propagator class, which essentially implements the Dyson equation, Eq. (3), combining G_0 and Σ . The former contains all the system parameters, including the regulator in mFRG; the latter encodes the interaction effects. Both the Propagator and Bubble classes can handle differentiated objects arising in mFRG (see Sec. III C). Finally, the loop function is used to contract two external legs of a four-point Vertex with a Propagator, yielding an instance of the SelfEnergy class, for example,

$$L(\Gamma, G) = \text{Diagram}, \quad (9)$$

These types of diagrams are required, e.g., for the mFRG flow equation of the self-energy or for the evaluation of the SDE after a previous bubble diagram computation.

C. Correlation function classes

In the following, we discuss the main building blocks of the code in more detail. We begin by outlining the self-energy and vertex classes. In addition, there are two helper classes: the first represents propagators, combining the bare propagator and the self-energy; the second combines a pair of propagators as needed for bubble-type diagrams.

1. The Vertex classes

In total, the code contains the four classes irreducible, rvert, fullvert, and GeneralVertex to store different types of four-point vertices.

The irreducible class contains the two-particle irreducible part of the vertex, R . In the PA, its 16 Keldysh components are just constants. It can easily be extended to hold nontrivial input data, for example, in the context of diagrammatic extensions⁴³ of dynamical mean-field theory⁴⁴ such as DFA⁴⁵ or DMF²RG.⁴⁶

The rvert class stores the two-particle reducible vertices $\gamma_{r \in \{a,p,t\}}$. Each of them is split up into their asymptotic classes,⁴⁷ K_1 , K_2 , and K_3 , where the $K_{2'}$ class is inferred from K_2 by crossing symmetry. Being one-, two-, and three-dimensional objects, respectively, each of those naturally has its own frequency grid. The rvert supplies several methods to store and read out data, either directly or interpolated. Conveniently, it can return all vertex parts where external legs either do or do not meet at the same bare vertex on the left or on the right-hand side by suitably combining the K_1 , $K_{2'}$, or K_2 and K_3 classes, respectively. This turned out to be very handy for keeping track of contributions for the different asymptotic classes during calculations. In addition, the rvert class can track and, if desired, enforce symmetries in the Keldysh-, spin-, and frequency domains (see Sec. II G 3 for details). For debugging purposes, functionality not using symmetries is provided as well.

The fullvertex class combines one instance of the irreducible class and three instances of the rvert class, one for each two-particle channel a, p, t . It can then return the value of the full vertex, which is the sum of the four contributions for a given

Keldysh and spin component, interpolated at a given combination of frequencies. As each individual `rvvert` instance, it can collect all those parts of the vertex where the external legs either do or do not meet at the same bare vertex on the left or on the right-hand side and includes functionality to exploit various symmetries. In addition, it can compute the p -norm of each asymptotic contribution, which is useful for debugging purposes and convergence criteria, e.g., in parquet computations.

While instances of the `fullvertex` class hold the data of the symmetry-reduced sector of a full vertex, certain diagrammatic equations involve subsets of vertex diagrams. One example is the r -channel-irreducible vertex used in the Bethe–Salpeter equations outlined in Sec. III B. Such diagrams do not necessarily obey all the symmetries of a full vertex, so they must be treated differently. These asymmetric cases are, therefore, encoded in the `GeneralVertex` class. It uses multiple instances of `fullvertex`, which together cover the symmetry-reduced sector of the asymmetric vertex data. Let us comment here that, while this approach is feasible, it turned out to be inconvenient in practice, as one always has to make sure that all sectors are covered, i.e., that all required `fullvertex` instances are provided. This is a source of logical errors that can sometimes be hard to find. In retrospect, it would have been better to pay the increased cost in memory to store all vertex contributions in the same object, making the code easier to read and to work with.

All vertex classes allow adding or subtracting two instances of the respective classes or multiplying a number with a vertex instance.

Splitting up the vertex functionality into so many different classes was made at the beginning of developing the code to provide enough flexibility, in particular regarding symmetries and a possible non-trivial input for the irreducible vertex. In hindsight, it turned out that for the computations performed in Ref. 1, this structure would not have been required in this generality.

2. The `SelfEnergy` class

The `SelfEnergy` class comes with a `dataBuffer` that stores the discrete values of the retarded and Keldysh components of the self-energy on a given frequency grid (see Secs. II G 4 and II G 8). When instantiating an object of the `SelfEnergy` type, a given frequency grid can either be supplied or a suitable one is generated automatically based on the value of the regulator Λ . In addition, the asymptotic value of the retarded component of the self-energy has to be set. Most of the time, this should be the Hartree value Σ_H , as the `SelfEnergy` inside the code is supposed to be used only for the dynamical, i.e., frequency-dependent, contributions of the self-energy, which excludes the constant Hartree value. For the sAM, the Hartree value is constant, $\Sigma_H = U/2$; in the asymmetric case, it has to be computed self-consistently beforehand. This can be performed inside the code using the `HartreeSolver` class (see Sec. III A 1).

The `SelfEnergy` class provides a host of methods used throughout the code. Most importantly, it can return the value of the self-energy either directly at a given input on the frequency grid (fast) or return an interpolated value at a given continuous frequency (not so fast). It can also set the value of Σ for a given input. In addition, one can compute the p -norm of Σ and the relative deviation to a different `SelfEnergy` instance using the maximum norm. This

is used to check convergence in parquet computations detailed in Sec. III B.

Finally, multiple operators are defined for the `SelfEnergy` class, which are used to add or subtract two `SelfEnergy` instances or to multiply some number with a `SelfEnergy` instance.

3. The `State` class

Instances of the `State` class are the high-level objects that are mainly used by the high-level algorithms discussed in Sec. III. The `State` class combines a `GeneralVertex` and a `SelfEnergy`, which together contain all non-trivial information that one might wish to compute. In that sense, it suffices to completely specify the “state” of the calculations. For the purpose of fRG calculations, the `State` class also holds the value of the flow parameter Λ .

As with the vertex classes and the `SelfEnergy` class, the `State` class also comes with operators that can be used to add and subtract states from one another and to multiply a number with a state. Under the hood, these operators just invoke the corresponding operators previously defined for the vertex and self-energy. Hence, all high-level algorithms can manipulate instances of the `State` class directly, e.g., by combining several iterations of the parquet solver in a mixing scheme.

4. The `Propagator` class

The `Propagator` class is special in the sense that it stores almost no data itself. Instead, it references instances of the `SelfEnergy` class and combines the analytical form of the bare propagator G_0 with the self-energy via the Dyson equation, $G = 1/[(G_0)^{-1} - \Sigma]$. To that end, it can return the value of a given propagator at some point, interpolated on the frequency grid of the referenced self-energy. This can be performed either directly for a given Keldysh component at some continuous frequency or vectorized over all Keldysh components. As G_0 depends on the formalism used and in mfRG on the choice of the regulator, separate methods for a variety of choices are provided. In addition, one can specify whether the full propagator G shall be computed, or the single-scale propagator S , the differentiated propagator including the Katanin extension,⁴⁸ or just the Katanin extension by itself (see Sec. III C). Note that the Katanin extension requires the self-energy differentiated with respect to the flow parameter Λ ; hence, the propagator class references *two* `SelfEnergy` instances, one non-differentiated and one differentiated.

5. The `Bubble` class

Finally, the `Bubble` class combines two propagators to yield a bubble in one of the three two-particle channels a , p , and t , according to Eqs. (C1a)–(C1c) in Ref. 1. For evaluating differentiated bubbles in mfRG, one of the propagators can be chosen to be the single-scale propagator S or the fully differentiated one \tilde{G} . In that case, the bubble already takes care of the product rule, giving (symbolically) $\dot{\Pi}^S = GS + SG$ or $\dot{\Pi} = \tilde{G}\dot{G} + \dot{G}\tilde{G}$. Otherwise, it just yields $\Pi = GG$. The `Bubble` class provides functions for obtaining the value of a bubble in a given channel at specified bosonic and fermionic frequencies, either for one specific Keldysh component directly or vectorized over the Keldysh structure. This class simplifies bubble computations using the `bubble_function` (see Sec. II D 1).

D. Main functions for diagrammatic computations

Computing bubbles and loops involves contractions over quantum numbers and Keldysh indices, including integrations over frequencies for all possible combinations of external arguments, and is by far the most costly part for the numerics. A clean and efficient implementation of this functionality is, therefore, paramount and should be of the highest priority when setting up a new code. In the following, we provide technical details on this most important part of the code.

1. The bubble function

The `bubble_function` implements Eqs. (C2a)–(C2c) from Ref. 1. It takes references to three vertices as arguments, one to store the result of the computation and two others to be connected by a `Bubble` object. This `Bubble` object can either be supplied as well or is initialized by an overload of the `bubble_function`, which in addition requires the two propagators that shall be used for the `Bubble`. The main work is then performed by an instance of the class `BubbleFunctionCalculator`, which performs the bubble contractions for each diagrammatic class separately. This is performed for every possible combination of external arguments, i.e., Keldysh indices and frequencies. At this point, the calculations are parallelized as outlined in Sec. II G 1. For each set of arguments, an `Integrand` object is instantiated, which puts together the two vertices and the bubble and performs the contraction over Keldysh indices if the flag `SWITCH_SUM_N_INTEGRAL` is set to 1. The `Integrand` class provides an operator that reads out the integrand at a given frequency. It is called by the integrator, invoked subsequently, and described in detail in Sec. II G 5. The results of all the frequency integrations are finally collected and *added* to the vertex object that was given as the first argument to the `bubble_function`. The choice not to output a completely new vertex but instead to add the result to an existing vertex has historical reasons to save memory. This increased the risk of logical errors during high-level algorithm implementations, though, and in hindsight, the `bubble_function` should better have been designed to output a completely new vertex object.

2. The loop function

The `loop` function implements Eq. (C3) from Ref. 1 and is structured similarly to the `bubble_function`. It takes a reference to self-energy for storing the result as well as references to a vertex and a propagator as arguments for the loop. For each external fermionic frequency, in which the computation is parallelized again, it invokes the integrator to perform a frequency integration using the `IntegrandSE` class. For the aAM, the asymptotic value of the just computed self-energy is extracted from the Hartree- and the $K_{1,t}$ and $K_{2,t}$ terms after the calculation. For the sAM, the asymptotic value of the self-energy is a known constant.

E. Postprocessing

The code provides a host of postprocessing functions. These are not required for the actual calculations themselves but are useful to extract additional information from their results, either as consistency checks or to infer derived quantities for later analysis.

1. Causality check for the self-energy

By causality, the imaginary part of the retarded component of the self-energy is strictly non-positive;⁴⁹ $\text{Im} \Sigma^R(\nu) \leq 0$ for all frequencies $\nu \in \mathbb{R}$. A violation of this condition not only constitutes an unphysical result but often leads to numerical instabilities. The code, therefore, provides the function `check_SE_causality` that checks this condition for a supplied instance of `SelfEnergy`. Typically, this function is invoked after each ODE step during an mFRG calculation or after each iteration of the parquet solver.

2. Fluctuation dissipation relations

In thermal equilibrium at temperature T , one has a fluctuation–dissipation relation (FDR)^{11,27} between the retarded and the Keldysh components of the propagator, $G^K(\nu) = 2i \tanh(\frac{\nu}{2T}) \text{Im} G^R(\nu)$, and the self-energy, $\Sigma^K(\nu) = 2i \tanh(\frac{\nu}{2T}) \text{Im} \Sigma^R(\nu)$. This relation can be used to infer the Keldysh components of the self-energy from the retarded component or vice versa; hence, it would in principle suffice to compute only one of the components. However, in the vectorized form of the code, both components of the self-energy are computed anyway. The FDR can hence be used as an internal consistency check, provided by the function `check_FDTs_selfenergy`. It computes Σ^K from Σ^R via the FDR and compares it to the independently computed Keldysh-component of the self-energy by computing the 2-norm of the difference.

As an additional consistency check, the fulfillment of fluctuation–dissipation relations for the K_1 classes, reading

$$\text{Im} K_1^R(\omega) = -\frac{i}{2} \tanh\left(\frac{\omega}{2T}\right) K_1^K(\omega), \quad (10)$$

can be examined. One may also want to check generalized FDRs for three-point and four-point contributions of the vertex.⁵⁰

3. Kramers–Kronig relation

For functions $f(\omega)$ that are analytic in the upper half plane, like retarded single-particle correlation functions, the Kramers–Kronig transform relates the real and imaginary parts via

$$\text{Re} f(\omega) = \frac{1}{\pi} \mathcal{P} \int_{-\infty}^{\infty} d\omega' \frac{\text{Im} f(\omega')}{\omega' - \omega}, \quad (11)$$

where \mathcal{P} denotes the Cauchy principal value. Inside the code, the function `check_Kramers_Kronig` can be used to test how well this generic analytic property is fulfilled.

4. Sum rule for the spectral function

The fermionic spectral function $A(\nu) = -\text{Im} G^R(\nu)/\pi$ must obey the sum rule

$$\int_{-\infty}^{\infty} d\nu A(\nu) = 1. \quad (12)$$

The function `sum_rule_spectrum` implements this integral as a consistency check.

5. Susceptibilities

Susceptibilities, which are of significant physical relevance, are derived from the vertex by contracting pairs of external legs. Diagrammatically, the formula for the a -channel susceptibility reads

$$\chi_a = \text{bubble} + \text{bubble} \circlearrowleft \Gamma \circlearrowright \text{bubble}, \quad (13)$$

and similarly for the susceptibilities in the p and t channel. The fully parametrized equations are provided in Eq. (C7) of Ref. 1. Linear combinations of these diagrammatic susceptibilities yield the physical susceptibilities [see Eq. (C8) of Ref. 1]. The code computes susceptibilities using the function `compute_postprocessed_susceptibilities`, which can be invoked after a completed calculation using the name of the file that stores the results. It iterates through all layers that correspond to ODE steps or parquet iterations (see Sec. II F), evaluates Eq. (C7) using the vertex and self-energy for each, and stores the results as a new dataset in the same file.

It was found in Ref. 47 that for converged parquet computations, susceptibilities can more easily be extracted directly from the K_1 class. As discussed in Refs. 1 and 51, one can also choose to compute susceptibilities that way during fRG computations, even though the two schemes are inequivalent if multiloop convergence is not reached. The two different schemes of computing susceptibilities can then be used to gauge the quality of the truncation.

6. Vertex slices

Finally, the function `save_slices_through_fullvertex` can be used to read out two-dimensional “slices” of the full vertex. It takes the filename corresponding to the results of a finished calculation as an argument, iterates through all layers, and saves a two-dimensional cut of all Keldysh components of the full vertex in the t -channel parametrization for zero transfer frequency ($\omega_t = 0, v_t, v_t'$) for a given spin component. While this function does not perform any non-trivial calculations, it is useful for visualization purposes. If desired, the function can be straightforwardly adapted to store vertex slices at finite transfer frequencies, enabling full scans through the three-dimensional structure of the four-point vertex.

F. I/O

We use the HDF5 file format³⁷ for input and output purposes throughout. To organize the data for output, the contents of a state are split into different datasets that correspond, e.g., to all the asymptotic classes of the vertex in each channel, the self-energy, the frequency grids, and the most important parameters of the calculation. The output file is then organized on a high level in terms of “ Λ layers,” the idea being that each layer enables access to a different state stored in the same file. Thereby, a single file contains, e.g., the results of a full mFRG flow, where each “ Λ layer” corresponds to a different value of the regulator. Alternatively, this structure can be used to store the results of all iterations needed for solving the parquet equations. Of course, one can equally well use just a single layer to store the end result of a computation, such as a converged solution of the parquet equations or the result of a PT2 computation.

The function `write_state_to_hdf` creates a new file with a fixed number of layers and saves an initial state into the first layer. Additional states generated during subsequent computations can be added to the same file (but into a different layer to be specified) using the function `add_state_to_hdf`. In effect, these functions are wrappers of a host of additional functions that are able to store various data structures, such as scalars, vectors, or even Eigen-matrices, in an HDF file.

When using parallelization, as detailed in Sec. II G 1, one has to ensure that only one single process writes data into the output file. Collisions, where multiple processes simultaneously try to write to the same location in memory, will cause the program to crash.

It is possible to read data from an existing HDF file to generate a new state for subsequent computations. For this purpose, the function `read_state_from_hdf` reads a state from a specified layer of a provided HDF file. One can thus do checkpointing: If all steps of an mFRG flow or all iterations of the parquet solver are stored separately, a computation that was interrupted can be continued from the last step stored. This design feature is useful for large computations that have to be split over several separate jobs or in the case of a hardware error causing a job to crash. Setting up checkpointing functionality is, therefore, strongly recommended.

G. Performance

In the following, we discuss parts of the code of special importance for performance. Of course, there is always a trade-off between accuracy and performance, as, e.g., an arbitrary high frequency resolution quickly becomes prohibitive. Nevertheless, efficient implementations are necessary for challenging computations.³² For the precision-focused calculations for which this codebase was developed, these parts are, therefore, of utmost importance.

1. MPI+OpenMP parallelization

As mentioned in the beginning, mFRG and parquet computations can be heavily parallelized since the correlation functions are (repeatedly) evaluated independently for every possible combination of external arguments. Parallelization is especially advisable for computing bubbles of two four-point vertices, as outlined in Sec. II D 1. We use the OpenMP interface for parallelization across multiple threads on a single node and the MPI interface for parallelization across multiple nodes. While OpenMP parallelization works with shared memory, meaning that all threads have access to the same data on the node that they are running on, one has to be careful with MPI parallelization working on distributed memory. Processes that run on different nodes to compute, say, a four-point vertex for different sets of external arguments cannot write their results into the same instance of a four-point vertex. Hence, we introduce additional buffers distributed across the nodes. After the computation of, say, a four-point vertex is finished, these buffers are collected, and their contents are put together to yield the full result. While this scheme is initially somewhat cumbersome to set up, it pays off tremendously, as the code’s performance scales well with the computational resources, including multiple nodes. This is because, first, computations for different external arguments are independent from each other, so there is minimal communication between the nodes. Second, the number of external arguments required for

precision-focused calculations is large, so individual threads have little downtime waiting for other threads to finish. For example, the most expensive calculations in Ref. 1 involved 125 points along each of the three frequency axes, which were parallelized across 32 nodes running 32 threads each. Provided enough CPU power, the resolution could, in principle, be increased further but is ultimately limited by memory.

2. Vectorization

As outlined in Sec. I C, KF calculations require computing 2^n Keldysh components of n -point functions. These components can be arranged into a matrix, yielding, e.g., a 4×4 matrix for the four-point vertex. This structure can be exploited for summing over Keldysh indices by using vectorization and the data structures of the Eigen library,³⁶ significantly improving performance. This works because all Keldysh components are stored in contiguous sections of memory. Of course, the other parts of the code have to be able to use these data structures properly, which is why all functions that enable, e.g., access to the correlation functions (see Sec. II C) have two versions: one that can handle matrix-valued data when vectorization is used, and another used otherwise.

When using vectorization, all Keldysh components have to be stored explicitly. As a consequence, identities that relate different Keldysh components, such as certain symmetries or FDRs, cannot be used to reduce the numerical effort. Although maximal exploitation of symmetries initially was one of our main objectives, we later found that vectorization over Keldysh components is preferential despite the larger memory costs.

In the finite- T MaF, we use vectorization to represent the Matsubara frequency dependence of all correlation functions. This leads to massive speedups when performing Matsubara sums as matrix-multiplications.

3. Symmetries

Many symmetries for reducing the number of data points to be computed directly can still be used together with vectorization over Keldysh indices. These include crossing symmetry of the vertex, which relates a vertex to itself with one pair of external fermionic legs exchanged; complex conjugation of the vertex; $SU(2)$ symmetry in the absence of a magnetic field (which, in combination with crossing symmetry, reduces the number of independent spin components to 1); and frequency symmetries in the presence of particle-hole symmetry. For explicit details on these symmetries, see Appendix A in Ref. 1.

Since frequency integrations are the most costly part of the computations, symmetry operations are not used for evaluating integrands on the fly. Instead, they are used to reduce the number of vertex components to be computed. Since the vectorized version of the code performs sums over Keldysh indices by matrix multiplication, the result of the integration contains all Keldysh components. Hence, we use the symmetry relations to reduce the other arguments, i.e., spin and frequency. Information about the symmetry-reduced components is encoded in symmetry tables. These contain entries for every channel, asymptotic class, spin component, and frequency sector and indicate whether a data point belongs to the symmetry-reduced sector or, otherwise, how to retrieve a value via symmetry relations.

4. Frequency grids

For numerical calculations, the continuous frequency dependence of correlation functions in the KF (and in the MaF at $T = 0$) must be discretized. Since these functions can become sharply peaked around certain frequencies, especially at lower temperatures, but simultaneously decay only slowly asymptotically (typically $\sim 1/\nu^2$ or even $\sim 1/\nu$ for some components), finding a suitable discretization that resolves all sharp structures but still captures the asymptotic decay is hard. Since the sharp features mostly occur at smaller frequencies (measured relative to the hybridization Δ), we use a frequency grid that provides high resolution at small frequencies and fewer points at high frequencies. To achieve this, an equidistant grid of an auxiliary variable $\Omega \in [-1, 1]$ is mapped to frequencies according to $\nu(\Omega) = A\Omega|\Omega|/\sqrt{1-\Omega^2}$. The parameter $A > 0$ can be suitably chosen automatically or by hand for all quantities, as further explained in Appendix G of Ref. 1. However, we do not recommend optimizing A automatically, as this can become expensive and unreliable in the presence of numerical artifacts.

The frequency grid is implemented in the `FrequencyGrid` class. It specifies the grid parameters such as the number of grid points or the scale factor A , and can access both continuous frequencies ν and auxiliary variables Ω corresponding to a given discrete index. Crucially, this also works the other way around, yielding the discrete index that corresponds to the frequency closest to a given continuous frequency. This is needed for interpolations, discussed in Sec. II G 7.

An instance of the `FrequencyGrid` class is instantiated in every instance of one of the correlation function classes to parameterize their respective frequency dependencies. The vertex classes naturally require up to three instances of the `FrequencyGrid` each.

The frequency grids are rescaled during `mfRG` flow calculations, which use the hybridization flow scheme (see Sec. III C). The `FrequencyGrid` class provides all the functionality required for that purpose.

As a side note, two alternative frequency grids have been implemented. One is a hybrid grid, which consists of a quadratic part at small frequencies, a linear part at intermediate frequencies, and a rational part at large frequencies. The other uses polar coordinates to parameterize the two-dimensional frequency dependence of three-point functions, i.e., the K_2 and K_2' classes. Which grid is to be used is controlled by the `GRID` flag (see Sec. II I). In our experience, the non-linear grid explained at the beginning of this section is the most useful if the scale parameters A are chosen suitably.

5. Frequency integration

The following passage is taken almost verbatim from the Ph.D. thesis of E. Walter.²⁸

Computing numerical integrals with high accuracy is a crucial ingredient for obtaining correct results in the context of the diagrammatic calculations discussed here. At the same time, the integrator is also critical for the performance of the computation, since evaluating integrals constitutes the computationally most expensive part of the code. For these reasons, we use an adaptive integration routine that automatically determines where to evaluate the integrand within the integration domain. Regions with sharp features require many evaluation points in order to get high accuracy,

while in regions where the integrand is smooth, fewer evaluations suffice, which increases the performance of the computation. Such an adaptive integrator is really indispensable for the problem at hand. Non-adaptive routines like a simple trapezoidal or Simpson rule on an equidistant grid often lead to systematically wrong results.

We use n -point integration rules that approximate integrals of the kind $\int_a^b F(x) dx \approx \sum_{j=1}^n F(x_j) w_j$ with nodes x_j and corresponding weights w_j . The integrator we use and which is implemented in the `Adapt` class in the code is an adaptive 4-point Gauss–Lobatto routine with a 7-point Kronrod extension and a 13-point Kronrod extension as an error estimate, as detailed in Ref. 53. The benefit of Gauss–Lobatto rules, compared to, e.g., the widely used Gauss–Kronrod rules, is that the nodes include the endpoints of the integration domain. This allows us to subdivide the domain at the nodes of the integration rule and reuse points that have been computed previously, which is preferential in terms of performance. Similarly, the Kronrod extensions of a Gauss–Lobatto rule reuse all points from a corresponding lower-point rule and simply add additional points, which effectively allows us to get two different rules from one set of evaluation points.

The nodes x_j of the 4-point Gauss–Lobatto rule with 7-point and 13-point Kronrod extensions are distributed as shown in Fig. 2. There, the lower row indicates the values of the nodes for integration boundaries $a = -1$, $b = 1$ (for other values of a , b , the values have to be rescaled correspondingly). The four-point Gauss–Lobatto rule (GL4) and four-point Gauss–Lobatto with seven-point Kronrod extension (GLK7) use the following points:

$$GL4(x_0, x_6) = \sum_{j \in \{0,2,4,6\}} F(x_j) w_j, \quad (14a)$$

$$GLK7(x_0, x_6) = \sum_{j=0}^6 F(x_j) w_j. \quad (14b)$$

The smaller marks between the nodes x_0, \dots, x_6 in the graphical representation above indicate the additional 6 points that are added in the 13-point Kronrod extension (GLK13), which are only known numerically (these and the weights w_j are found in Ref. 53).

The recursive algorithm of the integrator then works as shown in Fig. 3. Note that the error estimate I_s is determined only once for the full integral and then reused for each subinterval in order to avoid infinite recursions in subintervals. A typical recommended value for the relative accuracy is $\epsilon = 10^{-5}$, which is set by the global variable `integrator_tol` (see Table II).

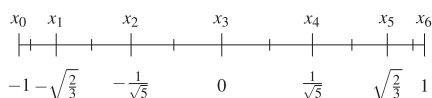


FIG. 2. Distribution of the nodes x_j of the 4-point Gauss–Lobatto rule with 7-point and 13-point Kronrod extensions. The lower row indicates the values of the nodes for integration boundaries $a = -1$, $b = 1$.

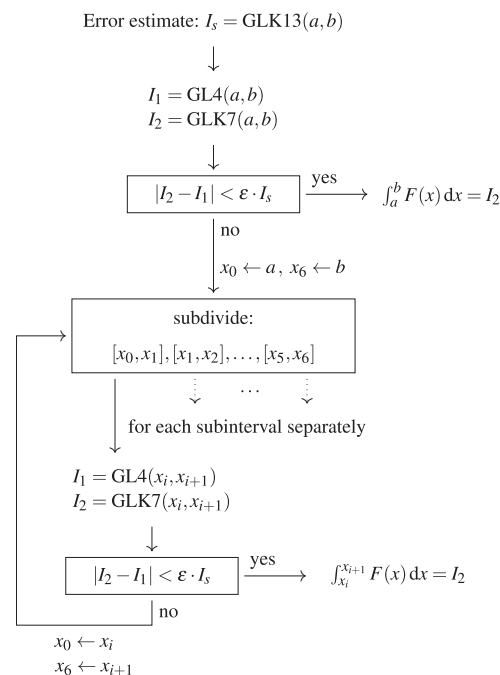


FIG. 3. Schematic illustration of the integration algorithm: an adaptive 4-point Gauss–Lobatto routine with a 7-point Kronrod extension and a 13-point Kronrod extension as an error estimate.

6. Asymptotic corrections to frequency integrals

In Sec. II G 5, it was explained how frequency integrations over a finite interval $[a, b]$ are performed. Since diagrammatic calculations require integrations over the full frequency axis (or summations over an infinite set of discrete Matsubara frequencies for the finite- T MaF), the contributions to the integral resulting from the high-frequency asymptotics of the integrands have to be treated as well. This is particularly relevant for slowly decaying integrands, which occur often, as the correlation functions arising in the present context typically only decay as $\sim 1/\nu$ or $\sim 1/\nu^2$.

In the KF and the zero- T MaF, involving continuous frequency integrations, a naïve treatment turned out to be sufficient: Since the frequency axes are discretized non-uniformly, as described in Sec. II G 4, the largest discrete frequency grid point is always so large that the high-frequency tails can be treated via quadrature, ignoring the minuscule contributions of even larger frequencies. For finite- T MaF computations, which involve infinite sums, the code provides two options for the treatment of high-frequency tails in the integrand: (i) The tails can be treated via quadrature by approximating the sum with an integral and then following the same logic as in the KF. (ii) For bubble computations, the lowest order contribution from the bare bubble, which is known analytically, can be used. This is justified by the fact that in the high-frequency asymptotic limit, the non-trivial contributions due to interactions encoded in the self-energy have decayed, and only the bare contribution is responsible for the asymptotic behavior. The first or second

option is chosen with the `ANALYTIC_TAILS` parameter flag (see also Sec. II I).

7. Interpolation routines

Whenever the value of a correlation function at some continuous frequency argument is required, in particular during frequency integrations, the data stored on discrete frequency grids has to be interpolated. In addition, the diagrammatic algorithms discussed here have feedback between the three two-particle channels, which all have their own channel-dependent parametrizations. This necessitates accurate interpolations between different frequency parametrizations; otherwise, errors accumulate over the course of a computation.

To handle the interpolation of multidimensional correlation functions, we implemented multilinear interpolation and cubic spline interpolation using cubic Hermite splines. While spline interpolation is robust against minor inaccuracies of the data points and offers faster convergence in the number of frequency points for smooth functions, multilinear interpolation is generally faster numerically. Having tried out both options, we prefer linear interpolation, as spline interpolation only really becomes useful for better precision if the function is already well resolved.

Regarding linear interpolation, the code offers options: One can either interpolate on the grid of frequencies ν or on the grid of auxiliary frequencies Ω , which are equidistantly spaced on the interval $[-1, 1]$ (see Sec. II G 4). We found the latter option to be more accurate. The global parameter `INTERPOLATION` specifies which type of interpolation shall be used (see also Sec. II I).

8. Data structures

The central low-level data structure used for storing and retrieving numerical data inside the code is the `dataBuffer` class. It was devised with the two main intentions of efficiency and flexibility in mind (see also our discussion of the main design choices for the codebase in the introduction, Sec. I). On the one hand, it should enable building integrands that return scalar- or vector-valued entries as efficiently as possible, particularly avoiding conditional (“if-else”) statements during runtime, as these prevent optimizations such as loop-vectorization or function inlining. On the other hand, it should be useable in all parts of the codebase, e.g., for both calculations with interpolations on continuous frequency grids and for finite- T MaF calculations, which only require indexing of discrete data points.

The `dataBuffer` class is structured as follows. It builds upon the `dataContainerBase` class, which is used to represent multi-dimensional tensors, allowing scalar and vector-valued access to contiguous elements. The `DataContainer` class then inherits `dataContainerBase`, adding frequency information. It contains a multi-dimensional frequency grid (see Sec. II G 4) to parameterize all its associated frequency arguments and provides functions to analyze the resolution of frequency grids. Inheriting the `DataContainer` class, the `Interpolator` classes then implement the different interpolation routines outlined in Sec. II G 7. Multilinear cubic spline interpolations require pre-computation and storage of interpolation coefficients, whereas linear interpolations happen on the fly. Finally, the `dataBuffer` class inherits both the

`Interpolator` and the `DataContainer` classes and can be used in actual computation. In addition, it can update and optimize grid parameters as required.

9. Template arguments

Another performance-critical aspect of the codebase is its heavy use of templates. In particular, the propagation of template arguments as specified by preprocessor flags enables the determination of the required diagrammatic combinations for any given computation at compile time. Selecting and combining the necessary vertex contributions this way, e.g., for contributions to specific asymptotic classes, enables further optimization by the compiler. However, the ubiquity of template arguments comes at the expense of readability in many places.

H. Tests

The code includes a large number (178 as of writing) of self-explanatory unit tests that run checks on the low-level parts of the codebase. They are implemented using the popular `Catch2` library⁵⁴ and are invoked from a separate C++ source file, `unit_tests.cpp`, which should be built separately from the main source file. From inside this file, more involved and expensive tests can be started if desired. These include detailed tests of the ODE solver or perturbation theory, which are too expensive to be part of the unit test suite. Finally, the code includes functionality to produce reference data that can be used later to compare the results of a calculation after changes to the code have been made. We have found it immensely useful to include many unit tests in the codebase, as they can tell almost immediately if a single technical part of the code has broken. Moreover, having a way to compare the results of very involved computations that involve large parts of the codebase at once is useful to catch logical errors. We wholeheartedly recommend both.

I. Parameters

Before any individual calculation can be started, a number of parameters have to be set. As the code provides a large degree of flexibility, the number of possible parameter choices is large. Most of these parameters are set inside the corresponding header files before compilation. The reason for this is that, depending on these choices, often different functionality of the code is invoked, depending, e.g., on the choice of formalism. This is achieved by defining preprocessor macros accordingly, which makes the corresponding functionality accessible. As discussed previously in too many preprocessor macros (“flags”), while this approach was useful for implementing new functionality quickly, in the long run, it turned out to be problematic with regard to the readability and maintainability of the code. Table I provides a list (albeit incomplete) of the most important preprocessor flags used in the code with a short description of each.

In addition, global parameters have to be set, which specify settings like the resolution of the frequency grid, convergence criteria, or start- and end-points of an mFRG flow. Table II provides a non-exhaustive list of those.

Finally, it should be mentioned that once the code has been compiled and the resulting executable is to be called, it requires three run-time arguments: The first one invokes an mFRG run if it

TABLE I. Incomplete list of the most important preprocessor macros to be set before compilation.

Macro name	Possible values	Description
ADAPTIVE_GRID	...	If defined, use the optimization routine to find the best scale factor A of the frequency grid; if undefined, just rescale the grid. Warning: Can be expensive and unreliable in the presence of numerical artifacts
ANALYTIC_TAILS	0, 1	0 for false; 1 for true. If true, the analytic expression for the bare bubble is used to treat the high-frequency asymptotics during bubble computations in the finite- T MaF
BARE_SE_FEEDBACK	...	If defined, only bare selfenergy is used. It only makes sense if STATIC_FEEDBACK is defined. Useful for benchmarks with previous Keldysh fRG schemes
CONTOUR_BASIS	0, 1	0 for false, 1 for true: If true, no Keldysh rotation is performed, and the contour basis is used instead to parameterize the Keldysh components of all correlation functions. It is useful for comparisons with results that use this convention. Not as well tested and, therefore, not recommended for production runs
DEBUG_SYMMETRIES	0, 1	0 for false; 1 for true. Performs computations without the use of symmetries, if true. Useful for debugging purposes
GRID	0, 1, 2	Controls which frequency grid is to be used. 0 for the non-linear grid, 1 for the hybrid grid, and 2 for the polar grid. Recommendation: 0. See also Sec. II G 4
KATANIN	...	If defined, the Katanin extension is used during fRG computations
KELDYSH_FORMALISM	...	Determines whether calculations shall be performed in the Keldysh or Matsubara formalism. 0 for Matsubara formalism (MaF); 1 for Keldysh formalism (KF)
MAX_DIAG_CLASS	1, 2, 3	Defines the diagrammatic classes that will be considered: 1 for only K_1 , 2 for K_1 and K_2 , and 3 for the full dependencies. Useful for debugging purposes and for computations in second-order perturbation theory, or if STATIC_FEEDBACK is defined, when only K_1 is required
NDEBUG	...	If defined, assert functions are switched off. Recommended setting for production runs
PARTICLE_HOLE_SYMM	0, 1	0 for false; 1 for true. If true, particle-hole symmetry is assumed
PT2_FLOW	...	If defined, only compute the flow equations up to $O(U^2)$. Only makes sense for pure K_1 calculations. It is useful as a consistency check together with independent PT2 calculations
REG	2, 3, 4, 5	Specifies the mFRG flow regulator to be used. 2: Δ -flow, 3: ω -flow, 4: U -flow, 5: T -flow. For details, see Sec. III C 2
REPARAMETRIZE_FLOWGRID	...	If defined, the flow parameter is reparametrized according to Sec. III C 1. Only recommended for the Δ -flow
SBE_DECOMPOSITION	0, 1	0 for false; 1 for true. If true, the SBE decomposition is used to parameterize the vertex and the flow equations. Only implemented in the MaF!
SELF_ENERGY_FLOW_CORRECTIONS	0, 1	0 for false; 1 for true. If true, corrections to the flow equations for the vertex from the self-energy, starting at $\ell = 3$, are included
STATIC_FEEDBACK	...	If defined, use static K_1 inter-channel feedback as performed in 11. Only makes sense for pure K_1 calculations
SWITCH_SUM_N_INTEGRAL	0, 1	0 for false; 1 for true. If true, the sum over internal Keldysh indices is performed before the frequency integration. Recommended setting: 1
USE_ANDERSON_ACCELERATION	0, 1	0 for false; 1 for true. If true, Anderson acceleration is used to converge parquet iterations and self-energy iterations in mFRG faster
USE_MPI	...	If defined, MPI is used for parallelization across multiple nodes
USE_SBEb_MFRG_EQS	0, 1	Determines which version of the SBE approximation shall be used. 0 for SBEa, 1 for SBEb. Only implemented in the MaF!
VECTORIZED_INTEGRATION	0, 1	0 for false; 1 for true. If true, integrals are performed with vector-valued integrands. For Keldysh, vectorization over Keldysh indices. For Matsubara at finite T , vectorization over the Matsubara sum
ZERO_TEMP	0, 1	0 for false; 1 for true. If true, temperature $T = 0$ is assumed

TABLE II. Incomplete list of global parameters to be set before compilation.

Parameter name	Type	Description
converged_tol	double	Tolerance for loop convergence in mFRG
COUNT	int	Used to set the number of frequency points in the MaF. For details, see the definitions in the file <code>frequency_parameters.hpp</code>
Delta_factor_K1	int	Scale factor for the frequency grid of the K1 vertex class
Delta_factor_SE	int	Scale factor for the frequency grid of the self-energy
Delta_factor_K2_w	int	Scale factor for the frequency grid of the bosonic frequency of the K2 and K2' vertex classes
Delta_factor_K2_v	int	Scale factor for the frequency grid of the fermionic frequency of the K2 and K2' vertex classes
Delta_factor_K3_w	int	Scale factor for the frequency grid of the bosonic frequency of the K3 vertex class
Delta_factor_K3_v	int	Scale factor for the frequency grid of the fermionic frequencies of the K3 vertex class
EQUILIBRIUM	bool	If true, use equilibrium FDRs for propagators
glb_mu	double	Chemical potential – w.l.o.g. ALWAYS set to 0.0 for the AM!
integrator_tol	double	Integrator tolerance
inter_tol	double	Tolerance for closeness to grid points when interpolating
INTERPOLATION	linear, linear_on_aux, cubic	Interpolation method to be used. <code>linear</code> : linear interpolation on the frequency grid. <code>linear_on_aux</code> : linear interpolation on the grid for the auxiliary frequency Ω . <code>cubic</code> : Interpolation with cubic splines (warning: expensive!)
Lambda_ini	double	Initial value of the regulator Λ for an mFRG flow
Lambda_fin	double	Final value of the regulator Λ for an mFRG flow
Lambda_scale	double	Scale of the log substitution, relevant in the hybridization flow
dLambda_initial	double	Initial step size for ODE solvers with adaptive step size control
nBOS	int	Number of bosonic frequency points for the K_1 vertex class
nFER	int	Number of fermionic frequency points for the self-energy
nBOS2	int	Number of bosonic frequency points for the K_2 and K_2' vertex classes
nFER2	int	Number of fermionic frequency points for the K_2 and K_2' vertex classes
nBOS3	int	Number of bosonic frequency points for the K_3 vertex class
nFER3	int	Number of fermionic frequency points for the K_3 vertex class
U_NRG	std::vector<double>	Vector with the values of U in units of Δ that an mFRG flow should cover. Serve as checkpoints for the flow. It is useful for benchmarking purposes if data from other methods at precise parameter points are available
VERBOSE	bool	If true, detailed information about all computational steps is written into the log file. Recommended setting for production runs: <code>false</code>
nmax_Selfenergy_iterations	int	Maximal number of self-energy iterations to be performed during an mFRG flow for $\ell \geq 3$. Default value: 10
tol_selfenergy_correction_abs	double	Absolute tolerance for self-energy iterations in mFRG. Default value: 10^{-9}
tol_selfenergy_correction_rel	double	Relative tolerance for self-energy iterations in mFRG. Default value: 10^{-5}

is a positive integer, specifying the maximal number of loop orders calculated during the mFRG flow. Alternatively, if it is set to 0 or -1 , a parquet or PT2 calculation is started, respectively. The second is a positive integer and specifies the number of nodes to be utilized. The third runtime argument defines the temperature for the

calculation and was introduced to easily enable parameter sweeps without having to recompile the code every time. Note that its value is irrelevant for calculations that have the flag `ZERO_TEMP` set to 1 or if an mFRG run is performed with the flag `REG` set to 5, which employs the temperature flow.

III. ALGORITHMS

In the third main part of the paper, we finally describe three diagrammatic algorithms that have been implemented. These are second-order perturbation theory (PT), a self-consistent solution of the parquet equations, and the flow equations provided by the multiloop functional renormalization group (mfRG). For all three methods, we first give some theoretical background before describing schematically how the algorithms are implemented and what functions are being used.

A. Perturbation theory

The simplest computations that can be performed with the code are perturbation theory calculations. While these are easy to implement in the second order, going to higher orders involves an increasing number of diagrams, which can in principle be evaluated separately. This is, however, not always straightforward, e.g., if symmetries are to be exploited: individual diagrams of the perturbation series do not all have the same symmetries as a full vertex, such that symmetry-related diagrams have to be provided, which can become tedious. Alternatively, the flag `DEBUG_SYMMETRIES` can be set to 1, see Sec. II I, in which case the code does not attempt to exploit symmetries. As higher-order perturbation theory has so far only been performed for testing purposes and consistency checks (see, e.g., Chap. 7 in Ref. 28), we refrain from going into further detail here. Instead, we focus just on the second-order case and on Hartree-Fock theory for the self-energy relevant to the aAM.

1. Hartree-Fock

As elaborated in Ref. 1, it is helpful to replace the bare propagator G_0 by the Hartree-propagator G_H , which is shifted by the Hartree-term of the self-energy,

$$G_0^R \rightarrow G_H^R = \frac{1}{\nu - \varepsilon_d + i\Delta - \Sigma_H^R}. \quad (15)$$

For the sAM, this is almost trivial, as the retarded component of the Hartree term reads $\Sigma_H^R = U/2$, which simply yields $G_H^R = (\nu + i\Delta)^{-1}$. For the aAM, on the other hand, the Hartree-term can be computed self-consistently.

For this purpose, the class `Hartree_Solver` provides the function `compute_Hartree_term_bracketing`. It computes Σ_H^R via

$$\Sigma_H^R = U \int \frac{d\nu'}{2\pi i} G_H^<(v'), \quad (16)$$

where in thermal equilibrium, the relation $G^<(v) = -2i n_F(v) \text{Im} G^R(v)$ is used with the Fermi function $n_F(v) = 1/(1 + e^{vT})$. As Σ_H^R enters both sides of Eq. (16), this calculation is performed self-consistently using a simple bracketing algorithm.

In addition, the `Hartree_Solver` class provides the function `compute_Hartree_term_one-shot`, which evaluates Eq. (16) just once, given a provided self-energy for $G^R(v)$. This function is invoked in the context of parquet iterations and evaluations of mfRG flow equations to update the Hartree term of the aAM.

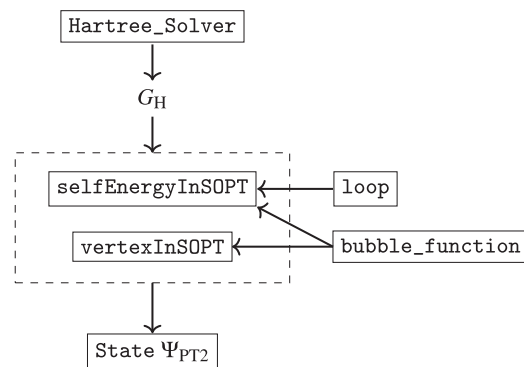


FIG. 4. Schematic depiction of the function `sopt_state`.

Finally, the `Hartree_solver` class provides functionality to check the fulfillment of the Friedel sum rule⁵⁵ $\langle n_\sigma \rangle = \frac{1}{2} - \frac{1}{\pi} \arctan [(\varepsilon_d + \Sigma(0))/\Delta]$, which the self-consistent Hartree term fulfills at $T = 0$.

2. Second order perturbation theory (PT2)

The self-energy and vertex in second-order perturbation theory are computed via the function `sopt_state`, which works as depicted in Fig. 4. It first initializes a bare state (see Sec. II C 3), given the system parameters and the current value of the regulator Λ . For the aAM, this already includes a self-consistent calculation of the Hartree term (see Sec. III A 1). Then, it invokes the function `selfEnergyInSOPT`, which computes the single diagram for the dynamical part of the self-energy in PT2 by first computing a bare bubble in the a -channel using the `bubble_function` (see Sec. II D 1), with two bare vertices, and then closing the loop over that bare bubble with the Hartree-propagator using the `loop` function (see Sec. II D 2).

Thereafter, the vertex is computed using the function `vertexInSOPT`, which simply invokes the `bubble_function` three times, once for each of the three two-particle channels a , p , and t , using two bare vertices, adding each result to the vertex.

In total, this procedure yields all diagrams for the dynamical part of the self-energy and the vertex in PT2, using the Hartree-propagator G_H . For the precise diagrammatic definition of PT2, see Appendix F in Ref. 1.

B. Parquet equations

The parquet formalism⁵⁶ provides a self-consistent set of equations for the self-energy Σ and the three two-particle reducible vertices γ_r with $r \in \{a, p, t\}$. The latter are given by the Bethe-Salpeter equations (BSEs)

$$\gamma_a = I_a \Gamma, \quad (17a)$$

$$\gamma_p = \frac{1}{2} I_p \Gamma, \quad (17b)$$

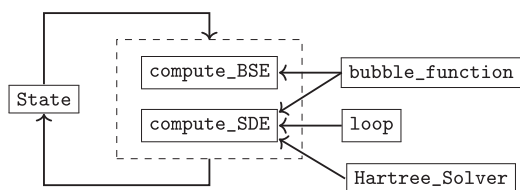


FIG. 5. Schematic depiction of the `parquet_solver` function.

$$\gamma_r = - (I_r + \Gamma) \quad (17c)$$

where $I_r = \Gamma - \gamma_r$ is the two-particle irreducible vertex in channel r . The self-energy is given by the Schwinger–Dyson equation (SDE),

$$\Sigma = - \text{tadpole} - \frac{1}{2} (\text{loop with } \Gamma), \quad (18)$$

which includes the Hartree term discussed in Sec. III A 1. Together, these equations close once the fully irreducible vertex R is provided, for example, by employing the PA, as discussed in Sec. I B.

In practice, these equations are solved iteratively. The code provides functions to evaluate the right-hand sides of the BSEs and the SDE, called `compute_BSE` and `compute_SDE`. Schematically, the parquet solver works as depicted in Fig. 5. Inside the code, a parquet computation is started by the function `run_parquet`. It first initializes a state using PT2, as detailed in Sec. III A 2, before the `parquet_solver` function is called. Internally, the `parquet_solver` calls `parquet_iteration`, which evaluates the BSEs and the SDE, given a provided input state, and combines them into an output state. The corresponding functions `compute_BSE` and `compute_SDE` use the machinery described in Secs. II C and II D to evaluate Eqs. (17) and (18). In practice, symmetrizing Eq. (17), i.e., computing the sum of the right-hand side as is and with I_r and Γ interchanged and dividing by two, has proven beneficial for stability.

In addition, we found it helpful to combine all three ways to evaluate the SDE, Eq. (18) (see Appendix D in Ref. 1).

The `parquet_solver` can either proceed directly from one iteration to the next, or it can combine multiple results from previous iterations using mixing schemes to improve convergence. For example, one can combine the two most recent iterations with a mixing factor as outlined in Eq. (G4) of Ref. 1. One may start with a mixing factor of around 0.5, which can be reduced automatically if the convergence properties of the calculation are poor. In addition, one can use Anderson acceleration^{57,58} to combine multiple previous iterations for a prediction of the next iteration. We have found that this leads to faster convergence in the vicinity of the solution but does not extend the parameter range where convergence can be reached.

The parquet solver can also be used for calculations in the random phase approximation (RPA). Switching off the BSEs in two of the three two-particle channels readily yields the RPA-ladder in the other channel.

C. mFRG

In fRG,⁵⁹ the self-energy and vertex are interpolated between the initial and final values of a single-particle parameter Λ introduced into the bare propagator G_0 . The initial value $\Lambda = \Lambda_i$ should be chosen such that the theory is solvable at that point; in practice, it typically suffices that very good approximations of Σ^{Λ_i} and Γ^{Λ_i} can be obtained by PT2 or by converging the parquet equations. The fRG then provides a set of differential “flow” equations in Λ for Σ^Λ and Γ^Λ , which yield the final results Σ^{Λ_f} and Γ^{Λ_f} at the actual point of interest $\Lambda = \Lambda_f$. In the multiloop fRG framework, these flow equations are derived from the parquet equations by differentiation with respect to the flow parameter Λ , as detailed in Ref. 18. This yields an infinite set of contributions of increasing “loop order” ℓ ,

$$\dot{\Gamma} = \sum_{r \in \{a,p,t\}} \dot{\gamma}_r, \quad (19a)$$

$$\dot{\gamma}_r = \sum_{\ell=1}^{\infty} \dot{\gamma}_r^{(\ell)}, \quad (19b)$$

where a dot represents a derivative with respect to Λ . Diagrammatically, the ℓ -loop contributions in the a channel read

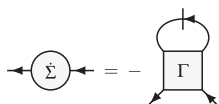
$$\dot{\gamma}_a^{(1)} = \text{square with loop and double line}, \quad (20a)$$

$$\dot{\gamma}_a^{(2)} = \text{square with loop and double line} + \text{square with loop and double line}, \quad (20b)$$

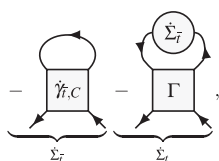
$$\dot{\gamma}_a^{(\ell+2)} = \text{square with loop and double line} + \text{square with loop and double line} + \text{square with loop and double line}, \quad (20c)$$

and analogously in the other two channels p and t . Here, $\gamma_r^{(\ell)} = \sum_{r' \neq \bar{r}} \gamma_{r'}^{(\ell)}$, and Eq. (20c) applies for all higher loop orders $\ell + 2 \geq 3$. The double-dashed bubble in Eq. (20) corresponds to a sum of two terms, $\tilde{\Pi} = \dot{G}G + G\dot{G}$, where $\dot{G} = S + G\dot{\Sigma}G$ with the single-scale propagator $S = \partial_\Lambda G|_{\Sigma=\text{const}}$ and the Katanin substitution.⁴⁸

The multiloop flow equation for the self-energy reads



$$\text{Diagram (21a): } \Sigma = - \Gamma \text{ (with double-dashed bubble on top)}$$



$$\text{Diagram (21b): } \Gamma = - \left(\text{Term 1} + \text{Term 2} \right)$$

with $\dot{\gamma}_{i,C} = \sum_\ell (\dot{\gamma}_{a,C}^{(\ell)} + \dot{\gamma}_{p,C}^{(\ell)})$, where the single-dashed line denotes the single-scale propagator S from above.

Historically, fRG flow equations have been derived from a generating functional, yielding an exact hierarchy of flow equations which couple n -point vertices of increasing order.⁶⁰ As the six-point vertex, which contributes to the flow equation of Γ , see Eq. (19) in Ref. 1, is inaccessible numerically, its contribution is often neglected completely, resulting in the so-called “one-loop” flow equations. This, however, results in an unphysical dependence of the final result of the flow on the choice of regulator (as the flow equations no longer constitute total derivatives) and also introduces a bias toward ladder diagrams.^{16,61}

The multiloop framework builds upon the one-loop scheme by iteratively adding precisely those two-particle reducible diagrammatic contributions to the flow equations that are required to reinstate total derivatives with respect to Λ and thereby reproduce the solution of the parquet equations. In that sense, it provides an alternative scheme for solving the parquet iterations via differential equations. From a computational standpoint, the mfRG flow equations introduce a complication compared to the one-loop flow equations, in that the right-hand sides of the flow equations for both Γ and Σ involve the differentiated self-energy and vertex. In order to still be able to use standard algorithms for ordinary differential equations, a scheme was outlined in Ref. 16 to include those differentiated quantities iteratively. Starting from the one-loop term Eq. (21a) to evaluate the flow Eq. (20) for Γ , these are then iterated with the multiloop corrections (21b) at every step of the flow until convergence is reached. The number of iterations required for convergence at this point can again be reduced using Anderson acceleration, as described in Sec. III B.

From the code, an mfRG-flow computation can be started with the function `n_loop_flow`, which requires only the string for the name of the output file and a set of parameters. It is overloaded to enable checkpointing, i.e., it is possible to continue a previously started computation from a given iteration. This is particularly useful for demanding jobs that take a long time, and it is highly recommended to any user.

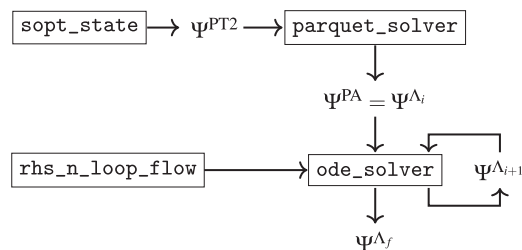


FIG. 6. Schematic depiction of the function `n_loop_flow`.

The function `n_loop_flow` works as shown in Fig. 6. It first initializes a state using PT2 with the function `sopt_state`, see Sec. III A 2, and then uses this result as a seed for a full parquet computation at the initial value of the regulator Λ_i with the `parquet_solver` function, see Sec. III B. This provides a suitable starting point for the following mfRG calculation.

The `ode_solver` function carries out the actual calculation of solving the mfRG flow. It uses an instance of the `rhs_n_loop_flow_t` class, which provides a wrapper to the function `rhs_n_loop_flow`, which in turn evaluates the right-hand side of the flow equations given an input state at a given value of Λ . This is performed iteratively by loop order according to flow Eq. (20), including self-consistent iterations for the self-energy starting at the three-loop level, as outlined earlier. The function `rhs_n_loop_flow` is structured as shown in Fig. 7. Starting from the self-energy and vertex from the previous step of the ODE-solver, it evaluates the right-hand sides of the flow equations by first computing the one-loop term of the flow equation for the self-energy, Eq. (21a), with the function `selfEnergyOneLoopFlow`. The result is then used to evaluate the one-loop term of the flow equation for the two-particle reducible vertices $\dot{\gamma}_r$ and Eq. (20), involving a fully differentiated bubble. Then, the one-loop result is used to evaluate the two-loop contribution, Eq. (20b), which consists of two terms: one where the differentiated one-loop contribution $\dot{\gamma}_r^{(1)}$ is used as the left part of a bubble contraction with the full vertex, and one where it is used on the right side. These two terms are computed using the functions `calculate_dGammaL` and `calculate_dGammaR`, respectively. Next, the three-loop contribution is computed, which involves both the one-loop and the two-loop results [see Eq. (20c)]. Again, the functions `calculate_dGammaL` and `calculate_dGammaR` are invoked, and in addition, the function `calculate_dGammaC` is invoked to compute the “center term” involving two bubble contractions of $\dot{\gamma}_r^{(1)}$ with the full vertex, once to the left and once to the right. As the structure of the flow equations does not change from this point on, this part is iterated until the maximally desired loop number n (which is given as a runtime parameter; see Sec. II I) is reached. The resulting center terms of the a and p channels are then used to evaluate the multiloop corrections to the self-energy, according to Eq. (21b). This updates the differentiated bubble used in the computation of the one-loop terms $\dot{\gamma}_r^{(1)}$, such that the whole process is finally iterated from that point on until convergence is reached, as determined by the parameters `tol_selfenergy_correction_abs` and

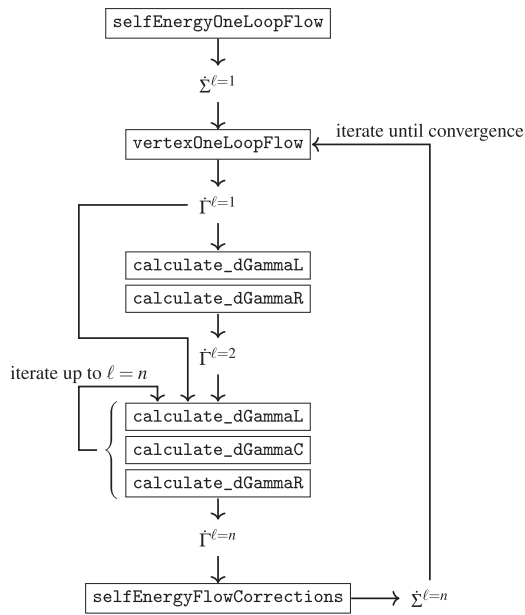


FIG. 7. Structure of the function `rhs_n_loop_flow`, including multiloop iterations up to loop order $\ell = n$ and self-consistent self-energy iterations due to the multiloop corrections.

`tol_selfenergy_correction_rel` (see Sec. II 1). All functions invoked by `rhs_n_loop_flow`, of course, make heavy use of the main functionality outlined in Sec. II D.

As a side note, it is possible to parameterize the vertex using the single-boson exchange (SBE) decomposition^{62–67} and to rewrite the mFRG flow equations in this language, as outlined in Ref. 68. This is achieved by setting the flag `SBE_DECOMPOSITION` to 1. Two versions of the SBE approximation can be used, known as “SBEa” and “SBEb” in the literature.⁶⁹ Which version is to be used is controlled by the flag `USE_SBEb_MFRG_EQS` (see Sec. II 1). This functionality is, so far, only implemented in the MaF. We, therefore, refrain from providing further details here.

In the final two parts of this section, we discuss the ODE-solver and the different flow schemes.

1. Details on the ODE-solver

To solve the mFRG flow equations accurately, a Cash–Karp routine⁷⁰ is implemented, which constitutes a fourth-order Runge–Kutta solver with adaptive step size control. An adaptive step-size control is crucial for obtaining accurate results and is hereby strongly recommended for solving fRG flow equations precisely. For a good first guess of the step size in the Δ -flow (see Sec. III C 2 a), the flow parameter is reparametrized as $\Lambda(t) = 5t|t|/\sqrt{1-t^2}$. For equidistant t , this parametrization provides large steps for large Λ and small steps for small Λ . This is sensible in the context of the Δ -flow, where Λ is gradually reduced to enter ever more challenging parameter regimes.

2. Flow schemes

In fRG, one chooses a regulator introduced into the bare propagator $G_0 \rightarrow G_0^\Lambda$, i.e., the flow scheme. While the solution of a truncated set of fRG flow equations will depend on this choice, a converged multiloop flow will not, as it reproduces the self-consistent solution of the parquet equations. It is generally advisable to choose the most convenient flow scheme for the problem at hand. In particular, the fRG flow can be used to compute a full parameter sweep in one go by choosing a physical parameter as the regulator. Compared to direct solutions of the parquet equations, which have to be computed individually at every point in parameter space, this makes mFRG computations more economical, provided they can be quickly converged in the loop order. In the following, we outline the flow schemes that have been implemented and can be used by setting the `REG` flag and the `Lambda_ini` and `Lambda_fin` parameters accordingly (see Tables I and II).

a. Δ -flow. The hybridization flow¹¹ uses Δ as the flow parameter, starting at a very large value and decreasing Δ to a smaller value, keeping the other parameters U and T fixed. The hybridization flow thus performs a parameter sweep in U/Δ for fixed T/U . The Keldysh fRG single-scale propagator reads

$$S^R(v) = \partial_\Delta G^R(v)|_{\Sigma=\text{const}} = -i[G^R(v)]^2.$$

In practice, we start the fRG flow from a solution of the parquet equations at large Δ (small U/Δ), where that solution can be easily obtained. For historical reasons, the hybridization flow is implemented as

$$G_\Lambda^R(v) = \frac{1}{v - \varepsilon_d + i(\Gamma + \Lambda)/2 - \Sigma_\Lambda^R(v)}, \quad (22)$$

inside the code, where Γ is fixed to some arbitrary value and Λ is used to fix the hybridization $\Delta = (\Gamma + \Lambda)/2$. Note that keeping T/U fixed during the Δ -flow is a somewhat unconventional choice, as in most works on the AM, the scale T/Δ is kept constant. As explained in Ref. 28, keeping T/Δ fixed during the Δ -flow would lead to additional sharply peaked terms in the single-scale propagator and has hence not been pursued yet.

b. U -flow. An alternative to the Δ -flow is the following flow scheme, first introduced in Ref. 71,

$$G_\Lambda^R(v) = \frac{\Lambda}{v - \varepsilon_d + i\Delta - \Lambda \Sigma_\Lambda^R(v)}, \quad (23)$$

starting at $\Lambda_i = 0$ (or very small, in practice) and flowing toward $\Lambda_f = 1$. The corresponding single-scale propagator then reads

$$S^R(v) = \partial_\Lambda G^R(v)|_{\Sigma=\text{const}} = \frac{v - \varepsilon_d + i\Delta}{[v - \varepsilon_d + i\Delta - \Lambda \Sigma_\Lambda^R(v)]^2}. \quad (24)$$

This flow scheme is called interaction- or U -flow because increasing Λ effectively amounts to increasing U . This can be shown by a simple rescaling argument: A bare diagram for Σ (or Γ) at order n has n factors of U and $2n - 1$ (or $2n - 2$) factors of $G_{0,\Lambda}$, each contributing one factor of Λ . The same scaling behavior in Λ can be achieved

without a Λ -dependent G_0 by multiplying U with Λ^2 and dividing out an extra Λ (or Λ^2). It hence holds that

$$\Sigma_\Lambda(U) = \Sigma(\Lambda^2 U)/\Lambda, \quad (25a)$$

$$\Gamma_\Lambda(U) = \Gamma(\Lambda^2 U)/\Lambda^2. \quad (25b)$$

Note that at zero temperature, the two flow schemes discussed so far should be equivalent: For $T = 0$, the only energy scales of the AM in the wideband limit are U and Δ , so there is only one external parameter U/Δ and it does not matter whether U is increased or Δ is decreased.

Historically, the U -flow has not been very popular, as it does not regulate IR divergences.⁵⁹ Nevertheless, it can be used for the AM. In Ref. 1, we found that, for a truncated 1-loop Keldysh fRG flow at *finite* T , this scheme produces inferior results compared to the Δ -flow when benchmarked against numerically exact NRG data. Still, the U -flow has the nice property that it keeps T/Δ fixed.

c. T-flow. Using temperature as the fRG flow parameter has been popular in the past when performing fRG computations in the MaF.^{72,73} It has been argued that temperature cannot be used for this purpose in Keldysh fRG computations,¹¹ the reason being that a truncated fRG flow does not preserve fluctuation–dissipation relations (FDRs). However, solutions to the parquet equations *do* fulfill the FDRs. If the FDRs are not used explicitly during mfRG calculations (as this would mix FDRs at different temperatures and hence introduce an inconsistency), it should also be possible to obtain these solutions by converging an mfRG flow. Instead of the standard FDR, which relates G^K and G^R , in this scheme, the general expression for the Keldysh component of the propagator should be used, which reads²⁸

$$G^K(v) = G^R(v) \left[\Sigma^K(v) - 2i\Delta \tanh\left(\frac{v}{2T}\right) \right] G^A(v). \quad (26)$$

The Keldysh component of the single-scale propagator is then

$$S^K(v) = \partial_T G^K(v) \Big|_{\Sigma=\text{const.}} = \frac{i\Delta v}{T^2 \cosh^2\left(\frac{v}{2T}\right)} |G^R(v)|^2. \quad (27)$$

Note that its retarded component is zero; $S^R(v) = 0$, as $G^R(v)$ does not depend explicitly on T . While preliminary numerical results suggest that this scheme indeed performs well, a systematic study of the temperature flow in Keldysh fRG is left for future work. So far, at the time of writing, the temperature flow described earlier can only be used in the KF; corresponding regulators in the MaF, as in Refs. 72 and 73, have not been implemented.

d. v-flow. Using a frequency regulator of the form $G_{0,\Lambda}(iv) = G_0(iv)\Theta_\Lambda(iv)$ with $\Theta_\Lambda(iv) = v^2/(v^2 + \Lambda^2)$ has been a popular choice in the literature for (m)fRG calculations in the Matsubara formalism.^{74,75} However, in this form, the frequency regulator cannot be used in the Keldysh formalism, as the analytical continuation of $\Theta_\Lambda(iv)$ gives $\Theta_\Lambda^R(v) = v^2/(v^2 - \Lambda^2 + 2|v|i0^+)$ with a branch cut

for $v < 0$. One can, however, change the form of the regulator to $\Theta_\Lambda(iv) = |v|/(|v| + \Lambda)$, for which the retarded counterpart reads

$$\Theta_\Lambda^R(v) = \frac{v}{v + i\Lambda}, \quad (28)$$

which *is* a well-behaved function. This choice is implemented as

$$G_\Lambda^R(v) = \frac{\Theta_\Lambda^R(v)}{v - \varepsilon_d + i\Delta - \Theta_\Lambda^R(v)\Sigma_\Lambda^R(v)}. \quad (29)$$

The corresponding single-scale propagator then reads

$$S^R(v) = -\frac{i}{v} \frac{[\Theta_\Lambda^R(v)]^2 (v - \varepsilon_d + i\Delta)}{[v - \varepsilon_d + i\Delta - \Theta_\Lambda^R(v)\Sigma_\Lambda^R(v)]^2}. \quad (30)$$

With this choice, all causality relations and FDRs are satisfied. However, this regulator has two drawbacks compared to the other flow schemes: First, it does not produce a parameter sweep, as Λ does not directly correspond to a physical parameter. Second, computations become ever more challenging for smaller Λ : Even if all correlation functions are reasonably smooth in frequency space for $\Lambda = 0$, for small but finite Λ , they exhibit sharp features. While this is not an issue for finite-temperature Matsubara calculations, where only sums over discrete Matsubara frequencies are performed, it turns out to be a major inconvenience in the Keldysh context.

IV. CONCLUSION

In this paper, we outline the structure and design of our C++ codebase for diagrammatic calculations of the AM in the Keldysh formalism. We explained the building blocks for representing real-frequency correlation functions and the central routines used to compute them. We elaborated on all performance-critical aspects, allowing one to handle the three-dimensional frequency dependence of the four-point vertex, and summarized the implementation of the parquet and mfRG equations. By discussing the most convenient features of the codebase—modularity, flexibility, performance, and scalability—but also some of its design flaws in detail, we hope to provide guidance and inspiration to others who plan to write code for similar purposes.

Our codebase forms the basis for numerous future projects involving the dynamical correlation functions of electronic many-body systems. Since the AM is very well understood, we want to generalize our treatment to more complicated models with unexplored physics, like lattice models, possibly including multiple bands. The main problem in that regard is the numerical complexity. In addition to their real-frequency Keldysh structure, all functions would acquire momentum dependencies and orbital indices. Parametrizing those naively appears prohibitively costly. Fortunately, the new quantum tensor cross interpolation (QTCI) scheme^{76–78} is currently being developed, which can be used to obtain highly compressed tensor network representations of correlation functions and promises exponential reductions in computational costs. It remains to be seen how efficiently the Keldysh four-point vertex can be compressed using this method. If it turned out to be highly compressible, one could combine the diagrammatic approaches outlined here with non-perturbative results from dynamical mean-field theory to access

truly strongly correlated parameter regimes (see related works^{79–81} in the MaF). In particular, computing non-local real-frequency dynamical vertex corrections beyond DMFT for observables like optical conductivities with high precision is a formidable long-term goal.

Another possible future direction relates to nonequilibrium phenomena, for example, the influence of the full four-point vertex on observables like differential conductivities.^{12,82} Nonequilibrium physics has been the most popular application of the KF in the past, and the AM with a finite bias voltage is tractable with only a minor increase in both the numerical costs and the implementation effort.

In order to leverage ongoing efforts in the QTCI framework, an interface to the corresponding Julia package⁸³ would be required. Given that, in recent years, multiple Julia codes have been developed to perform calculations of two-particle correlation functions,^{84–87} it would be natural to switch to that language in the future, especially since it allows much simpler structures and, in general, performs almost as well as C++.

ACKNOWLEDGMENTS

We acknowledge Marc Ritter, Marcel Gievers, Benedikt Schneider, Björn Sbierski, Nils Niggemann, Dominik Kiese, Aiman Al-Eryani, Lennart Klebl, and Jacob Beyer for insightful conversations about fRG code structures over the years, Henri Menke for the suggestion to use a combination of Doxygen, Sphinx, and Breathe for the technical code documentation, and Markus Frankenbach for comments on the paper.

N.R. acknowledges funding from a graduate scholarship from the German Academic Scholarship Foundation (“Studienstiftung des deutschen Volkes”) and additional support from the “Marianne-Plehn-Programm” of the state of Bavaria. A.G. and J.v.D. were supported by the Deutsche Forschungsgemeinschaft under Germany’s Excellence Strategy EXC-2111 (Project No. 390814868) and the Munich Quantum Valley, supported by the Bavarian state government with funds from the Hightech Agenda Bayern Plus. This work was supported by Grant No. INST 86/1885-1 FUGG of the German Research Foundation (DFG). F.B.K. acknowledges support from the Alexander von Humboldt Foundation through the Feodor Lynen Fellowship. The Flatiron Institute is a division of the Simons Foundation.

AUTHOR DECLARATIONS

Conflict of Interest

The authors have no conflicts to disclose.

Author Contributions

N.R. and A.G. contributed equally to this work.

Nepomuk Ritz: Funding acquisition (equal); Software (supporting); Writing – original draft (lead); Writing – review & editing (lead). **Anxiang Ge:** Software (lead); Writing – review & editing (supporting). **Elias Walter:** Conceptualization (lead); Software (equal). **Santiago Aguirre:** Conceptualization (equal); Software (equal). **Jan von Delft:** Funding acquisition (lead); Supervision (equal);

Writing – review & editing (equal). **Fabian B. Kugler:** Supervision (equal); Writing – review & editing (supporting).

DATA AVAILABILITY

The code, which includes a link to the technical documentation, can be found online (see Ref. 88). It is published under the MIT license.

REFERENCES

- 1 A. Ge, N. Ritz, E. Walter, S. Aguirre, J. von Delft, and F. B. Kugler, “Real-frequency quantum field theory applied to the single-impurity Anderson model,” *Phys. Rev. B* **109**, 115128 (2024).
- 2 T. Matsubara, “A new approach to quantum-statistical mechanics,” *Prog. Theor. Phys.* **14**, 351–378 (1955).
- 3 A. A. Abrikosov, L. P. Gorkov, and I. E. Dzyaloshinski, *Methods of Quantum Field Theory in Statistical Physics* (Courier Corporation, 2012).
- 4 G. Baym and N. D. Mermin, “Determination of thermodynamic Green’s functions,” *J. Math. Phys.* **2**, 232–234 (1961).
- 5 M. Jarrell and J. Gubernatis, “Bayesian inference and the analytic continuation of imaginary-time quantum Monte Carlo data,” *Phys. Rep.* **269**, 133–195 (1996).
- 6 A. W. Sandvik, “Stochastic method for analytic continuation of quantum Monte Carlo data,” *Phys. Rev. B* **57**, 10287–10290 (1998).
- 7 J. Schött, I. L. M. Locht, E. Lundin, O. Grånäs, O. Eriksson, and I. Di Marco, “Analytic continuation by averaging Padé approximants,” *Phys. Rev. B* **93**, 075104 (2016).
- 8 A. Ge, J. Halbinger, S.-S. B. Lee, J. von Delft, and F. B. Kugler, “Analytic continuation of multipoint correlation functions,” *Ann. Phys.* **536**, 2300504 (2024).
- 9 J. Kroha, P. Wölfle, and T. A. Costi, “Unified description of Fermi and non-Fermi liquid behavior in a conserving slave boson approximation for strongly correlated impurity models,” *Phys. Rev. Lett.* **79**, 261–264 (1997).
- 10 J. Kroha and P. Wölfle, “Fermi and non-Fermi liquid behavior of local moment systems within a conserving slave boson theory,” *Acta Phys. Pol., B* **29**, 3781 (1998).
- 11 S. G. Jakobs, “Functional renormalization group studies of quantum transport through mesoscopic systems,” Ph.D. thesis, RWTH Aachen, 2010.
- 12 S. G. Jakobs, M. Pletyukhov, and H. Schoeller, “Nonequilibrium functional renormalization group with frequency-dependent vertex function: A study of the single-impurity Anderson model,” *Phys. Rev. B* **81**, 195109 (2010).
- 13 S. G. Jakobs, M. Pletyukhov, and H. Schoeller, “Properties of multi-particle Green’s and vertex functions within Keldysh formalism,” *J. Phys. A: Math. Theor.* **43**, 103001 (2010).
- 14 F. B. Kugler, S.-S. B. Lee, and J. von Delft, “Multipoint correlation functions: Spectral representation and numerical evaluation,” *Phys. Rev. X* **11**, 041006 (2021).
- 15 S.-S. B. Lee, F. B. Kugler, and J. von Delft, “Computing local multipoint correlators using the numerical renormalization group,” *Phys. Rev. X* **11**, 041007 (2021).
- 16 F. B. Kugler and J. von Delft, “Multiloop functional renormalization group for general models,” *Phys. Rev. B* **97**, 035162 (2018).
- 17 F. B. Kugler and J. von Delft, “Multiloop functional renormalization group that sums up all parquet diagrams,” *Phys. Rev. Lett.* **120**, 057403 (2018).
- 18 F. B. Kugler and J. von Delft, “Derivation of exact flow equations from the self-consistent parquet relations,” *New J. Phys.* **20**, 123029 (2018).
- 19 J. Bezanson, A. Edelman, S. Karpinski, and V. B. Shah, “Julia: A fresh approach to numerical computing,” *SIAM Rev.* **59**, 65–98 (2017).
- 20 N. D. Matsakis and F. S. Klock II, “The rust language,” in *ACM SIGAda Ada Letters* (ACM, 2014), Vol. 34, pp. 103–104.
- 21 See <https://www.modular.com/max/mojo> for Mojo—The programming language for all AI developers.
- 22 B. Stroustrup, in *Programming—Principles and Practice Using C++*, 3rd ed. (Addison Wesley, Boston, MA, 2023).

- ²³R. Bulla, T. A. Costi, and T. Pruschke, "Numerical renormalization group method for quantum impurity systems," *Rev. Mod. Phys.* **80**, 395–450 (2008).
- ²⁴V. Zlatić and B. Horvatić, "Series expansion for the symmetric Anderson Hamiltonian," *Phys. Rev. B* **28**, 6904–6906 (1983).
- ²⁵P. B. Wiegmann and A. M. Tsvelick, "Exact solution of the Anderson model: I," *J. Phys. C: Solid State Phys.* **16**, 2281 (1983).
- ²⁶P. W. Anderson, "Localized magnetic states in metals," *Phys. Rev.* **124**, 41–53 (1961).
- ²⁷A. Kamenev, in *Field Theory of Non-Equilibrium Systems*, 2nd ed. (Cambridge University Press, 2023).
- ²⁸E. Walter, "Real-frequency dynamics of quantum impurity models studied with fRG, NRG, CFT," Ph.D. thesis, LMU München, 2021.
- ²⁹L. V. Keldysh, "Diagram technique for nonequilibrium processes," *Sov. Phys. JETP* **20**, 1018–1026 (1965).
- ³⁰J. Schwinger, "Brownian motion of a quantum oscillator," *J. Math. Phys.* **2**, 407–432 (1961).
- ³¹L. P. Kadanoff and G. A. Baym, *Quantum Statistical Mechanics* (Benjamin, New York, 1962).
- ³²ISO/IEC 14882:2017 - Programming languages—C++, International Organization for Standardization, 2017.
- ³³Kitware, Inc., CMake documentation, <https://cmake.org/documentation/>.
- ³⁴*GNU Scientific Library Reference Manual: For GSL version 1.12*, 3rd ed., edited by M. Galassi (Network Theory, Bristol, 2009).
- ³⁵See <https://www.boost.org/> for Boost C++ Libraries.
- ³⁶G. Guennebaud, B. Jacob *et al.*, Eigen: A C++ linear algebra library, <http://eigen.tuxfamily.org>.
- ³⁷The HDF Group, Hierarchical data format, version 5, <https://www.hdfgroup.org/HDF5/>.
- ³⁸See <https://www.openmp.org/> for the OpenMP API specification for parallel programming.
- ³⁹See <https://hpc.nmsu.edu/discovery/mpl/introduction/> for message passing interface: High performance computing.
- ⁴⁰D. van Heesch, Doxygen: A documentation system for C++, C, Java, Python and other languages, <https://www.doxygen.nl/>.
- ⁴¹See <https://www.sphinx-doc.org/> for Sphinx Documentation Generator.
- ⁴²See <https://breathe.readthedocs.io/en/latest/> for Breathe "latest" documentation.
- ⁴³G. Rohringer, H. Hafermann, A. Toschi, A. A. Katanin, A. E. Antipov, M. I. Katsnelson, A. I. Lichtenstein, A. N. Rubtsov, and K. Held, "Diagrammatic routes to nonlocal correlations beyond dynamical mean field theory," *Rev. Mod. Phys.* **90**, 025003 (2018).
- ⁴⁴A. Georges, G. Kotliar, W. Krauth, and M. J. Rozenberg, "Dynamical mean-field theory of strongly correlated fermion systems and the limit of infinite dimensions," *Rev. Mod. Phys.* **68**, 13–125 (1996).
- ⁴⁵A. Toschi, A. A. Katanin, and K. Held, "Dynamical vertex approximation: A step beyond dynamical mean-field theory," *Phys. Rev. B* **75**, 045118 (2007).
- ⁴⁶C. Taranto, S. Andergassen, J. Bauer, K. Held, A. Katanin, W. Metzner, G. Rohringer, and A. Toschi, "From infinite to two dimensions through the functional renormalization group," *Phys. Rev. Lett.* **112**, 196402 (2014).
- ⁴⁷N. Wentzell, G. Li, A. Tagliavini, C. Taranto, G. Rohringer, K. Held, A. Toschi, and S. Andergassen, "High-frequency asymptotics of the vertex function: Diagrammatic parametrization and algorithmic implementation," *Phys. Rev. B* **102**, 085106 (2020).
- ⁴⁸A. A. Katanin, "Fulfillment of Ward identities in the functional renormalization group approach," *Phys. Rev. B* **70**, 115109 (2004).
- ⁴⁹F. B. Kugler, "Improved estimator for numerical renormalization group calculations of the self-energy," *Phys. Rev. B* **105**, 245132 (2022).
- ⁵⁰E. Wang and U. Heinz, "Generalized fluctuation-dissipation theorem for nonlinear response functions," *Phys. Rev. D* **66**, 025008 (2002).
- ⁵¹C. Hille, F. B. Kugler, C. J. Eckhardt, Y.-Y. He, A. Kauch, C. Honerkamp, A. Toschi, and S. Andergassen, "Quantitative functional renormalization group description of the two-dimensional Hubbard model," *Phys. Rev. Res.* **2**, 033372 (2020).
- ⁵²D. Rohe, "Hierarchical parallelisation of functional renormalisation group calculations—hp-fRG," *Comput. Phys. Commun.* **207**, 160–169 (2016).
- ⁵³W. H. Press, S. A. Teukolsky, W. T. Vetterling, and B. P. Flannery, in *Numerical Recipes—The Art of Scientific Computing*, 3rd ed. (Cambridge University Press, 2007).
- ⁵⁴A modern, C++-native, test framework for unit-tests, TDD and BDD.
- ⁵⁵D. C. Langreth, "Friedel sum rule for Anderson's model of localized impurity states," *Phys. Rev.* **150**, 516–518 (1966).
- ⁵⁶N. E. Bickers, "Self-consistent many-body theory for condensed matter systems," in *Theoretical Methods for Strongly Correlated Electrons, CRM Series in Mathematical Physics*, edited by D. Sénéchal, A.-M. Tremblay, and C. Bourbonnais (Springer, New York, 2004).
- ⁵⁷D. G. Anderson, "Iterative procedures for nonlinear integral equations," *J. ACM* **12**, 547–560 (1965).
- ⁵⁸H. F. Walker and P. Ni, "Anderson acceleration for fixed-point iterations," *SIAM J. Numer. Anal.* **49**, 1715–1735 (2011).
- ⁵⁹W. Metzner, M. Salmhofer, C. Honerkamp, V. Meden, and K. Schönhammer, "Functional renormalization group approach to correlated fermion systems," *Rev. Mod. Phys.* **84**, 299–352 (2012).
- ⁶⁰C. Wetterich, "Exact evolution equation for the effective potential," *Phys. Lett. B* **301**, 90–94 (1993).
- ⁶¹F. B. Kugler and J. von Delft, "Fermi-edge singularity and the functional renormalization group," *J. Phys.: Condens. Matter* **30**, 195501 (2018).
- ⁶²F. Krien, "Efficient evaluation of the polarization function in dynamical mean-field theory," *Phys. Rev. B* **99**, 235106 (2019).
- ⁶³F. Krien, A. Valli, and M. Capone, "Single-boson exchange decomposition of the vertex function," *Phys. Rev. B* **100**, 155149 (2019).
- ⁶⁴F. Krien and A. Valli, "Parquetlike equations for the Hedin three-leg vertex," *Phys. Rev. B* **100**, 245147 (2019).
- ⁶⁵F. Krien, A. I. Lichtenstein, and G. Rohringer, "Fluctuation diagnostic of the nodal/antinodal dichotomy in the Hubbard model at weak coupling: A parquet dual fermion approach," *Phys. Rev. B* **102**, 235133 (2020).
- ⁶⁶F. Krien, A. Valli, P. Chalupa, M. Capone, A. I. Lichtenstein, and A. Toschi, "Boson-exchange parquet solver for dual fermions," *Phys. Rev. B* **102**, 195131 (2020).
- ⁶⁷F. Krien, A. Kauch, and K. Held, "Tiling with triangles: Parquet and GWy methods unified," *Phys. Rev. Res.* **3**, 013149 (2021).
- ⁶⁸M. Gievers, E. Walter, A. Ge, J. von Delft, and F. B. Kugler, "Multiloop flow equations for single-boson exchange fRG," *Eur. Phys. J. B* **95**, 108 (2022).
- ⁶⁹K. Fraboulet, S. Heinzlmann, P. M. Bonetti, A. Al-Eryani, D. Vilardi, A. Toschi, and S. Andergassen, "Single-boson exchange functional renormalization group application to the two-dimensional Hubbard model at weak coupling," *Eur. Phys. J. B* **95**, 202 (2022).
- ⁷⁰J. R. Cash and A. H. Karp, "A variable order Runge-Kutta method for initial value problems with rapidly varying right-hand sides," *ACM Trans. Math. Software* **16**, 201–222 (1990).
- ⁷¹C. Honerkamp, D. Rohe, S. Andergassen, and T. Enss, "Interaction flow method for many-fermion systems," *Phys. Rev. B* **70**, 235115 (2004).
- ⁷²C. Honerkamp and M. Salmhofer, "Temperature-flow renormalization group and the competition between superconductivity and ferromagnetism," *Phys. Rev. B* **64**, 184516 (2001).
- ⁷³B. Schneider, J. Reuther, M. G. Gonzalez, B. Sbierski, and N. Niggemann, "Temperature flow in pseudo-Majorana functional renormalization for quantum spins," *Phys. Rev. B* **109**, 195109 (2024).
- ⁷⁴A. Tagliavini, C. Hille, F. B. Kugler, S. Andergassen, A. Toschi, and C. Honerkamp, "Multiloop functional renormalization group for the two-dimensional Hubbard model: Loop convergence of the response functions," *SciPost Phys.* **6**, 009 (2019).
- ⁷⁵P. Chalupa-Gantner, F. B. Kugler, C. Hille, J. von Delft, S. Andergassen, and A. Toschi, "Fulfillment of sum rules and Ward identities in the multiloop functional renormalization group solution of the Anderson impurity model," *Phys. Rev. Res.* **4**, 023050 (2022).
- ⁷⁶H. Shinaoka, M. Wallerberger, Y. Murakami, K. Nogaki, R. Sakurai, P. Werner, and A. Kauch, "Multiscale space-time ansatz for correlation functions of quantum systems based on quantum tensor trains," *Phys. Rev. X* **13**, 021015 (2023).

- ⁷⁷Y. Núñez Fernández, M. Jeannin, P. T. Dumitrescu, T. Kloss, J. Kaye, O. Parcollet, and X. Waintal, "Learning Feynman diagrams with tensor trains," *Phys. Rev. X* **12**, 041018 (2022).
- ⁷⁸M. K. Ritter, Y. Núñez Fernández, M. Wallerberger, J. von Delft, H. Shinaoka, and X. Waintal, "Quantics tensor cross interpolation for high-resolution parsimonious representations of multivariate functions," *Phys. Rev. Lett.* **132**, 056501 (2024).
- ⁷⁹M. Kitatani, T. Schäfer, H. Aoki, and K. Held, "Why the critical temperature of high- T_c cuprate superconductors is so low: The importance of the dynamical vertex structure," *Phys. Rev. B* **99**, 041115 (2019).
- ⁸⁰D. Vilardi, C. Taranto, and W. Metzner, "Antiferromagnetic and d -wave pairing correlations in the strongly interacting two-dimensional Hubbard model from the functional renormalization group," *Phys. Rev. B* **99**, 104501 (2019).
- ⁸¹P. M. Bonetti, A. Toschi, C. Hille, S. Andergassen, and D. Vilardi, "Single-boson exchange representation of the functional renormalization group for strongly interacting many-electron systems," *Phys. Rev. Res.* **4**, 013034 (2022).
- ⁸²T. Fujii and K. Ueda, "Perturbative approach to the nonequilibrium Kondo effect in a quantum dot," *Phys. Rev. B* **68**, 155310 (2003).
- ⁸³M. K. Ritter *et al.*, *Quanticsci.jl*, 2022.
- ⁸⁴D. Kiese, T. Müller, Y. Iqbal, R. Thomale, and S. Trebst, "Multiloop functional renormalization group approach to quantum spin systems," *Phys. Rev. Res.* **4**, 023185 (2022).
- ⁸⁵D. Kiese, A. Ge, N. Ritz, J. von Delft, and N. Wentzell, "MatsubaraFunctions.jl: An equilibrium Green's function library in the Julia programming language," *SciPost Phys. Codebases* **24** (2024).
- ⁸⁶D. Kiese, A. Ge, N. Ritz, J. von Delft, and N. Wentzell, "Codebase release 0.1 for MatsubaraFunctions.jl," *SciPost Phys. Codebases* **24**-r0.1 (2024).
- ⁸⁷N. Niggemann, *Nilsniggemann/pmfrg.jl: v2.1.9*, 2023.
- ⁸⁸N. Ritz and A. Ge, *KeldyshQFT: A C++ Codebase for real-frequency multiloop functional renormalization group and parquet computations for the single-impurity Anderson model*.

2.7 Digression: Imaginary-frequency QFT in the single boson exchange formalism

Even though the Keldysh formalism provides direct access to real-frequency dynamic correlation functions, traditionally, most thermal quantum field theory calculations have been performed in the widespread *Matsubara formalism*. As introduced in Sec. 1.3.1, there are good practical reasons, from the convenient analytical structure of Matsubara functions to their easier numerical treatment compared to Keldysh functions. Still, the analytic continuation problem (see Sec. 1.3.2) is a major issue for numerical calculations of dynamic correlation functions. However, static quantities, i.e., dynamic functions in the limit $\omega \rightarrow 0$, do *not* require analytic continuation, since the real and imaginary axis of the complex frequency plane intersect at this point. Static quantities thus provide an ideal test case to benchmark a code written in the Keldysh formalism in the zero-frequency limit. For this reason, the codebase presented in Ref. [P2] was extended early on to enable calculations in both the finite temperature and the zero temperature Matsubara formalism. Indeed, corresponding comparisons of static quantities produced by calculations in the Matsubara and Keldysh formalisms were shown in Ref. [P1].

In addition, the Matsubara version of the code could provide a benchmark for the library MATSUBARAFUNCTIONS.JL, developed by our close collaborator Dominik Kiese [P3]. This software library, written in the JULIA programming language, implements optimized data structures to parametrize the discrete Matsubara frequency grids required for general n -point Green's functions in the Matsubara formalism. Furthermore, it provides tested, optimized, and even parallelized implementations of the most commonly used operations performed on Matsubara functions, such as frequency summations, extrapolations of Matsubara sums, and even analytic continuation using Padé approximants. Being set up in a very general way, its purpose is to provide a convenient and user-friendly way to numerically define and work with correlation functions in the Matsubara formalism without having to implement the appropriate data types and basic operations over and over again for every new code.

To test the implementation of MATSUBARAFUNCTIONS.JL, a solution of the parquet equations for the self-energy and vertex, decomposed in terms of the *single boson exchange formalism (SBE)*, was computed using a code written with the MATSUBARAFUNCTIONS.JL library and, independently, with our code written in C++ [P2]. The SBE formalism [Kri19; KV19; KVC19], which we will briefly introduce in the following, is an alternative to the parquet decomposition of the vertex and the subsequent decomposition of its 2PR parts into asymptotic classes, see Secs. 2.3.1 and 2.3.3. Its starting point is the observation that any diagram contributing to the vertex can be classified in terms of its *interaction reducibility* instead of its two-particle reducibility. Any diagram that is 2PR in channel $r \in \{a, p, t\}$ is also called interaction reducible in channel r if it can be disconnected by removing a bare vertex Γ_0 attached to a bubble in channel r (i.e. an object of the type Π_r). All interaction reducible diagrams in channel r are collected into the object ∇_r . These are called *single-boson exchange diagrams* since the bare vertex Γ_0 linking the two parts of the diagram that would be disconnected if removed mediates a single bosonic transfer frequency. Of course, the 2PR vertices γ_r also include diagrams that do not have this property. Those are hence called *multi-boson diagrams* in channel r and abbreviated as M_r , such that one can write $\gamma_r = \nabla_r - \Gamma_0 + M_r$ (the bare interaction Γ_0 is included in ∇_r but not in γ_r). Avoiding over-counting of the bare interaction, the

full vertex Γ is then decomposed as

$$\Gamma = \varphi^{U_{\text{irr}}} + \sum_r \nabla_r - 2\Gamma_0, \quad (2.49)$$

where $\varphi^{U_{\text{irr}}} = R - \Gamma_0 + \sum_r M_r$ is the part of Γ that is interaction irreducible in all three channels r . In the spirit of the parquet decomposition, which allows a classification of all contributing diagrams in terms of two-particle reducibility in each channel r , the vertex can now also be written in a decomposition of interaction reducible and interaction irreducible terms in each channel, $\Gamma = I_r + \gamma_r = T_r + \nabla_r$. Here, $T_r = I_r - \Gamma_0 + M_r$ comprises all interaction irreducible terms in channel r .

Of course, using the above definitions, the parquet equations can be decomposed into interaction reducible and interaction irreducible parts, too. For this, we refer to Refs. [Gie+22; P3]. More important at this point is the observation that the single-boson exchange terms ∇_r can be decomposed even further, writing

$$\nabla_r = \bar{\lambda}_r \bullet \eta_r \bullet \lambda_r, \quad (2.50)$$

with the (in frequency space) three-point *Hedin vertices* [Hed65]

$$\bar{\lambda}_r = \mathbf{1}_r + T_r \circ \Pi_r \circ \mathbf{1}_r \quad (2.51a)$$

$$\lambda_r = \mathbf{1}_r + \mathbf{1}_r \circ \Pi_r \circ T_r, \quad (2.51b)$$

and the *screened interaction* η_r , which is interaction reducible in channel r and, crucially, depends only on a single bosonic transfer frequency. In the preceding equations, the bullet point \bullet denotes contractions over all variables except frequency. For details, especially on how to compute the screened interaction, which is given via a Dyson equation, we refer to Ref. [Gie+22].

The parquet equations can be expressed entirely in terms of SBE objects and hence can be used to determine them self-consistently. The SBE decomposition can be argued to be favorable compared to the parquet decomposition for multiple reasons: First, if the two-particle fluctuations are captured to a large degree by the screened interactions η_r , an accurate numerical description is possible since these objects depend on one frequency only. Second, the SBE formalism enables an approximation beyond the parquet approximation, called the *SBE approximation*. It amounts to setting $R \approx \Gamma_0$ (as in the PA) and neglecting all multi-boson contributions, $M_r = 0$. Through the decomposition of the SBE terms, Eq. (2.50), it can be seen that all remaining objects in this approximation depend on at most two frequencies. This property is again numerically preferential since no genuine four-point objects depending on three independent frequencies, which are hardest to compute in practice, appear anymore. However, the range of applicability of the SBE approximation is still being debated. For example, in a recent study on the X-ray edge problem, it was shown that multi-boson terms already contribute to the leading logarithmic behavior of the dynamic particle-hole susceptibility [Gie+25], rendering the SBE approximation unjustified.

Still, the SBE formalism has by now become popular and has been employed in various recent parquet [KLR20; Kri+20; KKH21; Kie+24] and fRG schemes [Bon+22; Fra+22; Gie+22; Pat+25].

MatsubaraFunctions.jl: An equilibrium Green's function library in the Julia programming language

by

D. Kiese ¹, A. Ge ², N. Ritz ², J. von Delft ², and N. Wentzell¹

¹ Center for Computations Quantum Physics, Flatiron Institute,
162 5th Avenue, New York, NY 10010, USA

² Arnold Sommerfeld Center for Theoretical Physics, Center for NanoScience, and
Munich Center for Quantum Science and Technology,
Ludwig-Maximilians-Universität München, 80333 Munich, Germany

reprinted on pages **82–116**

Reproduced under terms of the [CC-BY license](#).

SciPost Phys. Codebases **24** (2024),

<https://doi.org/10.21468/SciPostPhysCodeb.24>

2024, The Authors, SciPost.

MatsubaraFunctions.jl: An equilibrium Green's function library in the Julia programming language

Dominik Kiese^{1*}, Anxiang Ge², Nepomuk Ritz², Jan von Delft² and Nils Wentzell¹

¹ Center for Computational Quantum Physics, Flatiron Institute,
162 5th Avenue, New York, NY 10010, USA

² Arnold Sommerfeld Center for Theoretical Physics, Center for NanoScience, and Munich
Center for Quantum Science and Technology, Ludwig-Maximilians-Universität München,
80333 Munich, Germany

* dkiese@flatironinstitute.org

Abstract

The Matsubara Green's function formalism stands as a powerful technique for computing the thermodynamic characteristics of interacting quantum many-particle systems at finite temperatures. In this manuscript, our focus centers on introducing `MatsubaraFunctions.jl`, a Julia library that implements data structures for generalized n -point Green's functions on Matsubara frequency grids. The package's architecture prioritizes user-friendliness without compromising the development of efficient solvers for quantum field theories in equilibrium. Following a comprehensive introduction of the fundamental types, we delve into a thorough examination of key facets of the interface. This encompasses avenues for accessing Green's functions, techniques for extrapolation and interpolation, as well as the incorporation of symmetries and a variety of parallelization strategies. Examples of increasing complexity serve to demonstrate the practical utility of the library, supplemented by discussions on strategies for sidestepping impediments to optimal performance.



Copyright D. Kiese *et al.*

This work is licensed under the Creative Commons
[Attribution 4.0 International License](https://creativecommons.org/licenses/by/4.0/).

Published by the SciPost Foundation.

Received 11-10-2023

Accepted 20-12-2023

Published 11-01-2024

doi:[10.21468/SciPostPhysCodeb.24](https://doi.org/10.21468/SciPostPhysCodeb.24)



Check for
updates

This publication is part of a bundle: Please cite both the article and the release you used.

DOI	Type
doi:10.21468/SciPostPhysCodeb.24	Article
doi:10.21468/SciPostPhysCodeb.24-r0.1	Codebase release

Contents

1 Motivation	2
2 Equilibrium Green's functions	3

3	Code structure	4
3.1	Basic types	4
3.2	Accessing and assigning Green's function data	6
3.3	Extrapolation of Matsubara sums	7
3.4	Padé approximants	8
3.5	Automated symmetry reduction	8
3.6	Running in parallel	9
3.7	Performance note	10
4	Examples	10
4.1	Hartree-Fock calculation in the atomic limit	10
4.2	<i>GW</i> calculation in the atomic limit	12
4.3	Multiboson exchange solver for the single impurity Anderson model	15
4.3.1	Single boson exchange decomposition of the parquet equations	16
4.3.2	Implementation in <code>MatsubaraFunctions.jl</code>	18
4.3.3	Benchmark results	22
5	Future directions	26
A	Extrapolation of Matsubara sums	27
B	Implementation details for the MBE solver	28
B.1	SU(2) symmetry	28
B.2	Time translation invariance	28
	References	29

1 Motivation

In condensed matter physics, strongly correlated electrons emerge as paradigmatic examples of quantum many-body systems that defy a description in terms of simple band theory, due to their strong interactions with each other and with the atomic lattice. Their study has led to a cascade of discoveries, ranging from high-temperature superconductivity in copper oxides (*cuprates*) [1, 2] to the Mott metal-insulator transition in various condensed matter systems such as, e.g., transition metal oxides or transition metal chalcogenides [3–5] and the emergence of quantum spin liquids in frustrated magnets [6, 7], to name but a few.

The study of correlated electron systems is equally exciting and challenging, not only because the construction of accurate theoretical models requires the consideration of many different degrees of freedom, such as spin, charge, and orbital degrees of freedom, as well as disorder and frustration, but also because of the scarcity of exactly solvable reference Hamiltonians. The single-band Hubbard model in more than one dimension, for example, has remained at the forefront of computational condensed matter physics for decades, although it in many respects can be regarded as the simplest incarnation of a realistic correlated electron system [8, 9]. It is therefore not surprising that a plethora of different numerical methods have been developed to deal with these models [10].

However, no single algorithm is capable of accurately describing all aspects of these complex systems: each algorithm has its strengths and weaknesses, and the choice of algorithm usually depends on the specific problem under investigation. For example, some algorithms, such as *exact diagonalization* (ED) [11–13] or the *density matrix renormalization*

group (DMRG) [14, 15] are better suited for studying ground-state properties, while others (quantum Monte Carlo (QMC) simulations [16–19], functional renormalization group (fRG) calculations [20–22], ...) perform better when one is interested in dynamic properties such as transport or response functions.

Another popular method, dynamical mean-field theory (DMFT) has been immensely successful; in particular it correctly predicts the Mott transition in the Hubbard model [23]. By approximating the electron self-energy to be local, it however disregards non-local correlation effects, leading to a violation of the Mermin-Wagner theorem [24, 25] as well as a failure to predict the pseudo-gap in the Hubbard model [10]. Non-local (e.g. cluster [26–29] or diagrammatic [30]) extensions of DMFT improve on that front, but are computationally much more expensive. Ultimately, the choice of algorithm is guided by the computational resources available and the trade-off between accuracy and efficiency, as well as by physical insights into which approximations may be justified more than others.

A common motif of many of these algorithms is that they rely on the computation of n -particle *Green's functions*, where usually $n = 1, 2$. Roughly speaking, these functions describe correlations within the physical system of interest, such as its response to an external perturbation. In thermal equilibrium, Green's functions are usually defined as imaginary-time-ordered correlation functions, which allows the use of techniques and concepts from statistical mechanics, such as the partition function and free energy. In Fourier space, the corresponding frequencies take on discrete and complex values. This *Matsubara* formalism is widely used to study strongly correlated electron systems, where it provides a powerful tool for calculating thermodynamic quantities, such as the specific heat and magnetic susceptibility, as well as dynamical properties, such as the electron self-energy and optical conductivity [31, 32].

In this manuscript, we present `MatsubaraFunctions.jl`, a software package written in Julia [33] that implements containers for Green's functions in thermal equilibrium. More specifically, it provides a convenient interface for quickly prototyping algorithms involving multivariable Green's functions of the form $G_{i_1 \dots i_n}(\omega_1, \dots, \omega_m)$, with lattice/orbital indices i_k ($k = 1, \dots, n$) and Matsubara frequencies ω_l ($l = 1, \dots, m$). In an attempt to mitigate monolithic code design and superfluous code reproduction, our goal is to promote a common interface between algorithms where these types of functions make up the basic building blocks. We implement this interface in Julia, since some more recently developed methods, such as the pseudofermion [34–41] and pseudo-Majorana fRG [42–45], seem to have been implemented in Julia as the preferred programming language. In the spirit of similar software efforts, such as the TRIQS library for C++ [46], this package therefore aims to provide a common foundation for these and related codes in Julia that is fast enough to facilitate large-scale computations on high-performance computing architectures [47], while remaining flexible and easy to use.

2 Equilibrium Green's functions

In this section, we give a brief introduction to equilibrium Green's functions and their properties. In its most general form, an imaginary time, n -particle Green's function $G^{(n)}$ is defined as the correlator [48]

$$G_{i_1 \dots i_{2n}}^{(n)}(\tau_1, \dots, \tau_{2n}) = \langle \hat{T} c_{i_1}^\dagger(\tau_1) c_{i_2}(\tau_2) \dots c_{i_{2n-1}}^\dagger(\tau_{2n-1}) c_{i_{2n}}(\tau_{2n}) \rangle, \quad (1)$$

where \hat{T} is the imaginary-time-ordering operator and $\langle \hat{O} \rangle = \frac{1}{Z} \text{Tr}(e^{-\beta \hat{\mathcal{H}}} \hat{O})$ denotes the thermal expectation value of an operator \hat{O} with respect to the Hamiltonian $\hat{\mathcal{H}}$ at temperature $T = 1/\beta$. Note that natural units are used throughout, in particular we set $k_B \equiv 1$. Here, $c^{(\dagger)}$ are fermionic or bosonic creation and annihilation operators and $Z = \text{Tr}(e^{-\beta \hat{\mathcal{H}}})$ is the partition function. The indices i_k represent additional degrees of freedom such as lattice site, spin and

orbital index. In order for the right-hand side in Eq. (1) to be well defined, it is necessary to restrict the τ arguments to an interval of length β , as can be seen, for example, from a spectral (*Lehmann*) representation of the expectation value [48]. Furthermore, the cyclicity of the trace implies that the field variables are anti-periodic in β for fermions, or periodic in β for bosons, respectively. This allows us to define their Fourier series expansion

$$c_i(\tau) = \frac{1}{\beta} \sum_{\nu_k} c_{i,k} e^{-i\nu_k \tau}, \quad \bar{c}_i(\tau) = \frac{1}{\beta} \sum_{\nu_k} \bar{c}_{i,k} e^{i\nu_k \tau}, \quad (2)$$

$$c_{i,k} = \int_0^\beta d\tau c_i(\tau) e^{i\nu_k \tau}, \quad \bar{c}_{i,k} = \int_0^\beta d\tau \bar{c}_i(\tau) e^{-i\nu_k \tau}, \quad (3)$$

where $\nu_k = \frac{\pi}{\beta} \begin{cases} 2k+1, \\ 2k, \end{cases}$ with $k \in \mathbb{Z}$ are the fermionic or bosonic Matsubara frequencies.¹

These definitions carry over to the n -particle Green's function $G^{(n)}$, giving

$$G_{i_1 \dots i_{2n}}^{(n)}(\tau_1, \dots, \tau_{2n}) = \frac{1}{\beta} \sum_{\nu_1} e^{i\nu_1 \tau_1} \dots \frac{1}{\beta} \sum_{\nu_{2n}} e^{-i\nu_{2n} \tau_{2n}} G_{i_1 \dots i_{2n}}^{(n)}(\nu_1, \dots, \nu_{2n}), \quad (4)$$

$$G_{i_1 \dots i_{2n}}^{(n)}(\nu_1, \dots, \nu_{2n}) = \int_0^\beta d\tau_1 e^{-i\nu_1 \tau_1} \dots \int_0^\beta d\tau_{2n} e^{i\nu_{2n} \tau_{2n}} G_{i_1 \dots i_{2n}}^{(n)}(\tau_1, \dots, \tau_{2n}). \quad (5)$$

3 Code structure

`MatsubaraFunctions.jl` is an open-source project distributed via Github [49] and licensed under the MIT license. Using Julia's built-in package manager, the code can be easily installed using

```
1 $ julia
2 julia> ]
3 pkg> add https://github.com/dominikkiese/MatsubaraFunctions.jl
```

from the terminal. Here, `]` activates the package manager from the Julia REPL, where `add` downloads the code and its dependencies. The following is an overview of the functionality of the package, starting with a discussion of its basic types and how to use them. A full documentation of the package is available from the github repository.

3.1 Basic types

The package evolves around three concrete Julia types: `MatsubaraFrequency`, `MatsubaraGrid` and `MatsubaraFunction`. A Matsubara frequency can be either fermionic or bosonic, that is, $\nu_k = \frac{\pi}{\beta}(2k+1)$ or $\nu_k = \frac{2\pi}{\beta}k$. For a given temperature $T = 1/\beta$ and Matsubara index k they can be constructed using

```
1 v = MatsubaraFrequency(T, k, Fermion)
2 w = MatsubaraFrequency(T, k, Boson)
```

Basic arithmetic operations on these objects include addition, subtraction and sign reversal, each of which creates a new `MatsubaraFrequency` instance.

¹This way, $e^{i\beta\nu_k} = -1$ for fermions and $e^{i\beta\nu_k} = +1$ for bosons such that anti-periodicity or periodicity, respectively, of $c_i(\tau)$ are ensured.

```

1 v1 = v + v # type(v1) = :Boson
2 v2 = w - v # type(v2) = :Fermion
3 v3 = -v    # type(v3) = :Fermion

```

MatsubaraGrids are implemented as sorted collections of uniformly (and symmetrically) spaced Matsubara frequencies. To construct them, users need only specify the temperature, number of positive frequencies, and the particle type.

```

1 T = 1.0
2 N = 128
3 g1 = MatsubaraGrid(T, N, Fermion) # total no. frequencies is 2N
4 g2 = MatsubaraGrid(T, N, Boson)   # total no. frequencies is 2N - 1

```

Note that the bosonic Matsubara frequency at zero is included in the positive frequency count. Grid instances are iterable

```

1 for v in g1
2   println(value(v))
3   println(index(v))
4 end

```

and can be evaluated using either a MatsubaraFrequency or Float64 as input.

```

1 idx = rand(eachindex(g1))
2 @assert g1(g1[idx]) == idx
3 @assert g1(value(g1[idx])) == idx

```

Here, we first select a random linear index `idx` and then evaluate `g1` using either the corresponding Matsubara frequency `g1[idx]` or its value. In the former case, `g1(g1[idx])` returns the corresponding linear index of the frequency in the grid, whereas `g1(value(g1[idx]))` finds the linear index of the closest mesh point.² The package supports storage of grid instances in H5 file format.

```

1 using HDF5
2 file = h5open("save_g1.h5", "w")
3 save_matsubara_grid!(file, "g1", g1)
4 g1p = load_matsubara_grid(file, "g1")
5 close(file)

```

Finally, a `MatsubaraFunction` is a collection of Matsubara grids with an associated tensor structure $G_{i_1 \dots i_n}$ for each point (ν_1, \dots, ν_m) in the Cartesian product of the grids. The indices i_k could, for example, represent lattice sites or orbitals. To construct a `MatsubaraFunction` users need to provide a tuple of `MatsubaraGrid` objects, as well as the dimension of each i_k .

```

1 T = 1.0
2 N = 128
3 g = MatsubaraGrid(T, N, Fermion)
4
5 # 1D grid, rank 1 tensor with index dimension 1 (scalar valued)
6 f1_complex = MatsubaraFunction(g, 1)
7 f1_real    = MatsubaraFunction(g, 1, Float64)
8
9 # 1D grid, rank 1 tensor with index dimension 5 (vector valued)

```

²In both cases the argument must be in bounds, otherwise an exception is thrown.

```

10 f2_complex = MatsubaraFunction(g, 5)
11 f2_real    = MatsubaraFunction(g, 5, Float64)
12
13 # 1D grid, rank 2 tensor with index dimension 5 (matrix valued)
14 f3_complex = MatsubaraFunction(g, (5, 5))
15 f3_real    = MatsubaraFunction(g, (5, 5), Float64)
16
17 # 2D grid, rank 2 tensor with index dimension 5 (matrix valued)
18 f4_complex = MatsubaraFunction((g, g), (5, 5))
19 f4_real    = MatsubaraFunction((g, g), (5, 5), Float64)

```

In addition, a floating point type can be passed to the constructor, which fixes the data type for the underlying multidimensional array.³ Similar to the grids, MatsubaraFunctions can be conveniently stored in H5 format.

```

1 using HDF5
2 file = h5open("save_f1_complex.h5", "w")
3 save_matsubara_function!(file, "f1_complex", f1_complex)
4 f1p = load_matsubara_function(file, "f1_complex")
5 close(file)

```

3.2 Accessing and assigning Green's function data

The library provides two possible ways to access the data of a MatsubaraFunction, using either the bracket (`[]`) or parenthesis (`()`) operator. While the notion of the former is that of a `Base.getindex`, the latter evaluates the MatsubaraFunction for the given arguments in such a way that its behavior is well-defined even for out-of-bounds access. The bracket can be used with a set of MatsubaraFrequency instances and tensor indices i_k , as well as with Cartesian indices for the underlying data array. It returns the value of the data exactly for the given input arguments, throwing an exception if they are not in bounds. In addition, the bracket can be used to assign values to a MatsubaraFunction as shown in the following example.

```

1 y = 0.5
2 T = 1.0
3 N = 128
4 g = MatsubaraGrid(T, N, Fermion)
5 f = MatsubaraFunction(g, 1)
6
7 for v in g
8     # if there is only one index of dimension 1, it does not need
9     # to be specified, i.e. f[v] can be used instead of f[v, 1]
10    # (also works for the '()' operator)
11    f[v] = 1.0 / (im * value(v) - y)
12 end
13
14 # access MatsubaraFunction data
15 v = g[rand(eachindex(g))]
16 println(f[v]) # fast data access, throws error if v is out of bounds

```

When `f` is evaluated using Matsubara frequencies within its grid, it returns the same result as if a bracket was used. However, if the frequencies are replaced by `Float64` values, a multilinear interpolation within the Cartesian product of the grids is performed. If the frequency / float arguments are out of bounds, MatsubaraFunctions falls back to extrapolation. The extrapolation algorithm distinguishes between one-dimensional and multidimensional frequency grids. In the 1D case, an algebraic decay is fitted to the high-frequency tail of

³By default, `ComplexF64` is used.

the `MatsubaraFunction`, which is then evaluated for the given arguments. The functional form of the asymptote is currently restricted to $f(\nu) = \alpha_0 + \frac{\alpha_1}{\nu} + \frac{\alpha_2}{\nu^2}$ (with $\alpha_0, \alpha_1, \alpha_2 \in \mathbb{C}$),⁴ which is motivated by the linear or quadratic decay that physical Green's functions typically exhibit. For multidimensional grids, a constant extrapolation is performed from the boundary. Different modes of evaluation are illustrated in an example below.

```

1 y = 0.5
2 T = 1.0
3 N = 128
4 g = MatsubaraGrid(T, N, Fermion)
5 f = MatsubaraFunction(g, 1)
6
7 for v in g
8     f[v] = 1.0 / (im * value(v) - y)
9 end
10
11 # access MatsubaraFunction data
12 v = g[rand(eachindex(g))]
13 println(f(v))           # fast data access, defined even if v is out of bounds
14 println(f(value(v)))   # slow data access, uses interpolation
15
16 # polynomial extrapolation in 1D, constant term set to 0 (the default)
17 vp = MatsubaraFrequency(T, 256, Fermion)
18 println(f(vp; extrp = ComplexF64(0.0)))

```

3.3 Extrapolation of Matsubara sums

A common task when working with equilibrium Green's functions is the calculation of Matsubara sums $\frac{1}{\beta} \sum_{\nu} f(\nu)$, where we have omitted additional indices of f for brevity. However, typical Green's functions decay rather slowly (algebraically) for large frequencies, which presents a technical difficulty for the accurate numerical calculation of their Matsubara sums: they may require some regulator function to control the convergence⁵ (difficult to implement) and a large number of frequencies to sum over (expensive). In contrast, there exist analytical results for simple functional forms of f even in cases where a straightforward numerical summation fails. `MatsubaraFunctions` provides the `sum_me` function, which can be used to calculate sums over complex-valued $f(\nu)$, if $f(z)$ (with $z \in \mathbb{C}$) decays to zero for large $|z|$ and is representable by a Laurent series in an elongated annulus about the imaginary axis (see App. A for details). An example for its use is shown below. Note that this feature is experimental and its API as well as the underlying algorithm might change in future versions.

```

1 y = 0.5
2 T = 1.0
3 N = 128
4 g = MatsubaraGrid(T, N, Fermion)
5 f = MatsubaraFunction(g, 1)
6
7 for v in g
8     f[v] = 1.0 / (im * value(v) - y)
9 end
10
11 # evaluate the series and compare to analytic result
12 rho(x, T) = 1.0 / (exp(x / T) + 1.0)
13 println(abs(sum_me(f) - (rho(+y, T) - 1.0)))

```

⁴Note that α_0 has to be provided by the user.

⁵For example, a factor $e^{i\nu 0^+}$ might be necessary in cases where f decays linearly in ν .

3.4 Padé approximants

Although the Matsubara formalism provides a powerful tool for the calculation of thermodynamic quantities, it lacks the ability to directly determine, for example, dynamic response functions or transport properties associated with real-frequency Green's functions, which facilitate comparison with experiments. There have been recent advances in the use of real-frequency quantum field theory [50–53], yet the calculation of dynamic real-frequency Green's functions remains a technically challenging endeavor. In many applications, therefore, one resorts to calculations on the imaginary axis and then performs an analytic continuation in the complex upper half-plane to determine observables on the real-frequency axis. The analytic continuation problem is ill-conditioned, because there may be significantly different real-frequency functions describing the same set of complex-frequency data within finite precision. Nevertheless, there has been remarkable progress in the development of numerical techniques such as the maximum entropy method [54–56] or stochastic analytical continuation [57,58]. These methods are particularly useful when dealing with stochastic noise induced by Monte Carlo random sampling. A corresponding implementation in Julia is, for example, provided by the ACFlow toolkit [59]. On the other hand, if the input data are known with a high degree of accuracy (as in the fRG and related approaches), analytic continuation using Padé approximants is a valid alternative. Here, one first fits a rational function to the complex frequency data which is then used as a proxy for the Green's function in the upper half-plane. If the function of interest has simple poles this procedure can already provide fairly accurate results, see e.g. Ref. [60]. In `MatsubaraFunctions` we implement the fast algorithm described in the appendix of Ref. [61], which computes an N -point Padé approximant for a given set of data points $\{(x_i, y_i) | i = 1, \dots, N\}$. A simple example of its use is shown below. Note that it might be necessary to use higher precision floating-point arithmetic to cope with rounding errors in the continued fraction representation used for calculating the Padé approximant.

```

1 # some dummy function
2 as = ntuple(x -> rand{BigFloat}, 4)
3 f(x) = as[1] / (1.0 + as[2] * x / (1.0 + as[3] * x / (1.0 + as[4] * x)))
4
5 # generate sample and compute Padé approximant
6 xdata = Vector{BigFloat}(0.01 : 0.01 : 1.0)
7 ydata = f.(xdata)
8 PA = PadéApprox(xdata, ydata)
9
10 @assert length(coeffs(PA)) == 5
11 @assert PA.(xdata) ≈ ydata

```

3.5 Automated symmetry reduction

In many cases, the numerical effort of computing functions in the Matsubara domain can be drastically reduced by the use of symmetries. For one-particle fermionic Green's functions $G_{i_1 i_2}(\nu)$, for example, complex conjugation implies that $G_{i_1 i_2}(\nu) = G_{i_2 i_1}^*(-\nu)$, relating positive and negative Matsubara frequencies. Our package provides an automated way to compute the set of irreducible `MatsubaraFunction` components,⁶ given a list of one or more symmetries as is illustrated in the following example

```

1 y = 0.5
2 T = 1.0
3 N = 128
4 g = MatsubaraGrid(T, N, Fermion)
5 f = MatsubaraFunction(g, 1)

```

⁶These are all elements of the underlying data array which cannot be mapped to each other by symmetries.

```

6
7 for v in g
8     f[v] = 1.0 / (im * value(v) - y)
9 end
10
11 # complex conjugation acting on Green's function
12 function conj(
13     w :: Tuple{MatsubaraFrequency},
14     x :: Tuple{Int64}
15 ) :: Tuple{Tuple{MatsubaraFrequency}, Tuple{Int64}, MatsubaraOperation}
16
17     return (-w[1],), (x[1],), MatsubaraOperation(sgn = false, con = true)
18 end
19
20 # compute the symmetry group
21 SG = MatsubaraSymmetryGroup([MatsubaraSymmetry{1, 1}(conj)], f)
22
23 # obtain another Green's function by symmetrization
24 function init(
25     w :: Tuple{MatsubaraFrequency},
26     x :: Tuple{Int64}
27 ) :: ComplexF64
28
29     return f[w, x...]
30 end
31
32 InitFunc = MatsubaraInitFunction{1, 1, ComplexF64}(init)
33 h = MatsubaraFunction(g, 1)
34 SG(h, InitFunc)
35 @assert h == f

```

Here, one first constructs an instance of type `MatsubaraSymmetry` by passing a function that maps the input arguments of `f` to new arguments extended by a `MatsubaraOperation`. The latter specifies whether the evaluation of `f` on the mapped arguments should be provided with an additional sign or complex conjugation. Next, the irreducible array elements are computed and an object of type `MatsubaraSymmetryGroup`⁷ is constructed from a vector of symmetries provided by the user. Here, the length of the vector is one (we only considered complex conjugation), but the generalization to multiple symmetries is straightforward (see Ref. [62] for more examples). A `MatsubaraSymmetryGroup` can be called with a `MatsubaraFunction` and an initialization function.⁸ This call will evaluate the `MatsubaraInitFunction` for all irreducible elements of the symmetry group of `f`, writing the result into the data array of `h`. Finally, all symmetry equivalent elements are determined without additional calls to the (costly) initialization function. Symmetry groups can be stored in H5 format as shown below.

```

1 using HDF5
2 file = h5open("save_SG.h5", "w")
3 save_matsubara_symmetry_group!(file, "SG", SG)
4 SGp = load_matsubara_symmetry_group(file, "SG")
5 close(file)

```

3.6 Running in parallel

To simplify code parallelization when using `MatsubaraFunctions.jl`, the package has some preliminary MPI support based on the `MPI.jl` wrapper and illustrated in an example below.

```

1 using MatsubaraFunctions
2 using MPI

```

⁷A `MatsubaraSymmetryGroup` contains all groups of symmetry equivalent elements and the operations needed to map them to each other.

⁸A `MatsubaraInitFunction` takes a tuple of Matsubara frequencies and tensor indices and returns a floating point type.

```

3
4 MPI.Init()
5 mpi_info()
6 mpi_println("I print on main.")
7 ismain = mpi_ismain() # ismain = true if rank is 0
8
9 y = 0.5
10 T = 1.0
11 N = 128
12 g = MatsubaraGrid(T, N, Fermion)
13 f = MatsubaraFunction(g, 1)
14
15 for v in g
16     f[v] = 1.0 / (im * value(v) - y)
17 end
18
19 # simple loop parallelization for UnitRange
20 for vidx in mpi_split(1 : length(g))
21     println("My rank is $(mpi_rank()): $(vidx)")
22 end
23
24 # simple (+) allreduce
25 mpi_allreduce!(f)

```

Calls of `MatsubaraSymmetryGroup` with an initialization function have an opt-in switch (`mode`) to enable parallel evaluation of the `MatsubaraInitFunction` (by default `mode = :serial`). If `mode = :polyester`, shared memory multithreading as provided by the `Polyester` Julia package [63] is used.⁹ This mode is recommended for initialization functions that are cheap to evaluate and are unlikely to benefit from `Threads.@threads` due to the overhead from invoking the Julia scheduler. For more expensive functions, users can choose between `mode = :threads`, which simply uses `Threads.@threads`, and `mode = :hybrid`. The latter combines both MPI and native Julia threads and can therefore be used to run calculations on multiple compute nodes.

3.7 Performance note

By default, types in `MatsubaraFunctions.jl` perform intrinsic consistency checks when they are invoked. For example, when computing the linear index of a `MatsubaraFrequency` in a `MatsubaraGrid`, we make sure that the particle types and temperatures match between the two. While this ensures a robust *modus operandi*, it unfortunately impacts performance, especially for larger projects. To deal with this issue, we have implemented a simple switch, `MatsubaraFunctions.sanity_checks()`, which, when turned off¹⁰ disables `@assert` expressions. It is not recommended to touch this switch until an application has been thoroughly tested, as it leads to wrong results on improper use. For the MBE solver discussed in Sec. 4.3.2, we found runtime improvements of up to 10% when the consistency checks were disabled.

4 Examples

4.1 Hartree-Fock calculation in the atomic limit

As a first example of the use of `MatsubaraFunctions.jl` we consider the calculation of the one-particle Green's function G using the Hartree-Fock (HF) approximation in the atomic limit of the Hubbard model, i.e., we consider the Hamiltonian

$$\hat{\mathcal{H}} = U\hat{n}_\uparrow\hat{n}_\downarrow - \mu(\hat{n}_\uparrow + \hat{n}_\downarrow), \quad (6)$$

⁹Here, the `batchsize` argument can be used to control the number of threads involved.

¹⁰`MatsubaraFunctions.sanity_checks() = false`.

where U denotes the Hubbard interaction and \hat{n}_σ are the density operators for spin up and down. In the following, we fix the chemical potential to $\mu = 0$, i.e., we consider the system in the strongly hole-doped regime.

The Hartree-Fock theory [64–66] is a widespread method in condensed matter physics used to describe, e.g., electronic structures and properties of materials [67, 68]. It is a mean-field approximation as it treats the electrons in a solid as independent particles being subject to an effective background field due to all the other particles.

In an interacting many-body system, the bare Green's function G_0 has to be dressed by self-energy insertions, here denoted by Σ , in order to obtain G , which is summarized in the Dyson equation

$$G = G_0[\mathbb{1} - \Sigma G_0]^{-1} = G_0 + G_0 \Sigma G_0 + G_0 \Sigma G_0 \Sigma G_0 + \dots, \quad (7)$$

where G_0 , G and Σ in general are matrix-valued. In HF theory one only considers the lowest order term contributing to the self-energy, which is linear in the interaction potential. For the spin-rotation invariant single-site system at hand, $\Sigma = \Sigma_\sigma = \Sigma$ and the HF approximation for the self-energy reads

$$\Sigma(\nu) \approx \frac{U}{\beta} \sum_{\nu'} G(\nu') e^{i\nu'0^+} = Un, \quad (8)$$

where n is the density per spin. The Dyson equation then takes the simple form

$$G(\nu) \approx [G_0^{-1}(\nu) - Un]^{-1}. \quad (9)$$

Below, we demonstrate how to set up and solve Eqs. (8) & (9) self-consistently for the density n using Anderson acceleration [69, 70] as provided by the NLSolve Julia package [71] in conjunction with MatsubaraFunctions.jl.

```

1 using MatsubaraFunctions
2 using NLSolve
3
4 const T = 0.3 # temperature
5 const U = 0.9 # interaction
6 const N = 1000 # no. frequencies
7
8 # initialize Green's function container
9 g = MatsubaraGrid(T, N, Fermion)
10 G = MatsubaraFunction(g, 1)
11
12 for v in g
13     G[v] = 1.0 / (im * value(v))
14 end
15
16 # set up fixed-point equation for NLSolve
17 function fixed_point!(F, n, G)
18
19     # calculate G
20     for v in grids(G, 1)
21         G[v] = 1.0 / (im * value(v) - U * n[1])
22     end
23
24     # calculate the residue
25     F[1] = density(G) - n[1]
26
27     return nothing
28 end
29
30 res = nlsolve((F, n) -> fixed_point!(F, n, G), [density(G)], method = :anderson)

```

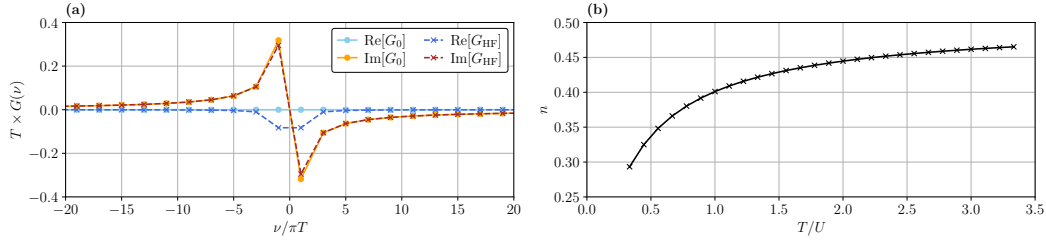


Figure 1: **Exemplary Hartree-Fock results.** (a) Comparison of the bare Green's function G_0 with the HF result G_{HF} for $T/U = \frac{1}{3}$. (b) Hartree-Fock density n as a function of temperature.

Here, we first build the `MatsubaraFunction` container for G and initialize it to $G_0(\nu) = \frac{1}{i\nu}$. This container is then passed to the fixed-point equation using an anonymous function, which mutates G on each call to incorporate the latest estimate of n .¹¹ Fig. 1 shows exemplary results for the full Green's function and HF density. As can be seen from Fig. 1(b) the latter deviates from its bare value $n_0 = \frac{1}{2}$ when the temperature is decreased and approaches $n = 0$ for $T \rightarrow 0$, as expected.

4.2 GW calculation in the atomic limit

In this section, we extend our Hartree-Fock code to include *bubble* corrections¹² in the calculation of the self-energy. The resulting equations, commonly known as the *GW* approximation, allow us to exemplify the use of more advanced library features, such as extrapolation of the single-particle Green's function and the implementation of symmetries. Therefore, they present a good starting point for the more involved application discussed in Sec. 4.3.1.

The *GW* approximation is a widely used method in condensed matter physics and quantum chemistry for calculating electronic properties of materials [72–74]. In addition to the Hartree term $\Sigma_{\text{H}} = Un$, which considers only the bare interaction, the mutual screening of the Coulomb interaction between electrons is partially taken into account. For spin-rotation invariant systems it is common practice to decouple these *screened interactions* η ¹³ into a density (or charge) component η^D and a magnetic (or spin) component η^M (see App. B), such that

$$\Sigma(\nu) \approx \frac{Un}{2} - \frac{1}{\beta} \sum_{\nu'} G(\nu') \left[\frac{1}{4} \eta^D(\nu - \nu') + \frac{3}{4} \eta^M(\nu - \nu') \right], \quad (10)$$

for the atomic limit Hamiltonian. The η are computed by summing a series of bubble diagrams in the particle-hole channel, i.e.,

$$\eta^{D/M}(\Omega) = \frac{\pm U}{1 \mp UP(\Omega)}, \quad (11)$$

where the *polarization bubble* P is given by

$$P(\Omega) = \frac{1}{\beta} \sum_{\nu} G(\Omega + \nu)G(\nu). \quad (12)$$

A diagrammatic representation of these relations is shown in Fig. 2. Finally, the set of equations is closed by computing G from the Dyson equation. Since the Green's function transforms as

¹¹Here, we make use of the `density` function, which calculates the Fourier transform $f(\tau \rightarrow 0^-)$ given a complex-valued input function $f(\nu)$.

¹²That is, Feynman diagrams formed by a closed loop of two single-particle Green's functions.

¹³Here, we denote the screened interactions by η instead of W to avoid conflicting notation with the code examples in Sec. 4.3.2.

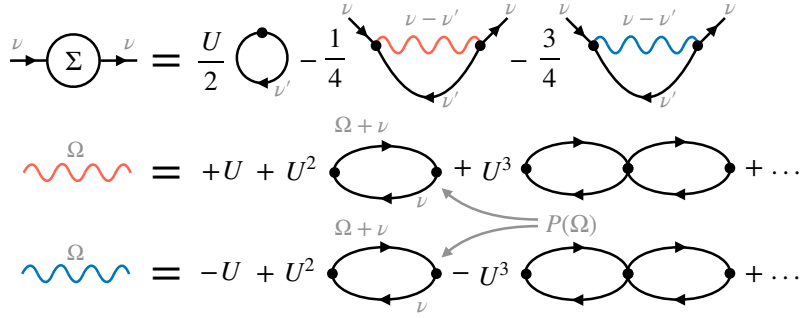


Figure 2: **Diagrammatic representation of spin-conserving GW equations in the atomic limit.** Wavy lines denote the screened interactions in the density (red) and magnetic (blue) channel. They are obtained by dressing the respective bare interactions with a series of bubble diagrams $P(\Omega)$, as illustrated in the second and third line from the top.

$G^*(\nu) = G(-\nu)$ under complex conjugation [48], we also have that

$$\begin{aligned}
 P(-\Omega) &= \frac{1}{\beta} \sum_{\nu} G(-\Omega + \nu)G(\nu) = \frac{1}{\beta} \sum_{\nu} G(-\Omega - \nu)G(-\nu) = \frac{1}{\beta} \sum_{\nu} G^*(\Omega + \nu)G^*(\nu) \\
 &= P^*(\Omega),
 \end{aligned}
 \tag{13}$$

and likewise $\Sigma^*(\nu) = \Sigma(-\nu)$. Thus, the numerical effort for evaluating Eqs. (10) and (12) can be reduced by a factor of two using a `MatsubaraSymmetryGroup` object. To structure the GW code, we first write a solver class which takes care of the proper initialization of the necessary `MatsubaraFunction` instances.

```

1 using MatsubaraFunctions
2 using HDF5
3
4 conj(w, x) = (-w[1],), (x[1],), MatsubaraOperation(sgn = false, con = true)
5
6 struct Gwsolver
7     T      :: Float64
8     U      :: Float64
9     N      :: Int64
10    G      :: MatsubaraFunction{1, 1, 2, ComplexF64}
11    Sigma  :: MatsubaraFunction{1, 1, 2, ComplexF64}
12    P      :: MatsubaraFunction{1, 1, 2, ComplexF64}
13    η_D    :: MatsubaraFunction{1, 1, 2, ComplexF64}
14    η_M    :: MatsubaraFunction{1, 1, 2, ComplexF64}
15    SGf    :: MatsubaraSymmetryGroup
16    SGb    :: MatsubaraSymmetryGroup
17
18    function Gwsolver(T, U, N)
19
20        # fermionic containers
21        gf = MatsubaraGrid(T, N, Fermion)
22        G = MatsubaraFunction(gf, 1)
23        Sigma = MatsubaraFunction(gf, 1)
24
25        # bosonic containers
26        gb = MatsubaraGrid(T, N, Boson)
27        P = MatsubaraFunction(gb, 1)
28        η_D = MatsubaraFunction(gb, 1)
29        η_M = MatsubaraFunction(gb, 1)
30
31        # symmetry groups
32        SGf = MatsubaraSymmetryGroup([MatsubaraSymmetry{1, 1}(conj)], G)
33        SGb = MatsubaraSymmetryGroup([MatsubaraSymmetry{1, 1}(conj)], P)

```

```

34
35     return new(T, U, N, G, Sigma, P, η_D, η_M, SGf, SGb)
36 end
37 end

```

As a second step, we implement the self-consistent equations, which we solve using Anderson acceleration. Note that we have rewritten the GW equation for the self-energy as

$$\Sigma(\nu) \approx U n - \frac{1}{\beta} \sum_{\nu'} G(\nu') \left[\frac{1}{4} \eta^D(\nu - \nu') + \frac{3}{4} \eta^M(\nu - \nu') + \frac{U}{2} \right], \quad (14)$$

which is beneficial since the product of G with the constant contributions to $\eta^{D/M}$ simply shifts the real part of the self-energy by $\frac{U n}{2}$ such that $\Sigma = \Sigma_H + \mathcal{O}(U^2)$.

```

1 function fixed_point!(F, x, S)
2
3     # update Sigma
4     unflatten!(S.Sigma, x)
5
6     # calculate G
7     for v in grids(S.G, 1)
8         S.G[v] = 1.0 / (im * value(v) - S.Sigma[v])
9     end
10
11    sum_grid = MatsubaraGrid(S.T, 4 * S.N, Fermion)
12
13    # calculate P using symmetries
14    function calc_P(wtpl, xtpl)
15
16        P = 0.0
17
18        for v in sum_grid
19            P += S.G(v + wtpl[1]) * S.G(v)
20        end
21
22        return S.T * P
23    end
24
25    S.SGb(S.P, MatsubaraInitFunction{1, 1, ComplexF64}(calc_P))
26
27    # calculate η_D and η_M
28    for w in S.P.grids[1]
29        S.η_D[w] = +S.U / (1.0 - S.U * S.P[w])
30        S.η_M[w] = -S.U / (1.0 + S.U * S.P[w])
31    end
32
33    # calculate Sigma using symmetries
34    function calc_Sigma(wtpl, xtpl)
35
36        Sigma = S.U * density(S.G)
37
38        for v in sum_grid
39            Sigma -= S.T * S.G(v) * (
40                0.25 * S.η_D(wtpl[1] - v; extrp = ComplexF64(+S.U)) +
41                0.75 * S.η_M(wtpl[1] - v; extrp = ComplexF64(-S.U)) +
42                0.50 * S.U)
43        end
44
45        return Sigma
46    end
47
48    S.SGf(S.Sigma, MatsubaraInitFunction{1, 1, ComplexF64}(calc_Sigma))
49
50    # calculate the residue
51    flatten!(S.Sigma, F)
52    F .= x
53

```

```
54 return nothing
55 end
```

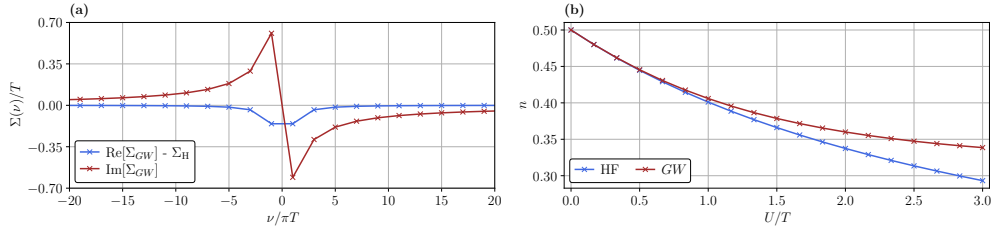


Figure 3: **Exemplary GW results.** (a) The complex-valued self-energy Σ_{GW} with its real part offset by the Hartree shift $\Sigma_H = Un_{GW}$ for $T/U = \frac{1}{3}$. (b) GW and Hartree-Fock densities as a function of U/T .

Here, we make use of the `flatten!` and `unflatten!` functions which allow us to parse `MatsubaraFunction` data into a one dimensional array.¹⁴ The fixed-point can now easily be computed with, for example,

```
1 const T = 0.3 # temperature
2 const U = 0.9 # interaction
3 const N = 1000 # no. frequencies
4
5 S = Gwsolver(T, U, N)
6 init = zeros(ComplexF64, length(S.Sigma))
7 res = nlsolve((F, x) -> fixed_point!(F, x, S), init, method = :anderson, m = 8, beta =
  ↪ 0.5, show_trace = true)
```

In Fig. 3 we show exemplary results for the self-energy and density obtained in *GW*. In contrast to the Hartree-Fock calculations in the previous section, Σ is now a frequency-dependent quantity, whose real part asymptotically approaches Un_{GW} . As can be seen from Fig. 3(b), these *GW* densities agree quantitatively with the HF result for weak interactions $U/T \lesssim \frac{1}{2}$, but yield larger densities for higher values of U as expected when the local interaction is partially screened.

4.3 Multiboson exchange solver for the single impurity Anderson model

Note: Readers who are not interested in the formal discussion presented below should feel free to skip this section and proceed directly to Section 5 on future directions.

In the following, we extend upon the previous computations for the Hubbard atom by coupling the single electronic level to a bath of non-interacting electrons. Specifically, we consider the *single-impurity Anderson model*, a minimal model for localized magnetic impurities in metals introduced by P.W. Anderson to explain the physics behind the Kondo effect [75]. It is defined by the Hamiltonian

$$H = \sum_{\sigma} \epsilon_d d_{\sigma}^{\dagger} d_{\sigma} + Un_{d,\uparrow} n_{d,\downarrow} + \sum_{k,\sigma} (V_k d_{\sigma}^{\dagger} c_{k,\sigma} + V_k^* c_{k,\sigma}^{\dagger} d_{\sigma}) + \sum_{k,\sigma} \epsilon_{k,\sigma} c_{k,\sigma}^{\dagger} c_{k,\sigma}, \quad (15)$$

describing an impurity d level ϵ_d , hybridized with conduction electrons of the metal via a matrix element V_k . The electrons in the localized d state, where $n_{d,\sigma} = d_{\sigma}^{\dagger} d_{\sigma}$, interact according to the interaction strength U , whereas the c electrons of the bath are

¹⁴We also export `flatten` which will allocate a new 1D array from the `MatsubaraFunction`.

non-interacting. Following [76], in a path-integral formulation for the partition function $Z = \int \prod_{\sigma} \mathcal{D}(\bar{d}_{\sigma}) \mathcal{D}(d_{\sigma}) \mathcal{D}(\bar{c}_{k,\sigma}) \mathcal{D}(c_{k,\sigma}) e^{-S}$ with the action $S = \int_0^{\beta} \mathcal{L}(\tau) d\tau$, the Lagrangian for the model is given by

$$\begin{aligned} \mathcal{L}(\tau) = & \sum_{\sigma} \bar{d}_{\sigma}(\tau) (\partial_{\tau} + \epsilon_d) d_{\sigma}(\tau) + \sum_{k,\sigma} \bar{c}_{k,\sigma}(\tau) (\partial_{\tau} + \epsilon_k) c_{k,\sigma}(\tau) \\ & + U n_{\uparrow}(\tau) n_{\downarrow}(\tau) + \sum_{k,\sigma} V_k [\bar{d}_{\sigma}(\tau) c_{k,\sigma}(\tau) + \bar{c}_{k,\sigma}(\tau) d_{\sigma}(\tau)], \end{aligned} \quad (16)$$

where $n_{\sigma}(\tau) = \bar{d}_{\sigma}(\tau) d_{\sigma}(\tau)$. Integrating over the only quadratically occurring Grassmann variables for the bath electrons, one formally obtains $Z = \int \prod_{\sigma} \mathcal{D}(\bar{d}_{\sigma}) \mathcal{D}(d_{\sigma}) e^{-S_{\text{red}}}$ with the reduced action given by

$$S_{\text{red}} = \int_0^{\beta} d\tau \int_0^{\beta} d\tau' \sum_{\sigma} \bar{d}_{\sigma}(\tau) [-G_{\sigma}^{(0)}(\tau - \tau')]^{-1} d_{\sigma}(\tau') + U \int_0^{\beta} d\tau n_{\uparrow}(\tau) n_{\downarrow}(\tau). \quad (17)$$

Switching to Matsubara frequencies as described in section 2, the non-interacting Green's function for the localized d electrons reads

$$G_{\sigma}^{(0)}(\nu_n) = \frac{1}{i\nu_n - \epsilon_d + \Delta(\nu_n)}. \quad (18)$$

Following [77] we choose an isotropic hybridization strength $V_k \equiv V$ and a flat density of states with bandwidth $2D$ for the bath electrons, leading to the hybridization function¹⁵ $\Delta(\nu_n) = i\frac{V^2}{D} \arctan \frac{D}{\nu_n}$. In the following, we set $V = 2$, measure energy in units of $V/2 = 1$ and set the half bandwidth to $D = 10$. In the context of this work, we focus on the particle-hole symmetric model, setting $\epsilon_d = -U/2$. Then, the Hartree term of the self-energy, $\Sigma_{\text{H}} = U/2$ is conveniently absorbed into the bare propagator,

$$G_{\sigma}^{(0)}(\nu_n) \rightarrow G_{\sigma}^{\text{H}}(\nu_n) = \frac{1}{i\nu_n - \epsilon_d + \Delta(\nu_n) - \Sigma_{\text{H}}} = \frac{1}{i\nu_n + \Delta(\nu_n)}. \quad (19)$$

Consequently, the Hartree propagator is used instead of the bare propagator throughout.

4.3.1 Single boson exchange decomposition of the parquet equations

Following [78], we now reiterate the single-boson exchange (SBE) decomposition of the four-point vertex and, subsequently, of the parquet equations. The starting point for the SBE decomposition, which was originally developed in [79–84], is the unambiguous classification of vertex diagrams according to their U -reducibility in each channel. In order to introduce this concept in the context of the parquet equations, we first have to discuss the similar concept of two-particle reducibility, which provides the basis for the parquet decomposition of the vertex,

$$\Gamma = \Lambda_{2\text{PI}} + \gamma_a + \gamma_p + \gamma_t. \quad (20)$$

This decomposition states that all diagrams which contribute to the two-particle vertex Γ can be classified as being part of one of four disjoint contributions: γ_r with $r \in \{a, p, t\}$ collects those diagrams which are two-particle reducible (2PR) in channel r , i.e., they can be disconnected by cutting a pair of propagator lines, which can either be aligned in an antiparallel (a), parallel (p) or transverse antiparallel (t) way. All remaining diagrams, which are not 2PR in either of the three channels, contribute to $\Lambda_{2\text{PI}}$, the fully two-particle irreducible (2PI) vertex. One can equally well decompose Γ w.r.t. its two-particle reducibility in one of the three channels,

¹⁵Note that we use a different sign convention for the hybridization function compared to [77].

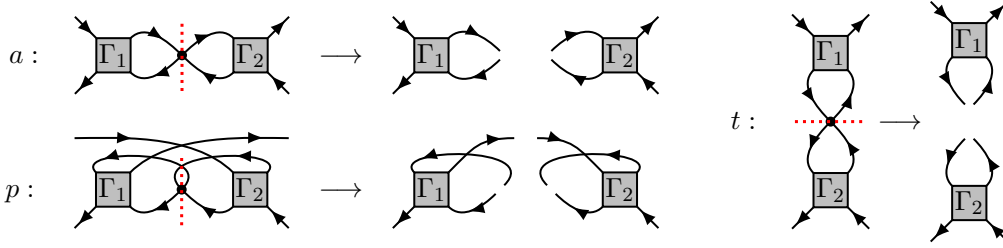


Figure 4: **Illustration of U -reducibility in the three two-particle channels a , p and t .** The Figure is analogous to Fig. 4 of [80] and adapted from [78]. Γ_1 and Γ_2 can be any vertex diagram or the unit vertex.

$\Gamma = I_r + \gamma_r$, which defines $I_r = \Lambda_{2\text{PI}} + \sum_{r' \neq r} \gamma_{r'}$, collecting all diagrams that are 2PI in channel r . The Bethe-Salpeter equations (BSEs) then relate the reducible diagrams to the irreducible ones,

$$\gamma_r = I_r \circ \Pi_r \circ \Gamma = \Gamma \circ \Pi_r \circ I_r. \quad (21)$$

This short-hand notation introduces the Π_r bubble, i.e., the propagator pair connecting the two vertices, see [78] for their precise channel-dependent definition, as well as for the connector symbol \circ , which channel-dependently denotes summation over internal frequencies and quantum numbers. The self-energy Σ , which enters the propagator via the Dyson equation $G = G_0 + G_0 \Sigma G$, is provided by the Schwinger-Dyson equation (SDE),

$$\Sigma = -\left(U + U \circ \Pi_p \circ \Gamma\right) \cdot G = -\left(U + \frac{1}{2}U \circ \Pi_a \circ \Gamma\right) \cdot G, \quad (22)$$

where U is the bare interaction and the symbol \cdot denotes the contraction of two vertex legs with a propagator. Together, equations (20), (21) and (22) are known as the *parquet equations* [85, 86] and can be solved self-consistently, if the 2PI vertex $\Lambda_{2\text{PI}}$ is provided [87–90]. Unfortunately, $\Lambda_{2\text{PI}}$ is the most complicated object, as its contributions contain nested contractions over internal arguments. Often, the parquet approximation (PA) is therefore employed, which truncates $\Lambda_{2\text{PI}}$ beyond the bare interaction U . In the context of the SBE decomposition relevant to this work, U -reducibility is an alternative criterion to the concept of two-particle reducibility for the classification of vertex diagrams. A diagram that is 2PR in channel r is also said to be U -reducible in channel r if it can be disconnected by removing one bare vertex that is attached to a Π_r bubble, as illustrated in Fig. 4. Furthermore, the bare vertex U is defined to be U -reducible in all three channels. The U -reducible diagrams in channel r are in the following denoted ∇_r and are said to describe *single-boson exchange* processes, as the linking bare interaction U , which would disconnect the diagram if cut, mediates just a single bosonic transfer frequency. The diagrams which are 2PR in channel r but not U -reducible in channel r are called multi-boson exchange diagrams and denoted M_r . With these classifications, the two-particle reducible vertices can be written as $\gamma_r = \nabla_r - U + M_r$, making sure to exclude U , which is contained in ∇_r but not in γ_r . The parquet decomposition (20) yields in this language,

$$\Gamma = \varphi^{U\text{irr}} + \sum_r \nabla_r - 2U, \quad \varphi^{U\text{irr}} = \Lambda_{2\text{PI}} - U + \sum_r M_r, \quad (23)$$

where $\varphi^{U\text{irr}}$ is the fully U -irreducible part of Γ . For a diagrammatic illustration of the first equation, see Fig. 8 in [78]. The channel-dependent decomposition of the vertex $\Gamma = I_r + \gamma_r = \nabla_r + T_r$ can also be split into U -reducible and U -irreducible parts in channel r , defining the U -irreducible remainder $T_r = I_r - U + M_r$ in channel r . Inserting all these definitions into the BSEs (21) and separating U -reducible and U -irreducible contributions gives the two sets of equations,

$$\nabla_r - U = I_r \circ \Pi_r \circ \nabla_r + U \circ \Pi_r \circ T_r = \nabla_r \circ \Pi_r \circ I_r + T_r \circ \Pi_r \circ U, \quad (24)$$

$$M_r = (I_r - U) \circ \Pi_r \circ T_r = T_r \circ \Pi_r \circ (I_r - U), \quad (25)$$

for each channel r . From equation (24) one can derive (see [78] for details) that the single-boson exchange terms can be written as $\nabla_r = \tilde{\lambda}_r \cdot \eta_r \cdot \lambda_r$, where $\tilde{\lambda}_r, \lambda_r$ denote the *Hedin vertices* [72] and η_r the screened interaction in channel r . The former are related to the U -irreducible vertex in channel r via $\tilde{\lambda}_r = \mathbf{1}_r + T_r \circ \Pi_r \circ \mathbf{1}_r = \mathbf{1}_r + \mathbf{1}_r \circ \Pi_r \circ T_r$ and can be understood as U -irreducible, amputated parts of three-point functions, as they depend on only two frequencies. In contrast to the GW approximation discussed in Sec. 4.2, the screened interaction η_r is now defined in terms of a Dyson equation, $\eta_r = U + U \cdot P_r \cdot \eta_r = U + \eta_r \cdot P_r \cdot U$, with the polarization $P_r = \lambda_r \circ \Pi_r \circ \mathbf{1}_r = \mathbf{1}_r \circ \Pi_r \circ \tilde{\lambda}_r$ dressed by vertex corrections. In the previous expressions, the connector \cdot denotes an internal summation similar to \circ , the only difference being that summation over frequencies is excluded. The corresponding unit vertex is denoted $\mathbf{1}_r$.

Lastly, one can rewrite the SDE in terms of the screened interaction and the Hedin vertex in channel r which yields, for example, $-\Sigma = (\eta_p \cdot \lambda_p) \cdot G = (\tilde{\lambda}_p \cdot \eta_p) \cdot G$ if one chooses $r = p$.

In summary, the SBE-equations to be solved read

$$\eta_r = U + U \cdot P_r \cdot \eta_r = U + \eta_r \cdot P_r \cdot U, \quad (26a)$$

$$P_r = \lambda_r \circ \Pi_r \circ \mathbf{1}_r = \mathbf{1}_r \circ \Pi_r \circ \tilde{\lambda}_r, \quad (26b)$$

$$\tilde{\lambda}_r = \mathbf{1}_r + T_r \circ \Pi_r \circ \mathbf{1}_r, \quad (26c)$$

$$\lambda_r = \mathbf{1}_r + \mathbf{1}_r \circ \Pi_r \circ T_r, \quad (26d)$$

$$T_r = \Gamma - \tilde{\lambda}_r \cdot \eta_r \cdot \lambda_r, \quad (26e)$$

$$\Gamma = \varphi^{U_{\text{irr}}} + \sum_r \tilde{\lambda}_r \cdot \eta_r \cdot \lambda_r - 2U, \quad (26f)$$

$$\varphi^{U_{\text{irr}}} = \Lambda_{2\text{PI}} - U + \sum_r M_r, \quad (26g)$$

$$M_r = (T_r - M_r) \circ \Pi_r \circ T_r = T_r \circ \Pi_r \circ (T_r - M_r), \quad (26h)$$

$$-\Sigma = (\eta_p \cdot \lambda_p) \cdot G = (\tilde{\lambda}_p \cdot \eta_p) \cdot G. \quad (26i)$$

As before, they require only the fully two-particle irreducible vertex $\Lambda_{2\text{PI}}$ as an input. Notably, if one employs the so-called SBE approximation [80], which amounts to setting $\Lambda_{2\text{PI}} = U$ as in the parquet approximation *and* neglecting multi-boson exchange contributions $M_r = 0$, all objects involved depend on at most two frequencies. This scheme is therefore numerically favorable compared to the PA if the SBE approximation can be justified [91]. In the context of this paper, we do not employ the SBE approximation, but include multi-boson exchange (MBE) contributions.

4.3.2 Implementation in MatsubaraFunctions.jl

In this section, we present the implementation of the PA in its MBE formulation using `MatsubaraFunctions.jl`. In doing so, we build upon the code structure developed in Sec. 4.2, i.e. we first define a solver class for which we later implement the self-consistent equations, as well as an interface to solve for the fixed point using Anderson acceleration, see Fig. 5. In order to keep the discussion concise, we refrain from showing all of the code and, instead, focus on computational bottlenecks and point out tricks to circumvent them. For completeness, however, we also make the entire code available via an open-source repository on Github, see Ref. [62] and provide additional implementation details in App. B.

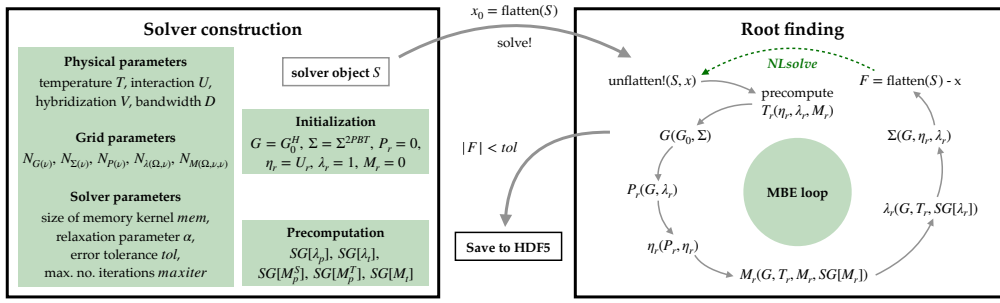


Figure 5: **Structure of the MBE code.** First, an instance S of type `MBESolver` is constructed by passing the SIAM parameters T , U , V and D and the sizes for the Matsubara grids. The self-energy Σ is initialized using second order perturbation theory (PT2), while all other MatsubaraFunctions are set to their bare values. In an optional step, MatsubaraSymmetryGroups for λ_r and M_r (here denoted by SG) can be precomputed. Next, the `solve!` function is used to find the fixed-point of the MBE equations using Anderson acceleration. To interface with `NLsolve`, the fields Σ , η_r , λ_r and M_r of S (which are sufficient to determine all other involved quantities) are flattened into a single one-dimensional array. After convergence, S is finally written to disk in H5 file format.

Extending the `GWsolver` from Sec. 4.2 to the `MBESolver` needed here is a straightforward endeavor, since we just have to add containers and symmetry groups for the Hedin and multi-boson vertices. Furthermore, we extend the solver to include buffers which store the result of evaluating Eqs. (26c), (26d) and (26h), such that repetitive allocations of the multidimensional data arrays for λ_r and M_r are avoided. Note that, due to the symmetries of the SIAM studied here, it suffices to include either λ_r or $\bar{\lambda}_r$, since $\lambda_r = \bar{\lambda}_r$. In addition, all containers can be implemented as real-valued.¹⁶

```

1 function calc_T(
2     w :: MatsubaraFrequency,
3     v :: MatsubaraFrequency,
4     vp :: MatsubaraFrequency,
5     η_S :: MatsubaraFunction{1, 1, 2, Float64},
6     λ_S :: MatsubaraFunction{2, 1, 3, Float64},
7     η_D :: MatsubaraFunction{1, 1, 2, Float64},
8     λ_D :: MatsubaraFunction{2, 1, 3, Float64},
9     η_M :: MatsubaraFunction{1, 1, 2, Float64},
10    λ_M :: MatsubaraFunction{2, 1, 3, Float64},
11    M_S :: MatsubaraFunction{3, 1, 4, Float64},
12    M_T :: MatsubaraFunction{3, 1, 4, Float64},
13    M_D :: MatsubaraFunction{3, 1, 4, Float64},
14    M_M :: MatsubaraFunction{3, 1, 4, Float64},
15    U :: Float64,
16    :: Type{ch_D}
17 ) :: Float64
18
19 # bare contribution
20 T = -2.0 * U
21
22 # SBE contributions
23 w1 = w + v + vp
24 η1_idx = MatsubaraFunctions.grid_index_extrp(w1, grids(η_D, 1))
25 λ1_idx1 = MatsubaraFunctions.grid_index_extrp(w1, grids(λ_D, 1))
26 λ1_idx2 = MatsubaraFunctions.grid_index_extrp(vp, grids(λ_D, 2))

```

¹⁶The Green's function G and the self-energy Σ are purely imaginary, such that $G = -i\tilde{G}$ and $\Sigma = -i\tilde{\Sigma}$. After plugging this factorization into Eqs. (26a)-(26i), all factors of i are cancelled out such that the resulting equations are entirely real.

```

27  λ1_idx3 = MatsubaraFunctions.grid_index_extrp( v, grids(λ_D, 2))
28
29  w2      = vp - v
30  v2      = w + v
31  η2_idx  = MatsubaraFunctions.grid_index_extrp(w2, grids(η_D, 1))
32  λ2_idx1 = MatsubaraFunctions.grid_index_extrp(w2, grids(λ_D, 1))
33  λ2_idx2 = MatsubaraFunctions.grid_index_extrp(v2, grids(λ_D, 2))
34
35  T += +0.5 * λ_S[λ1_idx1, λ1_idx2, 1] * η_S[η1_idx, 1] * λ_S[λ1_idx1, λ1_idx3, 1]
36  T += -0.5 * λ_D[λ2_idx1, λ1_idx3, 1] * η_D[η2_idx, 1] * λ_D[λ2_idx1, λ2_idx2, 1]
37  T += -1.5 * λ_M[λ2_idx1, λ1_idx3, 1] * η_M[η2_idx, 1] * λ_M[λ2_idx1, λ2_idx2, 1]
38
39  # MBE contributions
40  w_idx  = MatsubaraFunctions.grid_index_extrp( w, grids(M_S, 1))
41  v_idx  = MatsubaraFunctions.grid_index_extrp( v, grids(M_S, 2))
42  vp_idx = MatsubaraFunctions.grid_index_extrp(vp, grids(M_S, 2))
43
44  w1_idx = MatsubaraFunctions.grid_index_extrp(w1, grids(M_S, 1))
45  w2_idx = MatsubaraFunctions.grid_index_extrp(w2, grids(M_S, 1))
46  v2_idx = MatsubaraFunctions.grid_index_extrp(v2, grids(M_S, 2))
47
48  T += M_D[w_idx, v_idx, vp_idx, 1]
49  T += +0.5 * M_S[w1_idx, v_idx, vp_idx, 1]
50  T += +1.5 * M_T[w1_idx, v_idx, vp_idx, 1]
51  T += -0.5 * M_D[w2_idx, v_idx, v2_idx, 1]
52  T += -1.5 * M_M[w2_idx, v_idx, v2_idx, 1]
53
54  return T
55 end

```

Profiling the MBE code reveals that most of the time is spent calculating the irreducible vertices T_r , which are needed to compute both λ_r and M_r . In the former case, two legs of T_r are closed with a propagator bubble, while in the latter case, T_r enters both to the left and to the right of the respective (Bethe-Salpeter-like) equation. When optimizing the code, it is therefore crucial to find an efficient way to evaluate Eq. (26e). In the example above, an exemplary implementation of T_r in the density channel is shown. Here, we make use of the `grid_index_extrp` function, which given a Matsubara frequency and a grid g finds the linear index of the frequency in g or, if it is out of bounds, determines the bound of g that is closest. This function is normally used internally to perform constant extrapolation for `MatsubaraFunction` objects with grid dimension greater than one.¹⁷ Here, however, it can be used to precompute multiple linear indices at once, allowing us to exclusively use the `[]` operator and thus avoid unnecessary boundary checks. Note that we could have used tailfits for the screened interactions η_r , but opt to utilize constant extrapolation instead.¹⁸

Furthermore, when T_r is inserted into the equations for the Hedin and multiboson vertices, it is summed up along one fermionic axis. Therefore, some frequencies, e.g. $w_1 = w + v + vp$ in line 23 of the code snippet above, will assume the same value for many different external arguments. Hence, to circumvent repeated (but superfluous) `grid_index_extrp` calls, it is beneficial to precompute T_r on a finite grid, which needs to be large enough to maintain the desired accuracy. To this end, we add buffers for the irreducible vertices to our solver class, such that we can compute e.g. the density T^D and magnetic contributions T^M inplace and in parallel, as shown in the example below.

```

1 function calc_T_ph!(
2   T_D :: MatsubaraFunction{3, 1, 4, Float64},
3   T_M :: MatsubaraFunction{3, 1, 4, Float64},
4   η_S :: MatsubaraFunction{1, 1, 2, Float64},
5   λ_S :: MatsubaraFunction{2, 1, 3, Float64},

```

¹⁷Therefore it is not exported into the global namespace.

¹⁸Since η_r depends only on one frequency argument, it can be stored on a rather large grid, such that its asymptotic behavior is well-captured even without polynomial extrapolation.

```

6  η_D :: MatsubaraFunction{1, 1, 2, Float64},
7  λ_D :: MatsubaraFunction{2, 1, 3, Float64},
8  η_M :: MatsubaraFunction{1, 1, 2, Float64},
9  λ_M :: MatsubaraFunction{2, 1, 3, Float64},
10 M_S :: MatsubaraFunction{3, 1, 4, Float64},
11 M_T :: MatsubaraFunction{3, 1, 4, Float64},
12 M_D :: MatsubaraFunction{3, 1, 4, Float64},
13 M_M :: MatsubaraFunction{3, 1, 4, Float64},
14 U   :: Float64
15 )   :: Nothing
16
17 Threads.@threads for vp in grids(T_D, 3)
18   λ1_idx2 = MatsubaraFunctions.grid_index_extrp(vp, grids(λ_D, 2))
19   vp_idx  = MatsubaraFunctions.grid_index_extrp(vp, grids(M_S, 2))
20
21   for v in grids(T_D, 2)
22     w2 = vp - v
23     λ1_idx3 = MatsubaraFunctions.grid_index_extrp(v, grids(λ_D, 2))
24     η2_idx  = MatsubaraFunctions.grid_index_extrp(w2, grids(η_D, 1))
25     λ2_idx1 = MatsubaraFunctions.grid_index_extrp(w2, grids(λ_D, 1))
26     v_idx   = MatsubaraFunctions.grid_index_extrp(v, grids(M_S, 2))
27     w2_idx  = MatsubaraFunctions.grid_index_extrp(w2, grids(M_S, 1))
28
29     for w in grids(T_D, 1)
30       w1 = w + v + vp
31       v2 = w + v
32       η1_idx = MatsubaraFunctions.grid_index_extrp(w1, grids(η_D, 1))
33       λ1_idx1 = MatsubaraFunctions.grid_index_extrp(w1, grids(λ_D, 1))
34       λ2_idx2 = MatsubaraFunctions.grid_index_extrp(v2, grids(λ_D, 2))
35       w_idx  = MatsubaraFunctions.grid_index_extrp(w, grids(M_S, 1))
36       w1_idx = MatsubaraFunctions.grid_index_extrp(w1, grids(M_S, 1))
37       v2_idx = MatsubaraFunctions.grid_index_extrp(v2, grids(M_S, 2))
38
39       # compute SBE vertices
40       p1 = λ_S[λ1_idx1, λ1_idx2, 1] * η_S[η1_idx, 1] * λ_S[λ1_idx1, λ1_idx3, 1]
41       p2 = λ_D[λ2_idx1, λ1_idx3, 1] * η_D[η2_idx, 1] * λ_D[λ2_idx1, λ2_idx2, 1]
42       p3 = λ_M[λ2_idx1, λ1_idx3, 1] * η_M[η2_idx, 1] * λ_M[λ2_idx1, λ2_idx2, 1]
43
44       # compute MBE vertices
45       m1 = M_S[w1_idx, v_idx, vp_idx, 1]
46       m2 = M_T[w1_idx, v_idx, vp_idx, 1]
47       m3 = M_D[w2_idx, v_idx, v2_idx, 1]
48       m4 = M_M[w2_idx, v_idx, v2_idx, 1]
49
50       T_D[w, v, vp] = -2.0 * U + M_D[w_idx, v_idx, vp_idx, 1] + 0.5 * (p1 + m1 -
↪ p2 - m3) + 1.5 * (m2 - p3 - m4)
51       T_M[w, v, vp] = +2.0 * U + M_M[w_idx, v_idx, vp_idx, 1] - 0.5 * (p1 + m1 +
↪ p2 + m3) + 0.5 * (m2 + p3 + m4)
52     end
53   end
54 end
55
56 return nothing
57 end

```

Here, we also make use of the fact that many frequency arguments (and their respective linear indices) are shared between different channels, which speeds up the calculation of T even further. The implementation of, say, Eq. (26h) is now rather straightforward. M^D , for example, can be computed as shown below.

```

1 function calc_M!(
2   M   :: MatsubaraFunction{3, 1, 4, Float64},
3   Pi  :: MatsubaraFunction{2, 1, 3, Float64},
4   T   :: MatsubaraFunction{3, 1, 4, Float64},
5   M_D :: MatsubaraFunction{3, 1, 4, Float64},
6   SG  :: MatsubaraSymmetryGroup,
7   )   :: Type{ch_D}
8
9

```

```

10  # model the diagram
11  function f(wtpl, xtpl)
12
13      w, v, vp = wtpl
14      val      = 0.0
15      v1, v2   = grids(Pi, 2)(grids(T, 3)[1]), grids(Pi, 2)(grids(T, 3)[end])
16      Pi_slice = view(Pi, w, v1 : v2)
17      M_D_slice = view(M_D, w, v, :)
18      T_L_slice = view(T, w, v, :)
19      T_R_slice = view(T, w, vp, :)
20
21      v1 = grids(T, 3)(grids(M_D, 3)[1])
22      vr = grids(T, 3)(grids(M_D, 3)[end])
23
24      for i in 1 : v1 - 1
25          val -= (T_L_slice[i] - M_D_slice[1]) * Pi_slice[i] * T_R_slice[i]
26      end
27
28      for i in v1 : vr
29          val -= (T_L_slice[i] - M_D_slice[i - v1 + 1]) * Pi_slice[i] * T_R_slice[i]
30      end
31
32      for i in vr + 1 : length(T_L_slice)
33          val -= (T_L_slice[i] - M_D_slice[vr - v1 + 1]) * Pi_slice[i] * T_R_slice[i]
34      end
35
36      return temperature(M) * val
37  end
38
39  # compute multiboson vertex
40  SG(M, MatsubaraInitFunction{3, 1, Float64}(f); mode = :hybrid)
41
42  return nothing
43 end

```

Here, we utilize the corresponding `MatsubaraSymmetryGroup` object with the hybrid MPI + Threads parallelization scheme. In addition, we make use of views for the bubble and vertices to avoid repeated memory lookups in the Matsubara summation.

4.3.3 Benchmark results

In this section, we benchmark the presented implementation of the MBE parquet solver against an independent implementation in C++. Our motivation for this comparison is twofold: Firstly, we want to verify the overall correctness of both implementations and, secondly, we want to test how robust the multiboson formalism is to implementation details. This regards, for example, the treatment of correlation functions at the boundaries of their respective frequency grids. While the Julia code relies on (polynomial or constant) extrapolation, the C++ code replaces correlators with their asymptotic value instead. Ideally, these details should be irrelevant, except in the most difficult parameter regimes. Both codes used the physical parameters as stated after Eq. (18) and the frequency parameters according to Tab. 1. We begin by examining the static properties of the model including the quasiparticle residue Z given by

$$Z^{-1} = 1 - \left. \frac{d\text{Im}[\Sigma(\omega)]}{d\omega} \right|_{\omega \rightarrow 0}, \quad (27)$$

as well as the susceptibilities in the density (D) and magnetic (M) channels. The latter can be obtained from the screened interactions analogous to Ref. [92], that is

$$\chi^{D/M} = \frac{\eta^{D/M} - U^{D/M}}{(U^{D/M})^2}. \quad (28)$$

The corresponding results are summarized in Fig. 6. Both codes are in quantitative agreement and predict a strong enhancement of magnetic fluctuations at low temperatures. However, as

Table 1: **Frequency parameters for the benchmark results in Figs. 6-9.** We show the total number of frequencies used for the various Matsubara functions. Since the boxes are symmetric around zero there is an even (odd) number of Matsubara frequencies along fermionic (bosonic) directions.

	total no. frequencies
G	4096
Σ	512
η	1023
λ	575×512
M	$383 \times 320 \times 320$

has been noted in Ref. [77], the characteristic signature for the formation of a local magnetic moment at the impurity, a decrease of χ^D for temperatures $T \lesssim 2$ (for the specific choice of numerical parameters used here), is not captured by the parquet approximation. Instead, χ^D increases monotonically over the entire range of temperatures considered and the system remains in a metallic state with well-defined quasiparticles (i.e. $0 < Z < 1$).

Figure 7 shows a direct comparison of the MBE vertices and their evolution with decreasing temperature within both codes. As can be seen from the middle column, showing the screened interaction, Hedin and multiboson vertex in the magnetic channel, most of the long-lived magnetic correlations are already captured by the screened interaction itself and thus by the corresponding single-boson exchange diagrams. In contrast, low-energy scattering processes mediated by multiple bosons seem to be less relevant, as indicated by a comparatively small M^M contribution. This picture is somewhat reversed in the other channels (left and right column in Fig. 7). In the density channel, for example, the largest contribution originates from short and also long-lived multiboson fluctuations, especially at low temperatures.

Figure 8 presents further results for M^X as a function of its two fermionic frequencies ν and ν' (with fixed $\Omega = 0$). Remarkably, the structure of these objects is dominated by cross-like structures similar to those discussed in Ref. [92], which become more pronounced when T is decreased. A comparison of the data obtained with both codes (shown in the second row of Fig. 8), reveals that it is precisely these structures that seem difficult to capture in numerical calculations, and where small differences in the implementation can have a significant effect. However, the relative difference between the results from both codes is still small ($\lesssim 0.01$).

As a final benchmark of the codes, we have considered their respective serial and parallel performance for a single evaluation of the parquet equations in SBE decomposition (see Fig. 9). Surprisingly, the Julia code based on `MatsubaraFunctions.jl` outperforms the C++ implementation by about a factor of four when run in production mode (i.e., with internal sanity checks disabled). We would like to note that this is most likely *not* due to a fundamental performance advantage of Julia over C++, but simply the result of several optimizations (such as those presented in Sec. 4.3.2) that were more easy to implement using `MatsubaraFunctions.jl`.

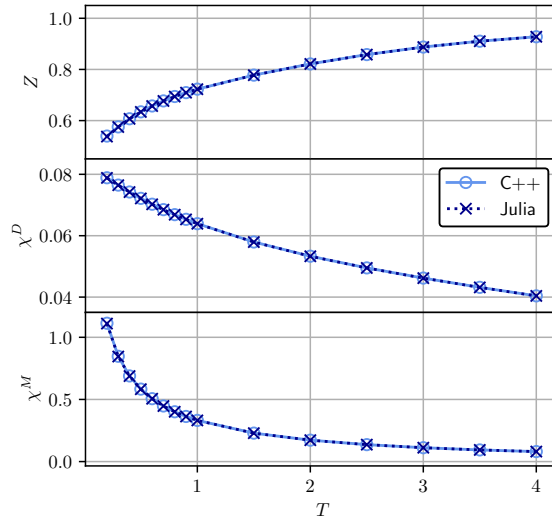


Figure 6: **Results for the quasi-particle residue Z and the density/magnetic susceptibility $\chi^{D/M}$.** The comparison shows good agreement between the two codes. Note that we approximated the derivative in Eq. (27) by a fourth order finite differences method.

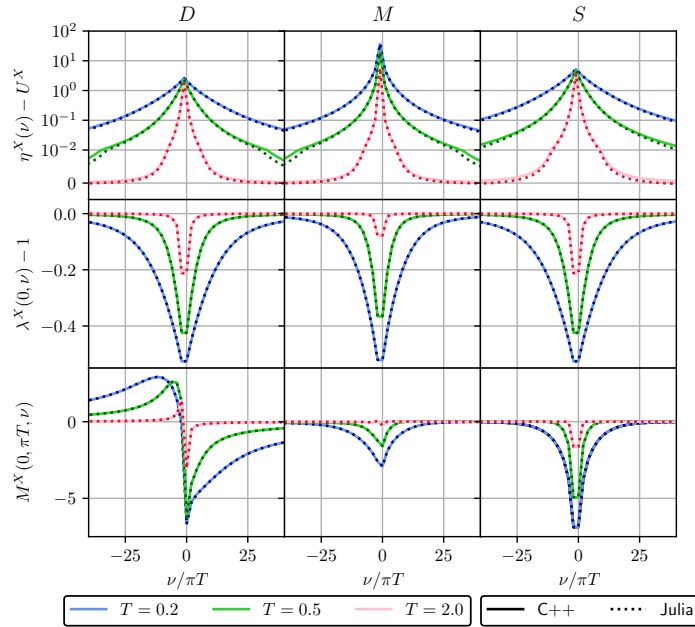


Figure 7: **Benchmark of vertex quantities between the Julia and C++ code.** We show frequency slices through various SBE ingredients (top to bottom: screened interactions, Hedini vertices, multiboson vertices) at different temperatures and channels. The comparison shows good agreement between both codes.

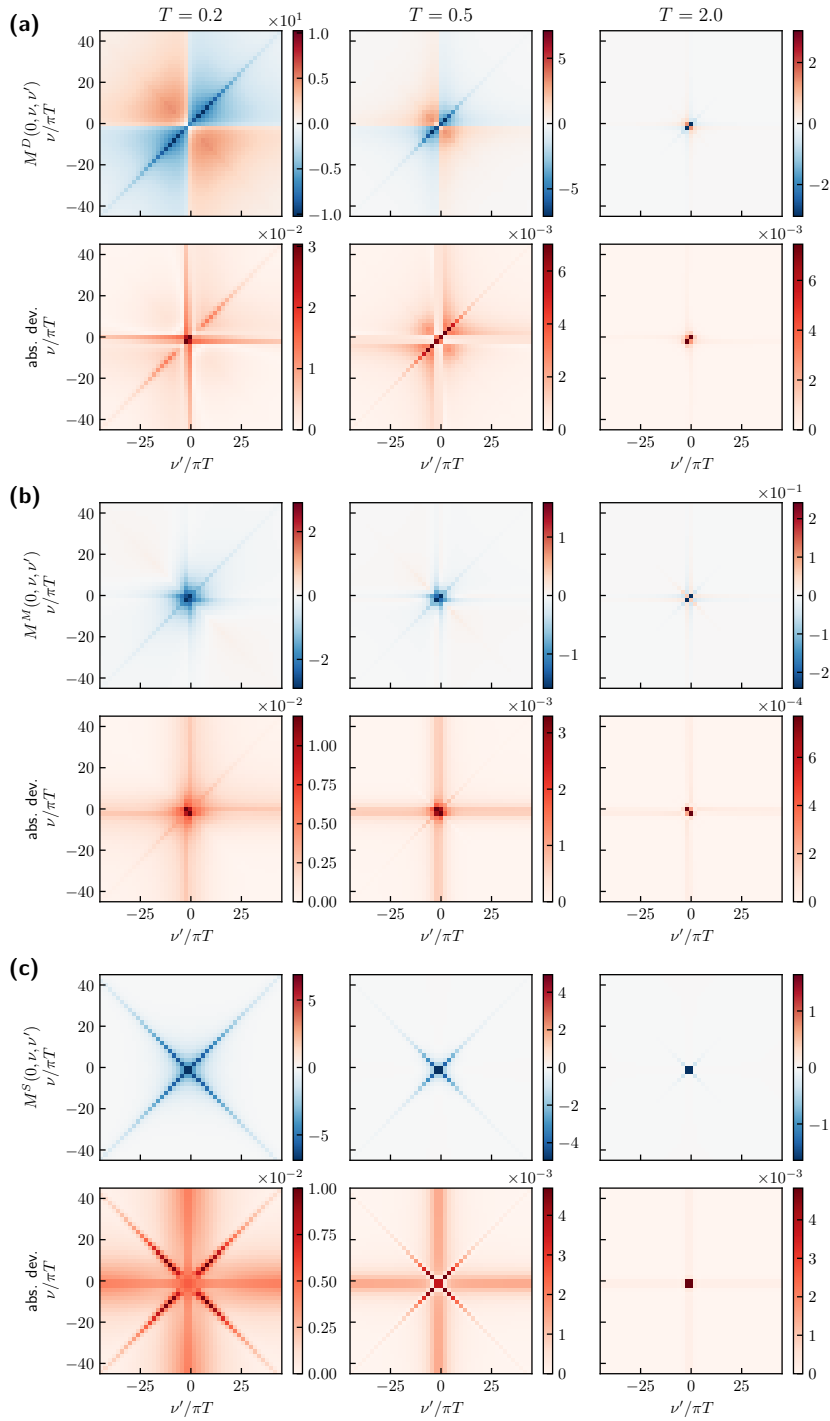


Figure 8: Slice through multi-boson contributions M^D , M^M and M^S . The upper panels show the data for different temperatures, the lower panels the absolute deviation between the Julia and the C++ implementation, respectively. For lower temperatures the features in the data require the computation and storage of a larger number of frequency points. The agreement of the data persists to the lowest temperature shown in this paper.

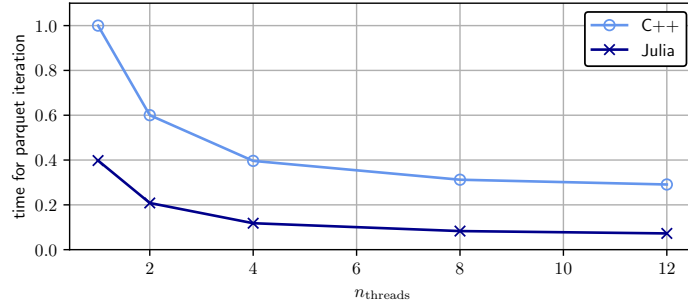


Figure 9: **Performance benchmark between the Julia and C++ code.** We show the time taken for a single evaluation of the parquet equations in SBE decomposition. Note that the runtimes have been normalized to the serial result of the C++ code.

5 Future directions

We have presented a first version of the `MatsubaraFunctions.jl` library and its basic functionality. Although the library already offers many features, most notably an automated interface for implementing and exploiting symmetries when working with Green’s functions (including several options for parallel evaluation), as well as high performance for larger projects (see Sec. 4.3.1 and the discussions therein), several generalizations of the interface and further optimizations are currently under development. In addition, we will add more support for generic grid types other than just Matsubara frequency grids. These could include, for example, momentum space grids and support for continuous variables (such as real frequencies). Note, however, that calculations in momentum or real space are already feasible with the current state of the package, if a suitable mapping from, say, wavevectors to indices is provided. Accuracy improvements for fitting high-frequency tails and more advanced extrapolation schemes for Matsubara sums are also in the works.

In the future, it will be very valuable to extend the ecosystem surrounding `MatsubaraFunctions.jl`. For example, many state-of-the-art diagrammatic solvers rely on the efficient evaluation of similar diagrams such as vertex-bubble-vertex contractions, which are a common feature of Bethe-Salpeter-type equations. These operations could be developed independently of the main library, providing even more quality-of-life options for the user. Moreover, such a toolkit would allow for the swift deployment of different types of solvers, including fRG solvers for quantum spin systems and self-consistent impurity solvers such as the MBE code presented in Sec. 4.3.2, to name but a few. With many new and exciting correlated materials becoming available, fast and flexible solvers are of utmost importance to facilitate scientific progress, and we strongly believe that a package like `MatsubaraFunctions.jl` could be a useful tool for their rapid development.

Acknowledgments

We would like to thank Fabian Kugler, Jae-Mo Lihm, Seung-Sup Lee, Friedrich Krien, Marc Ritter, Björn Sbierski and Benedikt Schneider for helpful discussions and collaboration on ongoing projects.

Funding information This work was funded in part by the Deutsche Forschungsgemeinschaft under Germany’s Excellence Strategy EXC-2111 (Project No. 390814868). It is part of

the Munich Quantum Valley, supported by the Bavarian state government with funds from the Hightech Agenda Bayern Plus. N.R. acknowledges funding from a graduate scholarship from the German Academic Scholarship Foundation (Studienstiftung des deutschen Volkes) and additional support from the ‘‘Marianne-Plehn-Programm’’ of the state of Bavaria. The numerical simulations were, in part, performed on the Linux clusters and the SuperMUC cluster (project 23769) at the Leibniz Supercomputing Center in Munich. The Flatiron Institute is a division of the Simons Foundation.

A Extrapolation of Matsubara sums

Suppose we want to compute the fermionic Matsubara sum $f(\tau \rightarrow 0^+) = \frac{1}{\beta} \sum_{\nu} f(\nu) e^{-i\nu 0^+}$. We assume that $f(z)$ with $z \in \mathbb{C}$ has a Laurent series representation in an elongated annulus about the imaginary axis which decays to zero for large $|z|$. If the poles and residues of f in the complex plane are known, this problem can in principle be solved by rewriting the Matsubara sum as a contour integral and applying Cauchy’s residue theorem after deforming the contour. Unfortunately, these poles are usually unknown and we have to resort to numerical calculations instead. There, however, we can only compute the sum over a finite (symmetric) grid of Matsubara frequencies, which converges very slowly if at all.

To tackle this problem, let us assume that f is known on a grid with sufficiently large maximum (minimum) frequency $\pm\Omega$, such that we can approximate

$$f(\nu) \approx \sum_{n=1}^N \frac{\alpha_n}{(i\nu)^n}, \quad (\text{A.1})$$

for $|\nu| > \Omega$. Neglecting the factor $e^{-i\nu 0^+}$ for brevity, this allows us to split up the expression for $f(\tau \rightarrow 0^+)$ as

$$\begin{aligned} \frac{1}{\beta} \sum_{\nu} f(\nu) &= \frac{1}{\beta} \sum_{\nu < -\Omega} f(\nu) + \frac{1}{\beta} \sum_{-\Omega \leq \nu \leq \Omega} f(\nu) + \frac{1}{\beta} \sum_{\nu > \Omega} f(\nu) \\ &\approx \frac{1}{\beta} \sum_{\nu < -\Omega} \sum_{n=1}^N \frac{\alpha_n}{(i\nu)^n} + \frac{1}{\beta} \sum_{-\Omega \leq \nu \leq \Omega} f(\nu) + \frac{1}{\beta} \sum_{\nu > \Omega} \sum_{n=1}^N \frac{\alpha_n}{(i\nu)^n}, \end{aligned} \quad (\text{A.2})$$

where (A.1) was used to approximate the semi-infinite sums. In many cases, the dominant asymptotic behavior of single-particle Green’s functions and one-dimensional slices through higher-order vertex functions is already well captured by an algebraic decay $(i\nu)^{-q}$ with $q = 1, 2$. Therefore, by truncating the asymptotic expansion at $N = 2$, we can rewrite the right-hand side as

$$\frac{1}{\beta} \sum_{\nu} f(\nu) \approx \frac{1}{\beta} \sum_{-\Omega \leq \nu \leq \Omega} f(\nu) + \sum_{n=1}^2 \left[\frac{1}{\beta} \sum_{\nu} \frac{\alpha_n}{(i\nu)^n} - \frac{1}{\beta} \sum_{-\Omega \leq \nu \leq \Omega} \frac{\alpha_n}{(i\nu)^n} \right]. \quad (\text{A.3})$$

The series in the bracket can be computed straightforwardly using Cauchy’s residue theorem and we find

$$\frac{1}{\beta} \sum_{\nu} f(\nu) e^{-i\nu 0^+} \approx \frac{1}{\beta} \sum_{-\Omega \leq \nu \leq \Omega} \left[f(\nu) - \frac{\alpha_2}{(i\nu)^2} \right] - \frac{\alpha_1}{2} - \beta \frac{\alpha_2}{4}. \quad (\text{A.4})$$

Thus, if the coefficients α_n are known (for example by fitting the high-frequency tails), this formula can provide a quick and dirty approximation to the infinite Matsubara sum.

B Implementation details for the MBE solver

In this section we provide additional information on the implementation of the MBE equations, which were introduced on a general basis in Sec. 4.3.1 of the main text. As for any application involving many-body Green's functions, it is crucial to choose an appropriate parametrization of the self-consistent equations that reflects the symmetries of the field theory under consideration. Here, we deal with the implementation of SU(2) symmetry (spin rotation invariance) as well as time translation invariance (energy conservation) for the MBE equations of the impurity model defined in Sec. 4.3.

B.1 SU(2) symmetry

Consider an SU(2) transformation $U = e^{i\epsilon\sigma}$, where $\epsilon \in \mathbb{R}^3$ and σ is the vector of Pauli matrices. Under U , the fermionic creation and annihilation operators transform into

$$c_s \rightarrow U_{ss'} c_{s'}, \quad c_s^\dagger \rightarrow c_{s'}^\dagger (U^\dagger)_{s's}, \quad (\text{B.1})$$

where we have omitted all indices except the spin $s = \{\uparrow, \downarrow\}$. For SU(2) symmetric actions it can be shown that single-particle Green's functions $G_{ss'}^{(1)}$ are diagonal and also invariant under spin flips, i.e. $G_{ss'}^{(1)} = G^{(1)} \delta_{ss'}$ [48]. Two-particle correlators $G_{s_1's_1 s_2's_2}^{(2)}$, on the other hand, can be decomposed into two components $G^{(2)|=}$ and $G^{(2)|\times}$, which preserve the total spin between incoming and outgoing particles

$$G_{s_1's_1 s_2's_2}^{(2)} = G^{(2)|=} \delta_{s_1's_1} \delta_{s_2's_2} + G^{(2)|\times} \delta_{s_1's_2} \delta_{s_2's_1}. \quad (\text{B.2})$$

Furthermore, the Bethe-Salpeter-like equations (24) can be diagonalized by introducing a singlet (S) and a triplet (T) component

$$\begin{aligned} G_p^{(2)|S} &= G_p^{(2)|=} - G_p^{(2)|\times}, \\ G_p^{(2)|T} &= G_p^{(2)|=} + G_p^{(2)|\times}, \end{aligned} \quad (\text{B.3})$$

in the p channel, and a density (D) and magnetic (M) contribution

$$\begin{aligned} G_t^{(2)|D} &= 2G_t^{(2)|=} + G_t^{(2)|\times}, \\ G_t^{(2)|M} &= G_t^{(2)|\times}, \end{aligned} \quad (\text{B.4})$$

in the t channel. Moreover, this change of basis has the advantage that physical response functions can be obtained directly from the screened interaction in the respective channel. The spin susceptibility χ^M , for example, is simply given by $-U^2 \chi^M = \eta^M + U$ for a local Hubbard U . For this reason, the $\{S, T, D, M\}$ basis is sometimes called the *physical* spin basis, whereas the decomposition into parallel ($=$) and crossed terms (\times) is known as the *diagrammatic* spin basis [48]. In the implementation of the MBE solver, the former is used.

B.2 Time translation invariance

The interacting part of the impurity action from Sec. 4.3 is static, i.e. the bare interaction U is τ -independent. Consequently, one and two-particle Green's functions are invariant under translations in imaginary time, which implies conservation of the total Matsubara frequency between incoming and outgoing legs [48] and, thus,

$$\begin{aligned} G^{(1)}(\nu, \nu') &= G^{(1)}(\nu) \times \beta \delta_{\nu|\nu'}, \\ G^{(2)}(\nu_{1'}, \nu_1, \nu_{2'}, \nu_2) &= G^{(2)}(\nu_{1'}, \nu_1, \nu_{2'}) \times \beta \delta_{\nu_{1'}+\nu_{2'}|\nu_1+\nu_2}. \end{aligned} \quad (\text{B.5})$$

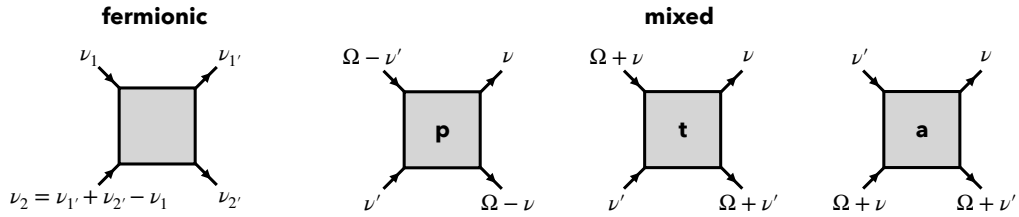


Figure 10: **Mixed frequency conventions.** In mixed notation, each 2PR channel is described in terms of one bosonic argument Ω and two fermionic frequencies ν, ν' as opposed to the purely fermionic notation shown on the left.

Note that we have suppressed additional indices, such as spin, for brevity. For two-particle quantities, it is convenient to adopt a *mixed* frequency convention for the 2PR channels, where, instead of three fermionic arguments, one bosonic transfer frequency Ω and two fermionic frequencies ν, ν' are used. The convention used for the MBE solver is shown in Fig. 10.

References

- [1] J. G. Bednorz and K. A. Müller, *Possible high T_c superconductivity in the Ba-La-Cu-O system*, Z. Phys. B - Condens. Matter **64**, 189 (1986), doi:[10.1007/BF01303701](https://doi.org/10.1007/BF01303701).
- [2] B. Keimer, S. A. Kivelson, M. R. Norman, S. Uchida and J. Zaanen, *From quantum matter to high-temperature superconductivity in copper oxides*, Nature **518**, 179 (2015), doi:[10.1038/nature14165](https://doi.org/10.1038/nature14165).
- [3] N. Mott, *Metal-insulator transitions*, CRC Press, Boca Raton, USA, ISBN 9780429094880 (2004), doi:[10.1201/b12795](https://doi.org/10.1201/b12795).
- [4] J. Hubbard, *Electron correlations in narrow energy bands*, Proc. R. Soc. Lond. A: Math. Phys. Sci. **276**, 238 (1963), doi:[10.1098/rspa.1963.0204](https://doi.org/10.1098/rspa.1963.0204).
- [5] M. Imada, A. Fujimori and Y. Tokura, *Metal-insulator transitions*, Rev. Mod. Phys. **70**, 1039 (1998), doi:[10.1103/RevModPhys.70.1039](https://doi.org/10.1103/RevModPhys.70.1039).
- [6] L. Savary and L. Balents, *Quantum spin liquids: A review*, Rep. Prog. Phys. **80**, 016502 (2016), doi:[10.1088/0034-4885/80/1/016502](https://doi.org/10.1088/0034-4885/80/1/016502).
- [7] J. Knolle and R. Moessner, *A field guide to spin liquids*, Annu. Rev. Condens. Matter Phys. **10**, 451 (2019), doi:[10.1146/annurev-conmatphys-031218-013401](https://doi.org/10.1146/annurev-conmatphys-031218-013401).
- [8] M. Qin, T. Schäfer, S. Andergassen, P. Corboz and E. Gull, *The Hubbard model: A computational perspective*, Annu. Rev. Condens. Matter Phys. **13**, 275 (2022), doi:[10.1146/annurev-conmatphys-090921-033948](https://doi.org/10.1146/annurev-conmatphys-090921-033948).
- [9] D. J. Scalapino, *A common thread: The pairing interaction for unconventional superconductors*, Rev. Mod. Phys. **84**, 1383 (2012), doi:[10.1103/RevModPhys.84.1383](https://doi.org/10.1103/RevModPhys.84.1383).
- [10] T. Schäfer et al., *Tracking the footprints of spin fluctuations: A multimethod, multimessenger study of the two-dimensional Hubbard model*, Phys. Rev. X **11**, 011058 (2021), doi:[10.1103/PhysRevX.11.011058](https://doi.org/10.1103/PhysRevX.11.011058).
- [11] H. Q. Lin, *Exact diagonalization of quantum-spin models*, Phys. Rev. B **42**, 6561 (1990), doi:[10.1103/PhysRevB.42.6561](https://doi.org/10.1103/PhysRevB.42.6561).

- [12] H. Q. Lin, J. E. Gubernatis, H. Gould and J. Tobochnik, *Exact diagonalization methods for quantum systems*, Comput. Phys. **7**, 400 (1993), doi:[10.1063/1.4823192](https://doi.org/10.1063/1.4823192).
- [13] A. Weiße and H. Fehske, *Computational many-particle physics*, Springer, Berlin, Heidelberg, Germany, ISBN 9783540746850 (2008), doi:[10.1007/978-3-540-74686-7](https://doi.org/10.1007/978-3-540-74686-7).
- [14] S. R. White, *Density matrix formulation for quantum renormalization groups*, Phys. Rev. Lett. **69**, 2863 (1992), doi:[10.1103/PhysRevLett.69.2863](https://doi.org/10.1103/PhysRevLett.69.2863).
- [15] U. Schollwöck, *The density-matrix renormalization group*, Rev. Mod. Phys. **77**, 259 (2005), doi:[10.1103/RevModPhys.77.259](https://doi.org/10.1103/RevModPhys.77.259).
- [16] N. Metropolis, A. W. Rosenbluth, M. N. Rosenbluth, A. H. Teller and E. Teller, *Equation of state calculations by fast computing machines*, J. Chem. Phys. **21**, 1087 (1953), doi:[10.1063/1.1699114](https://doi.org/10.1063/1.1699114).
- [17] D. Ceperley and B. Alder, *Quantum Monte Carlo*, Science **231**, 555 (1986), doi:[10.1126/science.231.4738.555](https://doi.org/10.1126/science.231.4738.555).
- [18] W. M. C. Foulkes, L. Mitas, R. J. Needs and G. Rajagopal, *Quantum Monte Carlo simulations of solids*, Rev. Mod. Phys. **73**, 33 (2001), doi:[10.1103/RevModPhys.73.33](https://doi.org/10.1103/RevModPhys.73.33).
- [19] F. Becca and S. Sorella, *Quantum Monte Carlo approaches for correlated systems*, Cambridge University Press, Cambridge, UK, ISBN 9781107129931 (2017), doi:[10.1017/9781316417041](https://doi.org/10.1017/9781316417041).
- [20] C. Wetterich, *Exact evolution equation for the effective potential*, Phys. Lett. B **301**, 90 (1993), doi:[10.1016/0370-2693\(93\)90726-X](https://doi.org/10.1016/0370-2693(93)90726-X).
- [21] P. Kopietz, L. Bartosch and F. Schütz, *Introduction to the functional renormalization group*, Springer, Berlin, Heidelberg, Germany, ISBN 9783642050930 (2010), doi:[10.1007/978-3-642-05094-7](https://doi.org/10.1007/978-3-642-05094-7).
- [22] W. Metzner, M. Salmhofer, C. Honerkamp, V. Meden and K. Schönhammer, *Functional renormalization group approach to correlated fermion systems*, Rev. Mod. Phys. **84**, 299 (2012), doi:[10.1103/RevModPhys.84.299](https://doi.org/10.1103/RevModPhys.84.299).
- [23] A. Georges, G. Kotliar, W. Krauth and M. J. Rozenberg, *Dynamical mean-field theory of strongly correlated fermion systems and the limit of infinite dimensions*, Rev. Mod. Phys. **68**, 13 (1996), doi:[10.1103/RevModPhys.68.13](https://doi.org/10.1103/RevModPhys.68.13).
- [24] N. D. Mermin and H. Wagner, *Absence of ferromagnetism or antiferromagnetism in one- or two-dimensional isotropic Heisenberg models*, Phys. Rev. Lett. **17**, 1307 (1966), doi:[10.1103/PhysRevLett.17.1307](https://doi.org/10.1103/PhysRevLett.17.1307).
- [25] P. C. Hohenberg, *Existence of long-range order in one and two dimensions*, Phys. Rev. **158**, 383 (1967), doi:[10.1103/PhysRev.158.383](https://doi.org/10.1103/PhysRev.158.383).
- [26] T. Maier, M. Jarrell, T. Pruschke and M. H. Hettler, *Quantum cluster theories*, Rev. Mod. Phys. **77**, 1027 (2005), doi:[10.1103/RevModPhys.77.1027](https://doi.org/10.1103/RevModPhys.77.1027).
- [27] G. Kotliar, S. Y. Savrasov, K. Haule, V. S. Oudovenko, O. Parcollet and C. A. Marianetti, *Electronic structure calculations with dynamical mean-field theory*, Rev. Mod. Phys. **78**, 865 (2006), doi:[10.1103/RevModPhys.78.865](https://doi.org/10.1103/RevModPhys.78.865).

- [28] A.-M. S. Tremblay, B. Kyung and D. Sénéchal, *Pseudogap and high-temperature superconductivity from weak to strong coupling. Towards a quantitative theory (review article)*, *Low Temp. Phys.* **32**, 424 (2006), doi:[10.1063/1.2199446](https://doi.org/10.1063/1.2199446).
- [29] A. I. Lichtenstein and M. I. Katsnelson, *Antiferromagnetism and d-wave superconductivity in cuprates: A cluster dynamical mean-field theory*, *Phys. Rev. B* **62**, R9283 (2000), doi:[10.1103/PhysRevB.62.R9283](https://doi.org/10.1103/PhysRevB.62.R9283).
- [30] G. Rohringer, H. Hafermann, A. Toschi, A. A. Katanin, A. E. Antipov, M. I. Katsnelson, A. I. Lichtenstein, A. N. Rubtsov and K. Held, *Diagrammatic routes to nonlocal correlations beyond dynamical mean field theory*, *Rev. Mod. Phys.* **90**, 025003 (2018), doi:[10.1103/RevModPhys.90.025003](https://doi.org/10.1103/RevModPhys.90.025003).
- [31] T. Matsubara, *A new approach to quantum-statistical mechanics*, *Prog. Theor. Phys.* **14**, 351 (1955), doi:[10.1143/PTP14.351](https://doi.org/10.1143/PTP14.351).
- [32] R. Kubo, *Statistical-mechanical theory of irreversible processes. I. General theory and simple applications to magnetic and conduction problems*, *J. Phys. Soc. Jpn.* **12**, 570 (1957), doi:[10.1143/JPSJ.12.570](https://doi.org/10.1143/JPSJ.12.570).
- [33] J. Bezanson, A. Edelman, S. Karpinski and V. B. Shah, *Julia: A fresh approach to numerical computing*, *SIAM Rev.* **59**, 65 (2017), doi:[10.1137/141000671](https://doi.org/10.1137/141000671).
- [34] J. Reuther and P. Wölfle, *$J_1 - J_2$ frustrated two-dimensional Heisenberg model: Random phase approximation and functional renormalization group*, *Phys. Rev. B* **81**, 144410 (2010), doi:[10.1103/PhysRevB.81.144410](https://doi.org/10.1103/PhysRevB.81.144410).
- [35] J. Reuther and R. Thomale, *Functional renormalization group for the anisotropic triangular antiferromagnet*, *Phys. Rev. B* **83**, 024402 (2011), doi:[10.1103/PhysRevB.83.024402](https://doi.org/10.1103/PhysRevB.83.024402).
- [36] J. Reuther, D. A. Abanin and R. Thomale, *Magnetic order and paramagnetic phases in the quantum $J_1 - J_2 - J_3$ honeycomb model*, *Phys. Rev. B* **84**, 014417 (2011), doi:[10.1103/PhysRevB.84.014417](https://doi.org/10.1103/PhysRevB.84.014417).
- [37] J. Reuther, R. Thomale and S. Trebst, *Finite-temperature phase diagram of the Heisenberg-Kitaev model*, *Phys. Rev. B* **84**, 100406 (2011), doi:[10.1103/PhysRevB.84.100406](https://doi.org/10.1103/PhysRevB.84.100406).
- [38] J. Thoenniss, M. K. Ritter, F. B. Kugler, J. von Delft and M. Punk, *Multiloop pseudofermion functional renormalization for quantum spin systems: Application to the spin- $\frac{1}{2}$ Kagomé Heisenberg model*, (arXiv preprint) doi:[10.48550/arXiv.2011.01268](https://doi.org/10.48550/arXiv.2011.01268).
- [39] D. Kiese, T. Müller, Y. Iqbal, R. Thomale and S. Trebst, *Multiloop functional renormalization group approach to quantum spin systems*, *Phys. Rev. Res.* **4**, 023185 (2022), doi:[10.1103/PhysRevResearch.4.023185](https://doi.org/10.1103/PhysRevResearch.4.023185).
- [40] M. K. Ritter, D. Kiese, T. Müller, F. B. Kugler, R. Thomale, S. Trebst and J. von Delft, *Benchmark calculations of multiloop pseudofermion fRG*, *Eur. Phys. J. B* **95**, 102 (2022), doi:[10.1140/epjb/s10051-022-00349-2](https://doi.org/10.1140/epjb/s10051-022-00349-2).
- [41] D. Kiese et al., *Pinch-points to half-moons and up in the stars: The Kagomé skymap*, *Phys. Rev. Res.* **5**, L012025 (2023), doi:[10.1103/PhysRevResearch.5.L012025](https://doi.org/10.1103/PhysRevResearch.5.L012025).
- [42] N. Niggemann, B. Sbierski and J. Reuther, *Frustrated quantum spins at finite temperature: Pseudo-Majorana functional renormalization group approach*, *Phys. Rev. B* **103**, 104431 (2021), doi:[10.1103/PhysRevB.103.104431](https://doi.org/10.1103/PhysRevB.103.104431).

- [43] N. Niggemann, J. Reuther and B. Sbierski, *Quantitative functional renormalization for three-dimensional quantum Heisenberg models*, SciPost Phys. **12**, 156 (2022), doi:[10.21468/SciPostPhys.12.5.156](https://doi.org/10.21468/SciPostPhys.12.5.156).
- [44] B. Sbierski, M. Bintz, S. Chatterjee, M. Schuler, N. Y. Yao and L. Pollet, *Magnetism in the two-dimensional dipolar XY model*, (arXiv preprint) doi:[10.48550/arXiv.2305.03673](https://doi.org/10.48550/arXiv.2305.03673).
- [45] N. Niggemann, Y. Iqbal and J. Reuther, *Quantum effects on unconventional pinch point singularities*, Phys. Rev. Lett. **130**, 196601 (2023), doi:[10.1103/PhysRevLett.130.196601](https://doi.org/10.1103/PhysRevLett.130.196601).
- [46] O. Parcollet, M. Ferrero, T. Ayril, H. Hafermann, I. Krivenko, L. Messio and P. Seth, *TRIQS: A toolbox for research on interacting quantum systems*, Comput. Phys. Commun. **196**, 398 (2015), doi:[10.1016/j.cpc.2015.04.023](https://doi.org/10.1016/j.cpc.2015.04.023).
- [47] D. Rohe, *Hierarchical parallelisation of functional renormalisation group calculations – hp-fRG*, Comput. Phys. Commun. **207**, 160 (2016), doi:[10.1016/j.cpc.2016.05.024](https://doi.org/10.1016/j.cpc.2016.05.024).
- [48] G. Rohringer, *New routes towards a theoretical treatment of nonlocal electronic correlations*, PhD thesis, Technische Universität Wien, Wien, Germany (2013), doi:[10.34726/hss.2013.21498](https://doi.org/10.34726/hss.2013.21498).
- [49] *MatsubaraFunctions.jl*, GitHub (2023), <https://github.com/dominikkiese/MatsubaraFunctions.jl>.
- [50] S. G. Jakobs, M. Pletyukhov and H. Schoeller, *Nonequilibrium functional renormalization group with frequency-dependent vertex function: A study of the single-impurity Anderson model*, Phys. Rev. B **81**, 195109 (2010), doi:[10.1103/PhysRevB.81.195109](https://doi.org/10.1103/PhysRevB.81.195109).
- [51] D. H. Schimmel, B. Bruognolo and J. von Delft, *Spin fluctuations in the 0.7 anomaly in quantum point contacts*, Phys. Rev. Lett. **119**, 196401 (2017), doi:[10.1103/PhysRevLett.119.196401](https://doi.org/10.1103/PhysRevLett.119.196401).
- [52] L. Weidinger and J. von Delft, *Keldysh functional renormalization group treatment of finite-ranged interactions in quantum point contacts*, (arXiv preprint) doi:[10.48550/arXiv.1912.02700](https://doi.org/10.48550/arXiv.1912.02700).
- [53] A. Ge, N. Ritz, E. Walter, S. Aguirre, J. von Delft and F. B. Kugler, *Real-frequency quantum field theory applied to the single-impurity Anderson model*, (arXiv preprint) doi:[10.48550/arXiv.2307.10791](https://doi.org/10.48550/arXiv.2307.10791).
- [54] M. Jarrell and J. E. Gubernatis, *Bayesian inference and the analytic continuation of imaginary-time quantum Monte Carlo data*, Phys. Rep. **269**, 133 (1996), doi:[10.1016/0370-1573\(95\)00074-7](https://doi.org/10.1016/0370-1573(95)00074-7).
- [55] D. Bergeron and A.-M. S. Tremblay, *Algorithms for optimized maximum entropy and diagnostic tools for analytic continuation*, Phys. Rev. E **94**, 023303 (2016), doi:[10.1103/PhysRevE.94.023303](https://doi.org/10.1103/PhysRevE.94.023303).
- [56] O. Goulko, A. S. Mishchenko, L. Pollet, N. Prokof'ev and B. Svistunov, *Numerical analytic continuation: Answers to well-posed questions*, Phys. Rev. B **95**, 014102 (2017), doi:[10.1103/PhysRevB.95.014102](https://doi.org/10.1103/PhysRevB.95.014102).
- [57] K. S. D. Beach, *Identifying the maximum entropy method as a special limit of stochastic analytic continuation*, (arXiv preprint) doi:[10.48550/arXiv.cond-mat/0403055](https://doi.org/10.48550/arXiv.cond-mat/0403055).

- [58] A. W. Sandvik, *Constrained sampling method for analytic continuation*, Phys. Rev. E **94**, 063308 (2016), doi:[10.1103/PhysRevE.94.063308](https://doi.org/10.1103/PhysRevE.94.063308).
- [59] L. Huang, *Acflow: An open source toolkit for analytical continuation of quantum Monte Carlo data*, Comput. Phys. Commun. **292**, 108863 (2023), doi:[10.1016/j.cpc.2023.108863](https://doi.org/10.1016/j.cpc.2023.108863).
- [60] C. Karrasch, R. Hedden, R. Peters, T. Pruschke, K. Schönhammer and V. Meden, *A finite-frequency functional renormalization group approach to the single impurity Anderson model*, J. Phys.: Condens. Matter **20**, 345205 (2008), doi:[10.1088/0953-8984/20/34/345205](https://doi.org/10.1088/0953-8984/20/34/345205).
- [61] H. J. Vidberg and J. W. Serene, *Solving the Eliashberg equations by means of N-point Padé approximants*, J. Low Temp. Phys **29**, 179 (1977), doi:[10.1007/BF00655090](https://doi.org/10.1007/BF00655090).
- [62] *MBEsolver.jl*, GitHub (2023), <https://github.com/dominikkiese/MBEsolver.jl>.
- [63] *Polyester.jl*, GitHub (2023), <https://github.com/JuliaSIMD/Polyester.jl>.
- [64] D. R. Hartree, *The wave mechanics of an atom with a non-Coulomb central field. Part I. Theory and methods*, Math. Proc. Camb. Philos. Soc. **24**, 89 (1928), doi:[10.1017/S0305004100011919](https://doi.org/10.1017/S0305004100011919).
- [65] V. Fock, *Näherungsmethode zur Lösung des quantenmechanischen Mehrkörperproblems*, Z. Phys. **61**, 126 (1930), doi:[10.1007/BF01340294](https://doi.org/10.1007/BF01340294).
- [66] J. C. Slater, *A simplification of the Hartree-Fock method*, Phys. Rev. **81**, 385 (1951), doi:[10.1103/PhysRev.81.385](https://doi.org/10.1103/PhysRev.81.385).
- [67] E. J. Baerends, D. E. Ellis and P. Ros, *Self-consistent molecular Hartree-Fock-Slater calculations I. The computational procedure*, Chem. Phys. **2**, 41 (1973), doi:[10.1016/0301-0104\(73\)80059-X](https://doi.org/10.1016/0301-0104(73)80059-X).
- [68] F. Neese, F. Wennmohs, A. Hansen and U. Becker, *Efficient, approximate and parallel Hartree-Fock and hybrid DFT calculations. A 'chain-of-spheres' algorithm for the Hartree-Fock exchange*, Chem. Phys. **356**, 98 (2009), doi:[10.1016/j.chemphys.2008.10.036](https://doi.org/10.1016/j.chemphys.2008.10.036).
- [69] D. G. Anderson, *Iterative procedures for nonlinear integral equations*, J. ACM **12**, 547 (1965), doi:[10.1145/321296.321305](https://doi.org/10.1145/321296.321305).
- [70] H. F. Walker and P. Ni, *Anderson acceleration for fixed-point iterations*, SIAM J. Numer. Anal. **49**, 1715 (2011), doi:[10.1137/10078356X](https://doi.org/10.1137/10078356X).
- [71] *NLsolve.jl*, GitHub (2023), <https://github.com/JuliaNLSolvers/NLsolve.jl>.
- [72] L. Hedin, *New method for calculating the one-particle Green's function with application to the electron-gas problem*, Phys. Rev. **139**, A796 (1965), doi:[10.1103/PhysRev.139.A796](https://doi.org/10.1103/PhysRev.139.A796).
- [73] F. Aryasetiawan and O. Gunnarsson, *The GW method*, Rep. Prog. Phys. **61**, 237 (1998), doi:[10.1088/0034-4885/61/3/002](https://doi.org/10.1088/0034-4885/61/3/002).
- [74] G. Onida, L. Reining and A. Rubio, *Electronic excitations: Density-functional versus many-body Green's-function approaches*, Rev. Mod. Phys. **74**, 601 (2002), doi:[10.1103/RevModPhys.74.601](https://doi.org/10.1103/RevModPhys.74.601).
- [75] P. W. Anderson, *Localized magnetic states in metals*, Phys. Rev. **124**, 41 (1961), doi:[10.1103/physrev.124.41](https://doi.org/10.1103/physrev.124.41).

- [76] A. C. Hewson, *Renormalized perturbation calculations for the single-impurity Anderson model*, J. Phys.: Condens. Matter **13**, 10011 (2001), doi:[10.1088/0953-8984/13/44/314](https://doi.org/10.1088/0953-8984/13/44/314).
- [77] P. Chalupa, T. Schäfer, M. Reitner, D. Springer, S. Andergassen and A. Toschi, *Fingerprints of the local moment formation and its Kondo screening in the generalized susceptibilities of many-electron problems*, Phys. Rev. Lett. **126**, 056403 (2021), doi:[10.1103/PhysRevLett.126.056403](https://doi.org/10.1103/PhysRevLett.126.056403).
- [78] M. Gievers, E. Walter, A. Ge, J. von Delft and F. B. Kugler, *Multiloop flow equations for single-boson exchange fRG*, Eur. Phys. J. B **95**, 108 (2022), doi:[10.1140/epjb/s10051-022-00353-6](https://doi.org/10.1140/epjb/s10051-022-00353-6).
- [79] F. Krien, *Efficient evaluation of the polarization function in dynamical mean-field theory*, Phys. Rev. B **99**, 235106 (2019), doi:[10.1103/PhysRevB.99.235106](https://doi.org/10.1103/PhysRevB.99.235106).
- [80] F. Krien, A. Valli and M. Capone, *Single-boson exchange decomposition of the vertex function*, Phys. Rev. B **100**, 155149 (2019), doi:[10.1103/PhysRevB.100.155149](https://doi.org/10.1103/PhysRevB.100.155149).
- [81] F. Krien and A. Valli, *Parquetlike equations for the Hedin three-leg vertex*, Phys. Rev. B **100**, 245147 (2019), doi:[10.1103/PhysRevB.100.245147](https://doi.org/10.1103/PhysRevB.100.245147).
- [82] F. Krien, A. I. Lichtenstein and G. Rohringer, *Fluctuation diagnostic of the nodal/antinodal dichotomy in the Hubbard model at weak coupling: A parquet dual fermion approach*, Phys. Rev. B **102**, 235133 (2020), doi:[10.1103/PhysRevB.102.235133](https://doi.org/10.1103/PhysRevB.102.235133).
- [83] F. Krien, A. Valli, P. Chalupa, M. Capone, A. I. Lichtenstein and A. Toschi, *Boson-exchange parquet solver for dual fermions*, Phys. Rev. B **102**, 195131 (2020), doi:[10.1103/PhysRevB.102.195131](https://doi.org/10.1103/PhysRevB.102.195131).
- [84] F. Krien, A. Kauch and K. Held, *Tiling with triangles: Parquet and GW γ methods unified*, Phys. Rev. Res. **3**, 013149 (2021), doi:[10.1103/PhysRevResearch.3.013149](https://doi.org/10.1103/PhysRevResearch.3.013149).
- [85] C. De Dominicis and P. C. Martin, *Stationary entropy principle and renormalization in normal and superfluid systems. I. Algebraic formulation*, J. Math. Phys. **5**, 14 (1964), doi:[10.1063/1.1704062](https://doi.org/10.1063/1.1704062).
- [86] C. De Dominicis and P. C. Martin, *Stationary entropy principle and renormalization in normal and superfluid systems. II. Diagrammatic formulation*, J. Math. Phys. **5**, 31 (1964), doi:[10.1063/1.1704064](https://doi.org/10.1063/1.1704064).
- [87] N. E. Bickers, D. J. Scalapino and S. R. White, *Conserving approximations for strongly correlated electron systems: Bethe-Salpeter equation and dynamics for the two-dimensional Hubbard model*, Phys. Rev. Lett. **62**, 961 (1989), doi:[10.1103/PhysRevLett.62.961](https://doi.org/10.1103/PhysRevLett.62.961).
- [88] N. E. Bickers and S. R. White, *Conserving approximations for strongly fluctuating electron systems. II. Numerical results and parquet extension*, Phys. Rev. B **43**, 8044 (1991), doi:[10.1103/PhysRevB.43.8044](https://doi.org/10.1103/PhysRevB.43.8044).
- [89] N. E. Bickers, *Parquet equations for numerical self-consistent-field theory*, Int. J. Mod. Phys. B **05**, 253 (1991), doi:[10.1142/S021797929100016X](https://doi.org/10.1142/S021797929100016X).
- [90] N. E. Bickers, *Self-consistent many-body theory for condensed matter systems*, in *Theoretical methods for strongly correlated electrons*, Springer, New York, USA, ISBN 9780387217178 (2004), doi:[10.1007/0-387-21717-7_6](https://doi.org/10.1007/0-387-21717-7_6).

- [91] P. M. Bonetti, A. Toschi, C. Hille, S. Andergassen and D. Vilardi, *Single-boson exchange representation of the functional renormalization group for strongly interacting many-electron systems*, Phys. Rev. Res. **4**, 013034 (2022), doi:[10.1103/PhysRevResearch.4.013034](https://doi.org/10.1103/PhysRevResearch.4.013034).
- [92] N. Wentzell, G. Li, A. Tagliavini, C. Taranto, G. Rohringer, K. Held, A. Toschi and S. Andergassen, *High-frequency asymptotics of the vertex function: Diagrammatic parametrization and algorithmic implementation*, Phys. Rev. B **102**, 085106 (2020), doi:[10.1103/physrevb.102.085106](https://doi.org/10.1103/physrevb.102.085106).

3 The numerical renormalization group and its consistency with quantum field theory

The final chapter of this thesis will take a slightly different viewpoint than the other sections. While the preceding chapters were devoted to the technical development, implementation, and application of quantum field theory methods to the many-body problem in real frequencies, this part will be motivated by the goal of combining qualitatively different approaches for the same purpose in the future.

Whereas the parquet formalism and the fRG discussed previously were explicitly only applied to the local single-impurity Anderson model in this work, the true strength of these quantum field theory methods lies in their applicability to systems in, in principle, arbitrary spatial dimensions. However, practical calculations become ever more challenging due to the additional spatial degrees of freedom in higher dimensions, which must be parametrized in addition to the frequency dependencies of the correlation functions involved. For this reason, this thesis focused on the simple local impurity model, allowing a detailed discussion of dynamical properties.

However, other, far more accurate and capable methods exist for treating local impurity systems, chief among which is the numerical renormalization group (NRG) already used as a benchmark in Ref. [P1]. While NRG can only be used to study systems with very few sites, it is useful in the context of higher-dimensional systems, too, as the single-impurity Anderson model naturally appears in the dynamical mean field theory (DMFT). As we will discuss in more detail later, DMFT is a non-perturbative method for computing dynamic correlation functions of lattice models. However, it approximates the self-energy to be local and is thus incapable of resolving non-local quantum fluctuations. At this point, QFT methods such as the parquet formalism or fRG are expected to provide a way forward since those methods can, in principle, straightforwardly treat a non-local self-energy. However, apart from the resulting technical challenges, the approximations typically made in those methods (such as the PA) may lead to a breakdown in the parameter regimes of interest to correlated materials, which are typically at intermediate to large interaction.

For this reason, it has been proposed to combine the two methods, enabling further progress. Concretely, one would use the non-perturbative but local DMFT to compute a local vertex and self-energy, employing NRG to solve the associated impurity problem. In a second step, these would be used in a non-local (i.e., including momentum dependence) parquet or fRG scheme to add the effect of non-local quantum fluctuations self-consistently. How such schemes would work in practice will be further detailed in the outlook (see Sec. 4.1).

Let us be clear that while such an approach has been demonstrated to be feasible in the Matsubara formalism [VTM19; Bon+22], such a calculation in real frequencies is, at present, technically out of reach. We will later comment on a promising technique to enable such computations by compressing the functions involved (see Sec. 4.2).

Furthermore, before such a calculation for a lattice model can be tackled, one should make sure that, already on a local level, the two methods are consistent. In this case, the exact relations the field theory formalism provides, such as the parquet equations, must be satisfied to a reasonable degree by the vertex and self-energy from NRG. Since NRG is not a field theory-based method and, as discussed later, comes with its own numerical inaccuracies (for the vertex, at least), this cannot be taken for granted. In particular, the functions produced by NRG have to be artificially broadened in order to yield smooth curves. Numerical artifacts at this step might compromise the accuracy at which integral equations, such as the parquet equations, which involve integrations over the full frequency axis, are fulfilled.

A local version of the parquet equations and other relations is sufficient for such a consistency check. Hence, the implementations presented and employed before in Refs. [P1; P2] can be employed. In the final publication reprinted in this thesis, Ref. [P4], we discuss precisely such a consistency check: Having performed NRG calculations for the single-impurity Anderson model in two qualitatively different parameter regimes, the resulting vertices and self-energies are scrutinized regarding their fulfillment of exact equations from quantum field theory. One set of equations will be, of course, the parquet equations. In addition, we will also discuss a Ward identity, relating self-energy and vertex, which implies a local conservation law, that is violated in the PA. Still, as NRG does not employ the PA, this equation should be satisfied, too, and we will indeed see that NRG does so remarkably accurately.

Before going into the details of this study, we will set the stage by briefly introducing the NRG, which was already used as a benchmark method in Ref. [P1], including its recent extension to multipoint functions. Since the NRG method is tailored to solve the single-impurity Anderson model, which already appeared throughout this thesis, we will take this opportunity to provide some background about the model and the physics that it captures. Finally, before reprinting the last publication included in this thesis, we will quickly introduce Ward identities and discuss their relevance.

3.1 Single-impurity Anderson model

The single-impurity Anderson model (SIAM), introduced by P. W. Anderson [And61] (for pedagogical introductions, see Refs. [Hew93; Del22]), describes a local quantum system that consists of a single electronic level coupled to non-interacting electrons. The former is a highly simplified description of a single impurity atom inside a metal, while the latter form a *bath* that is used to model the conduction electrons. Historically, the model's main purpose was to explain how local magnetic moments can form at impurities inside otherwise non-magnetic metals. It proved to be useful in deriving the Kondo model [Kon64], which is the starting point for Kondo's explanation of the resistance minimum observed in metals at low temperatures [HBB34]. This resistance minimum was one of the main puzzles in condensed matter physics at the time, since one would expect electric resistance to decrease monotonically with decreasing temperature, since phonons, the dominant source of electric resistance at finite temperature, should freeze out. However, when magnetic impurities are present in the metal in question, it was found that below a certain temperature (typically of a few K), electron scattering and hence electric resistance would start to increase with decreasing temperature. The reason for this, as found by Kondo, is that the coupling between the impurity and the bath enables higher-order spin-flip scattering processes. According to his calculation, the

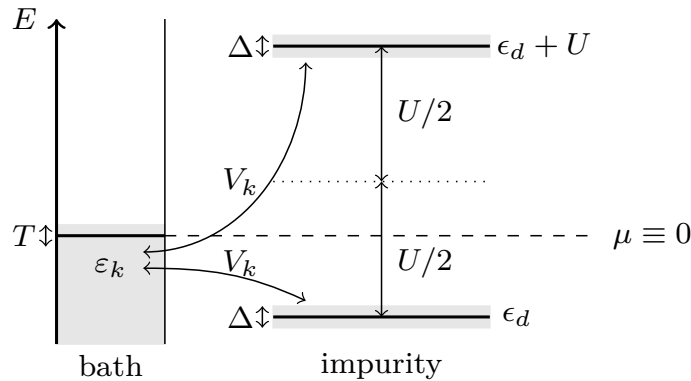


Figure 3.1 Pictorial sketch of the single-impurity Anderson model (SIAM). It consists of a single impurity site modeled by an electronic level representing d -shell electrons. The level can be occupied by at most two electrons; this entails an interaction energy U . The impurity is coupled by a hybridization term V_k to a “bath” of non-interacting c electrons with dispersion ε_k . In an effective description for the d electrons, the hybridization with the bath leads to a finite width Δ of the d level. Note that the sketch corresponds to a particle-hole asymmetric setting.

resulting electron scattering rate increases logarithmically with decreasing temperature.

While this result provided an accurate explanation for the occurrence of a resistance minimum, it led, in turn, to a new issue since it predicts a logarithmically diverging resistance in the limit $T \rightarrow 0$, which is not observed in the experiments. Instead, the resistance should flatten and approach a constant value. This issue became known as the *Kondo problem* and was eventually solved by Wilson, who introduced the NRG for this purpose [Wil75]. According to his explanation, the local moments at the impurity sites are screened by the conduction electrons of the bath at low temperatures, together forming a non-magnetic bound state, called a *spin singlet*. Hence, no spin-flip scattering events can occur once the singlet has formed. This phenomenon is called the *Kondo effect* and happens around a characteristic energy scale T_K , called the *Kondo temperature*, which is hence the binding energy of the singlet. The electrons still scatter off the impurities (which is why the resistance stays finite), but they do not flip their spin in the process.

As was apparent from Kondo’s work already, the Kondo effect cannot be described with diagrammatic perturbation theory alone. This observation is unsurprising since forming a bound state such as the Kondo spin singlet violates the adiabatic assumption [And00]. Additionally, it turns out that, starting from the SIAM, not even the starting point of Kondo’s considerations, a model of localized magnetic moments [Kon64], can be reproduced in the PA. As was shown explicitly in Ref. [Cha+21], charge fluctuations, as quantified by the static charge susceptibility, are not suppressed to a sufficient degree to predict the formation of local moments. This is because local moments come alongside irreducible vertex divergences [Sch+13; Gun+16; Cha+18; Spr+20; Efl+24], which are a formal artifact of the parquet decomposition. Since the parquet and fRG methods employed here both use the parquet decomposition, the physics of the Kondo effect hence cannot be reproduced by these methods alone.

Still, the SIAM is of interest here for mainly three reasons: First, it can be solved by NRG, which we will provide details on in Sec 3.2, thus providing an ideal benchmark for other methods as seen in Ref. [P1]. Second, it is a local model, meaning that all quantities involved do not depend on site indices or momenta, making their numerical computations easier. Third, the SIAM appears in DMFT and is hence routinely solved in studies of correlated materials.

The Hamiltonian of the SIAM is given by

$$H = \sum_{k,\sigma} \varepsilon_k c_{k,\sigma}^\dagger c_{k,\sigma} + \sum_{\sigma} \varepsilon_d n_{\sigma} + U n_{\uparrow} n_{\downarrow} + \sum_{k,\sigma} (V_k d_{\sigma}^\dagger c_{k,\sigma} + \text{H.c.}). \quad (3.1)$$

Its first term describes a band of non-interacting spinful c electrons and an energy dispersion ε_k , where k labels a continuous momentum. The next two terms describe the impurity site, which consists of a single (“ d ”) level at energy ε_d , where $n_{\sigma} = d_{\sigma}^\dagger d_{\sigma}$. Occupying this level by two electrons (which, according to Pauli’s exclusion principle, have to have opposite spin) costs a repulsive interaction energy U . The final part of the Hamiltonian describes the coupling, or *hybridization*, of the d level and the electron bath, letting the electrons tunnel between them with a hopping amplitude V_k . A sketch of the SIAM is given in Fig. 3.1. It also shows the effect of the hybridization term, which results in a finite width Δ of the d level. This result is derived by formally integrating out the c electrons in a path integral description, which is possible since they are non-interacting and hence appear at most quadratically in H . This prescription leads to another quadratic term for the d electrons in the form of a *hybridization function*,

$$\Delta^R(\nu) = \sum_k \frac{|V_k|^2}{\nu - \varepsilon_k + i0^+} = \int d\epsilon \frac{\rho(\epsilon)}{\nu - \epsilon + i0^+}, \quad (3.2)$$

with the *density of states* $\rho(\epsilon) = \sum_k |V_k|^2 \delta(\epsilon - \varepsilon_k)$. Choosing the tunneling amplitude between the d level and the bath to be constant and real, $V_k = V_k^* \equiv V$ and choosing a box-shaped density of states with half-bandwidth D , $\rho(\epsilon) = \frac{V^2}{2D} \theta(D - |\epsilon|)$, the hybridization function becomes

$$\Delta^R(\nu) = \frac{\Delta}{\pi} \ln \left| \frac{\nu + D}{\nu - D} \right| - i\Delta \theta(D - |\nu|), \quad (3.3)$$

with the *hybridization parameter* $\Delta = \frac{\pi V^2}{2D}$. In the wide-band limit $D \rightarrow \infty$, in particular employed in Ref. [P1], the real part of $\Delta^R(\nu)$, which behaves as $\mathcal{O}(\frac{\nu}{D})$, asymptotically vanishes and the hybridization function becomes imaginary and constant, $\Delta^R(\nu) \xrightarrow{D \rightarrow \infty} -i\Delta$.

The physically relevant *local moment regime* of the SIAM, where the impurity is on average occupied by a single electron (with either spin-up or spin-down; hence the impurity hosts a magnetic moment), occurs when the parameters are chosen such that the energies of the empty and double-occupied states lie (far) above the single-occupied level. The latter have energy ε_d ; the former have energy 0 and $2\varepsilon_d + U$, respectively. When accounting for the broadening of the level due to the hybridization, the respective differences should be larger than Δ for a local moment to form. This leads to the requirements $\varepsilon_d < -\Delta$ and $\varepsilon_d + U > \Delta$. In the special case of particle-hole symmetry, where $\varepsilon_d = -U/2$, both requirements imply that $U/\Delta \stackrel{!}{>} 2$.

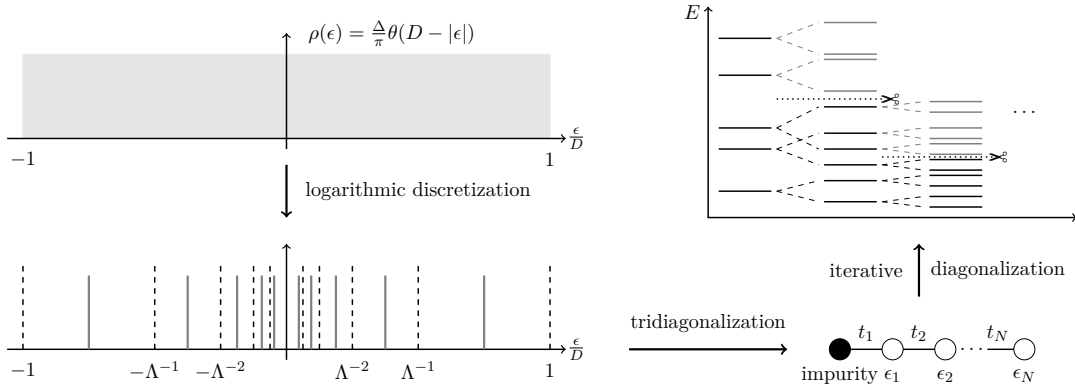


Figure 3.2 Schematic depiction of the NRG algorithm. In the first step, $\rho(\epsilon)$ is discretized logarithmically such that the resulting discrete spectrum becomes dense around the chemical potential. In a second step, the resulting discrete Hamiltonian is tridiagonalized to yield the Wilson chain, with exponentially decaying on-site energies and connecting tunneling amplitudes $\epsilon_n, t_n \sim \Lambda^{-n/2}$. The final step is an iterative diagonalization procedure, during which only the lowest-lying energy states of each shell are further resolved.

As a final side note, we mention that two landmark studies in the 1980s managed to solve the SIAM at zero temperature using the Bethe ansatz [Bet31], providing exact analytical formulas for static observables [TW83; AFL83]. In particular, there exists an analytic expression for the Kondo temperature T_K , which is customarily defined via the static magnetic susceptibility at zero temperature [Hal78a; Hal78b; BHP98; Mor+15; Fil+18],

$$T_K = \frac{1}{4\chi_m(0)} \simeq \sqrt{\frac{U\Delta}{2}} \exp \left[-\frac{\pi U}{8\Delta} + \frac{\pi\Delta}{2U} + \left(\epsilon_d + \frac{U}{2} \right) \frac{\pi}{\sqrt{2U\Delta}} \right]. \quad (3.4)$$

3.2 Numerical renormalization group

The numerical renormalization group (NRG) is a non-perturbative computational method for resolving all energy scales of quantum impurity models, all the way down to exponentially low energy scales as they appear in the Kondo problem, see, for example, Eq. (3.4). It was invented in 1975 by Wilson for this purpose [Wil75] and soon applied to the single-impurity Anderson model [KWW80] as well. After the invention of DMFT in the early 1990s [GK92; Jar92; Geo+96], NRG was applied as an impurity solver in this context, too [BHP98]. In recent years, it has been generalized such that it can be applied to multiorbital models as well [PB05; Sta+15; Sta+19; Den+19; Kug+19; Kug+20; Sta+21; KK22; KKK24].

The general strategy of NRG consists of three main steps, depicted and summarized in Fig. 3.2: First, the continuous density of states defining the hybridization function is discretized logarithmically. The resulting grid, determined by the *Wilson parameter* $\Lambda > 1$ ($\Lambda = 1$ would correspond to the original, continuous case), becomes dense around $\epsilon = 0$, i.e., the electron chemical potential. Second, by tridiagonalizing the resulting discrete Hamiltonian, the system is mapped onto a semi-infinite chain, called a *Wilson chain*, which consists of the impurity at the first site followed by discrete bath sites, with exponentially decaying on-site energies and connecting tunneling amplitudes $\epsilon_n, t_n \sim \Lambda^{-n/2}$ along the chain. Hence, different energy scales are represented by different

sections of the Wilson chain. This energy scale separation becomes essential in the third step: The impurity Hamiltonian (with the bath represented by the Wilson chain) is diagonalized iteratively by adding one site after another. Crucially, only the N_{keep} states with the lowest energy are retained during that iterative procedure. The other ones are being discarded, which limits the numerical effort required. Discarding high-energy states is justified because of the energy scale separation along the Wilson chain: Since the coupling to site $n + 1$ is exponentially smaller than to site n , only the lowest-lying energy states of site n influence the low-energy spectrum of the chain for which site $n + 1$ has been added. High-energy states on site n can hence safely be neglected. To be precise, this does not mean that they are discarded altogether, but that they are not resolved further during the iterative diagonalization procedure. Indeed, those states are used in the full-density-matrix NRG [WD07; PPA06] to construct a complete basis of approximate eigenstates, from which static and dynamic correlators can be computed using their respective Lehmann representations [AS05]. This formulation was employed for computing all two-point NRG quantities presented in the publications reprinted in this thesis, using a state-of-the-art implementation based on the QSpace tensor library [Wei12a; Wei12b; Wei20]. In addition, further, more recent technical developments, such as adaptive broadening of discrete spectral data [LW16; LDW17] and an improved estimator for the self-energy [Kug22] were exploited as well.

For the benchmarks of real-frequency quantum field theory methods presented in Ref. [P1], not only the two-point self-energy as computed by NRG was required but the four-point vertex of the SIAM as well. Furthermore, access to a local vertex is crucial to a future diagrammatic extension of DMFT. Computations of multipoint functions with NRG have become possible only recently [KLD21; LKD21; Lih+24] and constitute a significant further development of the NRG method. Here, we will reproduce only the basic ideas of the method; the details are beyond the scope of this thesis.

At the heart of multipoint NRG calculations lies a powerful, general spectral representation of n -point correlation functions. As detailed at length in Refs. [KLD21; Ge+24; Hal24], in a stationary state (such as in thermal equilibrium, for example), a general n -point function, i.e., an expectation value of a product of n operators, can be written in frequency space as

$$G(\omega_1, \dots, \omega_n) = 2\pi\delta(\omega_1 + \dots + \omega_n) \sum_p (\pm 1)^p \int d^{n-1}\omega'_p K(\omega_p - \omega'_p) S[\mathbf{O}_p](\omega'_p). \quad (3.5)$$

The boldface symbols in Eq. (3.5) denote permutations of the frequencies or operators involved, labeled by the index p ; for details, we refer to the works cited above. The main ingredients of Eq. (3.5) are the functions $K(\omega_p - \omega'_p)$ and $S[\mathbf{O}_p](\omega'_p)$. The former is merely a *convolution kernel*, known analytically. It does not depend on the system in question, but only on the formalism one is working in. For example, in the Keldysh formalism, the fully retarded convolution kernel, which combines $\eta - 1$ anti time ordering and $n - \eta$ time ordering factors, is given by the Fourier transform of

$$K^{[\eta]}(\mathbf{t}_p) = \prod_{i=1}^{\eta-1} [i\theta(t_{p(i+1)} - t_{p(i)})] \prod_{i=\eta}^{n-1} [-i\theta(t_{p(i)} - t_{p(i+1)})]. \quad (3.6)$$

All Keldysh components of the kernel can be expressed through the fully retarded kernel, see Ref. [KLD21] for details. By contrast, in the Matsubara formalism, where there is

only imaginary time ordering, the kernel function instead reads

$$K(\boldsymbol{\tau}_p) = \prod_{i=1}^{n-1} [-\theta(\tau_{p(i)} - \tau_{p(i+1)})]. \quad (3.7)$$

The other main ingredient to Eq. (3.5) are the functions $S[\mathbf{O}_p](\boldsymbol{\omega}'_p)$. Those are called *partial spectral functions* and contain the actual physical information about the system. In the time domain, they are given by the plain expectation values of the corresponding operator products,

$$S[\mathbf{O}](t_1, \dots, t_n) = \langle O_1(t_1) \cdots O_n(t_n) \rangle, \quad (3.8)$$

without any further time-ordering imposed. The partial spectral functions naturally have a Lehmann representation in terms of the eigenstates and eigenenergies of the Hamiltonian. For this reason, NRG is perfectly suited for computing them since the NRG algorithm yields a complete (if approximate) set of eigenstates, as explained before.

While the main ideas behind computations of multipoint functions with NRG are simple, computing such functions in practice turns out to be rather complicated. Being far beyond the scope of this work, the details can be found in Ref. [LKD21]. At this point, we only mention one further crucial issue: The multipoint NRG algorithm enables computing n -point correlation functions, particularly the four-point function. For this work, however, not the four-point correlator $G^{(4)}$, but the four-point vertex Γ is required. As detailed in Sec. (2.2), $G^{(4)}$ needs to be amputated (i.e., four external two-point propagators G have to be removed) to extract the vertex Γ . Doing so naively by simply dividing $G^{(4)}$ by four propagators G is non-surprisingly numerically unstable, especially in the high-frequency limit. For this reason, an alternative technique called *symmetric improved estimators* was developed in Ref. [Lih+24], with which Γ can be extracted from $G^{(4)}$ using only element-wise additions and multiplications of the correlation functions involved with auxiliary correlators. Furthermore, this method is symmetric with respect to all time or frequency arguments of the vertex. Also, it does not mix non-interacting and interacting correlators, making it numerically more stable than previous approaches. A similar method had been developed previously for extracting the self-energy without directly employing the Dyson equation [Kug22]. The original derivations for those improved estimators for the self-energy [Kug22] and four-point vertex [Lih+24] used equations of motion to relate the correlators involved to each other. Very recently, a compact derivation using functional integrals has been found, which easily generalizes to arbitrary n -point vertices [SDS25].

3.3 Ward identities

Before closing this section, we briefly introduce *Ward identities* in quantum field theory, which were not discussed previously but are of importance for the final publication included in this thesis. We give no extensive formal introduction (explicit formulas can be found in Ref. [P4]) but only recap some background here.

Ward identities are exact relations between correlation functions of different orders. The first Ward identity ever derived was used to ensure that the ultraviolet divergence of quantum electrodynamics cancels in all orders of perturbation theory [War50; Tak57]. Since then, Ward identities have become a standard concept in quantum field theory,

including many-body physics. Generally, Ward identities arise from local microscopic continuity equations for observables, which directly result from local (gauge) symmetries of the action and correlation functions or, equivalently, the generating functional. As such, Ward identities manifest such symmetries on the level of correlation functions. An explicit derivation in this spirit is provided in Ref. [P4], concretely for the U(1) Ward identity, which reflects the continuity equation for the local density operator. This Ward identity has been studied extensively in the past; however, previous papers either investigated this identity in the Matsubara formalism [Kat04; Kop+10; Haf+14; Kri+17; Kri18; Cha+22] or considered a one-dimensional limit in the real-frequency Keldysh formalism [Hey+17; Wal22]. In Ref. [P4], we provide for the first time an explicit derivation of the whole, two-dimensional U(1) Ward identity in the Keldysh formalism.

For studies of correlated electrons, Ward identities are essential for several reasons: First, as they relate correlation functions of different orders to each other, they can serve as a consistency check for methods used for computing these. Therefore, the U(1) Ward identity was studied in Ref. [P4]: NRG can by now be used to calculate the two-point self-energy and the four-point vertex, which are related via the (first-order) U(1) Ward identity. However, NRG itself makes no use of the Ward identity. Hence, it can be used to judge the accuracy of the final result of the NRG calculation. Second, the Ward identity might offer a way to improve approximation schemes used in quantum field theory, such as the PA, in the future. It is well known that the PA, while being designed to fulfill crossing symmetry of the vertex (as imposed by the Pauli principle), violates general conservation laws and, consequently, also Ward identities [Smi92; JKP17; KD18a]. By contrast, other methods, derived from approximations of the Luttinger–Ward functional [Bay62], also called “conserving approaches”, fulfill Ward identities by construction. However, these approximations, in turn, violate crossing symmetry. While not rigorously proven, it is believed that only the exact solution of the many-body problem can fulfill both conservation laws and crossing symmetry [STB04]. Still, on the level of individual low-order Ward identities, such as the one between the self-energy and the vertex studied in Ref. [P4], the PA might be improved upon in the future, e.g., by replacing the Schwinger–Dyson equation (2.40) with the Ward identity for computing the self-energy. While the Schwinger–Dyson equation could be violated, such an altered parquet scheme would guarantee fulfillment of the associated local continuity equation on the two-point and four-point levels. Investigating this further is a possible future research direction, especially in the context of non-equilibrium calculations in the Keldysh formalism, where the fulfillment of conservation laws is essential.

**Testing the parquet equations and the U(1) Ward identity
for real-frequency correlation functions from the multipoint
numerical renormalization group**

by

**N. Ritz¹, A. Ge¹, M. Frankenbach¹, M. Pelz¹, J. von Delft¹, and
F.B. Kugler^{2,3}**

¹ Arnold Sommerfeld Center for Theoretical Physics, Center for NanoScience, and
Munich Center for Quantum Science and Technology,
Ludwig-Maximilians-Universität München, 80333 Munich, Germany

² Institute for Theoretical Physics, University of Cologne, 50937 Cologne, Germany

³ Center for Computational Quantum Physics, Flatiron Institute,
162 5th Avenue, New York, New York 10010, USA

reprinted on pages 126–150

Preprint at [arXiv:2504.05910](https://arxiv.org/abs/2504.05910).

Submitted to *Phys. Rev. Research*.

Testing the parquet equations and the U(1) Ward identity for real-frequency correlation functions from the multipoint numerical renormalization group

Nepomuk Ritz ¹, Anxiang Ge ¹, Markus Frankenbach ¹, Mathias Pelz ¹, Jan von Delft ¹, and Fabian B. Kugler ^{2,3}

¹*Arnold Sommerfeld Center for Theoretical Physics, Center for NanoScience, and Munich Center for Quantum Science and Technology, Ludwig-Maximilians-Universität München, 80333 Munich, Germany*

²*Institute for Theoretical Physics, University of Cologne, 50937 Cologne, Germany*

³*Center for Computational Quantum Physics, Flatiron Institute, 162 5th Avenue, New York, NY 10010, USA*

(Dated: April 9, 2025)

Recently, it has become possible to compute real-frequency four-point correlation functions of quantum impurity models using a multipoint extension of the numerical renormalization group (mpNRG). In this work, we perform several numerical consistency checks of the output of mpNRG by investigating exact relations between two- and four-point functions. This includes the Bethe–Salpeter equations and the Schwinger–Dyson equation from the parquet formalism, which we evaluate in two formally identical but numerically nonequivalent ways. We also study the first-order U(1) Ward identity between the vertex and the self-energy, which we derive for the first time in full generality in the real-frequency Keldysh formalism. We generally find good agreement of all relations, often up to a few percent, both at weak and at strong interaction.

I. INTRODUCTION

A promising route toward computing dynamical correlation functions of realistic models for correlated electronic systems lies in combining different numerical methods. One example is the idea of using the non-perturbative but local dynamical mean-field theory (DMFT) [1] as a correlated starting point for subsequent diagrammatic calculations [2]. Recent methodical advancements in the Keldysh formalism (KF) even put real-frequency dynamical correlation functions directly comparable to experiments within reach [3–7].

A suitable impurity solver for this purpose is the numerical renormalization group (NRG) [8]. In its recent multipoint extension (mpNRG) [3, 4], it can provide both the self-energy and the four-point (4p) vertex of a self-consistently determined DMFT impurity model. These may then be used as a starting point for nonlocal diagrammatic extensions [2], for example in the form of the dynamical vertex approximation (DGA) [9, 10] using the parquet formalism [11] or (closely related [12–14]) the functional renormalization group [15, 16]. However, for this to be a reliable strategy, the results from mpNRG must be of sufficient quality, which a priori cannot be taken for granted due to numerical restrictions.

NRG computations converged in all numerical parameters produce numerically exact results for two-point (2p) quantities such as the self-energy in the low-energy regime. However, there is a danger of overbroadening at large energies due to the logarithmic bath discretization in NRG. This may raise doubts as to how well exact relations involving integrations over all frequencies are fulfilled. Furthermore, even though the accuracy of the mpNRG 4p vertex has recently been drastically improved using the symmetric estimator technique [17], numerical restrictions such as a relatively small number of kept states and a correspondingly large discretization parameter still hold. It is, therefore, of interest to test to what extent the correlation functions produced by mpNRG fulfill exact relations that arise in a quantum field theory (QFT) description of the many-electron problem. In addition, the fulfillment of

such relations can serve as a guide for future developments of mpNRG.

In this paper, we study a host of exact relations between real-frequency correlation functions. We perform our calculations for the single-impurity Anderson model [18], which arises in DMFT and which NRG is tailored to solve. Along with the basics of the formalism and all employed methods, the model is introduced in Sec. II. We consider two different datasets from (mp)NRG: one at weak and one at strong interaction. In Sec. III, we first discuss the fulfillment of the Bethe–Salpeter equations (BSEs) and the Schwinger–Dyson equation (SDE) from the parquet formalism. Then, we consider the Ward identity (WI) arising from the local U(1) gauge invariance of the theory. For the first time, we derive it in full generality in the KF and check its fulfillment in mpNRG. We find that both the parquet equations and the WI are fulfilled rather well, in many components up to a few percent, and comment on larger discrepancies wherever they occur. Finally, we conclude in Sec. IV and provide details on technicalities in the Appendices A–G.

II. FORMALISM

Our main objects of interest are real-frequency dynamical 2p and 4p correlation functions in the KF. Their non-trivial contributions which arise from electron-electron interactions are encapsulated in the self-energy Σ and the 4p vertex Γ ,

$$\Sigma = \text{---} \circlearrowleft \Sigma \text{---}, \quad \Gamma = \text{---} \square \Gamma \text{---}. \quad (1)$$

The self-energy enters the Dyson equation,

$$G = \text{---} \leftarrow = \text{---} \leftarrow G_0 + \text{---} \leftarrow \circlearrowleft \Sigma \text{---} \leftarrow G, \quad (2)$$

determining the one-particle propagator G , where G_0 is the non-interacting (“bare”) propagator. From the retarded component of the propagator, the experimentally measurable spectral function is deduced as $A(\nu) = -\text{Im} G^R(\nu)/\pi$. The vertex

determines the two-particle correlation function $G^{(4)}$,

$$G^{(4)} = \begin{array}{c} \text{---} \text{---} \\ \text{---} \end{array} - \begin{array}{c} \text{---} \\ \text{---} \end{array} + \begin{array}{c} \text{---} \\ \text{---} \end{array} + \begin{array}{c} \text{---} \text{---} \\ \text{---} \end{array} \Gamma \begin{array}{c} \text{---} \text{---} \\ \text{---} \end{array}, \quad (3)$$

which yields physical susceptibilities upon contracting pairs of external legs. An explicit form of the equations shown here only diagrammatically is provided in App. F 1.

A. The (multipoint) numerical renormalization group

The NRG is a computational technique to resolve all energy scales of quantum impurity systems in a non-perturbative fashion. Its main idea consists of logarithmically discretizing the energy spectrum of the conduction electrons and iteratively diagonalizing the resulting Hamiltonian. To this end, the discretized Hamiltonian is transformed into a semi-infinite chain with exponentially decreasing hopping amplitudes. This chain Hamiltonian is then solved iteratively by adding one energy shell at a time and diagonalizing the effective Hamiltonian at each step. By systematically keeping only the low-energy states while discarding the high-energy states from each shell, the numerical effort remains manageable. Importantly, the discarded states from each shell can be gathered into a *complete* set of approximate energy eigenstates [19].

Afterward, (multipoint) correlation functions can be computed by convolving analytically known kernel functions with a set of so-called partial spectral functions (PSFs). The latter are obtained from their respective Lehmann representations, using the eigenenergies and (discarded) eigenstates obtained from NRG.

Originally invented by Wilson to solve the Kondo problem [20], the NRG was soon applied to the single-impurity Anderson model [21]. Later, NRG was also used as a DMFT impurity solver, first in the single-orbital context [22] and then also for multiorbital models [23–33] and most recently in two-site cellular DMFT studies [34, 35]. The recent extension of NRG to multipoint correlation functions (mpNRG) [3, 4, 17] now enables its application to vertex-based extensions of DMFT. This work is meant to be a preliminary step toward that goal.

Details on the NRG implementations employed in this work and the numerical parameters chosen can be found in App. B. In the following, it is self-explanatory whether the “standard” NRG or its multipoint extension is employed to compute 2p or higher-point functions, respectively. We will therefore not distinguish between the two in the main text.

B. Single-impurity Anderson model

The Hamiltonian of the single-impurity Anderson model [18] is

$$H = \sum_{\epsilon\sigma} \epsilon c_{\epsilon\sigma}^\dagger c_{\epsilon\sigma} + \sum_{\sigma} \epsilon_d n_{\sigma} + U n_{\uparrow} n_{\downarrow} + \sum_{\epsilon\sigma} (V_{\epsilon} d_{\sigma}^\dagger c_{\epsilon\sigma} + \text{H.c.}), \quad (4)$$

where the impurity site is described by a local d level with on-site energy ϵ_d . The d level hybridizes with spinful conduction

electrons, created by $c_{\epsilon\sigma}^\dagger$, via matrix elements V_{ϵ} . Electrons on the impurity site, where $n_{\sigma} = d_{\sigma}^\dagger d_{\sigma}$, interact with interaction strength U . The non-interacting c electrons occur quadratically in the functional integral and can be integrated out, yielding a frequency-dependent retarded hybridization function $\Delta^R(\nu)$ as an additional quadratic term for the d electrons.

We choose the hybridization function as

$$\Delta^R(\nu) = \frac{\Delta}{\pi} \ln \left| \frac{\nu + D}{\nu - D} \right| - i\Delta \theta(D - |\nu|), \quad (5)$$

with a box-shaped imaginary part of half-bandwidth D and strength Δ . In the often-employed wide-band limit, its real part can be neglected and the hybridization function reduces to a constant, $\Delta^R(\nu) \xrightarrow{D \rightarrow \infty} -i\Delta$.

C. Parquet formalism

The parquet formalism [11, 36–38] provides exact self-consistent equations for the vertex and the self-energy. Its starting point is the parquet decomposition, which classifies all diagrammatic contributions to the vertex w.r.t. their two-particle reducibility,

$$\Gamma = R + \sum_{r \in \{a, p, t\}} \gamma_r. \quad (6)$$

Any diagram that contributes to Γ is either two-particle reducible in one of the three two-particle channels a , p , or t (and thus included in the two-particle reducible vertices γ_r), or it is two-particle irreducible in all three channels and thus part of the fully two-particle irreducible vertex R . The parquet formalism provides self-consistent relations for the reducible vertices γ_r in the form of the BSEs,

$$\gamma_r = I_r \circ \Pi_r \circ \Gamma = \Gamma \circ \Pi_r \circ I_r. \quad (7)$$

Here, $I_r = \Gamma - \gamma_r$, Π_r denotes a pair of propagators used to connect two vertices, and the symbol \circ is a short-hand notation for contractions over all quantum numbers as well as frequency integrations.

In addition, self-energy and vertex are related by the SDE,

$$\Sigma = - \left[\Gamma_0 + \frac{1}{2} \Gamma_0 \circ \Pi_r \circ \Gamma \right] \cdot G. \quad (8)$$

Here, the second term can be parametrized w.r.t. either of the three two-particle channels, and the symbol \cdot is used to denote the contraction with a single propagator in Eq. (8). Together, the BSEs and the SDE are known as the parquet equations. They are exact relations, which however require the input of the fully irreducible vertex R . In a purely diagrammatic treatment, approximations are employed at this stage, the most common being the parquet approximation $R \simeq \Gamma_0$, which only considers the first-order contribution to R from the bare vertex Γ_0 . As this neglects higher-order irreducible diagrams, which start at the fourth order in Γ_0 , the parquet approximation is only justified for weak to intermediate interaction strengths. In this work, the parquet approximation is *not* employed, as the NRG provides the full vertex non-perturbatively, including its irreducible part.

D. Asymptotic vertex classes

For efficiently treating the reducible vertices γ_r , they are decomposed into asymptotic classes as introduced in Ref. 39. This decomposition captures the high-frequency asymptotic behavior of the vertices by separating its diagrammatic contributions into so-called asymptotic classes in each channel $r \in \{a, p, t\}$. These asymptotic classes do or do not depend on one or both the fermionic frequencies in the natural frequency parametrization of the respective two-particle channel, $\gamma_r(\omega_r, \nu_r, \nu'_r) = K_{1,r}(\omega_r) + K_{2,r}(\omega_r, \nu_r) + K_{2',r}(\omega_r, \nu'_r) + K_{3,r}(\omega_r, \nu_r, \nu'_r)$. Diagrams that belong to classes that do not depend on a given frequency will thus give a finite contribution to the vertex in the high-frequency limit. In their remaining arguments, however, they ultimately decay. Formally, the asymptotic classes can be defined as

$$K_{1,r}(\omega_r) = \lim_{\nu_r \rightarrow \infty} \lim_{\nu'_r \rightarrow \infty} \gamma_r(\omega_r, \nu_r, \nu'_r) \quad (9a)$$

$$K_{2,r}(\omega_r, \nu_r) = \lim_{\nu'_r \rightarrow \infty} \gamma_r(\omega_r, \nu_r, \nu'_r) - K_{1,r}(\omega_r) \quad (9b)$$

$$K_{2',r}(\omega_r, \nu'_r) = \lim_{\nu_r \rightarrow \infty} \gamma_r(\omega_r, \nu_r, \nu'_r) - K_{1,r}(\omega_r) \quad (9c)$$

$$K_{3,r}(\omega_r, \nu_r, \nu'_r) = \gamma_r(\omega_r, \nu_r, \nu'_r) - K_{1,r}(\omega_r) - K_{2,r}(\omega_r, \nu_r) - K_{2',r}(\omega_r, \nu'_r), \quad (9d)$$

in each channel r . They can be visualized graphically as

$$\begin{aligned} \gamma_a(\omega_a, \nu_a, \nu'_a) &= \begin{array}{c} \nu_a + \frac{\omega_a}{2} \swarrow \quad \searrow \nu'_a + \frac{\omega_a}{2} \\ \text{---} \gamma_a \text{---} \\ \nu_a - \frac{\omega_a}{2} \swarrow \quad \searrow \nu'_a - \frac{\omega_a}{2} \end{array} \\ &= \begin{array}{c} \omega_a \text{ (red arrow)} \\ \text{---} K_{1,a} \text{---} \\ \nu_a \text{ (blue arrow)} \quad \nu'_a + \nu_a \text{ (blue arrow)} \end{array} + \begin{array}{c} \omega_a \text{ (red arrow)} \\ \text{---} K_{2,a} \text{---} \\ \nu'_a \text{ (blue arrow)} \quad \nu_a + \nu'_a \text{ (blue arrow)} \end{array} \\ &+ \begin{array}{c} \omega_a \text{ (red arrow)} \\ \text{---} K_{2',a} \text{---} \\ \nu_a \text{ (blue arrow)} \quad \nu'_a + \nu_a \text{ (blue arrow)} \end{array} + \begin{array}{c} \omega_a \text{ (red arrow)} \\ \text{---} K_{3,a} \text{---} \\ \nu_a \text{ (blue arrow)} \quad \nu'_a \text{ (blue arrow)} \end{array} \quad (10) \end{aligned}$$

for the a channel, and correspondingly for the p - and t channels. Note that the symmetric estimator technique in NRG provides the $K_{1,r}$, $K_{2,r}$ and $K_{2',r}$ classes in each channel r separately, but not so for K_3 . Instead, it only gives the sum of the irreducible vertex R and all three $K_{3,r}$ classes, obtained by subtracting the asymptotic contributions from the full vertex. That object is used to define the ‘‘vertex core’’,

$$\Gamma_{\text{core}} = \Gamma - [\Gamma_0 + \sum_{r \in \{a, p, t\}} (K_{1,r} + K_{2,r} + K_{2',r})] \quad (11a)$$

$$= R - \Gamma_0 + \sum_{r \in \{a, p, t\}} K_{3,r}, \quad (11b)$$

which thus contains all diagrams that genuinely depend on three frequencies and decay in every direction.

As a side note, the vertex can alternatively be parametrized using the single-boson exchange (SBE) decomposition [40–

45], which classifies the diagrams according to their interaction reducibility instead of their two-particle reducibility. This formalism naturally exploits the asymptotic behavior of individual classes of diagrams as well. In fact, asymptotic classes can be related to SBE objects and vice-versa [46]. We will not employ the SBE decomposition in this work.

E. Keldysh formalism

The KF [47–49] is an alternative to the widespread Matsubara formalism (MF) and is applicable both in and out of thermal equilibrium. In this work, we use it exclusively for equilibrium computations. There, its main advantage over the MF lies in the fact that it enables computing dynamical correlation functions in *real* time or frequency, whereas the MF gives an imaginary frequency description. Obtaining experimentally measurable observables such as the spectral function in the MF thus requires analytical continuation, a numerically ill-conditioned problem.

Working in the KF entails significant practical complications. For instance, since each operator has a contour index, the 4p vertex has $2^4 = 16$ Keldysh components. Next, unlike in the finite-temperature MF, KF objects have a continuous frequency dependence, which must be discretized in numerical treatments. This is especially challenging for 4p functions that depend on three independent frequencies (in equilibrium) and limits the accuracy of the computations if done naively. Also, in bubble or loop contractions of diagrams, integrations over frequencies have to be performed instead of simple summations over Matsubara frequencies, which again is numerically much more demanding.

For computing correlation functions with mpNRG, most of these complications become relevant only in later stages of the calculations. As explained in detail in Ref. 3, the actual NRG algorithm is agnostic of the formalism. From the approximate eigenenergies and eigenstates of the impurity model with a discretized bath, one obtains a set of PSFs. These, in turn, can be used to compute correlation functions in any formalism, be it the MF, the zero-temperature formalism, or the KF. To this end, the PSFs are convoluted with a set of formalism-dependent kernel functions; for the KF, the Keldysh index structure enters via the Keldysh kernels. Only at this step, namely the convolutions, does it become necessary to specify a discretized frequency grid, which can be chosen arbitrarily in principle. Numerically, the convolution of the PSFs with the kernel functions is easy to perform. Since the PSFs consist of delta peaks, the frequency integrals reduce to simple sums. Beyond that point, no frequency integrations are necessary within mpNRG. In this work, they enter at a later stage, when the output of mpNRG is used to evaluate the parquet equations or the U(1) WI. Moreover, the vertex is related to the 4p correlator through the amputation of external legs. Naively, this requires divisions of the 4p correlator by 2p propagators, which can become numerically unstable. Using the recently developed symmetric improved estimators [17], the vertex can be computed using only element-wise multiplications and additions.

III. RESULTS

We consider two separate parameter sets throughout. One is at weak interaction, $u = U/(\pi\Delta) = 0.5$, and $T/U = 0.01$ ($T/\Delta \approx 0.16$) in the wide-band limit, where $\Delta^R(\nu) \rightarrow -i\Delta$, corresponding to one of the datasets studied in Ref. 6. For this parameter set, the PA is justified and a self-consistent solution of the parquet equations can easily be obtained. The other one is at strong interaction, at a much lower temperature and for a finite bandwidth, $U/\Delta = 5$ ($u \approx 1.59$), $T/\Delta = 0.0025$ and $D/\Delta = 25$, corresponding to one of the datasets studied in Ref. 17. Here, the PA is not justified anymore and a self-consistent solution of the parquet equations in the PA with the methods employed in Ref. 6 is out of reach in the KF. Using the standard formula [50] for the Kondo temperature at particle-hole symmetry, $T_K \simeq \sqrt{\frac{U\Delta}{2}} \exp(-\frac{\pi U}{8\Delta} + \frac{\pi\Delta}{2U})$, one obtains $T_K/\Delta \approx 1.3$ and $T_K/\Delta \approx 0.30$ for the weak- and strong-interaction parameter sets, respectively.

For each parameter set, we performed a “standard” NRG calculation for the self-energy and a multipoint NRG calculation for the vertex. The NRG parameters of these calculations are summarized in App. B. The self-energy and vertex obtained this way were then used to evaluate all equations of interest here, utilizing the KELDYSHQFT codebase [51].

All NRG vertex data was generated on a logarithmic frequency grid, $\nu/\Delta \in \{-10^2, \dots, -10^{-2}, 0, 10^{-2}, \dots, 10^2\}$, with 30 points per decade, i.e. 241 points per frequency axis. The vertex was computed in the t channel parametrization according to the conventions of Ref. 17. This data had to be transferred to the conventions of Ref. 5 (see App. C for details), during which not only the frequency parametrizations were adapted, but also the data was interpolated onto the non-linear grids introduced in [5, 6] and implemented in [7, 51]. The transferred data was subsequently used to evaluate all equations relevant to this work.

All one-dimensional functions of interest here are either symmetric or antisymmetric in frequency. We hence restrict their plots to positive frequencies using semi-logarithmic axes. For comparing two dynamical quantities $a(\nu)$ and $b(\nu)$, we use their maximal relative difference, which we define as

$$\delta_{\text{rel}}^{\text{max}}(a, b) \equiv \max_{\nu} |a(\nu) - b(\nu)| / \max_{\nu} |b(\nu)|. \quad (12)$$

We normalize w.r.t. the maximal absolute value of b across the whole real-frequency axis to avoid an overemphasis on deviations in regions where the functions a and b are small.

The results in the main text are shown for a single Keldysh component, since the other components follow from (generalized) fluctuation-dissipation relations (FDRs) in thermal equilibrium. In the case of 2p functions, we focus on the retarded component. For the self-energy, the other non-trivial “Keldysh” component obeys the standard fermionic FDR,

$$\Sigma^K(\nu) = 2i \tanh(\frac{\nu}{2T}) \text{Im} \Sigma^R(\nu). \quad (13)$$

As explained in detail in Ref. 5, for the $K_{1,r}$ classes (corresponding to bosonic 2p functions), symmetries and causality reduce the number of naively 16 Keldysh components to only

two. These are related via the standard bosonic FDR,

$$K_{1,r}^K(\omega_r) = 2i \coth(\frac{\omega_r}{2T}) \text{Im} K_{1,r}^R(\omega_r), \quad (14)$$

where the “retarded” R component refers to the 11|21 component, and the “Keldysh” K component refers to the 11|22 component for the t channel or the 12|12 component for the a and p channel, respectively.

For 2p functions, we compute only the retarded components with NRG and deduce the Keldysh component, if needed, directly from the FDRs. Generalized FDRs that relate different Keldysh components of the full three-dimensional vertex in thermal equilibrium have been derived in [52–54]. On the 4p level, these were already studied in Ref. 17 (see Fig. 19 therein), so we refrain from repeating such an analysis here. We only comment on the generalized FDR for one special Keldysh component of the K_2 class in App. A, for which the BSE studied in Sec. III A is violated comparatively strongly.

A. Bethe–Salpeter equations

We begin by testing the fulfillment of the BSEs, considered separately for K_1 and K_2 . Since NRG does not provide the individual K_3 classes but only the vertex core, the BSEs for the K_3 classes cannot be verified explicitly. Indeed, while a full parquet decomposition of the vertex in the MF proceeds by (matrix-) inversion of the BSEs, this has not yet been done in the KF, where the frequency dependence of all functions is continuous. Therefore, it is not possible at this point to study the BSEs for the full γ_r s in the KF.

The BSEs for K_1 follow from the limit $\nu_r, \nu'_r \rightarrow \infty$ of Eq. (7),

$$K_{1,r} = \Gamma_0 \circ \Pi_r \circ (\Gamma_0 + K_{1,r} + K_{2,r}) \quad (15a)$$

$$= (\Gamma_0 + K_{1,r} + K_{2,r}) \circ \Pi_r \circ \Gamma_0, \quad (15b)$$

or, diagrammatically,

$$= \quad (16)$$

in the a channel and likewise in the p and t channels. We verified that it makes no difference numerically if $K_{2,r}$ or $K_{2',r}$ is used in the BSEs. Figure 1 shows the fulfillment of the BSEs for $K_{1,r;\uparrow\downarrow}^R$, the retarded Keldysh component of the $\uparrow\downarrow$ spin component in all three two-particle channels. All other spin components are related via crossing and SU(2) spin symmetry. We show both the real and imaginary parts even though, for these retarded functions, they are connected by Kramers–Kronig relations. Indeed, NRG exploits the Kramers–Kronig relations, fulfilling them by construction. However, the implementation of the BSEs does not enforce them explicitly but evaluates real and imaginary parts separately.

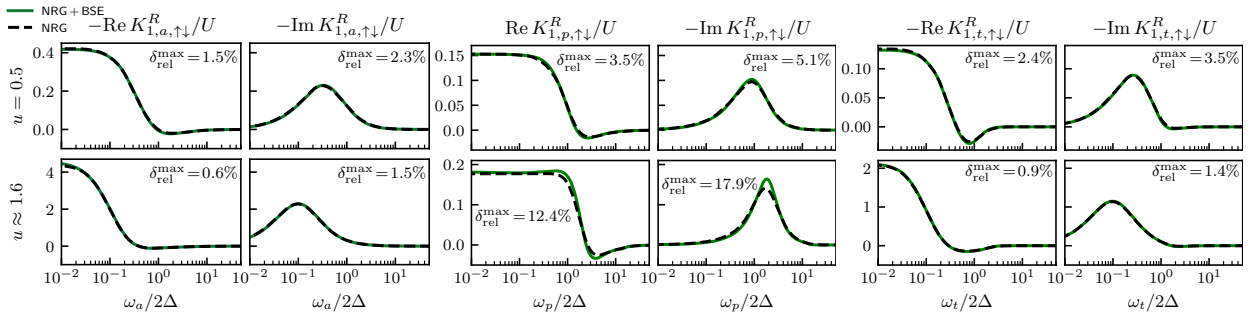


FIG. 1. Retarded Keldysh component and $\uparrow\downarrow$ spin component of the $K_{1,r}$ vertex classes in the three two-particle channels $r \in \{a, p, t\}$. We compare the result of NRG (black dashed lines) and the result after one evaluation of the BSEs according to Eq. (15a) (green lines), using $K_{1,r}$ and $K_{2,r}$ as well as the self-energy inside Π_r from NRG, using symmetric estimators for all quantities [17, 55]. In this and all following plots, results for two separate data sets are shown: the top panels are at “weak interaction”, for which $u = U/(\pi\Delta) = 0.5$ and $T/U = 0.01$ ($T/\Delta \approx 0.16$) in the wide-band limit $D \rightarrow \infty$, the bottom panels at “strong interaction” $U/\Delta = 5, T/\Delta = 0.0025, D/\Delta = 25$. All quantities shown here are symmetric or anti-symmetric in frequency, thus the plots are restricted to positive frequencies. Real- and imaginary parts are related by Kramers–Kronig relations, which are enforced in NRG but not in the implementation of the BSEs. Other spin components follow from crossing symmetry. The only other non-trivial Keldysh component is related via the fluctuation-dissipation theorem, Eq. (14). We observe excellent agreement up to a few percent, particularly for the dominating a channel. Especially at strong interaction, the slight deviations in the p channel are negligible, as $K_{1,p}$ is smaller by about one order of magnitude compared to the other channels.

For both parameter sets we observe excellent fulfillment of the BSEs for K_1 up to a few percent. The agreement is particularly good for the a channel that dominates already at weak interaction and more so at strong interaction. Since the a channel is related to the t channel by crossing symmetry, it is no surprise that the agreement of the BSE in the t channel is excellent as well. Only in the p channel do the deviations reach about 18% for the strong-interaction dataset. In particular, the peak in the imaginary part, which lies at larger frequencies compared to the other channels, is not reproduced perfectly. This is to be expected as NRG becomes less accurate at larger frequencies. Still, since $K_{1,p}$ is smaller compared to the other two channels by about one order of magnitude at strong interaction, these deviations are arguably negligible.

Taking the limit $v_r \rightarrow \infty$ of Eq. (7) gives the BSEs for the sum of K_1 and K_2 in channel r ,

$$K_{1,r} + K_{2,r} = \lim_{v_r \rightarrow \infty} \Gamma \circ \Pi_r \circ I_r = \Gamma \circ \Pi_r \circ \Gamma_0. \quad (17)$$

To obtain K_2 , K_1 hence has to be subtracted, which diagrammatically gives

$$\text{Diagram of } K_{2,a} = \text{Diagram of } \Gamma - \text{Diagram of } K_{1,a} \quad (18)$$

in the a channel, and likewise in the p and t channels. Similarly, taking the limit $v_r \rightarrow \infty$ yields the BSEs for $K_{2,r}$. As $K_{2,r}$ and K_2 are related by crossing symmetry, we found equivalent results in both cases up to numerical errors. In Fig. 2, we show a one-dimensional slice of the fulfillment of the BSEs for $K_{2,r}$ w.r.t. ω_r at $v_r = 0$ for the 11|12 Keldysh component in channels a, t and 12|11 in the p channel. We chose these Keldysh components to avoid situations where the data vanish identically. Of course, K_2 depends on two frequencies

independently, and we show another one-dimensional slice of the BSEs w.r.t. v_r at $\omega_r = 0$ in Fig. 3. The K_2 classes have five Keldysh components that are not related by causality and symmetries, which in thermal equilibrium, however, are again related via (generalized) FDRs. We show the full two-dimensional frequency dependence of all of them in Figs. 14, 15 and 16 in App. E.

For the one-dimensional cut through K_2 at $v_r = 0$ in Fig. 2, we observe a generally good fulfillment of the BSEs, again up to a few percent in the a and t channels. As for K_1 discussed previously, the strongest violations occur in the p channel. Especially in the imaginary parts, the peaks become slightly broader and higher after one evaluation of the BSE. As for K_1 , these peaks lie at larger frequencies than for the a and t channels. Since NRG is less accurate at large frequencies due to the logarithmic bath discretization, such a discrepancy is, therefore, unsurprising. Improving the NRG computations in this regard requires a convergence analysis in the bath discretization parameter while retaining a sufficient number of kept states. At present, this is one of the main bottlenecks and out of reach for multipoint calculations.

The other one-dimensional cut through K_2 in Fig. 3 for $\omega_r = 0$, shows a similar result. However, for strong interaction in the a channel, the data is not entirely smooth. Still, the slightly rugged structures can be argued to be negligible in practice. They can be attributed to the conversions between different frequency parametrizations, see App. C.

Looking closely at the two-dimensional plots for the K_2 classes in App. E, one notices that some Keldysh components fulfill the BSE less accurately than others. To highlight this fact, we plot another one-dimensional slice of K_2 at zero bosonic frequency in Fig. 4, this time for the 11|22 component in the a and t channels and the 12|12 component in the p channel. We observe significant mismatches, especially in the real parts, in all three channels. The different Keldysh compo-

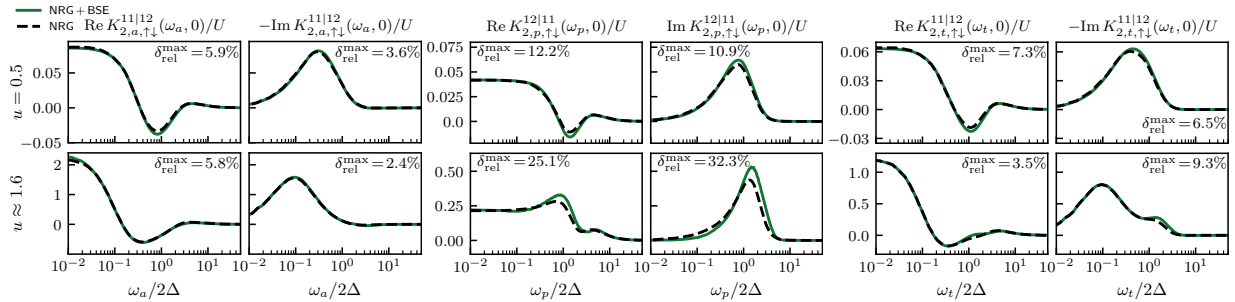


FIG. 2. Fulfillment of the BSE for the $\uparrow\downarrow$ spin component of $K_{2,r}$ in all channels r at zero fermionic frequency, for the 11|12 Keldysh component in channels a, t and the 12|11 Keldysh component in channel p . There generally is good agreement up to a few percent. The strongest violations occur at the peak in the imaginary part of the p channel. As for K_1 , the peaks in the p channel lie at larger frequencies than in the a and t channels. The slight violation of the BSE at those peaks reflects the fact that, due to the logarithmic bath discretization, NRG is less accurate at large frequencies than at small frequencies.

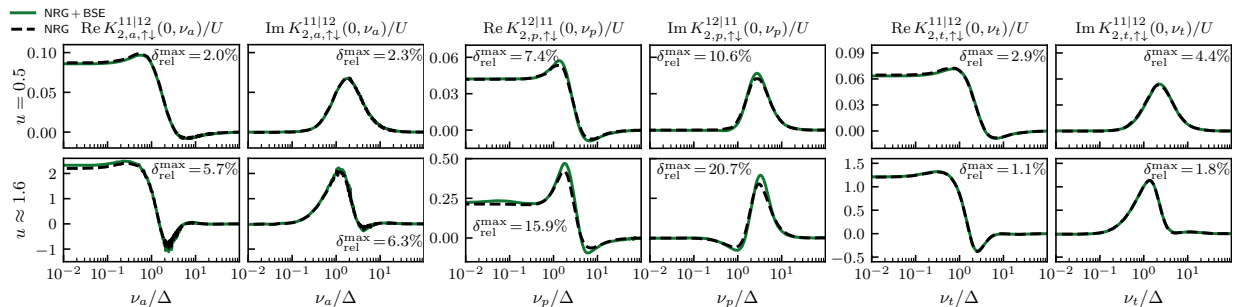


FIG. 3. Fulfillment of the BSE for $K_{2,r}$ as in Fig. 2, but at zero bosonic frequency. We observe that it is satisfied to a similar degree. The rugged structures at small frequencies, particularly visible in the a channel at strong interaction, can be attributed to minor interpolation errors due to different frequency parametrizations used in NRG and QFT.

nents of K_2 are related by generalized FDRs. Since the BSE is very well fulfilled for some components but less for others, one could suspect that generalized FDRs are violated by NRG. However, in App. A we exemplarily study the generalized FDR for the component shown in Fig. 4 and find that it is very well fulfilled. In App. A, we also discuss a symmetry relating $K_{2,p}$ and $K_{2,t}$, observing that it is very well fulfilled, too. We leave it for future work to identify the origin of the discrepancy in the BSE for some Keldysh components of K_2 . Problems with overbroadening of PSFs at very small bosonic frequencies have previously been observed in mpNRG [56], which might also account for the current inconsistencies.

We finally note that, for the strong-interaction dataset, the magnitude of K_2 is comparable to K_1 shown before, whereas at weaker interaction K_2 is much smaller. This shows that the strong-interaction parameters correspond to a regime in which low-order perturbation theory cannot be applied anymore, and evaluating the BSEs thus constitutes a highly non-trivial consistency check of the quality of the NRG data.

B. Schwinger–Dyson equation

The first term of the SDE (8) for the self-energy is a constant. The second term can be evaluated in multiple ways, and we discuss three formally identical methods in the following. First, one can view the full vertex as a single entity and contract it with the bare vertex in any channel r , followed by a loop contraction with G . Diagrammatically, this can be visualized as

$$\text{Diagram of } \Sigma \text{ (circle with } \Sigma \text{)} = - \text{Diagram of } \text{bubble contraction} - \frac{1}{2} \text{Diagram of } \text{loop contraction with } \Gamma \text{.} \quad (19)$$

Numerically, this is the least favorable way to evaluate the SDE, as interpolations of $K_{1,r'} \neq r$, $K_{2(l'),r'} \neq r$ vertex components and Γ_{core} are required to compute the bubble contraction in channel r , due to the different native frequency parametrizations in the three channels. Inaccuracies from channel transformations can be reduced by applying the parquet decomposition to the vertex and contracting each reducible vertex γ with the bare vertex in its native frequency parametrization, closing the missing loop subsequently. We call this strategy simply “SDE”, and it is depicted, e.g., in Fig. 16 of Ref. 6.

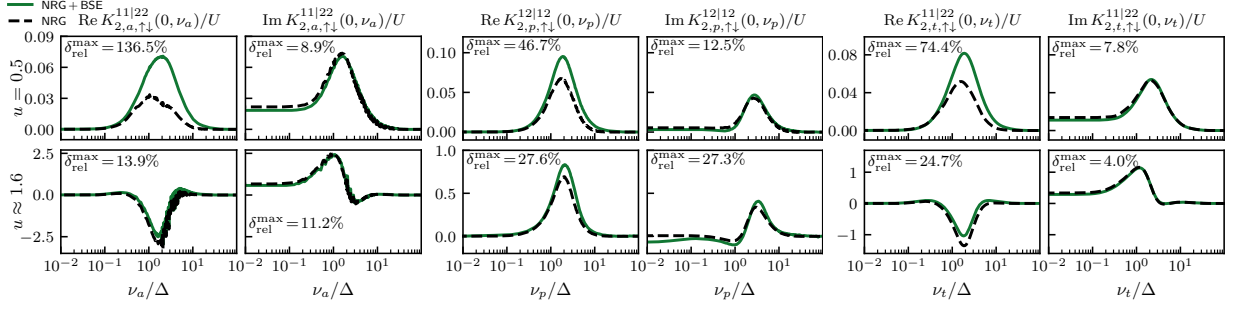


FIG. 4. Fulfillment of the BSE as in Fig. 3, but showing the Keldysh components 11|22 in the a and t channels and 12|12 in the p channel. We observe significant mismatches in the real parts in all three channels, especially at weak interaction.

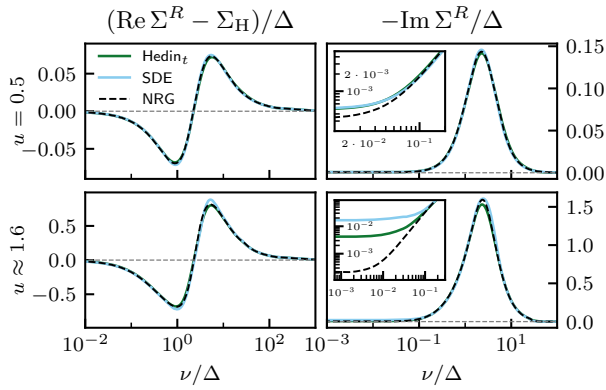


FIG. 5. Real (left) and imaginary (right) parts of the dynamical part of the retarded self-energy. Results for weak and strong interaction are shown in the top and bottom panels, respectively. We compare the results from (i) the “Hedin $_t$ ” version, Eq. (20), where a loop is closed directly over the sum of $K_{1,t}$ and $K_{2,t}$, (ii) the “SDE” version, Eq. (19), where Γ is decomposed into K_1 , K_2 , and K_2' , contracted with Γ_0 in the respective channel, and the contribution from Γ_{core} is contracted in the t channel, and (iii) a “standard” 2p NRG calculation. The “Hedin” version better captures the peaks at finite frequencies and is more accurate in the limit $\nu \rightarrow 0$ than the “SDE” version.

Using a vertex from NRG, this method can only be applied to K_1 , K_2 , and K_2' in each channel, since the vertex core (including K_3) is treated as a single entity (which is here parametrized in the t channel, as the original NRG vertex).

The third way to evaluate the SDE utilizes the BSEs. Contracting the full vertex with the bare vertex in channel r yields $K_{1,r} + K_{2,r}$ in that channel (see, e.g., Eq. (18)). Assuming fulfillment of the BSEs, one can thus evaluate the SDE by closing a loop over $K_{1,r} + K_{2,r}$ directly, without a prior bubble contraction with the bare vertex. Since $K_{1,r} + K_{2,r}$ is a three-point object, we call this the “Hedin $_r$ ” strategy [57], depending on the channel r used. Diagrammatically, it can be depicted as

$$\Sigma_{\text{Hedin}_a} = \text{Diagram of a loop with vertices } K_{1,a} + K_{2,a} \text{ and a bare vertex } \Gamma_0 \text{ attached to the loop.} \quad (20)$$

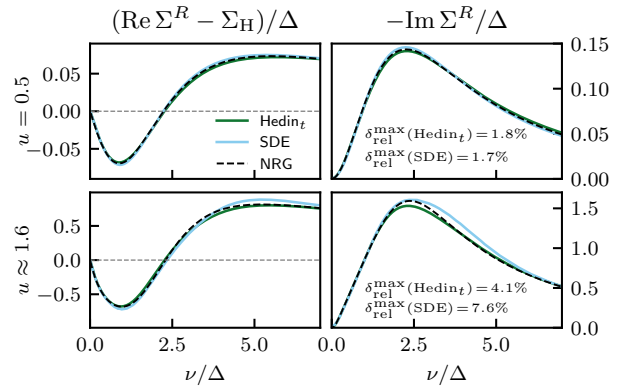


FIG. 6. Same as in Fig. 5, but on a linear frequency scale to make deviations in the high-energy peaks more apparent. Although not entirely perfect, the “Hedin” strategy yields more accurate results at strong interaction. This is easily understood since the “SDE” version requires Γ_{core} , which is more difficult to resolve numerically than K_1 and K_2 used in the “Hedin” version and becomes increasingly more important at large interactions.

in the a channel, and similarly in the other channels. Here, we will use the “Hedin $_t$ ” version to minimize numerical interpolation errors, as the NRG vertex is parametrized in the t channel. Note that it makes no difference whether one uses the sum of $K_{1,r}$ and $K_{2,r}$ or $K_{2',r}$, as both versions are related by crossing symmetry. For a numerically exact result that fulfills the BSEs exactly, all ways of evaluating the SDE should give identical results. However, as seen previously, the NRG vertices satisfy the BSEs only up to a few percent. Furthermore, the vertex core only enters the “SDE” version, which, being the only genuinely three-dimensional object, is more difficult to resolve numerically than K_1 and K_2 used in the “Hedin” version. Lastly, the “SDE” version requires one evaluation of the BSEs for $K_1 + K_2$, as a contraction with the bare vertex to be computed in the first step. This brings about additional interpolation and integration errors.

Indeed, while both methods yield almost identical results at weak interaction, we see at strong interaction in Figs. 5 and 6 that the “Hedin” way of evaluating the SDE reproduces the NRG self-energy more accurately than the “SDE” strat-

egy: Although not entirely perfect, its deviations from the 2p computation at the peaks of the real and imaginary parts of the retarded component, most clearly shown in Fig. 6, are smaller. Furthermore, both methods deviate slightly from the 2p result at very small frequencies. As shown in the insets of Fig. 5, the asymptotic value of $\text{Im}\Sigma^R$ in the limit $\nu \rightarrow 0$ is more accurate for the ‘‘Hedin’’ result, at least for the strong-interaction dataset. We conclude that the NRG vertex fulfills the SDE well, especially if evaluated with the ‘‘Hedin’’ version. Whether this observation carries over to lattice problems, where the self-energy has an additional momentum dependence and cannot be computed with NRG alone, remains to be studied. Indeed, the two strategies for evaluating the SDE might require different ways of treating the momentum dependence; see, e.g., a recent study using the SBE formalism and a truncated-unity approach for the momenta [58].

C. U(1) Ward identity

Finally, we discuss the first-order U(1) Ward identity (WI), which is an exact relation between the self-energy and the vertex. It arises from a local U(1) gauge invariance of the action and all correlation functions. This implies a local continuity equation for the density operator [59]. For electronic models such as the Anderson or Hubbard models, the U(1) WI has been extensively studied in the MF [59–63]. In the KF, however, so far only its dependence on a single frequency argument for the special case of vanishing transfer frequency was investigated [5, 64]. Here, we study a new, more general ‘‘two-dimensional’’ version (depending on two independent frequencies) of this WI in the KF. Using frequency conservation, spin conservation, and spin-flip symmetry (the latter two following from SU(2) spin symmetry), it reads

$$\begin{aligned} & \Sigma^{\bar{\alpha}_1'|\alpha_1}(\nu_+) - \Sigma^{\alpha_1'|\bar{\alpha}_1}(\nu_-) \\ & \stackrel{!}{=} \sum_{\alpha_2'\alpha_2\alpha_3} \int \frac{d\tilde{\nu}}{2\pi i} \left\{ \omega G^{\alpha_3|\alpha_2'}(\tilde{\nu}_+) \Gamma_D^{\alpha_2'\alpha_1'|\alpha_2\alpha_1}(\omega, \nu, \tilde{\nu}) G^{\alpha_2|\alpha_3}(\tilde{\nu}_-) \right. \\ & + \sum_{\alpha_1} \left[\Delta^{\bar{\alpha}_2|\alpha_1}(\tilde{\nu}_+) G^{\alpha_1|\alpha_2'}(\tilde{\nu}_+) \Gamma_D^{\alpha_2'\alpha_1'|\alpha_2\alpha_1}(\omega, \nu, \tilde{\nu}) G^{\alpha_2|\alpha_3}(\tilde{\nu}_-) \right. \\ & \left. \left. - G^{\alpha_3|\alpha_2'}(\tilde{\nu}_+) \Gamma_D^{\alpha_2'\alpha_1'|\alpha_2\alpha_1}(\omega, \nu, \tilde{\nu}) G^{\alpha_2|\alpha_1}(\tilde{\nu}_-) \Delta^{\alpha_1|\bar{\alpha}_2}(\tilde{\nu}_-) \right] \right\}, \end{aligned} \quad (21)$$

where $\Gamma_D = \Gamma_{t,\uparrow\uparrow} + \Gamma_{t,\uparrow\downarrow}$ and we defined the short-hand notation $\nu_{\pm} = \nu \pm \frac{\omega}{2}$ (and, likewise, for $\tilde{\nu}$). A bar over a Keldysh index means that this index is flipped ($\bar{1} = 2$; $\bar{2} = 1$). We provide a detailed derivation of Eq. (21) in App. III C and the appendices referenced therein. Let us note that Eq. (21) is not restricted to thermal equilibrium but holds in the non-equilibrium steady-state as well. For explicitly time-dependent problems, the more general form, Eq. (F22), also derived in App. III C, should be used. Let us also note that there is no contribution to Eq. (21) to first order in the bare interaction Γ_0 : For the self-energies on the LHS, the first-order contribution comes simply from the constant Hartree term and

$\alpha_1' \backslash \alpha_1$	1	2
1	$-2i\text{Im}\Sigma^R(\nu)$	$-\Sigma^K(\nu)$
2	$\Sigma^K(\nu)$	$2i\text{Im}\Sigma^R(\nu)$
$\alpha_1' \backslash \alpha_1$	1	2
1	$2[\Sigma^A(\frac{\omega}{2}) - \Sigma_H]$	$\Sigma^K(\frac{\omega}{2})$
2	$\Sigma^K(\frac{\omega}{2})$	$2[\Sigma^R(\frac{\omega}{2}) - \Sigma_H]$

TABLE I. Top: LHS of Eq. (21) for $\omega = 0$. Bottom: LHS of Eq. (21) for $\nu = 0$ and particle-hole symmetry.

vanishes upon taking the difference. Consequently, the first-order contribution to the RHS must vanish, too. This is easily verified by replacing $\Gamma \rightarrow \Gamma_0$ and $G \rightarrow G_0$ and performing the integral (which can be done analytically). Therefore, the WI provides a non-trivial consistency check for the higher-order dynamical parts of Γ .

Note that another WI follows from SU(2) spin symmetry. It is almost identical to Eq. (21), the only difference being that, instead of Γ_D , the $\Gamma_M = \Gamma_{t,\uparrow\uparrow} - \Gamma_{t,\uparrow\downarrow}$ component is required on the RHS. For more details on the SU(2) WI, see App. G 4.

We now restrict ourselves to $\alpha_1' = \alpha_1 = 2$ and consider two one-dimensional limits: First, as shown in App. G 6, in the wide-band limit and for $\omega = 0$, one recovers the special form of the WI studied in Refs. 5 and 64,

$$\begin{aligned} -2\text{Im}\Sigma^R(\nu) &= \frac{\Delta}{i\pi} \int d\tilde{\nu} G^R(\tilde{\nu}) G^A(\tilde{\nu}) \left\{ \Gamma_{\uparrow\downarrow+\uparrow\uparrow}^{12|21}(\tilde{\nu}, \nu|\nu, \tilde{\nu}) \right. \\ & \left. - \tanh\left(\frac{\tilde{\nu}}{2T}\right) \left[\Gamma_{\uparrow\downarrow+\uparrow\uparrow}^{12|22}(\tilde{\nu}, \nu|\nu, \tilde{\nu}) - \Gamma_{\uparrow\downarrow+\uparrow\uparrow}^{22|21}(\tilde{\nu}, \nu|\nu, \tilde{\nu}) \right] \right\}. \end{aligned} \quad (22)$$

Note that Σ could generally retain an additional anomalous contribution coming from the RHS of Eq. (21) in the limit $\omega \rightarrow 0$ if the vertex behaves like $1/\omega$. Since the vertex of the Anderson impurity model is continuous and non-singular, we neglect this part here.

Second, for the case of particle-hole symmetry, one obtains another equation for the imaginary part of Σ^R from the other one-dimensional limit $\nu = 0$: Using $\Sigma^R(\nu) - \Sigma_H = -[\Sigma^A(-\nu) - \Sigma_H]$ at particle-hole symmetry, its LHS becomes

$$\Sigma^R\left(\frac{\omega}{2}\right) - \Sigma^A\left(-\frac{\omega}{2}\right) = 2[\Sigma^R\left(\frac{\omega}{2}\right) - \Sigma_H]. \quad (23)$$

For completeness, we list all four Keldysh components of the LHS of Eq. (21) for the special cases $\omega = 0$ in the top part of Tab. I and $\nu = 0$ together with particle-hole symmetry in the bottom part of Tab. I. Since all components are related either via complex conjugation or via the FDR, Eq. (13), we focus on only one component, $\alpha_1' = \alpha_1 = 2$.

We first test the WI for $\omega = 0$, which yields the imaginary part of Σ , see Eq. (22) and Tab. I. In Fig. 7, we observe excellent fulfillment of the WI, especially at weak interaction. Only at strong interaction, $-\text{Im}\Sigma^R$ reaches unphysical negative values at small frequencies, albeit of rather small magnitude. In NRG, the correct sign of $\text{Im}\Sigma^R$ is enforced by the symmetric improved estimator [55].

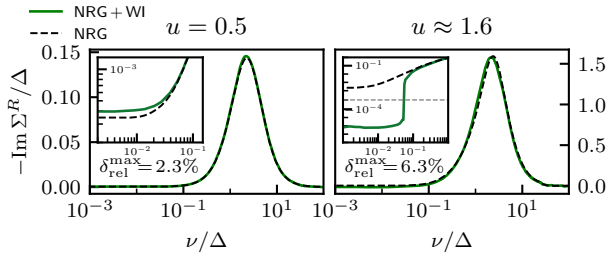


FIG. 7. Fulfillment of the U(1) WI (22) for $\omega = 0$ and $\alpha_l = 2$. We observe excellent fulfillment, especially at weak interaction. Only at strong interaction and very small frequencies, $-\text{Im}\Sigma^R$ reaches unphysical negative values.

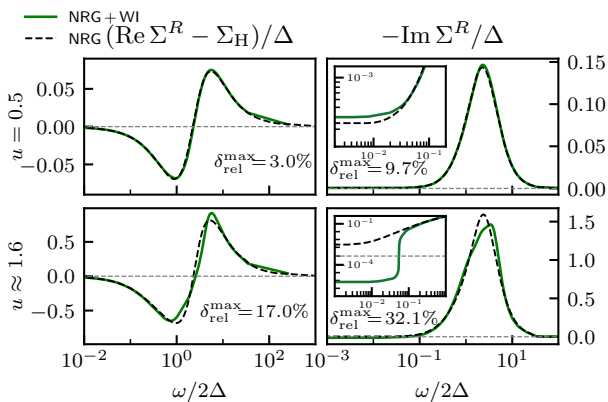


FIG. 8. Fulfillment of the U(1) WI (23) valid at particle-hole symmetry at $\nu = 0$ for $\alpha_l = \alpha_1 = 2$. The real and imaginary parts are shown on the left and right, weak and strong interactions at the top and bottom, respectively. We observe good fulfillment of the WI, especially at weak interaction. At strong interaction, the peaks of both $\text{Re}\Sigma^R$ and $\text{Im}\Sigma^R$ are not reproduced very accurately by the WI, and $-\text{Im}\Sigma^R$ again shows unphysical negative values at small frequencies.

Next, we investigate the $\nu = 0$ limit of the WI, which gives both real and imaginary parts of Σ . Figure 8 shows good fulfillment of the WI throughout, especially at weak interaction. At strong interaction, the peaks in both $\text{Re}\Sigma^R$ and $\text{Im}\Sigma^R$ are captured less accurately and $-\text{Im}\Sigma^R$ again becomes negative at small frequencies. The inaccuracies in the peaks probably stem from the first term on the RHS of Eq. (21), involving a factor ω which might exacerbate the numerical inaccuracies of the NRG vertex at large ω . By contrast, in the other one-dimensional limit $\omega = 0$, this term is zero.

The full two-dimensional frequency dependence of the generalized WI, one of the main results of this work, is plotted in Fig. 9. There, we see once more that the qualitative fulfillment of the WI is excellent throughout. Quantitatively, the largest deviations occur along the one-dimensional cuts at $\nu = 0$, shown already in Fig. 8.

IV. CONCLUSION

In this paper, we scrutinized the real-frequency 4p vertex of the single-impurity Anderson model as computed by NRG. We performed numerical consistency checks for the 2p self-energy and the 4p vertex based on the parquet equations and the generalized U(1) WI. The latter was derived, for the first time, in full generality in the KF. We investigated two data sets: One at weak interaction, where perturbative approaches like the parquet approximation are justified, and one in a non-perturbative regime at strong interaction. We generally found good agreement throughout, often up to a few percent. Only in a small number of cases did major discrepancies, worth addressing in the future, appear. Some underestimated peaks in a few Keldysh components of K_2 suggest that the multipoint NRG calculations might not have been converged in all numerical parameters.

We tested two numerically nonequivalent ways of evaluating the SDE for the self-energy and found that it is fulfilled well both times, but especially using the ‘‘Hedin’’ strategy, where the K_1 and K_2 classes of the vertex are used directly. This is because the more naive evaluation of the SDE includes the vertex core and requires an intermediate contraction with a bare vertex, which introduces additional numerical errors. In the final part of the paper, we observed that the generalized WI is fulfilled well for both datasets. Only at strong interaction, minor deviations appeared, particularly in the imaginary part at small frequencies.

The very good fulfillment of the QFT equations studied in this work in our view encourages the use of the NRG vertex and self-energy as a starting point for a non-local diagrammatic extension of DMFT for lattice problems. To this end, several further steps need to be taken. First, the computation of correlation functions such as the vertex from PSFs should be significantly accelerated: Using quantum tensor cross interpolation (QTCI) [65–68], an exponentially fine resolution for the vertex can be afforded at linear cost, provided the vertex is compressible. Indeed, in a recent proof-of-principle study in the MF, the parquet equations for the single-impurity Anderson model were solved entirely in the QTCI framework [69]. First numerical experiments indicate that the vertex is compressible even in the KF, at least up to the percent level. Furthermore, the computation of the vertex from PSFs can be formulated and carried out entirely in the QTCI language, thereby significantly reducing the required numerical costs. An efficient implementation of this procedure is underway [70]. Second, including additional momentum dependencies of correlation functions in the KF has so far not been feasible due to the additional numerical cost and, especially, the memory demand. Again, the QTCI framework promises a solution to that problem, as it can be generalized to functions that depend on arbitrarily many multidimensional variables.

Third, to enable calculations for experimentally studied correlated materials, the formalism and numerical codes must be generalized to multi-orbital models. Here, NRG quickly encounters a fundamental barrier, as the numerical effort of NRG computations for multi-orbital models increases exponentially in the number of orbitals. At the time of this writ-

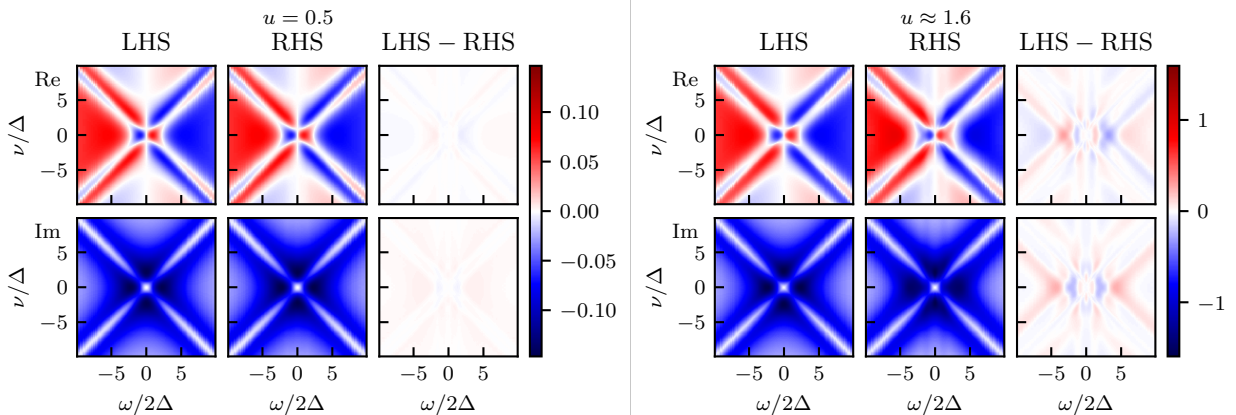


FIG. 9. Generalized U(1) WI (21) for $\alpha_1' = \alpha_1 = 2$, across its full two-dimensional real-frequency dependence for both weak and strong interaction. The qualitative fulfillment of the WI is excellent throughout.

ing, standard NRG calculations are limited to four orbitals and multipoint NRG is limited to at most two orbitals. One could try using a different method than NRG for computing the local self-energy and vertex. A promising candidate currently being developed is a “tangent-space Krylov solver” [71], a tensor-network technique that iteratively generates dynamical contributions on top of a ground state produced by the density matrix renormalization group [72]. First numerical experiments show that this approach can be straightforwardly applied to multi-orbital models. Furthermore, it promises to be more accurate than NRG at large frequencies, since it does not rely on logarithmic discretization [73]. However, this approach has not yet been generalized to finite temperature and, most importantly, to multipoint functions.

Regarding the WI, for future perturbative diagrammatic calculations which employ, e.g., the parquet approximation, one might think of replacing the SDE of the parquet formalism with the WI. For instance, the one-dimensional special case, Eq. (22), could be used to compute the imaginary part of the retarded self-energy from the vertex. Using the Kramers–Kronig relation and the FDR, all components of Σ follow from that result. At the cost of possibly violating the SDE, the U(1) local gauge invariance implying fulfillment of the local continuity equation for the density operator would then be granted on the 2p and 4p level, which is not given in the standard parquet approximation with the SDE. Especially in the context of non-equilibrium calculations in the KF, where charge conservation is essential, this might prove useful.

DATA AND CODE AVAILABILITY

NRG computations were performed with the MuNRG package [4, 74, 75] based on the QSpace tensor library [76–79]. The latest version of QSpace is available [80], and a public release of MuNRG is intended. The code used for the evaluation of the parquet equations and the WI is an extension of the KELDYSHQFT package and can be found on GitHub, see

Ref. 51. The raw data, data analysis, and plotting scripts can be found in Ref. 81.

ACKNOWLEDGMENTS

We thank Jeongmin Shim, Jae-Mo Lihm and Seung-Sup Lee for generating and sharing some of the PSF data used for the vertex computations and Jae-Mo Lihm and Seung-Sup Lee for insightful comments on the manuscript. The authors gratefully acknowledge the computational resources given by grant INST 86/1885-1 FUGG of the German Research Foundation (DFG) and the Gauss Centre for Supercomputing e.V. for funding this project by providing computing time on the GCS Supercomputer SuperMUC-NG at the Leibniz Supercomputing Centre in Munich. NR acknowledges funding from a graduate scholarship from the German Academic Scholarship Foundation (“Studienstiftung des deutschen Volkes”) and additional support from the “Marianne-Plehn-Programm” of the state of Bavaria. NR, AG, MF, MP, and JvD were supported by the Deutsche Forschungsgemeinschaft under Germany’s Excellence Strategy EXC-2111 (Project No. 390814868), and through the project LE3883/2-2, and by the Munich Quantum Valley, supported by the Bavarian state government with funds from the Hightech Agenda Bayern Plus. NR, AG, MF, and MP acknowledge support from the International Max Planck Research School for Quantum Science and Technology (IMPRS-QST). FBK acknowledges funding from the Ministry of Culture and Science of the German State of North Rhine-Westphalia (NRW Rückkehrprogramm). The Flatiron Institute is a division of the Simons Foundation.

APPENDICES

In App. A, we comment on the surprisingly large violation of the BSE for $K_{2,p}$, observed in Fig. 3 at weak interaction. The following appendices provide details on many technical

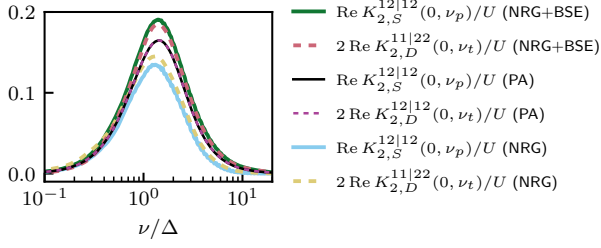


FIG. 10. Both sides of Eq. (A8) for the NRG vertex and for the result after a single evaluation of the BSE at weak interaction, $u = 0.5$. Like in Fig. 3, the BSE is clearly violated. However, the symmetry relation (A8) is fulfilled very well by NRG and, by extension, also for the NRG+BSE result. We conclude that the discrepancy is not due to an inconsistency of the NRG vertex on the level of the symmetry, Eq. (A8). Instead, it seems that some Keldysh components of the K_2 vertex suffer from inaccuracies in NRG, given the numerical settings summarized in App. B. This suspicion is supported by the deviation of NRG from an independently obtained solution of the parquet equations in the PA, shown as a black dotted line, which are unexpectedly large at the weak interaction $u = 0.5$.

aspects: In App. B, we specify the numerical parameters chosen for the self-energy and vertex computations with NRG. In App. C, we summarize the differences between the conventions used in the mpNRG and KELDYSHQFT codes and explain how to convert the vertex from one convention to the other. In App. D, we take a closer look at the BSE at very large frequencies and show that inaccuracies due to the finite size of the frequency grid are minimal. In App. E, we show the full frequency dependence of all non-trivial Keldysh components of K_2 and their BSEs, which were omitted in the main text. In App. F, we derive the generalized WI in the KF studied in the main text. Finally, the subsections of App. G detail several, in part lengthy calculations required for the preceding sections.

Appendix A: Comment on the violation of the BSE for K_2

In Fig. 4, we observed a surprisingly large mismatch in the height of the peak of the real part in all channels at weak interaction. Here, we take a closer look at this discrepancy and perform two more consistency checks: First, as derived in Ref. 82, particle-hole symmetry and SU(2) spin symmetry can be exploited to relate certain spin components of the 2PR vertices in the p and t channels. Using the notation $\Gamma_{\uparrow\downarrow\uparrow\downarrow} \equiv \Gamma_{\uparrow\downarrow}$, $\Gamma_{\uparrow\downarrow\downarrow\uparrow} \equiv \Gamma_{\uparrow\downarrow}$, $\Gamma_{\uparrow\uparrow\uparrow\uparrow} \equiv \Gamma_{\uparrow\uparrow}$, we define the commonly used “singlet”, “triplet”, “magnetic” and “density” spin components as

$$S/T = \uparrow\downarrow \mp \overline{\uparrow\downarrow} \quad (\text{A1a})$$

$$M/D = \uparrow\uparrow \mp \uparrow\downarrow \quad (\text{A1b})$$

By particle-hole, SU(2) spin and crossing symmetry, the full vertex Γ fulfills the relation (see Eq. (2.135) in [82])

$$\Gamma_{1'2'|12}^{\uparrow\downarrow} = \Gamma_{21'|12'}^{\uparrow\uparrow} + \Gamma_{11'|22'}^{\uparrow\downarrow}, \quad (\text{A2})$$

where the multi-indices comprise all vertex arguments except spin. Combining Eqs. (A1) and Eq. (A2), one obtains

$$\Gamma_{1'2'|12}^{S/T} = \Gamma_{21'|12'}^{D/M} \pm \Gamma_{11'|22'}^{D/M}, \quad (\text{A3})$$

where crossing symmetry was employed once. From Eq. (A3), we can derive corresponding equations for the asymptotic classes. Focusing on K_2 , where the large discrepancy occurs in Fig. 4, we insert the native frequency parametrization in the p channel [5],

$$(v_1', v_2' | v_1, v_2)_p = \left(\frac{\omega}{2} + v, \frac{\omega}{2} - v | \frac{\omega}{2} + v', \frac{\omega}{2} - v'\right), \quad (\text{A4})$$

which gives

$$\begin{aligned} & \Gamma_{1'2'|12}^{S/T} \left(\frac{\omega}{2} + v, \frac{\omega}{2} - v | \frac{\omega}{2} + v', \frac{\omega}{2} - v'\right) \\ &= \Gamma_{21'|12'}^{D/M} \left(v' - \frac{\omega}{2}, \frac{\omega}{2} + v | \frac{\omega}{2} + v', v - \frac{\omega}{2}\right) \\ & \quad \pm \Gamma_{11'|22'}^{D/M} \left(-v' - \frac{\omega}{2}, \frac{\omega}{2} + v | \frac{\omega}{2} - v', v - \frac{\omega}{2}\right). \end{aligned} \quad (\text{A5})$$

Exchanging external legs from in- to outgoing or vice versa leads to a sign flip in the corresponding frequency arguments. This is due to our convention used for Fourier transforms, see also App. G 3 below, and has been accounted for in Eq. (A5). The remaining indices now only label Keldysh components. Comparing to the native parametrization in the t channel [5],

$$(v_1', v_2' | v_1, v_2)_t = \left(v' + \frac{\omega}{2}, v - \frac{\omega}{2} | v' - \frac{\omega}{2}, v + \frac{\omega}{2}\right), \quad (\text{A6})$$

we can write Eq. (A5) as

$$\begin{aligned} \Gamma_{1'2'|12;p}^{S/T}(\omega, v, v') &= \Gamma_{21'|12';t}^{D/M}(-\omega, v, v') \\ & \quad \pm \Gamma_{11'|22';t}^{D/M}(-\omega, v, -v'), \end{aligned} \quad (\text{A7})$$

where the additional subscript labels the native frequency parametrization used. Taking the limit $v' \rightarrow \infty$ results in an equation for K_2 . Focusing on the S spin component and the $12|12$ Keldysh component (see Fig. 4) gives

$$\begin{aligned} K_{2,S}^{12|12}(\omega_p, v_p) &= K_{2,D}^{21|12}(-\omega_t, v_t) + K_{2,D}^{11|22}(-\omega_t, v_t) \\ &= 2K_{2,D}^{11|22}(-\omega_t, v_t), \end{aligned} \quad (\text{A8})$$

where we used that the $21|12$ and $11|22$ Keldysh components of $K_{2,t}$ are identical, since they are connected by parity, see Eq. (4.48b) in Ref. 5.

Setting $\omega_r = 0$, we plot in Fig. 10 both sides of Eq. (A8) for the NRG vertex and for the result after a single evaluation of the BSE at weak interaction. As was the case in Fig. 4, there is a significant mismatch between the two results. However, Eq. (A8) is fulfilled very well for the NRG vertex. Since the BSEs are symmetric by construction, the NRG+BSE result is then symmetric as well, which is indeed confirmed in Fig. 10. We conclude that the violation of the BSE is not inherent to the p channel alone but that the NRG vertex is consistent on the level of Eq. (A8). For comparison, in Fig. 10, we also plot the result from a solution of the parquet equations in the PA, independently obtained with our KELDYSHQFT code [51].

Due to the small influence of the higher-order contributions to the 2PI vertex R , neglected in the PA, at weak interaction $u = 0.5$, one would expect good agreement between the PA and NRG. However, while this is the case at small frequencies, the peak for $v/\Delta \gtrsim 1$ does not match. It is hence no surprise that the NRG result does not fulfill the BSE, since it deviates from the PA result (which fulfills the BSE by construction). Improving the NRG result requires numerically more challenging parameter settings: Increasing the number of frequency bins per decade or reducing the discretization parameter would presumably give more accurate results (see also App. B for details on the NRG parameters). Finding suitably optimized parameter settings for NRG would go beyond the scope of this paper and is left for future work.

Second, we exemplarily study the generalized FDR for $K_{2,S}^{12|12}$. It can be derived from Eq. (84) in Ref. [54] and reads

$$K_{2,S}^{12|12}(\omega_p, \nu_p) = \coth\left(\frac{-\omega_p}{2T}\right) \left[K_{2,S}^{21|11}(\omega_p, \nu_p)^* - K_{2,S}^{12|11}(\omega_p, \nu_p) \right] + \tanh\left(\frac{\nu_p + \omega_p/2}{2T}\right) \left[K_{2,S}^{21|11}(\omega_p, \nu_p)^* - K_{2,S}^{22|12}(\omega_p, \nu_p) \right]. \quad (\text{A9})$$

Evaluating and comparing the LHS and the RHS of Eq. (A9) for the NRG vertex and the NRG vertex after one evaluation of the BSE at weak interaction yields Fig. 11. We see that the FDR is fulfilled exceptionally well both times. Very minor inaccuracies occur in the NRG+BSE result, which can be attributed to the finite numerical accuracy of the integrations required for evaluating the BSE. Strictly speaking, the one-dimensional cut at $\omega_p = 0$ had to be excluded in Fig. 11, due to the diverging coth term on the RHS of Eq. (A9). Therefore, we show an additional one-dimensional plot at $\omega_p = 0$ in Fig. 12, taking the limit properly: Using the short-hand notation $\left[K_{2,S}^{21|11}(\omega_p, \nu_p)^* - K_{2,S}^{12|11}(\omega_p, \nu_p) \right] \equiv \tilde{K}_2(\omega_p)$, we employ L'Hôpital's rule to approximate the first term on the RHS of Eq. (A9) as

$$\lim_{\omega_p \rightarrow 0} \coth\left(\frac{-\omega_p}{2T}\right) \tilde{K}_2(\omega_p) \approx -2T \frac{\tilde{K}_2(0+\Delta\omega_p) - \tilde{K}_2(0-\Delta\omega_p)}{2\Delta\omega_p}, \quad (\text{A10})$$

where we approximated the derivative by a finite difference ($\Delta\omega_p$ is the step size of the frequency grid around $\omega_p = 0$). This way, we obtain Fig. 12, where, for $\omega_p = 0$ too, the generalized FDR is fulfilled very well. We conclude that the NRG vertex is consistent on the level of the symmetries and the generalized FDR exemplarily checked in this section.

Appendix B: NRG computations

The NRG computations performed for this work are based on the QSpace tensor library [76–80]. We employ the full density-matrix NRG [83, 84], using adaptive broadening [74, 75] for obtaining 2p dynamical correlators. The 4p vertex was computed using the recent generalization of the NRG

	Λ	n_z	N_{keep}	E_{step}	σ_{LG}	γ_{L}	α	γ
Σ	2	6	5000	—	—	—	2	4
K_1, K_2	4	4	300/200	16	0.4	T	—	—
Γ_{core}	4	4	300/200	8/16	0.4	T	—	—

TABLE II. NRG parameters for the self-energy and vertex calculations. If two values are specified, the first (second) one corresponds to the setting for weak (strong) interaction.

method to multipoint functions [3, 4]. Symmetric improved estimators were used both for the self-energy [55] and the vertex [17]. To compute the vertex, the PSF produced by NRG had to be convoluted with the appropriate kernel functions. In order to do so on logarithmic grids with reasonable computational effort, we employed the following strategy (described in more detail in Ref. [70]): The broadened Keldysh frequency kernels were first precomputed on extremely fine, equidistant, one-dimensional grids with a grid spacing of $100/2^{15} \approx 0.003$ in units of the hybridization parameter Δ . The resulting kernel functions were brought into matrix form and compressed using SVDs with a tolerance of 10^{-6} . To obtain the vertex, these compressed kernel matrices were contracted with the PSFs, using trilinear interpolation from points on a cuboid surrounding the respective frequency points of the logarithmic grid.

We state the numerical parameters chosen for the NRG calculations in Tab. II. Λ is the Wilson parameter used to logarithmically discretize the non-interacting bath. (The limit $\Lambda \searrow 1$ would correspond to the original continuous bath.) Spectral data are averaged over n_z shifted versions of the logarithmic discretization grid, following Žitko's discretization scheme [85, 86]. N_{keep} specifies the maximal number of kept SU(2) multiplets in each shell during the iterative diagonalization. In principle, a convergence analysis in both n_z and N_{keep} would be required to produce optimal results. While $N_{\text{keep}} = 5000$ from experience is large enough to compute the self-energy accurately, this is unfeasible numerically for the multi-point vertex computations at this point.

E_{step} specifies the number of frequency bins per decade on the logarithmic grid for the PSFs of the vertex. σ_{LG} and γ_{L} are broadening parameters used for the log-Gaussian broadening of the PSFs, see, e.g., see App. E.2 in Ref. 17. In contrast to Ref. 17, where $\sigma_{\text{LG}} = 0.3$ and $\gamma_{\text{L}} = 0.5T$ were used for the vertex at strong interaction, we chose the slightly larger broadening employed already for weak interaction. The reason is that we observed slight under-broadening of $\tilde{K}_{2,r}$ at small frequencies with the broadening parameters of Ref. 17. α and γ are similar broadening parameters used in the log-Gaussian broadening for 2p NRG computations, as specified in Eqs. (17b) and (21) of Ref. 74.

Appendix C: Conversions between mpNRG and QFT conventions

To convert the Keldysh vertex from the conventions of NRG, as, e.g., outlined in Ref. 17, to the conventions of the KELDYSHQFT code [5–7], the following steps must be taken:

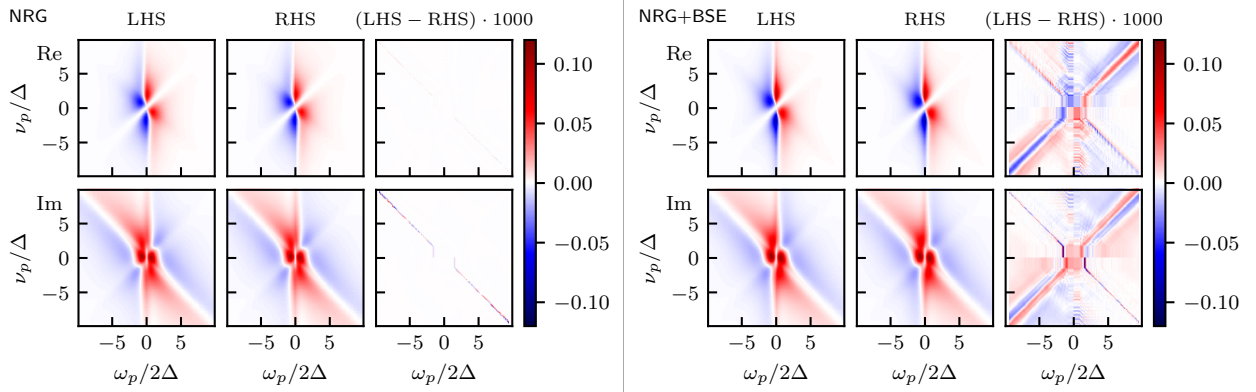


FIG. 11. Fulfillment of the generalized FDR (A9) for $K_{2,S}^{12|12}(\omega_p, \nu_p)$ at weak interaction from the NRG vertex (left) and after one evaluation of the BSE (right). Both times, the FDR is fulfilled exceptionally well. The slight discrepancies across the anti-diagonal $\nu_p + \omega_p/2 = 0$ are negligible interpolation errors where the second term in Eq. (A9) vanishes. In addition, very minor additional inaccuracies appear in the NRG+BSE result. We attribute these to the finite numerical accuracy of the integrations required for evaluating the BSE.

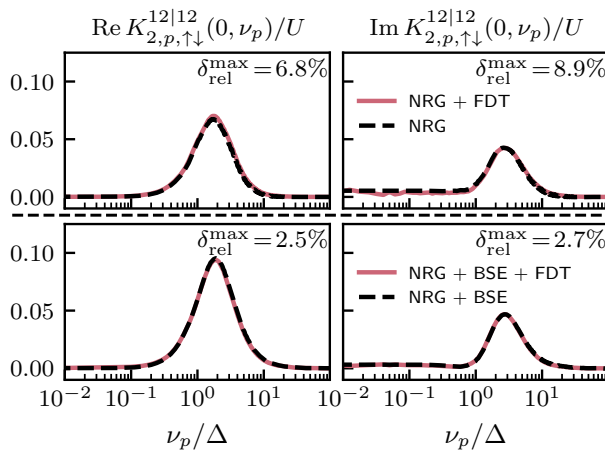


FIG. 12. Same as Fig. 11 for $\omega_p \rightarrow 0$, evaluated as explained in Eq. (A10). Also in this case, the generalized FDR is fulfilled very well. The minor wiggles in the top right panel at small frequencies probably stem from the finite difference used in Eq. (A10).

- (i) multiply the vertex by a global sign
- (ii) swap the middle Keldysh indices $(12|34) \leftrightarrow (13|24)$
- (iii) swap $K_{2,p} \leftrightarrow K_{2',p}$
- (iv) convert the frequency parametrization according to

$$[\omega_t]^{NRG} = -\omega_t \quad (C1a)$$

$$[v_t]^{NRG} = v_t' + \frac{\omega}{2} \quad (C1b)$$

$$[v_t']^{NRG} = v_t + \frac{\omega}{2}. \quad (C1c)$$

Using the conversions between the t -channel and the a - and p -channel parametrizations as given in App. A of Ref. 5, we

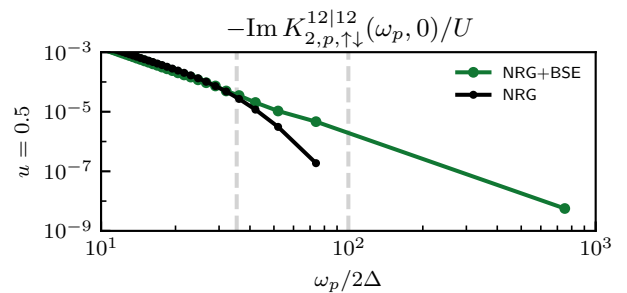


FIG. 13. One-dimensional slice through one component of K_2 , cf. Fig. 2, on logarithmic axes. The dots indicate the frequency grid points chosen in the KELDYSHQFT code used to evaluate the BSE, onto which the NRG data was interpolated. The first vertical dashed line marks the maximal frequency at which all NRG vertex components required for evaluating the BSE were available. The second dashed line marks the maximal frequency for which the shown vertex component was computed by NRG. Starting at the first dashed line, we see very minor deviations below 0.1% compared to the maximal value of the vertex component shown.

further have

$$[\omega_t]^{NRG} = v_a' - v_a = v_p' - v_p \quad (C2a)$$

$$[v_t]^{NRG} = v_a - \frac{\omega_a}{2} = v_p + \frac{\omega_p}{2} \quad (C2b)$$

$$[v_t']^{NRG} = v_a + \frac{\omega_a}{2} = -v_p' + \frac{\omega_p}{2}. \quad (C2c)$$

Appendix D: Fulfillment of the BSE at large frequencies

In this section, we show that the finite extent of the frequency grid only minimally influences the fulfillment of the BSE. Figure 13 shows a one-dimensional slice through one component of K_2 , corresponding to one panel in Fig. 2, focusing on the region at very large frequencies. The black

line shows the vertex component as computed by NRG, already interpolated onto the frequency grid chosen in the KELDYSHQFT code. The green line shows the same component after one evaluation of the BSE with the same code. Two vertical dashed lines highlight special points on the frequency axis: The one at $\frac{\omega_p}{2\Delta} = 100$ marks the maximal frequency for which the shown vertex component had been computed by NRG. The other one at $\frac{\omega_p}{2\Delta} = \frac{100}{2\sqrt{2}} \approx 35$ marks the maximal frequency where all NRG vertex components needed for evaluating the BSE were available. It is smaller than the other frequency due to the $\omega/2$ shifts in the QFT parametrizations and the rotations required when transforming between native channel parametrizations, see App. C. We see that, up to this point, the fulfillment of the BSE is close to perfect. Afterwards, small deviations appear, which is to be expected, since not all components required on the RHS of the BSE are available anymore. However, the deviations are smaller than 0.1%, compared to the height of the peak of the component shown, cf. Fig. 2, and hence numerically negligible. Beyond the second dashed line, no NRG data is available anymore.

Appendix E: Full frequency dependence of K_2

In Sec. III A, we restricted the discussion of the fulfillment of the BSEs for K_2 to two one-dimensional slices through a single Keldysh component. For completeness, we show the full two-dimensional frequency dependence of all five nonequivalent Keldysh components of K_2 in Figs. 14, 15, and 16. We plot the vertex components as produced by NRG in the first rows, the result after a single evaluation of the BSE (18) in the second, and their absolute difference in the third. As always, we show data for both weak and strong interaction, whereas we restricted the frequency interval shown for strong interaction to smaller frequencies than for weak interaction to make the non-trivial structures of the vertex more clearly visible. In accordance with our discussion in Sec. III A, we observe good agreement of the BSE throughout. Notably, many components show sharp structures around $\omega_r = 0$, which are nevertheless extended along the v_r direction, in particular in the a and t channels, already at weak interaction. Resolving these accurately poses a numerical challenge.

Appendix F: Derivation of the generalized U(1) Ward identity in the KF

The goal of this section is to provide a self-contained derivation of one of the main results of this work, namely the general two-dimensional form of the U(1) WI in the KF, Eq. (21). We start from textbook definitions of the basic quantities involved and lay out all required calculations without omitting technical details.

1. Setup and definitions

Our starting point is the partition function expressed using a functional integral and the action, which contains a non-interacting as well as an interacting term,

$$\mathcal{Z} = \int \mathcal{D}[\bar{d}, d] e^{iS[\bar{d}, d]} \quad (\text{F1})$$

$$\begin{aligned} S[\bar{d}, d] &= S_0[\bar{d}, d] + S_{\text{int}}[\bar{d}, d] \\ &= \int_{\mathcal{C}} dt \left\{ \int_{\mathcal{C}} dt' \bar{d}_{\sigma_1'}^{j_1'}(t') [G_0^{-1}]_{\sigma_1'}^{j_1'}(t'|t) d_{\sigma_1}^{j_1}(t) \right. \\ &\quad \left. + \frac{1}{4} \bar{d}_{\sigma_1'}^{j_1'}(t) \bar{d}_{\sigma_2'}^{j_2'}(t) [\Gamma_0]_{\sigma_1' \sigma_2'}^{j_1' j_2'} d_{\sigma_2}^{j_2}(t) d_{\sigma_1}^{j_1}(t) \right\} \quad (\text{F2}) \end{aligned}$$

$$[G_0^{-1}]_{\sigma_1'}^{j_1'}(t'|t) = \delta_{\mathcal{C}}(t' - t) \delta_{j_1', j_1} \delta_{\sigma_1', \sigma_1} i \partial_t - h_{\sigma_1' \sigma_1}^{j_1' j_1}(t'|t). \quad (\text{F3})$$

Here, G_0^{-1} is the inverse bare propagator and $h_{\sigma_1' \sigma_1}^{j_1' j_1}(t'|t)$ the single-particle Hamiltonian, which for the SIAM contains the level shift and the hybridization function. In this expression, repeated indices are meant to be summed over and time integrations are performed over the Keldysh contour \mathcal{C} , see, e.g., [5] for details. In the context of this work, the single-particle term is diagonal in the spin indices, but we keep both indices for now, to make the discussion general enough to still apply to a model that, e.g., includes an external magnetic field.

To make the following computations more compact, we introduce a multi-index notation, writing

$$\begin{aligned} S[\bar{d}, d] &= \int_{tt'} \bar{d}_{t'} [G_0^{-1}]_{t'|t} d_t \\ &\quad + \frac{1}{4} \sum_{1'2'12} \int_{\mathcal{C}} dt \bar{d}_{1'}(t) \bar{d}_{2'}(t) [\Gamma_0]_{1'2'|12} d_2(t) d_1(t) \quad (\text{F4}) \end{aligned}$$

$$[G_0^{-1}]_{t'|t} = \delta(t' - t) i \partial_t - h_{t'|t} \quad (\text{F5})$$

where non-bold indices ($1', 2', 1, 2$ in Eq. (F4)) comprise Keldysh indices, spin indices and more general quantum numbers one might consider, and the bold indices combine the non-bold indices with time indices.

Using this notation, correlation functions are defined as follows. The two-point (2p) and four-point (4p) functions read,

$$G_{1|1'} = -i \langle d_1 \bar{d}_{1'} \rangle \quad (\text{F6})$$

$$G_{12|1'2'}^{(4)} = i \langle d_1 d_2 \bar{d}_{2'} \bar{d}_{1'} \rangle, \quad (\text{F7})$$

where the bracket $\langle \dots \rangle$ denotes the standard functional integral

$$\langle \dots \rangle = \frac{1}{\mathcal{Z}} \int \mathcal{D}[\bar{d}, d] (\dots) e^{iS[\bar{d}, d]}, \quad (\text{F8})$$

corresponding to expectation values of operators time-ordered on the Keldysh contour \mathcal{C} . The self-energy Σ is introduced via the Dyson equation,

$$G_{1|1'} = [G_0]_{1|1'} + \int_{2'2} [G_0]_{1|2'} \Sigma_{2'|2} G_{2|1'} \quad (\text{F9})$$

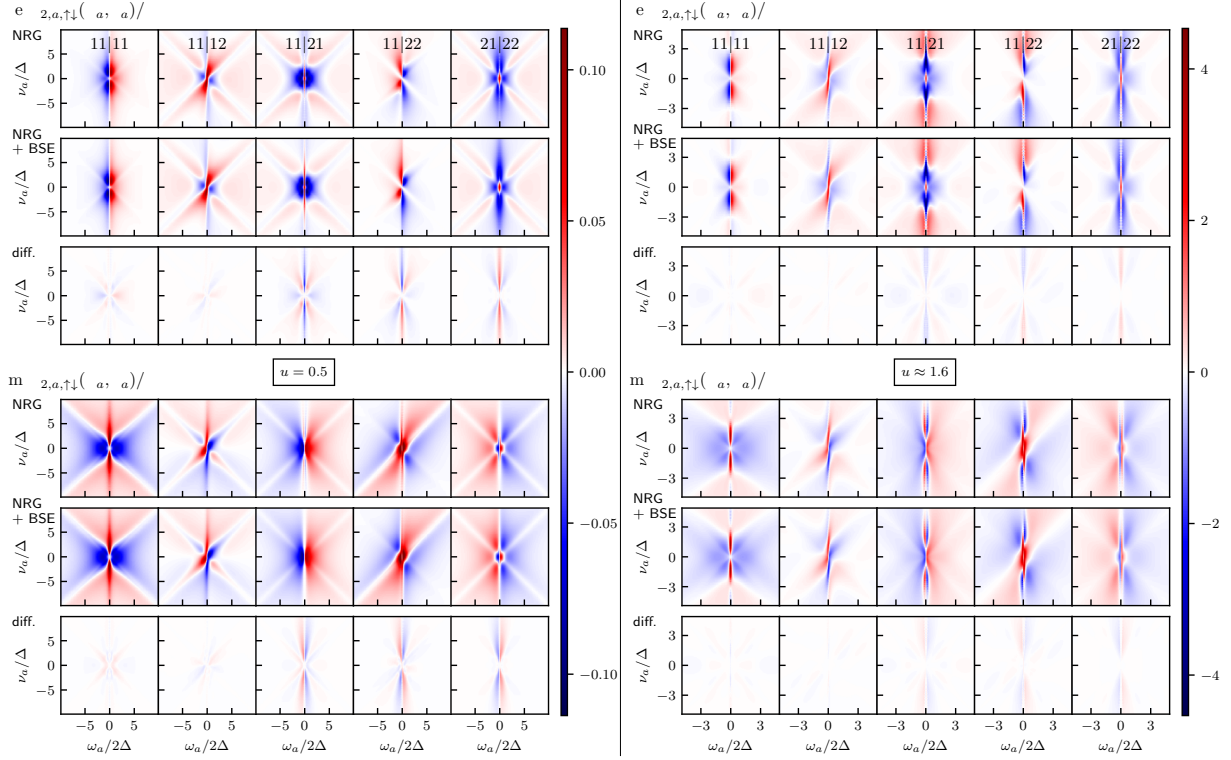


FIG. 14. Fulfillment of the BSE for the full frequency dependence of both the real and imaginary parts of K_2 in the a channel. The first rows show the vertex components as produced by NRG, the second the result after a single evaluation of the BSE (18) and the third their absolute differences. Results for weak (strong) interaction are shown on the left (right). At weak interaction, we restrict the shown frequency intervals to $\pm 10\Delta$. At strong interaction, we zoom into a smaller region of $\pm 5\Delta$ to highlight the increasingly sharp structures of the vertex. We observe good agreement of the BSE throughout.

$$\Leftrightarrow G_{1'1}^{-1} = [G_0^{-1}]_{1'1} - \Sigma_{1'1}, \quad (\text{F10})$$

and, after employing the tree expansion for the 4p function,

$$iG_{12|1'2'}^{(4)} = G_{1|1'}G_{2|2'} - G_{1|2'}G_{2|1'} + iG_{c;12|1'2'}^{(4)}, \quad (\text{F11})$$

the 4p vertex Γ is introduced via the connected part of the 4p function,

$$G_{c;12|1'2'}^{(4)} = - \int_{3'4'|34} G_{1|3'}G_{2|4'}\Gamma_{3'4'|34}G_{3|1'}G_{4|2'}. \quad (\text{F12})$$

2. Equation of motion for the equal-time Green function

We consider the infinitesimal U(1) gauge transformation

$$d_{\sigma}^j(t) \longrightarrow d_{\sigma}^j(t) + \underbrace{i\varepsilon_{\sigma}^j(t)d_{\sigma}^j(t)}_{\delta d_{\sigma}^j(t)} \quad (\text{F13a})$$

$$\bar{d}_{\sigma'}^j(t') \longrightarrow \bar{d}_{\sigma'}^j(t') - \underbrace{i\varepsilon_{\sigma'}^j(t')\bar{d}_{\sigma'}^j(t')}_{\delta \bar{d}_{\sigma'}^j(t')}, \quad (\text{F13b})$$

or, written in multi-index notation,

$$d_{\mathbf{t}} \longrightarrow d_{\mathbf{t}} + i\varepsilon_{\mathbf{t}}d_{\mathbf{t}} \equiv d_{\mathbf{t}} + \delta d_{\mathbf{t}} \quad (\text{F14a})$$

$$\bar{d}_{\mathbf{t}'} \longrightarrow \bar{d}_{\mathbf{t}'} - i\varepsilon_{\mathbf{t}'}\bar{d}_{\mathbf{t}'} \equiv \bar{d}_{\mathbf{t}'} + \delta \bar{d}_{\mathbf{t}'}. \quad (\text{F14b})$$

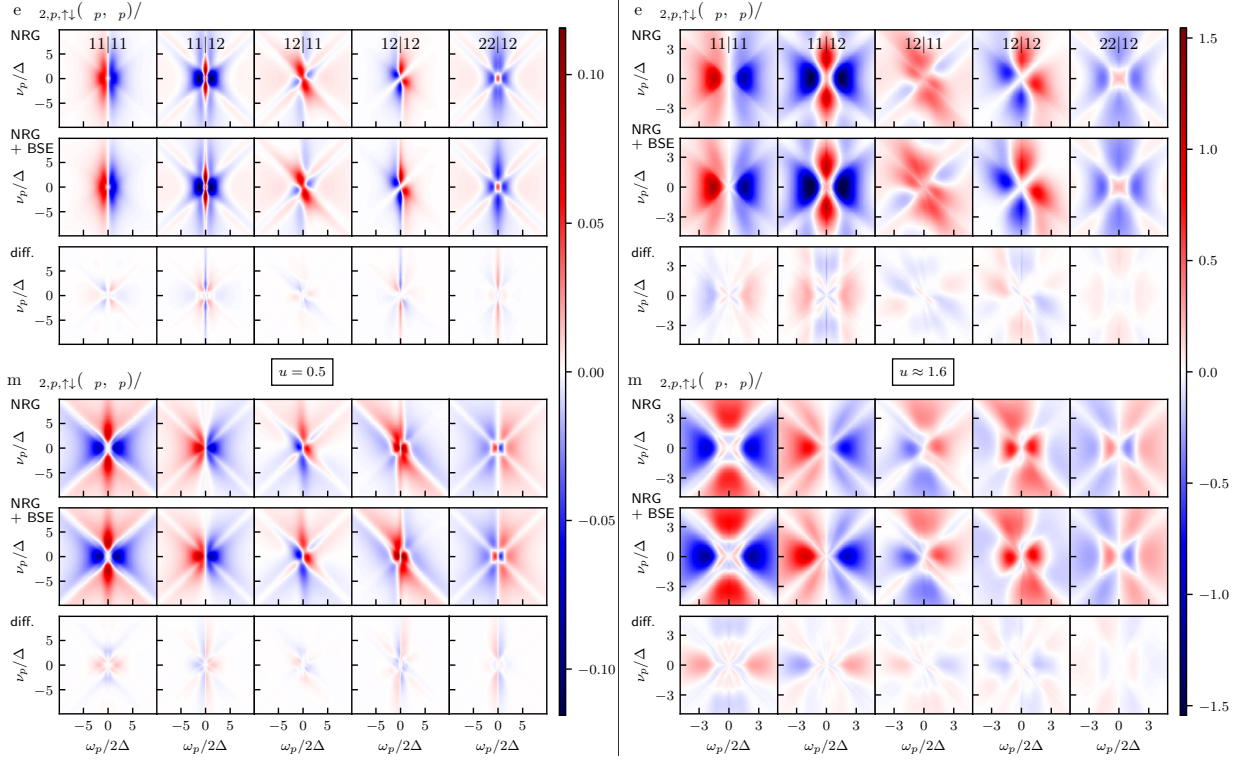
Here and from now on, repeated indices are not summed over, unless indicated explicitly. Since this transformation is supposed to be a symmetry of the theory to $\mathcal{O}(\varepsilon)$, we demand invariance of \mathcal{Z} as well as all correlation functions under this transformation to $\mathcal{O}(\varepsilon)$. This generates an infinite set of consistency relations between correlation functions.

As the U(1) transformation is non-anomalous, meaning that the path integral measure is invariant under this transformation, we therefore require

$$0 \stackrel{!}{=} \delta \mathcal{Z} = \int \mathcal{D}[\bar{d}, d] \delta S[\bar{d}, d] e^{iS[\bar{d}, d]}. \quad (\text{F15})$$

Since S_{int} is trivially invariant, the only contribution comes from the non-interacting part S_0 . We have

$$\begin{aligned} \delta S_0[\bar{d}, d] &= \int_{\mathbf{t}\mathbf{t}'} \{ \delta \bar{d}_{\mathbf{t}'} [G_0^{-1}]_{\mathbf{t}'\mathbf{t}} d_{\mathbf{t}} + \bar{d}_{\mathbf{t}'} [G_0^{-1}]_{\mathbf{t}'\mathbf{t}} \delta d_{\mathbf{t}} \} \\ &= \int_{\mathbf{t}\mathbf{t}'} \{ -i\varepsilon_{\mathbf{t}'} \bar{d}_{\mathbf{t}'} [\delta(\mathbf{t}' - \mathbf{t})i\partial_{\mathbf{t}} - h_{\mathbf{t}'|\mathbf{t}}] d_{\mathbf{t}} \} \end{aligned}$$

FIG. 15. Same as in Fig. 14 for the p channel.

$$\begin{aligned}
& + \bar{d}_{\nu'} \left[\delta(\mathbf{t}' - \mathbf{t}) i \partial_t - h_{\nu'|\mathbf{t}} \right] i \varepsilon_{\mathbf{t}} d_{\mathbf{t}} \} \\
& = - \int_{\mathbf{t}} \bar{d}_{\mathbf{t}} (\partial_t \varepsilon_{\mathbf{t}}) d_{\mathbf{t}} + \int_{\mathbf{t}\mathbf{t}'} \bar{d}_{\nu'} (i \varepsilon_{\nu'} - i \varepsilon_{\mathbf{t}}) h_{\nu'|\mathbf{t}} d_{\mathbf{t}} \\
& = \int_{\mathbf{t}} \varepsilon_{\mathbf{t}} \partial_t (\bar{d}_{\mathbf{t}} d_{\mathbf{t}}) + \int_{\mathbf{t}\mathbf{t}'} \bar{d}_{\nu'} (i \varepsilon_{\nu'} - i \varepsilon_{\mathbf{t}}) h_{\nu'|\mathbf{t}} d_{\mathbf{t}} \\
& = \int_{\mathbf{t}} \varepsilon_{\mathbf{t}} \left\{ \partial_t (\bar{d}_{\mathbf{t}} d_{\mathbf{t}}) + i \int_{\tilde{\mathbf{t}}} \bar{d}_{\mathbf{t}} h_{\mathbf{t}|\tilde{\mathbf{t}}} d_{\tilde{\mathbf{t}}} - i \int_{\tilde{\mathbf{t}}} \bar{d}_{\tilde{\mathbf{t}}} h_{\tilde{\mathbf{t}}|\mathbf{t}} d_{\mathbf{t}} \right\}, \tag{F16}
\end{aligned}$$

where we applied the product rule and integrated by parts in the second to last step. Since $\varepsilon_{\mathbf{t}}$ is an arbitrary function, using this result in Eq. (F15), we get

$$0 \stackrel{!}{=} \partial_t \langle \bar{d}_{\mathbf{t}} d_{\mathbf{t}} \rangle + i \int_{\tilde{\mathbf{t}}} (h_{\mathbf{t}|\tilde{\mathbf{t}}} \langle \bar{d}_{\mathbf{t}} d_{\tilde{\mathbf{t}}} \rangle - h_{\tilde{\mathbf{t}}|\mathbf{t}} \langle \bar{d}_{\tilde{\mathbf{t}}} d_{\mathbf{t}} \rangle), \tag{F17}$$

where we performed a relabelling of all indices. Employing the definition of the 2p function in Eq. (F6), together with the anticommutation property of the Grassmann variables, we write this result as

$$i \partial_t G_{\mathbf{t}|\mathbf{t}} = \int_{\tilde{\mathbf{t}}} \left[h_{\mathbf{t}|\tilde{\mathbf{t}}} G_{\tilde{\mathbf{t}}|\mathbf{t}} - (\mathbf{t} \leftrightarrow \tilde{\mathbf{t}}) \right], \tag{F18}$$

which is an equation of motion for the equal-time Green's function. This equation is trivially fulfilled if time-translation invariance is assumed. We state it here primarily for later use.

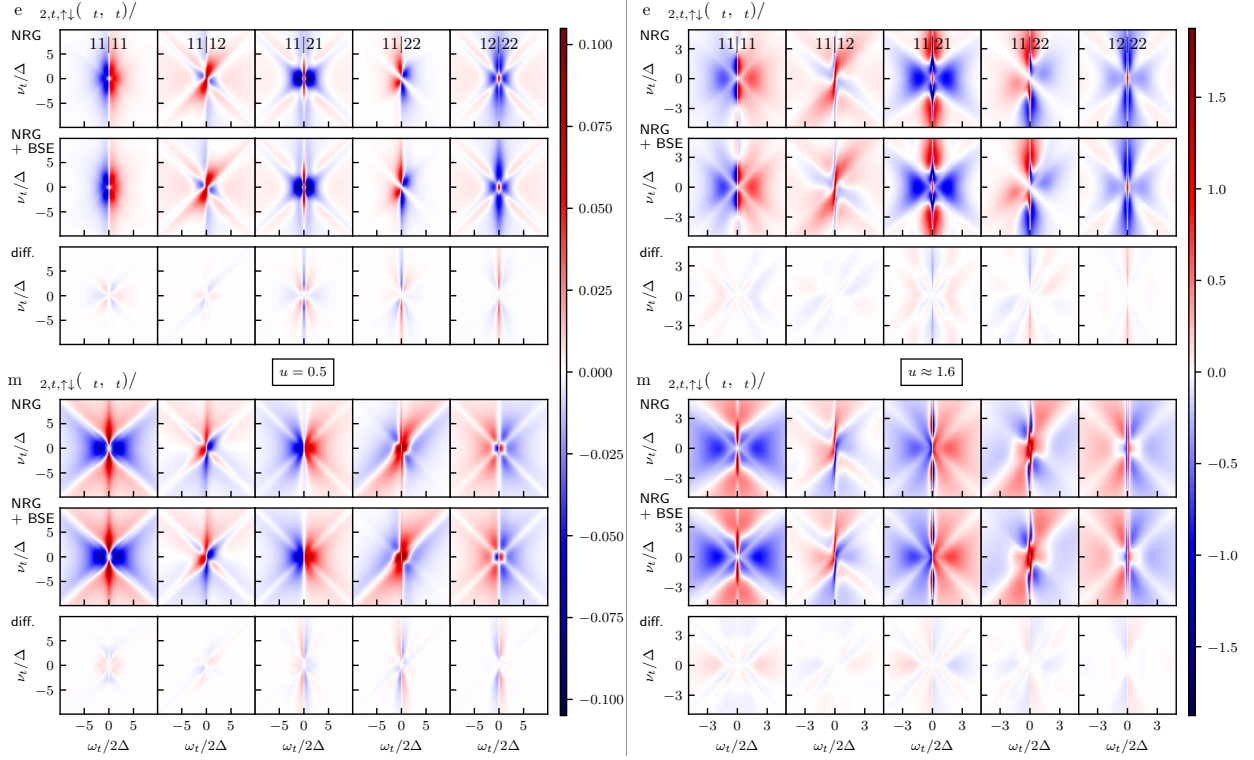
3. First-order WI

The first-order WI is derived by requiring that the 2p function remain invariant under the U(1) transformation. Using the definition, Eq. (F6), we have

$$\begin{aligned}
0 & \stackrel{!}{=} \delta G_{\mathbf{1}|\mathbf{1}'} \\
& = -i \int \mathcal{D}[\bar{d}, d] \left\{ \delta d_{\mathbf{1}} \bar{d}_{\mathbf{1}'} + d_{\mathbf{1}} \delta \bar{d}_{\mathbf{1}'} \right. \\
& \quad \left. + i d_{\mathbf{1}} \bar{d}_{\mathbf{1}'} \delta S[\bar{d}, d] \right\} e^{iS[\bar{d}, d]} \\
& = -i \int \mathcal{D}[\bar{d}, d] \left\{ (i \varepsilon_{\mathbf{1}} d_{\mathbf{1}}) \bar{d}_{\mathbf{1}'} + d_{\mathbf{1}} (-i \varepsilon_{\mathbf{1}'} \bar{d}_{\mathbf{1}'} \right. \\
& \quad \left. + i d_{\mathbf{1}} \bar{d}_{\mathbf{1}'} \delta S_0[\bar{d}, d] \right\} e^{iS[\bar{d}, d]} \\
& = \int \mathcal{D}[\bar{d}, d] d_{\mathbf{1}} \bar{d}_{\mathbf{1}'} (\varepsilon_{\mathbf{1}} - \varepsilon_{\mathbf{1}'} + \delta S_0[\bar{d}, d]) e^{iS[\bar{d}, d]}. \tag{F19}
\end{aligned}$$

Again, this must hold for arbitrary $\varepsilon_{\tilde{\mathbf{t}}}$, so that, using Eq. (F16),

$$\begin{aligned}
0 & \stackrel{!}{=} \int \mathcal{D}[\bar{d}, d] d_{\mathbf{1}} \bar{d}_{\mathbf{1}'} \left\{ \delta(\mathbf{1} - \tilde{\mathbf{t}}) - \delta(\mathbf{1}' - \tilde{\mathbf{t}}) + \partial_{\tilde{\mathbf{t}}} (\bar{d}_{\tilde{\mathbf{t}}} d_{\tilde{\mathbf{t}}}) \right. \\
& \quad \left. + i \int_{\mathbf{t}} (\bar{d}_{\tilde{\mathbf{t}}} h_{\tilde{\mathbf{t}}|\mathbf{t}} d_{\mathbf{t}} - \bar{d}_{\mathbf{t}} h_{\mathbf{t}|\tilde{\mathbf{t}}} d_{\tilde{\mathbf{t}}}) \right\} e^{iS[\bar{d}, d]} \\
& = [\delta(\mathbf{1} - \tilde{\mathbf{t}}) - \delta(\mathbf{1}' - \tilde{\mathbf{t}})] \langle d_{\mathbf{1}} \bar{d}_{\mathbf{1}'} \rangle + \partial_{\tilde{\mathbf{t}}} \langle d_{\mathbf{1}} \bar{d}_{\mathbf{1}'} \bar{d}_{\tilde{\mathbf{t}}} d_{\tilde{\mathbf{t}}} \rangle \\
& \quad + i \int_{\mathbf{t}} \left[h_{\tilde{\mathbf{t}}|\mathbf{t}} \langle d_{\mathbf{1}} \bar{d}_{\mathbf{1}'} \bar{d}_{\tilde{\mathbf{t}}} d_{\mathbf{t}} \rangle - (\tilde{\mathbf{t}} \leftrightarrow \mathbf{t}) \right]. \tag{F20}
\end{aligned}$$

FIG. 16. Same as in Figs. 14 and 15 for the t channel.

Using the definition of the 4p function, Eq. (F7), and relabeling indices, we obtain

$$0 \stackrel{!}{=} [\delta(\mathbf{1}-\mathbf{t}) - \delta(\mathbf{1}'-\mathbf{t})] iG_{\mathbf{1}\mathbf{1}'} - i\partial_t G_{\mathbf{1}\mathbf{t}}^{(4)} + \int_{\tilde{\mathbf{1}}} [h_{\tilde{\mathbf{1}}}\bar{\Gamma}_{\mathbf{1}\tilde{\mathbf{1}}\mathbf{t}\mathbf{1}'}^{(4)} - (\mathbf{t} \leftrightarrow \tilde{\mathbf{1}})]. \quad (\text{F21})$$

This is the first-order U(1) WI, expressed through real-time arguments in the contour basis.

Next, we insert the tree expansion for the 4p function, Eq. (F11), into Eq. (F21) and use the Dyson equation, Eq. (F10), as well as Eq. (F12) to express the U(1) WI in terms of the self-energy Σ and the 4p vertex Γ . This gives

$$i\Sigma_{s'\mathbf{t}}\delta(\mathbf{t}-\mathbf{s}) - \delta(\mathbf{s}'-\mathbf{t})i\Sigma_{\mathbf{t}s} \stackrel{!}{=} \int_{\tilde{\mathbf{1}}\mathbf{4}'\mathbf{3}} \left\{ \left[G_0^{-1} \right]_{\mathbf{t}\tilde{\mathbf{1}}}^{\rightarrow} \Gamma_{\tilde{\mathbf{1}}\mathbf{4}'\mathbf{3}s} \Gamma_{s'\mathbf{4}'\mathbf{3}s} G_{\mathbf{3}\mathbf{t}} - G_{\mathbf{t}\mathbf{4}'} \Gamma_{s'\mathbf{4}'\mathbf{3}s} G_{\mathbf{3}\tilde{\mathbf{1}}} \left[G_0^{-1} \right]_{\tilde{\mathbf{1}}\mathbf{t}}^{\leftarrow} \right\}. \quad (\text{F22})$$

The derivation of this result can be found in App. G1.

Next, a Keldysh rotation is performed, and the open index \mathbf{t} is contracted, as detailed in App. G2. We furthermore assume time translation invariance and use a Fourier transform to frequency space, see App. G3. We also impose SU(2) spin symmetry, see App. G4. With the short-hand notation $\mathbf{v}_{\pm} = \mathbf{v} \pm \frac{\theta}{2}$

(and, likewise, for $\tilde{\mathbf{v}}$), the resulting equation then reads

$$\begin{aligned} & \Sigma^{\alpha_1'|\bar{\alpha}_1}(\mathbf{v}_-) - \Sigma^{\bar{\alpha}_1'|\alpha_1}(\mathbf{v}_+) \\ &= \sum_{\alpha_2'|\alpha_2\alpha_3\alpha_1} \int_{\tilde{\mathbf{v}}} \frac{d\tilde{\mathbf{v}}}{2\pi i} \left\{ G^{\alpha_2|\alpha_2'}(\tilde{\mathbf{v}}_+) \Gamma_D^{\alpha_2'\alpha_1'|\alpha_2\alpha_1}(\omega, \mathbf{v}, \tilde{\mathbf{v}}) \right. \\ & \quad \times G^{\alpha_2|\alpha_1}(\tilde{\mathbf{v}}_-) [G_0^{-1}]^{\alpha_1|\bar{\alpha}_2}(\tilde{\mathbf{v}}_-) \\ & \quad - [G_0^{-1}]^{\bar{\alpha}_2|\alpha_1}(\tilde{\mathbf{v}}_+) G^{\alpha_1|\alpha_2'}(\tilde{\mathbf{v}}_+) \\ & \quad \left. \times \Gamma_D^{\alpha_2'\alpha_1'|\alpha_2\alpha_1}(\omega, \mathbf{v}, \tilde{\mathbf{v}}) G^{\alpha_2|\alpha_2}(\tilde{\mathbf{v}}_-) \right\}, \end{aligned} \quad (\text{F23})$$

where we applied crossing symmetry in the first two arguments of Γ and performed a relabeling of the Keldysh indices compared to App. G2. The U(1) WI for the self-energy has been derived in the context of lattice problems in the MF before, see, e.g., App. A in Ref. 62 or Sec. E.1 in Ref. 59. Equation (F23) can be seen as a generalization of these results to the KF. The simpler form of the WI in those works, however, involves the 2PI vertex, which is at present not accessible with NRG in the KF. We therefore use the form of Eq. (F23), which involves only the full 4p vertex.

Finally, using the explicit form of the inverse bare propagator for the single-impurity Anderson model without a magnetic field,

$$[G_0^{-1}]^{\alpha_1'|\alpha_1}(\mathbf{v}) = \delta_{\alpha_1',\bar{\alpha}_1}(\mathbf{v} - \varepsilon_d) - \Delta^{\alpha_1'|\alpha_1}(\mathbf{v}), \quad (\text{F24})$$

see App. G5 for details, we obtain Eq. (21) from the main text.

Appendix G: Explicit calculations

Most of the calculations below follow standard text-book strategies, which we formulate here in general notation, adapted to our conventions.

1. Representation of Eq. (F21) in terms of Σ and Γ

Inserting the tree expansion for the 4p function, Eq. (F11), into Eq. (F21) gives

$$\begin{aligned}
0 &\stackrel{\text{!}}{=} [\delta(1-t) - \delta(1'-t)] iG_{1|1'} \\
&\quad - \partial_t [G_{1|t} G_{t|1'}] + G_{1|1'} \partial_t G_{t|t} \\
&\quad - i \int_{\bar{1}} [h_{t|\bar{1}} (G_{1|t} G_{\bar{1}|1'} - G_{1|1'} G_{\bar{1}|t}) - (t \leftrightarrow \bar{1})] \\
&\quad - i \partial_t G_{c;1t|t1'}^{(4)} + \int_{\bar{1}} [h_{t|\bar{1}} G_{c;1\bar{1}|t1'}^{(4)} - (t \leftrightarrow \bar{1})] \\
&= [\delta(1-t) - \delta(1'-t)] iG_{1|1'} \\
&\quad - \partial_t [G_{1|t} G_{t|1'}] - i \int_{\bar{1}} [h_{t|\bar{1}} G_{1|t} G_{\bar{1}|1'} - (t \leftrightarrow \bar{1})] \\
&\quad - i \partial_t G_{c;1t|t1'}^{(4)} + \int_{\bar{1}} [h_{t|\bar{1}} G_{c;1\bar{1}|t1'}^{(4)} - (t \leftrightarrow \bar{1})]. \quad (\text{G1})
\end{aligned}$$

In Eq. (G1), we used Eq. (F18) for $i\partial_t G_{t|t}$, leading to a cancellation of some terms. Now, we write the inverse bare Green's function, Eq. (F5), as

$$\begin{aligned}
[G_0^{-1}]_{\bar{t}|t} &= \delta(\bar{t}-t) i\partial_t - h_{\bar{t}|t} = -\delta(\bar{t}-t) i\bar{\partial}_t - h_{\bar{t}|t} \\
\Rightarrow \int_{\bar{t}} [G_0^{-1}]_{\bar{t}|t} &= i\partial_t - \int_{\bar{t}} h_{\bar{t}|t} = -i\bar{\partial}_t - \int_{\bar{t}} h_{\bar{t}|t}, \quad (\text{G2})
\end{aligned}$$

$$\begin{aligned}
\text{and } [G_0^{-1}]_{t|\bar{t}} &= \delta(t-\bar{t}) i\partial_{\bar{t}} - h_{t|\bar{t}} = -\delta(t-\bar{t}) i\bar{\partial}_{\bar{t}} - h_{t|\bar{t}} \\
\Rightarrow \int_{\bar{t}} [G_0^{-1}]_{t|\bar{t}} &= i\partial_{\bar{t}} - \int_{\bar{t}} h_{t|\bar{t}} = -i\bar{\partial}_{\bar{t}} - \int_{\bar{t}} h_{t|\bar{t}}. \quad (\text{G3})
\end{aligned}$$

The second formulation arises from an integration by parts in the non-interacting action, letting the time derivative act on the barred Grassmann variable to the left of G_0^{-1} in Eq. (F4). The arising boundary term vanishes due to the closed time contour in the KF: As the time evolution returns to the same (in this case thermal) density matrix it started from at the initial time t_0 , the Grassmann variables at the initial and final times can differ by at most a phase. For the product $\bar{d}d$, the two phases cancel exactly. Therefore, the boundary term

$$\int_{\mathcal{C}} dt \partial_t [\bar{d}^j(t) d^j(t)] = \bar{d}^+(t_0) d^+(t_0) - \bar{d}^-(t_0) d^-(t_0) \quad (\text{G4})$$

vanishes. We can thus rewrite the disconnected part (second line) of Eq. (G1) as

$$\begin{aligned}
&-i\partial_t [G_{1|t} G_{t|1'}] + \int_{\bar{1}} [h_{t|\bar{1}} G_{1|t} G_{\bar{1}|1'} - (t \leftrightarrow \bar{1})] \\
&= [-i\partial_t G_{1|t}] G_{t|1'} - \int_{\bar{1}} h_{\bar{1}|t} G_{1|\bar{1}} G_{t|1'}
\end{aligned}$$

$$\begin{aligned}
&+ G_{1|t} [-i\partial_t G_{t|1'}] + \int_{\bar{1}} h_{t|\bar{1}} G_{1|t} G_{\bar{1}|1'} \\
&= \left[-iG_{1|t} \bar{\partial}_t - \int_{\bar{1}} G_{1|\bar{1}} h_{\bar{1}|t} \right] G_{t|1'} \\
&\quad + G_{1|t} \left[-i\partial_t G_{t|1'} + \int_{\bar{1}} h_{t|\bar{1}} G_{\bar{1}|1'} \right] \\
&= \int_{\bar{1}} \left\{ G_{1|\bar{1}} [G_0^{-1}]_{\bar{1}|t} G_{t|1'} - G_{1|t} [G_0^{-1}]_{t|\bar{1}} G_{\bar{1}|1'} \right\}. \quad (\text{G5})
\end{aligned}$$

Introducing the 4p vertex Γ via Eq. (F12), the 4p part (third line) of Eq. (G1) is written as

$$\begin{aligned}
&-i\partial_t G_{c;1t|t1'}^{(4)} + \int_{\bar{1}} [h_{t|\bar{1}} G_{c;1\bar{1}|t1'}^{(4)} - (t \leftrightarrow \bar{1})] \\
&= \int_{3'4'34} \left\{ i\partial_t [G_{1|3'} G_{t|4'} \Gamma_{3'4'|34} G_{3|t} G_{4|1'}] \right. \\
&\quad \left. - \int_{\bar{1}} [h_{t|\bar{1}} G_{1|3'} G_{\bar{1}|4'} \Gamma_{3'4'|34} G_{3|t} G_{4|1'} \right. \\
&\quad \quad \left. - h_{\bar{1}|t} G_{1|3'} G_{t|4'} \Gamma_{3'4'|34} G_{3|\bar{1}} G_{4|1'}] \right\} \\
&= - \int_{3'4'34} \left\{ \right. \\
&\quad G_{1|3'} \left[-i\partial_t G_{t|4'} + \int_{\bar{1}} h_{t|\bar{1}} G_{\bar{1}|4'} \right] \Gamma_{3'4'|34} G_{3|t} G_{4|1'} \\
&\quad \left. + G_{1|3'} G_{t|4'} \Gamma_{3'4'|34} \left[-iG_{3|t} \bar{\partial}_t - \int_{\bar{1}} G_{3|\bar{1}} h_{\bar{1}|t} \right] G_{4|1'} \right\} \\
&= \int_{3'4'34} \int_{\bar{1}} \left\{ G_{1|3'} [G_0^{-1}]_{t|\bar{1}} G_{\bar{1}|4'} \Gamma_{3'4'|34} G_{3|t} G_{4|1'} \right. \\
&\quad \left. - G_{1|3'} G_{t|4'} \Gamma_{3'4'|34} G_{3|\bar{1}} [G_0^{-1}]_{\bar{1}|t} G_{4|1'} \right\}. \quad (\text{G6})
\end{aligned}$$

We thus obtain

$$\begin{aligned}
0 &\stackrel{\text{!}}{=} [\delta(1-t) - \delta(1'-t)] iG_{1|1'} \\
&\quad + \int_{\bar{1}} \left\{ (-i) G_{1|\bar{1}} [G_0^{-1}]_{\bar{1}|t} G_{t|1'} + i G_{1|t} [G_0^{-1}]_{t|\bar{1}} G_{\bar{1}|1'} \right. \\
&\quad \left. + \int_{3'4'34} \left(G_{1|3'} [G_0^{-1}]_{t|\bar{1}} G_{\bar{1}|4'} \Gamma_{3'4'|34} G_{3|t} G_{4|1'} \right. \right. \\
&\quad \quad \left. \left. - G_{1|3'} G_{t|4'} \Gamma_{3'4'|34} G_{3|\bar{1}} [G_0^{-1}]_{\bar{1}|t} G_{4|1'} \right) \right\}. \quad (\text{G7})
\end{aligned}$$

Inserting the Dyson equation, Eq. (F10), into the second and third single-particle term and using that $\int_{\bar{1}} G_{1|\bar{1}}^{-1} G_{\bar{1}|1'} = \int_{\bar{1}} G_{1|\bar{1}} G_{\bar{1}|1'}^{-1} = \delta(1-1')$, we get

$$\begin{aligned}
&\int_{\bar{1}} \left\{ G_{1|\bar{1}} [G_0^{-1}]_{\bar{1}|t} G_{t|1'} - G_{1|t} [G_0^{-1}]_{t|\bar{1}} G_{\bar{1}|1'} \right\} \\
&= \underbrace{\delta(1-t) G_{t|1'}}_{\delta(1-t) G_{1|1'}} - \underbrace{G_{1|t} \delta(t-1')}_{G_{1|1'} \delta(t-1')} \\
&\quad + \int_{\bar{1}} \left\{ G_{1|\bar{1}} \Sigma_{\bar{1}|t} G_{t|1'} - G_{1|t} \Sigma_{t|\bar{1}} G_{\bar{1}|1'} \right\}, \quad (\text{G8})
\end{aligned}$$

and hence, using the cancellation with the first term of Eq. (G7),

$$0 \stackrel{\text{!}}{=} \int_{\bar{1}} \left\{ i G_{1|t} \Sigma_{t|\bar{1}} G_{\bar{1}|1'} - i G_{1|\bar{1}} \Sigma_{\bar{1}|t} G_{t|1'} \right\}$$

$$+ \int_{3'4'34} \left(G_{1|3'} [G_0^{-1}]_{t|\bar{1}} \overrightarrow{G_{\bar{1}|4'} \Gamma_{3'4'|34} G_{3|t} G_{4|1'}} - G_{1|3'} G_{t|4'} \Gamma_{3'4'|34} G_{3|\bar{1}} [G_0^{-1}]_{\bar{1}|t} \overleftarrow{G_{4|1'}} \right). \quad (\text{G9})$$

Multiplying with $\int_{\bar{1}} G_{s'|1}^{-1}$ from the left and with $\int_{1'} G_{1'|s}^{-1}$ from the right, we obtain

$$\begin{aligned} 0 &\stackrel{\dagger}{=} \int_{\bar{1}} \left\{ i\delta(s' - t) \Sigma_{t|\bar{1}} \delta(\bar{1} - s) - i\delta(s' - \bar{1}) \Sigma_{\bar{1}|t} \delta(t - s) \right. \\ &\quad + \int_{3'4'34} \left(\delta(s' - 3') [G_0^{-1}]_{t|\bar{1}} \overrightarrow{G_{\bar{1}|4'} \Gamma_{3'4'|34} G_{3|t}} \delta(4 - s) \right. \\ &\quad \left. \left. - \delta(s' - 3') G_{t|4'} \Gamma_{3'4'|34} G_{3|\bar{1}} [G_0^{-1}]_{\bar{1}|t} \overleftarrow{G_{4|1'}} \delta(4 - s) \right) \right\} \\ &= \delta(s' - t) i \Sigma_{t|s} - \delta(t - s) i \Sigma_{s'|t} \\ &\quad + \int_{\bar{1}4'3} \left\{ [G_0^{-1}]_{t|\bar{1}} \overrightarrow{G_{\bar{1}|4'} \Gamma_{s'4'|3s} G_{3|t}} \right. \\ &\quad \left. - G_{t|4'} \Gamma_{s'4'|3s} G_{3|\bar{1}} [G_0^{-1}]_{\bar{1}|t} \overleftarrow{\phantom{G_{\bar{1}|4'} \Gamma_{s'4'|3s} G_{3|t}}}, \right. \end{aligned} \quad (\text{G10})$$

which is Eq. (F22).

2. Keldysh rotation of Eq. (F22)

The Green's functions in the Keldysh and contour bases are related by the Keldysh rotation $G^{\alpha|\alpha'} = D^{\alpha|j} G^{j|j'} (D^{-1})^{j'|\alpha'}$, with the matrices

$$D = \frac{1}{\sqrt{2}} \begin{pmatrix} 1 & -1 \\ 1 & 1 \end{pmatrix}; \quad D^{-1} = \frac{1}{\sqrt{2}} \begin{pmatrix} 1 & 1 \\ -1 & 1 \end{pmatrix} \quad (\text{G11})$$

$$(G^{\alpha|\alpha'}) = \begin{pmatrix} 0 & G^A \\ G^R & G^K \end{pmatrix}; \quad (G^{j|j'}) = \begin{pmatrix} G^{-|-} & G^{-|+} \\ G^{+|-} & G^{+|+} \end{pmatrix}. \quad (\text{G12})$$

The inverse transformation is $G^{j|j'} = (D^{-1})^{j|\alpha} G^{\alpha|\alpha'} D^{\alpha'|j'}$ (summation convention implied). The same transformation applies to the self-energy, whose Keldysh structure reads

$$(\Sigma^{\alpha'|\alpha}) = \begin{pmatrix} \Sigma^{1|1} & \Sigma^{1|2} \\ \Sigma^{2|1} & \Sigma^{2|2} \end{pmatrix} = \begin{pmatrix} \Sigma^K & \Sigma^R \\ \Sigma^A & 0 \end{pmatrix}. \quad (\text{G13})$$

Likewise, for the vertex one has

$$\Gamma^{j_1' j_2' | j_1 j_2} = (D^{-1})^{j_1' |\alpha_1'} (D^{-1})^{j_2' |\alpha_2'} \Gamma^{\alpha_1' \alpha_2' | \alpha_1 \alpha_2} D^{\alpha_1 | j_1} D^{\alpha_2 | j_2}. \quad (\text{G14})$$

To perform the Keldysh rotation of Eq. (F22), we proceed as follows. First, to avoid a trivially vanishing result after contracting the open multi-index t , we multiply the whole equation with the contour index $-j_t$. We then contract t , leaving out the integration over time for now, as that will follow later when doing the Fourier transformation into frequency space. Only focusing on the Keldysh index structure, this gives

$$(-j_s) \Sigma^{j_s' | j_s} - (-j_{s'}) \Sigma^{j_s' | j_s} \quad (\text{G15})$$

for the LHS of Eq. (F22). The Keldysh rotation is now performed by multiplying with D from the left and with D^{-1} from the right. To compute the Keldysh rotation of $-j_{s'} \Sigma^{s'|s}$, we write it as a matrix product, $-j_{s'} \Sigma^{s'|s} = \Sigma_{\bar{s}} \sigma_z^{s'|\bar{s}} \Sigma^{\bar{s}|s} = (\sigma_z \Sigma^c)^{s'|\bar{s}}$, where σ_z is the third Pauli matrix and the superscript c of Σ in the last expression indicates that it is given in the contour basis. For the Keldysh basis, we use the superscript k . Applying the Keldysh rotation and inserting an identity gives

$$\begin{aligned} (D \sigma_z \Sigma^c D^{-1})^{\alpha'|\alpha} &= (D \sigma_z D^{-1} D \Sigma^c D^{-1})^{\alpha'|\alpha} = (\sigma_x \Sigma^k)^{\alpha'|\alpha} \\ &= \Sigma^{\bar{\alpha}'|\alpha}. \end{aligned} \quad (\text{G16})$$

Here, we used $D \sigma_z D^{-1} = \sigma_x$. This first Pauli matrix flips the corresponding Keldysh index, which is what the bar over the first Keldysh index denotes in the final expression. Concretely, $\bar{1} = 2$; $\bar{2} = 1$. The other term, $-j_s \Sigma^{s'|s} = (\Sigma^c \sigma_z)^{s'|s}$, is transformed analogously and gives $\Sigma^{\alpha'|\bar{\alpha}_s}$. After the Keldysh rotation, the LHS of Eq. (F22) thus reads $\Sigma^{\alpha_s'|\bar{\alpha}_s} - \Sigma^{\bar{\alpha}_s'|\alpha_s}$.

The right-hand side of the WI, Eq. (F22), is transformed analogously. Again focusing only on the Keldysh index structure, after contracting t , the first term can be written as

$$\begin{aligned} &\sum_{j_t, j_{\bar{1}}, j_{4'}, j_3} (-j_t) [G_0^{-1}]^{j_t | j_{\bar{1}}} G^{j_{\bar{1}} | j_{4'}} \Gamma^{j_{4'} | j_3 j_s} G^{j_3 | j_t} \\ &= \text{Tr} \left\{ \sigma_z [G_0^{-1}]^c G^c \Gamma^{c: j_{s'} | j_s} G^c \right\} \\ &= \text{Tr} \left\{ D \sigma_z D^{-1} D [G_0^{-1}]^c D^{-1} D G^c D^{-1} D \Gamma^{c: j_{s'} | j_s} D^{-1} D G^c D^{-1} \right\}, \end{aligned} \quad (\text{G17})$$

where we inserted identities and used the cyclicity of the trace. Again using $D \sigma_z D^{-1} = \sigma_x$, which flips the corresponding Keldysh index, and performing the Keldysh rotation for the two remaining open indices in Γ , the first term of the RHS of Eq. (F22) reads

$$\sum_{\alpha_t, \alpha_{\bar{1}}, \alpha_{4'}, \alpha_3} [G_0^{-1}]^{\bar{\alpha}_t | \alpha_{\bar{1}}} G^{\alpha_{\bar{1}} | \alpha_{4'}} \Gamma^{\alpha_{4'} | \alpha_{s'} \alpha_{4'} | \alpha_3 \alpha_s} G^{\alpha_3 | \alpha_t}. \quad (\text{G18})$$

The second term is transformed analogously, such that the Keldysh structure of the full WI, Eq. (F22), reads

$$\begin{aligned} &\Sigma^{\alpha_s' | \bar{\alpha}_s} - \Sigma^{\bar{\alpha}_s' | \alpha_s} \\ &= \sum_{\alpha_t, \alpha_{\bar{1}}, \alpha_{4'}, \alpha_3} \left\{ [G_0^{-1}]^{\bar{\alpha}_t | \alpha_{\bar{1}}} G^{\alpha_{\bar{1}} | \alpha_{4'}} \Gamma^{\alpha_{4'} | \alpha_{s'} \alpha_{4'} | \alpha_3 \alpha_s} G^{\alpha_3 | \alpha_t} \right. \\ &\quad \left. - G^{\alpha_t | \alpha_{4'}} \Gamma^{\alpha_{s'} \alpha_{4'} | \alpha_3 \alpha_s} G^{\alpha_3 | \alpha_{\bar{1}}} [G_0^{-1}]^{\alpha_{\bar{1}} | \bar{\alpha}_t} \right\} \end{aligned} \quad (\text{G19})$$

after Keldysh rotation. In a final step, we apply crossing symmetry to the first two arguments of Γ for a favorable frequency parametrization later on. This yields an additional minus sign and swaps the first two Keldysh indices of the vertices, such that the Keldysh structure of Eq. (F22) can be written as

$$\begin{aligned} &\Sigma^{\alpha_s' | \bar{\alpha}_s} - \Sigma^{\bar{\alpha}_s' | \alpha_s} \\ &= \sum_{\alpha_t, \alpha_{\bar{1}}, \alpha_{4'}, \alpha_3} \left\{ G^{\alpha_t | \alpha_{4'}} \Gamma^{\alpha_{s'} \alpha_{4'} | \alpha_3 \alpha_s} G^{\alpha_3 | \alpha_{\bar{1}}} [G_0^{-1}]^{\alpha_{\bar{1}} | \bar{\alpha}_t} \right. \\ &\quad \left. - [G_0^{-1}]^{\bar{\alpha}_t | \alpha_{\bar{1}}} G^{\alpha_{\bar{1}} | \alpha_{4'}} \Gamma^{\alpha_{4'} \alpha_{s'} | \alpha_3 \alpha_s} G^{\alpha_3 | \alpha_t} \right\} \end{aligned} \quad (\text{G20})$$

3. Fourier transform of Eq. (F22)

We insert the Fourier transforms of all functions, which read $G(t_1|t_{1'}) = \int_{v_1 v_{1'}} e^{iv_1 t_1} G(v_1|v_{1'}) e^{-iv_{1'} t_{1'}}$ for all 2p functions G , G_0^{-1} , and Σ and $\Gamma(t_1' t_2' | t_1 t_2) = \int_{v_1' v_2' v_1 v_2} e^{iv_1' t_1'} e^{iv_2' t_2'} \Gamma(v_1' v_2' | v_1 v_2) e^{-iv_1 t_1} e^{-iv_2 t_2}$ for the 4p vertex. Here and from now on, we use the compact notation $\int \frac{d\nu}{2\pi i} = \int_\nu$ for frequency integrals. In this section, we temporarily drop the Keldysh and spin indices of all functions and purely focus on their time- and frequency-dependence.

We transform the whole Eq. (F22) with respect to t_s and $t_{s'}$ by applying $\int_{t_s t_{s'}} e^{-iv' t_{s'}} e^{iv t_s}$ on both sides. We furthermore divide the whole equation by i . For the LHS, we get

$$\int_{t_s t_{s'}} e^{-iv' t_{s'}} e^{iv t_s} \left\{ \delta(t_t - t_s) \int_{v_s' v_t} e^{iv_s' t_{s'}} e^{-iv_t t_s} \Sigma(v_s' | v_t) \right\}$$

$$\begin{aligned} & - \delta(t_{s'} - t_t) \int_{v_t v_s} e^{iv_t t_t} e^{-iv_s t_s} \Sigma(v_t | v_s) \Big\} \\ &= e^{iv t_t} \int_{v_s' v_t} e^{-iv_t t_t} \Sigma(v_s' | v_t) \int_{t_{s'}} e^{i(v_s' - v') t_{s'}} \\ & - e^{-iv' t_t} \int_{v_t v_s} e^{iv_t t_t} \Sigma(v_t | v_s) \int_{t_s} e^{i(v - v_s) t_s} \\ &= e^{iv t_t} \int_{v_t} e^{-iv_t t_t} \Sigma(v' | v_t) - e^{-iv' t_t} \int_{v_t} e^{iv_t t_t} \Sigma(v_t | v) \\ &= e^{i(v - v') t_t} [\Sigma(v') - \Sigma(v)]. \end{aligned} \quad (\text{G21})$$

In the last step, we imposed time-translation invariance, which entails frequency conservation, $\Sigma(v' | v) \equiv \Sigma(v) \delta(v' - v)$.

The transformation of the RHS is more tedious, but straightforward, as proceeds analogously. It gives

$$e^{i(v - v') t_t} \int_{v_t} \left\{ [G_0^{-1}](v_t) G(v_t) \Gamma(v', v_t | v' - v + v_t, v) G(v' - v + v_t) - G(v_t + v - v') \Gamma(v', v_t + v - v' | v_t, v) G(v_t) [G_0^{-1}](v_t) \right\}. \quad (\text{G22})$$

Here, we used energy conservation both for the 2p functions and for the 4p vertex, for which we have $\Gamma(v_1' v_2' | v_1 v_2) \equiv \Gamma(v_1' v_2' | v_1, v_2) \delta(v_1' + v_2' - v_1 - v_2)$. We now perform a final Fourier transform with respect to t_t , applying $\int_{\omega} e^{i\omega t_t}$ to the full equation with the transfer frequency ω . This yields the delta function $\delta(v - v' + \omega)$, which allows us to replace $v' = v + \omega$ by formally integrating over v' . The full WI in frequency space thus reads

$$\begin{aligned} & \Sigma(v + \omega) - \Sigma(v) \\ &= \int_{v_t} \left\{ [G_0^{-1}](v_t) G(v_t) \Gamma(v + \omega, v_t | v_t + \omega, v) G(v_t + \omega) \right. \\ & \quad \left. - G(v_t - \omega) \Gamma(v + \omega, v_t - \omega | v_t, v) G(v_t) [G_0^{-1}](v_t) \right\}. \end{aligned} \quad (\text{G23})$$

To make the frequency parametrizations of the vertices of both terms on the RHS match, we now shift $v_t \rightarrow v_t + \omega$ in the second term and subsequently rename $v_t \rightarrow \tilde{v}$, which gives

$$\begin{aligned} & \Sigma(v + \omega) - \Sigma(v) \\ &= \int_{\tilde{v}} \left\{ [G_0^{-1}](\tilde{v}) G(\tilde{v}) \Gamma(v + \omega, \tilde{v} | \tilde{v} + \omega, v) G(\tilde{v} + \omega) \right. \\ & \quad \left. - G(\tilde{v}) \Gamma(v + \omega, \tilde{v} | \tilde{v} + \omega, v) G(\tilde{v} + \omega) [G_0^{-1}](\tilde{v} + \omega) \right\}. \end{aligned} \quad (\text{G24})$$

Finally, we shift the external fermionic frequency $v \rightarrow v - \omega/2$ and the integration frequency $\tilde{v} \rightarrow \tilde{v} - \omega/2$ and subsequently flip $\omega \rightarrow -\omega$ to symmetrize the equation. Using the short-hand notation $v_{\pm} = v \pm \frac{\omega}{2}$ (and, likewise, for \tilde{v}) again, we arrive at

$$\Sigma(v_-) - \Sigma(v_+)$$

$$\begin{aligned} &= \int_{\tilde{v}} \left\{ [G_0^{-1}](\tilde{v}_+) G(\tilde{v}_+) \Gamma(v_-, \tilde{v}_+ | \tilde{v}_-, v_+) G(\tilde{v}_-) \right. \\ & \quad \left. - G(\tilde{v}_+) \Gamma(v_-, \tilde{v}_+ | \tilde{v}_-, v_+) G(\tilde{v}_-) [G_0^{-1}](\tilde{v}_-) \right\}. \end{aligned} \quad (\text{G25})$$

This way, the vertex is parametrized in the a channel convention as defined in App. A of Ref. 5. In a final step, we apply crossing symmetry in the first two arguments of Γ :

$$\begin{aligned} & \Sigma(v_-) - \Sigma(v_+) \\ &= \int_{\tilde{v}} \left\{ G(\tilde{v}_+) \Gamma(\tilde{v}_+, v_- | \tilde{v}_-, v_+) G(\tilde{v}_-) [G_0^{-1}](\tilde{v}_-) \right. \\ & \quad \left. - [G_0^{-1}](\tilde{v}_+) G(\tilde{v}_+) \Gamma(\tilde{v}_+, v_- | \tilde{v}_-, v_+) G(\tilde{v}_-) \right\}. \end{aligned} \quad (\text{G26})$$

At the expense of a minus sign, the vertex is then parametrized in the t channel parametrization and we will subsequently write $\Gamma(\tilde{v}_+, v_- | \tilde{v}_-, v_+) = \Gamma_t(\omega, v, \tilde{v})$.

4. Spin structure of Eq. (F22) in the case of SU(2) symmetry

After contracting the open index σ_t , the spin structure of Eq. (F22) reads

$$\begin{aligned} \text{LHS}_{\sigma_s' | \sigma_s} &= \sum_{\sigma_t, \sigma_1, \sigma_4', \sigma_3} \left([G_0^{-1}]_{\sigma_t | \sigma_1} G_{\sigma_1 | \sigma_4'} \Gamma_{\sigma_4' \sigma_4 | \sigma_3 \sigma_s} G_{\sigma_3 | \sigma_t} \right. \\ & \quad \left. - G_{\sigma_t | \sigma_4'} \Gamma_{\sigma_4' \sigma_4 | \sigma_3 \sigma_s} G_{\sigma_3 | \sigma_1} [G_0^{-1}]_{\sigma_1 | \sigma_t} \right), \end{aligned} \quad (\text{G27})$$

where we abbreviated the left-hand side as

$$\Sigma_{\sigma_s' | \sigma_s}^{\alpha_1' | \bar{\alpha}_1} (v - \frac{\omega}{2}) - \Sigma_{\sigma_s' | \sigma_s}^{\bar{\alpha}_1' | \alpha_1} (v + \frac{\omega}{2}) \equiv \text{LHS}_{\sigma_s' | \sigma_s}. \quad (\text{G28})$$

We now consider the case in which SU(2) symmetry holds. This implies that all 2p functions are diagonal in their spin arguments, e.g. $\Sigma_{\sigma_1'|\sigma_1} \sim \delta_{\sigma_1',\sigma_1}$. For the 4p vertex, we have $\Gamma_{\sigma_1'\sigma_2'|\sigma_1\sigma_2} \sim \delta_{\sigma_1'+\sigma_2',\sigma_1+\sigma_2}$. Restricting ourselves to $\sigma_s = \uparrow$, we have

$$\text{LHS}_{\uparrow\uparrow} = \sum_{\sigma} \left([G_0^{-1}]_{\sigma|\sigma} G_{\sigma|\sigma} \Gamma_{\uparrow\sigma|\sigma\uparrow} G_{\sigma|\sigma} - G_{\sigma|\sigma} \Gamma_{\uparrow\sigma|\sigma\uparrow} G_{\sigma|\sigma} [G_0^{-1}]_{\sigma|\sigma} \right). \quad (\text{G29})$$

Using $G_{\uparrow\uparrow} = G_{\downarrow\downarrow}$, we can suppress the spin-indices for the 2p functions and write

$$\text{LHS} = \left([G_0^{-1}] G \Gamma_{\uparrow\uparrow+\uparrow\downarrow} G - G \Gamma_{\uparrow\uparrow+\uparrow\downarrow} G [G_0^{-1}] \right). \quad (\text{G30})$$

where we used the notation introduced in App. A, $\Gamma_{\uparrow\downarrow\uparrow\downarrow} \equiv \Gamma_{\uparrow\downarrow}, \Gamma_{\uparrow\downarrow\downarrow\uparrow} \equiv \Gamma_{\uparrow\downarrow}, \Gamma_{\uparrow\uparrow\uparrow\uparrow} \equiv \Gamma_{\uparrow\uparrow}$ and $\Gamma_{\uparrow\downarrow+\uparrow\uparrow} = \Gamma_{\uparrow\downarrow} + \Gamma_{\uparrow\uparrow}$. Again applying crossing symmetry in the first two arguments of Γ yields the $\uparrow\uparrow + \uparrow\downarrow = D$ spin component, so we write

$$\text{LHS} = \left(G \Gamma_D G [G_0^{-1}] - [G_0^{-1}] G \Gamma_D G \right). \quad (\text{G31})$$

As mentioned in Sec. III C, in addition to U(1) symmetry, the SU(2) symmetry of the action can be exploited as well to derive another, almost identical, WI. Its derivation works in almost the same way, the only difference being that the generators of SU(2) transformations, i.e. the Pauli matrices, modify the spin structure of the equation. As explained in Ref. [61], the result is given by a slight modification of Eq. (G29),

$$\text{LHS}_{\uparrow\uparrow} = \sum_{\sigma} \sigma \left([G_0^{-1}]_{\sigma|\sigma} G_{\sigma|\sigma} \Gamma_{\uparrow\sigma|\sigma\uparrow} G_{\sigma|\sigma} - G_{\sigma|\sigma} \Gamma_{\uparrow\sigma|\sigma\uparrow} G_{\sigma|\sigma} [G_0^{-1}]_{\sigma|\sigma} \right), \quad (\text{G32})$$

where $\sigma = \uparrow \rightarrow +1$ and $\sigma = \downarrow \rightarrow -1$. Compared to Eq. (G29), this only changes the sign with which the $\uparrow\downarrow$ component enters in Eq. (G30). Once again applying crossing symmetry to parametrize the vertex in the t channel yields the $\uparrow\uparrow - \uparrow\downarrow = M$. The rest of the WI is unchanged. In this work, we do not discuss the SU(2) WI further.

5. Fourier transform, Keldysh rotation, and explicit form of G_0^{-1} for the single-impurity Anderson model

In this section, we compute the Fourier transform of the inverse bare Green's function G_0^{-1} and its Keldysh rotation explicitly. As seen in Eqs. (G2) and (G3), we can write G_0^{-1} using derivatives acting either to the left or to the right. Both versions must yield the same result for the Fourier transform, which we will now show. Starting with the derivative acting to the right, we compute

$$\begin{aligned} [G_0^{-1}]_{1'1}(\mathbf{v}_1|\mathbf{v}_1) &= \int_{t_1't_1} e^{-i\mathbf{v}_1't_1'} [\overset{\rightarrow}{G_0^{-1}}]_{1'1}(t_1'|t_1) e^{i\mathbf{v}_1 t_1} \\ &= \int_{t_1't_1} e^{-i\mathbf{v}_1't_1'} \left[\delta_{1',1} \delta_{\mathcal{E}}(t_1' - t_1) i \overset{\rightarrow}{\partial}_{t_1} - h_{1'1}(t_1'|t_1) \right] e^{i\mathbf{v}_1 t_1} \end{aligned}$$

$$\begin{aligned} &= \int_{t_1't_1} e^{-i\mathbf{v}_1't_1'} [\delta_{1',1} \delta_{\mathcal{E}}(t_1' - t_1)(-\mathbf{v}_1) - h_{1'1}(t_1'|t_1)] e^{i\mathbf{v}_1 t_1} \\ &= j_{1'} \delta_{1',1} \mathbf{v}_1 \int_{t_1} e^{i(\mathbf{v}_1 - \mathbf{v}_1')t_1} - \int_{t_1't_1} e^{-i\mathbf{v}_1't_1'} h_{1'1}(t_1'|t_1) e^{i\mathbf{v}_1 t_1} \\ &= j_{1'} \delta_{1',1} \mathbf{v}_1 \delta(\mathbf{v}_1 - \mathbf{v}_1') - h_{1'1}(\mathbf{v}_1'|\mathbf{v}_1). \end{aligned} \quad (\text{G33})$$

Likewise, using the derivative acting to the left, we obtain

$$\begin{aligned} &\int_{t_1't_1} e^{-i\mathbf{v}_1't_1'} [\delta_{1',1} \delta_{\mathcal{E}}(t_1' - t_1)(-\mathbf{v}_1') - h_{1'1}(t_1'|t_1)] e^{i\mathbf{v}_1 t_1} \\ &= j_1 \delta_{1',1} \mathbf{v}_1 \delta(\mathbf{v}_1 - \mathbf{v}_1') - h_{1'1}(\mathbf{v}_1'|\mathbf{v}_1), \end{aligned} \quad (\text{G34})$$

which is the same result. Writing the first term in matrix form ($[G_0^{-1}]_{\mathbf{v}\text{-part}}^{j'j} = \begin{pmatrix} -\mathbf{v}^0 \\ 0 \end{pmatrix}$), we perform a Keldysh rotation as in Sec. G 2, multiplying with D^{-1} from the left and with D from the right to obtain ($[G_0^{-1}]_{\mathbf{v}\text{-part}}^{\alpha'\alpha} = \begin{pmatrix} 0 & \mathbf{v} \\ \mathbf{v} & 0 \end{pmatrix}$), which is the expected result. Using energy conservation, writing $[G_0^{-1}]_{1'1}(\mathbf{v}_1'|\mathbf{v}_1) = [G_0^{-1}]_{1'1}(\mathbf{v}_1) \delta(\mathbf{v}_1' - \mathbf{v}_1)$, we therefore have

$$[G_0^{-1}]_{\sigma_1'|\sigma_1}^{\alpha_1'|\alpha_1}(\mathbf{v}) = \delta_{\alpha_1',\bar{\alpha}_1} \delta_{\sigma_1',\sigma_1} \mathbf{v} - h_{\sigma_1'|\sigma_1}^{\alpha_1'|\alpha_1}(\mathbf{v}). \quad (\text{G35})$$

For the single-impurity Anderson model without a magnetic field, the single-particle Hamiltonian is given by the shift of the impurity level plus the hybridization function,

$$h_{\sigma_1'|\sigma_1}^{\alpha_1'|\alpha_1}(\mathbf{v}) = \delta_{\alpha_1',\bar{\alpha}_1} \delta_{\sigma_1',\sigma_1} \varepsilon_d + \Delta_{\sigma_1'|\sigma_1}^{\alpha_1'|\alpha_1}(\mathbf{v}). \quad (\text{G36})$$

6. Derivation of Heyder's result for the special case $\omega = 0$

We obtain the special case of the WI already studied in the literature [5, 64] by taking $\alpha_{1'} = \alpha_1 = 2$ and setting $\omega \equiv 0$ in Eq. (21). The LHS of Eq. (21) then becomes

$$\Sigma^{2|1}(\mathbf{v}) - \Sigma^{1|2}(\mathbf{v}) = \Sigma^A(\mathbf{v}) - \Sigma^R(\mathbf{v}) = -2i \text{Im} \Sigma^R(\mathbf{v}).$$

Using that the frequency arguments of all 2p functions are identical in this case, we focus only on the Keldysh structure of $-\text{RHS}$ of Eq. (21), which we write as the trace over matrix products in Keldysh space,

$$\begin{aligned} &\text{Tr} \left\{ \begin{pmatrix} \Delta^A & 0 \\ \Delta^K & \Delta^R \end{pmatrix} \begin{pmatrix} 0 & G^A \\ G^R & G^K \end{pmatrix} \begin{pmatrix} \Gamma^{1|1} & \Gamma^{1|2} \\ \Gamma^{2|1} & 0 \end{pmatrix} \begin{pmatrix} 0 & G^A \\ G^R & G^K \end{pmatrix} \right. \\ &\quad \left. - \begin{pmatrix} 0 & G^A \\ G^R & G^K \end{pmatrix} \begin{pmatrix} \Gamma^{1|1} & \Gamma^{1|2} \\ \Gamma^{2|1} & 0 \end{pmatrix} \begin{pmatrix} 0 & G^A \\ G^R & G^K \end{pmatrix} \begin{pmatrix} \Delta^R & \Delta^K \\ 0 & \Delta^A \end{pmatrix} \right\}. \end{aligned} \quad (\text{G37})$$

The first term on the RHS of Eq. (21), being $\sim \omega$, obviously vanishes. Here, we have already flipped the Keldysh index α_2 of the hybridization functions and fixed the Keldysh indices $\alpha_{1'}$ and α_1 of Γ to 2, using that $\Gamma^{22|22} = 0$ by causality. Evaluating the matrix product and computing the trace gives

$$\begin{aligned} &\Delta^R G^R (\Gamma^{1|1} G^A + \Gamma^{1|2} G^K) + (\Delta^K G^A + \Delta^R G^K) \Gamma^{2|1} G^A \\ &\quad - (G^R \Gamma^{1|1} + G^K \Gamma^{2|1}) G^A \Delta^A - G^R \Gamma^{1|2} (G^R \Delta^K + G^K \Delta^A). \end{aligned} \quad (\text{G38})$$

Reshuffling terms and using the FDR $G^K = \text{th}(G^R - G^A)$ and likewise for Δ^K , where “th” is a short-hand notation for $\tanh(\frac{v}{2T}) = 1 - 2n_F(v)$, several terms cancel and we obtain

$$\begin{aligned} & G^R G^A (\Delta^R - \Delta^A) \Gamma^{1|1} + \text{th}[\Gamma^{1|2} (G^R \Delta^A G^A - G^R \Delta^R G^A) \\ & \quad + \Gamma^{2|1} (\Delta^R G^A G^R - G^A \Delta^A G^R)] \\ & = G^R G^A (\Delta^R - \Delta^A) [\Gamma^{1|1} - \text{th}(\Gamma^{1|2} - \Gamma^{2|1})]. \end{aligned} \quad (\text{G39})$$

In the wide-band limit, where $\Delta^R - \Delta^A = -2i\Delta$, the whole equation becomes

$$\begin{aligned} 2\text{Im}\Sigma^R(v) & = 2i\Delta \int_{\tilde{v}} G^R(\tilde{v}) G^A(\tilde{v}) \left\{ \Gamma^{21|12}(v, \tilde{v}|\tilde{v}, v) \right. \\ & \quad \left. - [1 - 2n_F(\tilde{v})] [\Gamma^{21|22}(v, \tilde{v}|\tilde{v}, v) - \Gamma^{22|12}(v, \tilde{v}|\tilde{v}, v)] \right\}, \end{aligned} \quad (\text{G40})$$

where we reinstated the frequency arguments. Multiplying the whole equation with (-1) and using crossing symmetry for the vertices twice, this becomes precisely Eq. (8.13) in Ref. 5.

Appendix H: Diagrammatic representation of the U(1) WI

In this section, we provide a compact diagrammatic representation of the U(1) WI. This representation is useful to motivate the result of the Keldysh rotation and of the Fourier transform carried out explicitly in App. G2 and App. G3.

Introducing the bare 3p “Hedin” vertex as

$$\delta_{1't1} = \delta(1' - t) \delta(t - 1) = \begin{array}{c} 1 \\ \swarrow \delta \\ \Gamma \\ \searrow \delta \\ 1' \end{array} t, \quad (\text{H1})$$

where t labels a “bosonic” multi-index that is contracted, Eq. (F22) can be written as

$$\begin{aligned} & i\Sigma_{s'|1} \delta_{1ts} - i\delta_{s't1} \Sigma_{1|s} = \delta_{2t2'} \Gamma_{s'4'|3s} \times \\ & \left\{ [G_0^{-1}]_{2|\bar{1}} G_{\bar{1}|4'} G_{3|2'} - G_{2|4'} G_{3|\bar{1}} [G_0^{-1}]_{\bar{1}|2'} \right\}. \end{aligned} \quad (\text{H2})$$

For ease of notation, repeated multi-indices are meant to be contracted.

Introducing a diagrammatic notation for G_0^{-1} ,

$$[G_0^{-1}]_{1'|1} = \begin{array}{c} \leftarrow \textcircled{G_0^{-1}} \leftarrow \\ 1' \quad 1 \end{array},$$

we can depict Eq. (H2) diagrammatically as

$$= \begin{array}{c} \begin{array}{c} s \\ \swarrow \delta \\ \Gamma \\ \searrow \delta \\ s' \end{array} \textcircled{G_0^{-1}} \begin{array}{c} s \\ \swarrow \delta \\ \Gamma \\ \searrow \delta \\ s' \end{array} t \\ - \\ \begin{array}{c} s \\ \swarrow \delta \\ \Gamma \\ \searrow \delta \\ s' \end{array} \textcircled{G_0^{-1}} \begin{array}{c} s \\ \swarrow \delta \\ \Gamma \\ \searrow \delta \\ s' \end{array} t, \end{array} \quad (\text{H3})$$

where touching diagram components mean a direct contraction between the two, without a connecting propagator.

In these expressions, the Keldysh rotation and the Fourier transform are mere basis transformations to be carried out consistently. After choosing a frequency convention and accordingly labeling the legs, the frequency arguments can be read off from the diagrams. Hence, we merely need the Keldysh and frequency structure of the bare Hedin vertex δ , which turns out to be very analogous to that of the bare interaction Γ_0 . First, in (H1) the delta functions that enforce equal times simply become a delta function that frequency conservation. Second, the Keldysh structure of δ is given by

$$\delta^{\alpha_{1'} 1 \alpha_1} = \begin{pmatrix} 0 & 1 \\ 1 & 0 \end{pmatrix} = \sigma_x^{\alpha_{1'} \alpha_1}, \quad (\text{H4a})$$

$$\delta^{\alpha_{1'} 2 \alpha_1} = \begin{pmatrix} 1 & 0 \\ 0 & 1 \end{pmatrix} = \delta_{\alpha_{1'} \alpha_1} \quad (\text{H4b})$$

for $\alpha_t = 1$ and $\alpha_t = 2$, respectively. Equation (21) is obtained for the choice $\alpha_t = 1$.

- [1] A. Georges, G. Kotliar, W. Krauth, and M. J. Rozenberg, Dynamical mean-field theory of strongly correlated fermion systems and the limit of infinite dimensions, *Rev. Mod. Phys.* **68**, 13 (1996).
- [2] G. Rohringer, H. Hafermann, A. Toschi, A. A. Katanin, A. E. Antipov, M. I. Katsnelson, A. I. Lichtenstein, A. N. Rubtsov, and K. Held, Diagrammatic routes to nonlocal correlations be-

yond dynamical mean field theory, *Rev. Mod. Phys.* **90**, 025003 (2018).

- [3] F. B. Kugler, S.-S. B. Lee, and J. von Delft, Multipoint correlation functions: Spectral representation and numerical evaluation, *Phys. Rev. X* **11**, 041006 (2021).
- [4] S.-S. B. Lee, F. B. Kugler, and J. von Delft, Computing local multipoint correlators using the numerical renormalization group, *Phys. Rev. X* **11**, 041007 (2021).

- [5] E. Walter, *Real-frequency dynamics of quantum impurity models studied with fRG, NRG, CFT*, Ph.D. thesis, LMU München (2021).
- [6] A. Ge, N. Ritz, E. Walter, S. Aguirre, J. von Delft, and F. B. Kugler, Real-frequency quantum field theory applied to the single-impurity Anderson model, *Phys. Rev. B* **109**, 115128 (2024).
- [7] N. Ritz, A. Ge, E. Walter, S. Aguirre, J. von Delft, and F. B. Kugler, KeldyshQFT: A C++ codebase for real-frequency multiloop functional renormalization group and parquet computations of the single-impurity Anderson model, *The Journal of Chemical Physics* **161**, 054118 (2024).
- [8] R. Bulla, T. A. Costi, and T. Pruschke, Numerical renormalization group method for quantum impurity systems, *Rev. Mod. Phys.* **80**, 395 (2008).
- [9] A. Toschi, A. A. Katanin, and K. Held, Dynamical vertex approximation: A step beyond dynamical mean-field theory, *Phys. Rev. B* **75**, 045118 (2007).
- [10] K. Held, A. A. Katanin, and A. Toschi, Dynamical vertex approximation: An introduction, *Prog. Theor. Phys. Supp.* **176**, 117 (2008).
- [11] N. E. Bickers, Self-Consistent Many-Body Theory for Condensed Matter Systems, in *Sénéchal D., Tremblay A.-M., Bourbonnais C. (eds), Theoretical Methods for Strongly Correlated Electrons, CRM Series in Mathematical Physics* (Springer, New York, 2004).
- [12] F. B. Kugler and J. von Delft, Multiloop functional renormalization group that sums up all parquet diagrams, *Phys. Rev. Lett.* **120**, 057403 (2018).
- [13] F. B. Kugler and J. von Delft, Multiloop functional renormalization group for general models, *Phys. Rev. B* **97**, 035162 (2018).
- [14] F. B. Kugler and J. von Delft, Derivation of exact flow equations from the self-consistent parquet relations, *New J. Phys.* **20**, 123029 (2018).
- [15] W. Metzner, M. Salmhofer, C. Honerkamp, V. Meden, and K. Schönhammer, Functional renormalization group approach to correlated fermion systems, *Rev. Mod. Phys.* **84**, 299 (2012).
- [16] C. Taranto, S. Andergassen, J. Bauer, K. Held, A. Katanin, W. Metzner, G. Rohringer, and A. Toschi, From infinite to two dimensions through the functional renormalization group, *Phys. Rev. Lett.* **112**, (2014).
- [17] J.-M. Lihm, J. Halbinger, J. Shim, J. von Delft, F. B. Kugler, and S.-S. B. Lee, Symmetric improved estimators for multipoint vertex functions, *Phys. Rev. B* **109**, 125138 (2024).
- [18] P. W. Anderson, Localized Magnetic States in Metals, *Phys. Rev.* **124**, 41 (1961).
- [19] F. B. Anders and A. Schiller, Real-time dynamics in quantum-impurity systems: A time-dependent numerical renormalization-group approach, *Phys. Rev. Lett.* **95**, 196801 (2005).
- [20] K. G. Wilson, The renormalization group: Critical phenomena and the Kondo problem, *Rev. Mod. Phys.* **47**, 773 (1975).
- [21] H. R. Krishna-murthy, J. W. Wilkins, and K. G. Wilson, Renormalization-group approach to the Anderson model of dilute magnetic alloys. I. Static properties for the symmetric case, *Phys. Rev. B* **21**, 1003 (1980).
- [22] R. Bulla, A. C. Hewson, and T. Pruschke, Numerical renormalization group calculations for the self-energy of the impurity Anderson model, *Journal of Physics: Condensed Matter* **10**, 8365 (1998).
- [23] T. Pruschke and R. Bulla, Hund's coupling and the metal-insulator transition in the two-band Hubbard model, *The European Physical Journal B* **44**, 217–224 (2005).
- [24] K. M. Stadler, Z. P. Yin, J. von Delft, G. Kotliar, and A. Weichselbaum, Dynamical mean-field theory plus numerical renormalization-group study of spin-orbital separation in a three-band Hund metal, *Phys. Rev. Lett.* **115**, 136401 (2015).
- [25] K. Stadler, G. Kotliar, A. Weichselbaum, and J. von Delft, Hundness versus Mottness in a three-band Hubbard–Hund model: On the origin of strong correlations in Hund metals, *Annals of Physics* **405**, 365–409 (2019).
- [26] X. Deng, K. M. Stadler, K. Haule, A. Weichselbaum, J. von Delft, and G. Kotliar, Signatures of Mottness and Hundness in archetypal correlated metals, *Nature Communications* **10**, 10.1038/s41467-019-10257-2 (2019).
- [27] F. B. Kugler, S.-S. B. Lee, A. Weichselbaum, G. Kotliar, and J. von Delft, Orbital differentiation in Hund metals, *Phys. Rev. B* **100**, 115159 (2019).
- [28] F. B. Kugler, M. Zingl, H. U. R. Strand, S.-S. B. Lee, J. von Delft, and A. Georges, Strongly correlated materials from a numerical renormalization group perspective: How the Fermi-liquid state of Sr₂RuO₄ emerges, *Phys. Rev. Lett.* **124**, 016401 (2020).
- [29] K. M. Stadler, G. Kotliar, S.-S. B. Lee, A. Weichselbaum, and J. von Delft, Differentiating Hund from Mott physics in a three-band Hubbard-Hund model: Temperature dependence of spectral, transport, and thermodynamic properties, *Phys. Rev. B* **104**, 115107 (2021).
- [30] F. B. Kugler and G. Kotliar, Is the orbital-selective Mott phase stable against interorbital hopping?, *Phys. Rev. Lett.* **129**, 096403 (2022).
- [31] F. B. Kugler, C.-J. Kang, and G. Kotliar, Low-energy perspective on two-orbital Hund metals and the case of LaNiO₂, *Phys. Rev. B* **110**, 155101 (2024).
- [32] M. Grundner, F. B. Kugler, O. Parcollet, U. Schollwöck, A. Georges, and A. Hampel, Liv2o4: Hund-assisted orbital-selective mottness (2024), [arXiv:2409.17268 \[cond-mat.str-el\]](https://arxiv.org/abs/2409.17268).
- [33] J. Lee-Hand, H. LaBollita, F. B. Kugler, L. V. Muñoz, J. Kaye, S. Beck, A. Hampel, A. Georges, and C. E. Dreyer, Fermi-liquid t^2 resistivity: Dynamical mean-field theory meets experiment (2024), [arXiv:2412.16363 \[cond-mat.mtrl-sci\]](https://arxiv.org/abs/2412.16363).
- [34] A. Gleis, S.-S. B. Lee, G. Kotliar, and J. von Delft, Emergent properties of the periodic anderson model: A high-resolution, real-frequency study of heavy-fermion quantum criticality, *Phys. Rev. X* **14**, 041036 (2024).
- [35] A. Gleis, S.-S. B. Lee, G. Kotliar, and J. von Delft, Dynamical scaling and planckian dissipation due to heavy-fermion quantum criticality, *Phys. Rev. Lett.* **134**, 106501 (2025).
- [36] L. D. Landau, A. A. Abrikosov, and I. M. Khalatnikov, An asymptotic expression for the photon Green function in quantum electrodynamics, *Dokl. Akad. Nauk SSSR* **95**, 1177 (1954).
- [37] C. De Dominicis and P. C. Martin, Stationary Entropy Principle and Renormalization in Normal and Superfluid Systems. I. Algebraic Formulation, *Journal of Mathematical Physics* **5**, 14 (1964).
- [38] C. De Dominicis and P. C. Martin, Stationary Entropy Principle and Renormalization in Normal and Superfluid Systems. II. Diagrammatic Formulation, *Journal of Mathematical Physics* **5**, 31 (1964).
- [39] N. Wentzell, G. Li, A. Tagliavini, C. Taranto, G. Rohringer, K. Held, A. Toschi, and S. Andergassen, High-frequency asymptotics of the vertex function: Diagrammatic parametrization and algorithmic implementation, *Phys. Rev. B* **102**, 085106 (2020).
- [40] F. Krien, Efficient evaluation of the polarization function in dynamical mean-field theory, *Phys. Rev. B* **99**, 235106 (2019).
- [41] F. Krien, A. Valli, and M. Capone, Single-boson exchange decomposition of the vertex function, *Phys. Rev. B* **100**, 155149 (2019).

- [42] F. Krien and A. Valli, Parquetlike equations for the Hedin three-leg vertex, *Phys. Rev. B* **100**, 245147 (2019).
- [43] F. Krien, A. I. Lichtenstein, and G. Rohringer, Fluctuation diagnostic of the nodal/antinodal dichotomy in the Hubbard model at weak coupling: A parquet dual fermion approach, *Phys. Rev. B* **102**, 235133 (2020).
- [44] F. Krien, A. Valli, P. Chalupa, M. Capone, A. I. Lichtenstein, and A. Toschi, Boson-exchange parquet solver for dual fermions, *Phys. Rev. B* **102**, 195131 (2020).
- [45] F. Krien, A. Kauch, and K. Held, Tiling with triangles: parquet and $GW\gamma$ methods unified, *Phys. Rev. Res.* **3**, 013149 (2021).
- [46] M. Gievers, E. Walter, A. Ge, J. v. Delft, and F. B. Kugler, Multiloop flow equations for single-boson exchange fRG, *The European Physical Journal B* **95** (2022).
- [47] L. V. Keldysh, Diagram technique for nonequilibrium processes, *Sov. Phys. JETP* **20**, 1018 (1965).
- [48] J. Schwinger, Brownian Motion of a Quantum Oscillator, *J. Math. Phys.* **2**, 407 (1961).
- [49] L. P. Kadanoff and G. A. Baym, *Quantum statistical mechanics* (Benjamin, New York, 1962).
- [50] A. Tsvetick and P. Wiegmann, Exact results in the theory of magnetic alloys, *Adv. Phys.* **32**, 453 (1983).
- [51] N. Ritz and A. Ge, *KeldyshQFT: A C++ Codebase for real-frequency multiloop functional renormalization group and parquet computations for the single impurity Anderson model*.
- [52] E. Wang and U. Heinz, Generalized fluctuation-dissipation theorem for nonlinear response functions, *Phys. Rev. D* **66**, 025008 (2002).
- [53] A. Ge, *Analytic continuation of correlators from the Matsubara to the Keldysh formalism*, *Master's thesis*, LMU München (2020).
- [54] A. Ge, J. Halbinger, S.-S. B. Lee, J. von Delft, and F. B. Kugler, Analytic continuation of multipoint correlation functions, *Annalen der Physik* **536**, 2300504 (2024).
- [55] F. B. Kugler, Improved estimator for numerical renormalization group calculations of the self-energy, *Phys. Rev. B* **105**, 245132 (2022).
- [56] J.-M. Lihm and S.-S. Lee, private communication.
- [57] L. Hedin, New method for calculating the one-particle Green's function with application to the electron-gas problem, *Phys. Rev.* **139**, A796 (1965).
- [58] M. Patricolo, M. Gievers, K. Fraboulet, A. Al-Eryani, S. Heinzelmann, P. M. Bonetti, A. Toschi, D. Vilardi, and S. Andergassen, Single-boson exchange formulation of the Schwinger-Dyson equation and its application to the functional renormalization group, *SciPost Phys.* **18**, 078 (2025).
- [59] F. Krien, *Conserving dynamical mean-field approaches to strongly correlated systems*, *Ph.D. thesis*, Hamburg University (2018).
- [60] A. A. Katanin, Fulfillment of Ward identities in the functional renormalization group approach, *Phys. Rev. B* **70**, 115109 (2004).
- [61] P. Kopietz, L. Bartosch, L. Costa, A. Isidori, and A. Ferraz, Ward identities for the Anderson impurity model: derivation via functional methods and the exact renormalization group, *J. Phys. A* **43**, 385004 (2010).
- [62] F. Krien, E. G. C. P. van Loon, H. Hafermann, J. Otsuki, M. I. Katsnelson, and A. I. Lichtenstein, Conservation in two-particle self-consistent extensions of dynamical mean-field theory, *Phys. Rev. B* **96**, 075155 (2017).
- [63] P. Chalupa-Gantner, F. B. Kugler, C. Hille, J. von Delft, S. Andergassen, and A. Toschi, Fulfillment of sum rules and Ward identities in the multiloop functional renormalization group solution of the Anderson impurity model, *Phys. Rev. Res.* **4**, 023050 (2022).
- [64] J. Heyder, F. Bauer, D. Schimmel, and J. von Delft, Derivation of Oguri's linear conductance formula for interacting fermions within the Keldysh formalism, *Phys. Rev. B* **96**, 125141 (2017).
- [65] H. Shinaoka, M. Wallerberger, Y. Murakami, K. Nogaki, R. Sakurai, P. Werner, and A. Kauch, Multiscale space-time ansatz for correlation functions of quantum systems based on quantics tensor trains, *Phys. Rev. X* **13**, 021015 (2023).
- [66] Y. Núñez Fernández, M. Jeannin, P. T. Dumitrescu, T. Kloss, J. Kaye, O. Parcollet, and X. Waintal, Learning Feynman Diagrams with Tensor Trains, *Phys. Rev. X* **12**, 041018 (2022).
- [67] M. K. Ritter, Y. Núñez Fernández, M. Wallerberger, J. von Delft, H. Shinaoka, and X. Waintal, Quantics tensor cross interpolation for high-resolution parsimonious representations of multivariate functions, *Phys. Rev. Lett.* **132**, 056501 (2024).
- [68] Y. N. Fernández, M. K. Ritter, M. Jeannin, J.-W. Li, T. Kloss, T. Louvet, S. Terasaki, O. Parcollet, J. von Delft, H. Shinaoka, and X. Waintal, Learning tensor networks with tensor cross interpolation: new algorithms and libraries, *SciPost Phys.* **18**, 104 (2025).
- [69] S. Rohshap, M. K. Ritter, H. Shinaoka, J. von Delft, M. Wallerberger, and A. Kauch, *Two-particle calculations with quantics tensor trains – solving the parquet equations* (2024), [arXiv:2410.22975 \[cond-mat.str-el\]](https://arxiv.org/abs/2410.22975).
- [70] M. Frankenbach, A. Ge, M. Ritter, N. Ritz, and J. von Delft, Compressing local vertex functions from MuNRG using tensor cross interpolation, to be published (2025).
- [71] O. Kovalska, A. Gleis, and J. von Delft, Projected Krylov Approach for efficient matrix product state based computation of real-frequency spectral functions, in preparation (2025).
- [72] S. R. White, Density matrix formulation for quantum renormalization groups, *Phys. Rev. Lett.* **69**, 2863 (1992).
- [73] F. D. Picoli, M. Huang, A. Gleis, and J. von Delft, Tangent-Space Krylov Solver for Quantum Impurity Systems, in preparation (2025).
- [74] S.-S. B. Lee and A. Weichselbaum, Adaptive broadening to improve spectral resolution in the numerical renormalization group, *Phys. Rev. B* **94**, 235127 (2016).
- [75] S.-S. B. Lee, J. von Delft, and A. Weichselbaum, Double-holon origin of the subpeaks at the Hubbard band edges, *Phys. Rev. Lett.* **119**, 236402 (2017).
- [76] A. Weichselbaum, Non-Abelian symmetries in tensor networks: A quantum symmetry space approach, *Annals of Physics* **327**, 2972 (2012).
- [77] A. Weichselbaum, Tensor networks and the numerical renormalization group, *Phys. Rev. B* **86**, 245124 (2012).
- [78] A. Weichselbaum, X-symbols for non-Abelian symmetries in tensor networks, *Phys. Rev. Res.* **2**, 023385 (2020).
- [79] A. Weichselbaum, QSpace - An open-source tensor library for Abelian and non-Abelian symmetries, *SciPost Phys. Codebases*, **4**, 40 (2024).
- [80] A. Weichselbaum, Codebase release 4.0 for QSpace, *SciPost Phys. Codebases*, **4**, 40 (2024).
- [81] Data for: Testing the parquet equations and the U(1) Ward identity for real-frequency correlation functions from the multipoint numerical renormalization group, <https://opendata.physik.lmu.de/8amqyCuZsv1xFDN/>.
- [82] G. Rohringer, *New routes towards a theoretical treatment of nonlocal electronic correlations*, *Ph. D. Thesis*, Technische Universität Wien (2013).
- [83] R. Peters, T. Pruschke, and F. B. Anders, Numerical renormalization group approach to Green's functions for quantum impurity models, *Phys. Rev. B* **74**, 245114 (2006).

- [84] A. Weichselbaum and J. von Delft, Sum-rule conserving spectral functions from the numerical renormalization group, *Phys. Rev. Lett.* **99**, 076402 (2007).
- [85] R. Žitko and T. Pruschke, Energy resolution and discretization artifacts in the numerical renormalization group, *Phys. Rev. B* **79**, 085106 (2009).
- [86] R. Žitko, Adaptive logarithmic discretization for numerical renormalization group methods, *Computer Physics Communications* **180**, 1271 (2009).

4 Outlook

At the beginning of Ch. 3, we motivated our study of the output of NRG in Ref. [P4] by the possibility of using NRG as an impurity solver for dynamical mean-field theory (DMFT) calculations serving as a starting point for a subsequent nonlocal diagrammatic extension. By combining the non-perturbative albeit local nature of DMFT with quantum field theory in the form of, e.g., the parquet equations or fRG, which can be formulated for nonlocal correlation functions, this idea in the long run promises to enable precise studies of correlated materials in regimes where perturbative approximations such as the PA break down.

In this chapter, we discuss these proposals in more detail. After summarizing the main ideas behind DMFT, we list a few suggestions for nonlocal extensions in Sec. 4.1, focusing on diagrammatic extensions. We discuss three methods concretely, which are based on the parquet equations and fRG, respectively. The main issue all diagrammatic extensions of DMFT share is that, due to the additional momentum dependencies, the functions involved, especially the vertices, are challenging to resolve and compute numerically. In the final section of this thesis, Sec. 4.2, we therefore discuss the main ideas behind the quantics tensor cross interpolation technique, which currently is the most promising candidate method for keeping the numerical resources required for such calculations in check.

4.1 Diagrammatic extensions of dynamical mean field theory

The *dynamical mean-field theory* is a widely used method in condensed matter physics [Geo+96]. Historically, its first main achievement was the explanation of the metal-to-insulator (“Mott”) transition in transition-metal oxides. By now, it has become a standard tool for studying correlated materials, often in combination with other methods such as density functional theory [Kot+06]. Motivated by previous work on perturbation theory in large dimensions [MV89; GK92; Jar92], DMFT’s main approximation is to neglect spatial fluctuations. Local quantum fluctuations are, however, fully taken into account. Formally, DMFT approximates the self-energy to be local, i.e., momentum independent,¹

$$\Sigma(\nu, \mathbf{k}) \equiv \Sigma(\nu). \quad (4.1)$$

This approximation is justified in high dimensions when the vicinity of a given lattice site has little spatial structure and becomes exact in the limit of infinite dimensions or infinite coordination number of the lattice. Additionally and crucially, DMFT is also exact in two more vastly different limiting cases: First, for non-interacting systems ($\Gamma_0 = 0$), the self-energy vanishes identically, so Eq. (4.1) holds trivially. Second, in the atomic limit,

¹ It is a common misconception that DMFT only yields local quantities. That is not true: For instance, the two-point Green’s function $G(\nu, \mathbf{k}) = [\nu - \varepsilon_{\mathbf{k}} - \Sigma(\nu)]^{-1}$ is momentum dependent in DMFT. However, the momentum dependence enters only through the bare dispersion $\varepsilon_{\mathbf{k}}$ and is not renormalized by the self-energy.

when the tunneling amplitudes between different lattice sites $t_{ij} = 0$ vanish, there are no nonlocal contributions to the self-energy because the system can simply be described as a collection of independent, uncoupled sites. DMFT's property of being exact under these three qualitatively different circumstances makes it widely applicable and a good approximation in many cases.

The actual DMFT algorithm works as follows. Focusing on a single lattice site, the influence from the neighboring sites is approximated as an electron bath without spatial structure. This description readily yields an impurity model (see Sec. 3.1), with the effect of the surrounding lattice captured by the frequency-dependent hybridization function $\Delta(\nu)$, which becomes the dynamical mean field. Solving the resulting impurity model yields a local self-energy $\Sigma(\nu)$. That is the hard part, since a many-body problem still has to be solved and numerous “impurity solvers” have been used for this purpose, the gold standard being NRG, see Sec. 3.2. Next, DMFT asserts that the resulting impurity Green's function corresponds to the local lattice Green's function,²

$$\frac{1}{\nu - \epsilon_d - \Delta(\nu) - \Sigma(\nu)} \stackrel{!}{=} \sum_{\mathbf{k}} \frac{1}{\nu - \epsilon_{\mathbf{k}} - \Sigma(\nu)}. \quad (4.2)$$

Solving Eq. (4.2) for $\Delta(\nu)$ defines a new impurity model to be solved. Hence, the previous steps have to be iterated until convergence.

Despite its success, the DMFT approximation, describing only local correlations, is a severe limitation in some cases. In particular, DMFT cannot predict momentum-dependent many-body effects. One example is the opening of a pseudogap in the spectral function of the Hubbard model or of cuprates [Kei+15], which opens only in parts of the Brillouin zone. Also, DMFT violates the Mermin–Wagner theorem [MW66] because the long-range quantum fluctuations, responsible for inhibiting long-range order at low temperatures, are neglected. Furthermore, it can be shown using symmetry arguments that the vertex corrections to the current-current correlation function and, by extension, to the optical conductivity, see Sec. 1.2.3, vanish in single-site DMFT [Khu90; Geo+96].

For these reasons, there is a need for *nonlocal extensions* of DMFT. Most naturally, not just a single site but a cluster of multiple sites is treated inside the DMFT algorithm. That can be done in momentum space, which is called the “dynamical cluster approximation” (DCA) [Het+98] or in real space, giving rise to “cellular DMFT” (CDMFT) [Kot+01; LK00]. For a review of these *cluster extensions of DMFT*, see Ref. [Mai+05]. While the cluster size controls the accuracy of the methods, it is also their main limitation since treating large clusters is numerically costly due to the exponentially increasing dimension of the underlying Hilbert space. Cluster extensions are, therefore, restricted to small cluster sizes, limiting their ability to describe long-range correlation effects. Still, good results can be obtained if the correlation length is comparatively small, such as in the strong-coupling pseudogap phase of the Hubbard model [Sch+21; Mei+24].

The system size is no issue for the second class of nonlocal extensions of DMFT, namely *diagrammatic extensions* [Roh+18], which typically can be used to compute nonlocal correlation functions in the thermodynamic limit. In keeping with the topic of this thesis,

² The chemical potentials can be absorbed in the impurity level shift ϵ_d and the lattice dispersion $\epsilon_{\mathbf{k}}$, respectively.

we will focus here on parquet and fRG-based schemes.³

In the parquet formalism, the simplest method for extending the local approximation of the self-energy is the *ladder dynamical vertex approximation* (ladder D Γ A) [TKH07; HKT08; Kus06; Hel22]. Starting from the local self-energy Σ and a local 2PI vertex in a given channel I_r from DMFT, the BSE in that channel, see Eq. (2.37), is evaluated to yield a momentum-dependent vertex. As previously mentioned in Sec. 3.1, for certain parameters, I_r can diverge, even in the absence of a physical phase transition. Such *irreducible vertex divergences* are compensated by γ_r , so that the full Γ stays finite, and are hence a formal artifact of the parquet decomposition. Conveniently, ladder D Γ A can be formulated in such a way that the irreducible vertex I_r does not have to be used explicitly [Roh+18; Kug19]: Plugging the BSE into the parquet decomposition, Eqs. (2.36), one can write

$$\Gamma = I_r + I_r \circ \Pi_r \circ \Gamma \quad \Leftrightarrow \quad I_r^{-1} = \Gamma^{-1} + \Pi_r. \quad (4.3)$$

Since I_r^{-1} is approximated to be local, one can set

$$\Gamma^{-1} + \Pi_r = \Gamma^{\text{imp},-1} + \Pi_r^{\text{imp}}, \quad (4.4)$$

with the momentum-dependent lattice quantities on the left and the local quantities corresponding to the self-consistent DMFT impurity model on the right. Equation (4.4) can be solved to yield

$$\Gamma = \Gamma^{\text{imp}} + \Gamma^{\text{imp}} \circ (\Pi_r - \Pi_r^{\text{imp}}) \circ \Gamma, \quad (4.5)$$

which can be evaluated without resorting to irreducible vertices. In the next step, the SDE, Eq. (2.39), is evaluated, which yields a momentum-dependent self-energy. Iterating this scheme until convergence results in self-consistently computed nonlocal contributions to Σ and Γ . However, since one specific two-particle channel r has to be picked in Eq.(4.5), ladder D Γ A does not correspond to a channel unbiased approach like the parquet equations or the fRG.⁴

The most natural way of improving upon the restrictions of ladder D Γ A is the full *parquet* D Γ A [TKH07; HKT08; Kus06; Hel22], which uses the full set of parquet equations, i.e., the BSEs in all three channels and the SDE. The only input required for those, see Sec. 2.3.1, is the fully 2PI vertex R . Consequently, parquet D Γ A approximates R to be local and taken as input from DMFT, $R \equiv R^{\text{imp}}$. Apart from that, all other quantities involved are fully momentum dependent. While being channel unbiased and self-consistent on the two-particle level, this scheme poses several severe challenges: First, one needs explicit access to R^{imp} , which is, at present, not possible with multipoint NRG in the Keldysh formalism (see also Ref. [P4]). In the Matsubara formalism, the (local) BSEs can be inverted to yield R^{imp} . However, irreducible vertex divergences may be present again, manifest in R^{imp} . Second, at large interactions, R^{imp} can be sizeable, which may make it hard to find a converged solution of the parquet equations, like we have seen in Ref. [P1]. Third, parametrizing the vertices requires vast numerical resources since all four-point

³ Numerous further proposals have been made involving dual fermions [RKL08], dual bosons [RKL12], or the TRILEX approach [AP15], which all come with different limitations that go beyond the scope of this text. For a review, see Ref. [Roh+18].

⁴ In particular, the full vertex only acquires a single momentum dependence through Eq. (4.5), not all three.

objects involved (except R^{imp}) depend on both three frequencies and three momenta independently. Additionally, evaluating the parquet equations becomes resource-intensive since this has to be done independently for all combinations of external arguments.

Regarding the last issues, major improvements are to be expected when employing the newly developed *quantics tensor cross interpolation* technique (QTCI), introduced below in Sec. 4.2, which can be used to find an efficient, compressed representation of high-dimensional functions. Indeed, the parquet equations can be evaluated using only functions in the QTCI representation, as demonstrated recently in the Matsubara formalism [Roh+24]. Regarding the first two issues of parquet DfA, a conceptually elegant alternative is the proposal to use the fRG in combination with DMFT, called *DMF²RG* [Tar+14; Wen+15; VTM19; Bon+22] to continuously interpolate between the DMFT impurity problem and the lattice theory using a regulator Λ . This regulator is introduced into the bare nonlocal propagator,

$$G_0^\Lambda(\nu, \mathbf{k}) = \frac{1}{\nu - (1 - \Lambda)\varepsilon_{\mathbf{k}} - \Lambda[\Delta(\nu) + \epsilon_d]}, \quad (4.6)$$

where Λ flows from 1 to 0 in the spirit of Eqs. (2.44). Since the fRG flow equations only require the full vertex but no irreducible vertices on the RHS, see Eqs. (2.45), the full vertex of the impurity model Γ^{imp} can be used as a starting point and irreducible vertex divergences are no issue. However, a one-loop truncation would pose a severe limitation, as exemplified in Ref. [P1] for local fRG, restricting the accuracy of DMF²RG. Augmenting the one-loop fRG flow by the iterative multiloop flow equations, see Sec. 2.3.4, should, in principle, yield a self-consistent and controlled result, reproducing the parquet DfA. However, the previously mentioned issues of multiloop fRG apply again: Starting at third loop order, self-consistency between the flow equations for Σ and Γ is required, complicating a numerical solution. Furthermore, in the Keldysh formalism, contributions at higher loop orders may become increasingly sharply peaked [Ge25] and hence difficult to resolve. Additionally, as in parquet DfA, the four-point objects have to be parametrized with three frequencies and three momenta, which is numerically overwhelming using naive schemes. For this reason, in the final part of this thesis, we summarize the main ideas behind the QTCI method, which is expected to help overcome this challenge.

4.2 Quantics tensor cross interpolation

The *quantics tensor cross interpolation* (QTCI) technique [Rit+24] combines two ideas to find compressed representations of high-dimensional functions: The *quantics representation* of multivariate functions and the *tensor cross interpolation* (TCI) method. The quantics representation was developed in Refs. [Ose09; Kho11; Kho18] but was only recently applied in the context of a quantum field theory description of the many-electron problem [Shi+23]. Its main idea is a binary representation of each variable of the studied functions. For simplicity, considering a one-dimensional function $f(x)$, which depends on the continuous variable (rescaled to the unit interval) $x \in [0, 1)$, it is discretized on a regular grid of $2^\mathcal{L}$ points,

$$x = \frac{\sigma_1}{2^1} + \frac{\sigma_2}{2^2} + \dots + \frac{\sigma_\mathcal{L}}{2^\mathcal{L}}, \quad (4.7)$$

where the discrete variables $\sigma_i \in \{0, 1\}$ are called ‘‘quantics bits’’. Accordingly, the function f is henceforth represented using these discrete bits, $f = f(\sigma_1, \sigma_2, \dots, \sigma_\mathcal{L})$, cor-

responding to a $2^{\mathcal{L}}$ tensor. Each bit encodes the structure of the function f at a different length scale: σ_1 resolves the coarsest structure, and $\sigma_{\mathcal{L}}$ resolves the finest structure. The number \mathcal{L} of bits has to be chosen by hand, depending on the demands of the problem. Crucially, adding a single further bit effectively doubles the resolution. At this point, however, it also doubles the number of tensor components.

The quantics representation can be generalized straightforwardly to functions with multiple variables, simply by using an independent binary representation for each. To preserve the property of the first bits encoding the large-scale information and the later bits encoding the small-scale structure, the bits should be grouped accordingly. There are different strategies for doing this, the details of which go beyond the scope of this text [YL22; Rit+24; Núñ+25].

A function represented through quantics bits can be formally “unfolded” as a *tensor train* (TT) or *matrix product state* (MPS),

$$f(\sigma_1, \sigma_2, \dots, \sigma_{\mathcal{L}}) = [M_1]_{1\alpha_1}^{\sigma_1} [M_2]_{\alpha_1\alpha_2}^{\sigma_2} \cdots [M_{\mathcal{L}}]_{\alpha_{\mathcal{L}-1}1}^{\sigma_{\mathcal{L}}}, \quad (4.8)$$

where summation over the repeated virtual indices α_i is implied. In the “worst case scenario”, when f has full rank, the dimension of the virtual indices, also called *bond dimension*, increases exponentially towards the middle of the TT. This scaling implies that the memory required to store the TT increases exponentially with \mathcal{L} . However, if f does not have full rank, an approximate representation using a TT with a lower bond dimension may still be accurate. Therein lies the power of this factorized representation: A restriction of the maximal bond dimension χ can potentially lead to exponential savings in the resources required for storing the TT. Obtaining a TT representation of a tensor in the form of Eq. (4.8) requires a factorization algorithm. Traditionally, a singular value decomposition (SVD) would be employed since it would yield the TT representation with the smallest possible χ for a given accuracy. However, performing an SVD requires the full tensor f to be stored in memory, which quickly becomes overwhelming.

At this point, the *tensor cross interpolation* (TCI) algorithm comes in [OT10; Ose11]. The TCI is a factorization method designed to construct a low-rank representation of a given tensor without requiring the full tensor to be stored in memory. Instead, it deterministically samples a subset of the tensor’s elements, adaptively increasing the TT’s maximal bond dimension χ until the desired accuracy is achieved. In the field of many-body physics, the TCI was first used to compute high-dimensional integrals as occurring when evaluating high-order diagrams in quantum Monte Carlo calculations, which requires efficiently sampling the highly complex integrands depending on many variables [Núñ+22; Erp+23]. Especially since its application to functions represented in the quantics representation [Rit+24] yielding *quantics tensor trains* (QTTs), the TCI has been applied to numerous problems in the recent past [Roh+24; TSS25] and optimized implementations of the TCI algorithm have been developed [Núñ+25]. Crucially, elementary operations such as additions, integrations, etc., can be performed on QTTs directly. Hence, there is no need to ever deal with the full tensors; their QTT representations suffice. Instead of the grid size, χ is now the crucial parameter in these algorithms, since they typically scale with $\sim \chi^3$ (Fourier transform) or $\sim \chi^4$ (convolution, element-wise multiplication, ...), but only linearly in \mathcal{L} [Núñ+25]. Hence, these algorithms permit an exponentially fine resolution at linear cost, provided χ is bounded, i.e., when the QTT

has low rank.

That happens for functions represented as QTTs when the functions show independent structures at different length scales. It turns out that this is the case for many functions appearing in physics and beyond since most functions have some structure that can be found and encoded with the TCI algorithm and are typically not dominated by random noise, which would be incompressible. However, systematically predicting whether the QTT representation of a given function has low rank is an active field of research [Lin24]. So far, QTCI-compressible functions have been found simply by trial and error. Crucially, it seems that the electron correlation functions discussed in this thesis are compressible by QTCI [TSS25; MSW24; Śro+24]. In particular, it was recently demonstrated in Ref. [Roh+24] that the parquet equations for the Hubbard atom and the SIAM can be solved entirely in the QTT language in the Matsubara formalism. In addition to representing the Matsubara self-energy and vertices as QTTs, this required advanced methods using matrix product operators to perform operations on QTTs and affine transformations for switching frequency parametrizations. Extending these calculations to real frequencies and including momentum dependencies is a formidable open problem. A systematic study of the QTCI compressibility of the local Keldysh vertex of the SIAM, discussed at length in this thesis, is currently being done and will be published soon [Fra+25].

In conclusion, we have shown in this thesis that computing the full three-dimensional real-frequency dependence of four-point correlation functions with quantum field theory methods is feasible. We demonstrated this by solving the parquet and fRG flow equations in the PA for the SIAM within the Keldysh formalism. Extending these methods to correlated lattice systems will require combining them with the non-perturbative DMFT, for which mpNRG can serve as an impurity solver. We confirmed the compatibility of mpNRG with quantum field theory methods through explicit checks of the parquet equations and the U(1) Ward identity using mpNRG output. When further complemented by the QTCI framework, these developments set the stage for computing real-frequency and momentum-resolved response functions of strongly correlated systems.

Bibliography

- [P1] A. Ge, N. Ritz, E. Walter, S. Aguirre, J. von Delft, and F. B. Kugler. “Real-frequency quantum field theory applied to the single-impurity Anderson model.” In: *Physical Review B* 109.11 (2024). DOI: [10.1103/PhysRevB.109.115128](https://doi.org/10.1103/PhysRevB.109.115128) (cit. on pp. [v](#), [9](#), [19](#), [22](#), [23](#), [27](#), [28](#), [55](#), [56](#), [79](#), [117](#), [118](#), [120](#), [122](#), [153](#), [154](#)).
- [P2] N. Ritz, A. Ge, E. Walter, S. Aguirre, J. von Delft, and F. B. Kugler. “KeldyshQFT: A C++ codebase for real-frequency multiloop functional renormalization group and parquet computations of the single-impurity Anderson model.” In: *The Journal of Chemical Physics* 161.5 (2024). DOI: [10.1063/5.0221340](https://doi.org/10.1063/5.0221340) (cit. on pp. [v](#), [23](#), [28](#), [29](#), [56](#), [79](#), [118](#)).
- [P3] D. Kiese, A. Ge, N. Ritz, J. von Delft, and N. Wentzell. “Matsubara-Functions.jl: An equilibrium Green’s function library in the Julia programming language.” In: *SciPost Physics Codebases* (2024). DOI: [10.21468/SciPostPhysCodeb.24](https://doi.org/10.21468/SciPostPhysCodeb.24) (cit. on pp. [v](#), [79](#), [80](#)).
- [P4] N. Ritz, A. Ge, M. Frankenbach, M. Pelz, J. von Delft, and F. B. Kugler. *Testing the parquet equations and the U(1) Ward identity for real-frequency correlation functions from the multipoint numerical renormalization group*. 2025. DOI: [10.48550/arXiv.2504.05910](https://doi.org/10.48550/arXiv.2504.05910) (cit. on pp. [v](#), [19](#), [23](#), [25](#), [118](#), [123](#), [124](#), [151](#), [153](#)).
- [Abb+99] P. Abbamonte, C. A. Burns, E. D. Isaacs, P. M. Platzman, L. L. Miller, S. W. Cheong, and M. V. Klein. “Resonant Inelastic X-Ray Scattering from Valence Excitations in Insulating Copper Oxides.” In: *Physical Review Letters* 83.4 (1999). DOI: [10.1103/PhysRevLett.83.860](https://doi.org/10.1103/PhysRevLett.83.860) (cit. on p. [5](#)).
- [Abr65] A. A. Abrikosov. “Electron scattering on magnetic impurities in metals and anomalous resistivity effects.” In: *Physics Physique Fizika* 2.1 (1965). DOI: [10.1103/PhysicsPhysiqueFizika.2.5](https://doi.org/10.1103/PhysicsPhysiqueFizika.2.5) (cit. on p. [21](#)).
- [AFL83] N. Andrei, K. Furuya, and J. H. Lowenstein. “Solution of the Kondo problem.” In: *Reviews of Modern Physics* 55.2 (1983). DOI: [10.1103/RevModPhys.55.331](https://doi.org/10.1103/RevModPhys.55.331) (cit. on p. [121](#)).
- [Agu20] S. Aguirre. “Multiloop functional renormalization group in the Keldysh formalism—A study of the single-impurity Anderson model.” Master’s Thesis. LMU München, 2020 (cit. on p. [55](#)).
- [Ame+11] L. J. P. Ament, M. van Veenendaal, T. P. Devereaux, J. P. Hill, and J. van den Brink. “Resonant inelastic x-ray scattering studies of elementary excitations.” In: *Reviews of Modern Physics* 83.2 (2011). DOI: [10.1103/RevModPhys.83.705](https://doi.org/10.1103/RevModPhys.83.705) (cit. on p. [5](#)).
- [And00] P. W. Anderson. “Brainwashed by Feynman?” In: *Physics Today* 53.2 (2000). DOI: [10.1063/1.882955](https://doi.org/10.1063/1.882955) (cit. on pp. [15](#), [119](#)).
- [And61] P. W. Anderson. “Localized Magnetic States in Metals.” In: *Physical Review* 124.1 (1961). DOI: [10.1103/PhysRev.124.41](https://doi.org/10.1103/PhysRev.124.41) (cit. on p. [118](#)).

- [AP15] T. Ayral and O. Parcollet. “Mott physics and spin fluctuations: A unified framework.” In: *Physical Review B* 92.11 (2015). DOI: [10.1103/PhysRevB.92.115109](https://doi.org/10.1103/PhysRevB.92.115109) (cit. on p. 153).
- [AS05] F. B. Anders and A. Schiller. “Real-Time Dynamics in Quantum-Impurity Systems: A Time-Dependent Numerical Renormalization-Group Approach.” In: *Physical Review Letters* 95.19 (2005). DOI: [10.1103/PhysRevLett.95.196801](https://doi.org/10.1103/PhysRevLett.95.196801) (cit. on p. 122).
- [AS23] A. Altland and B. Simons. *Condensed Matter Field Theory*. 3rd ed. Cambridge University Press, 2023. DOI: [10.1017/9781108781244](https://doi.org/10.1017/9781108781244) (cit. on pp. 1, 7).
- [Bay62] G. Baym. “Self-Consistent Approximations in Many-Body Systems.” In: *Physical Review* 127.4 (1962). DOI: [10.1103/PhysRev.127.1391](https://doi.org/10.1103/PhysRev.127.1391) (cit. on p. 124).
- [Ber+17] A. K. Bera, B. Lake, F. H. L. Essler, L. Vanderstraeten, C. Hubig, U. Schollwöck, A. T. M. N. Islam, A. Schneidewind, and D. L. Quintero-Castro. “Spinon confinement in a quasi-one-dimensional anisotropic Heisenberg magnet.” In: *Physical Review B* 96.5 (2017). DOI: [10.1103/PhysRevB.96.054423](https://doi.org/10.1103/PhysRevB.96.054423) (cit. on p. 4).
- [Bet31] H. Bethe. “Zur Theorie der Metalle.” In: *Zeitschrift für Physik* 71.3 (1931). DOI: [10.1007/BF01341708](https://doi.org/10.1007/BF01341708) (cit. on p. 121).
- [BF28] M. Born and V. Fock. “Beweis des Adiabatenatzes.” In: *Zeitschrift für Physik* 51.3 (1928). DOI: [10.1007/BF01343193](https://doi.org/10.1007/BF01343193) (cit. on p. 14).
- [BG96] G. A. Baker and P. Graves-Morris. *Padé Approximants*. 2nd ed. Encyclopedia of Mathematics and its Applications. Cambridge University Press, 1996. DOI: [10.1017/CB09780511530074](https://doi.org/10.1017/CB09780511530074) (cit. on p. 9).
- [BHP98] R. Bulla, A. C. Hewson, and T. Pruschke. “Numerical renormalization group calculations for the self-energy of the impurity Anderson model.” In: *Journal of Physics: Condensed Matter* 10.37 (1998). DOI: [10.1088/0953-8984/10/37/021](https://doi.org/10.1088/0953-8984/10/37/021) (cit. on p. 121).
- [Bic04] N. E. Bickers. “Self-Consistent Many-Body Theory for Condensed Matter Systems.” In: *Theoretical Methods for Strongly Correlated Electrons*. Ed. by D. Sénéchal, A.-M. Tremblay, and C. Bourbonnais. New York: Springer, 2004. DOI: [10.1007/0-387-21717-7_6](https://doi.org/10.1007/0-387-21717-7_6) (cit. on p. 21).
- [Blo32] F. Bloch. “Zur Theorie des Austauschproblems und der Remanenzerscheinung der Ferromagnetika.” In: *Zeitschrift für Physik* 74.5 (1932). DOI: [10.1007/BF01337791](https://doi.org/10.1007/BF01337791) (cit. on p. 7).
- [BM61] G. Baym and N. D. Mermin. “Determination of Thermodynamic Green’s Functions.” In: *Journal of Mathematical Physics* 2.2 (1961). DOI: [10.1063/1.1703704](https://doi.org/10.1063/1.1703704) (cit. on pp. 9, 11).
- [Bon+22] P. M. Bonetti, A. Toschi, C. Hille, S. Andergassen, and D. Vilaridi. “Single-boson exchange representation of the functional renormalization group for strongly interacting many-electron systems.” In: *Physical Review Research* 4.1 (2022). DOI: [10.1103/PhysRevResearch.4.013034](https://doi.org/10.1103/PhysRevResearch.4.013034) (cit. on pp. 80, 117, 154).

- [BSW89] N. E. Bickers, D. J. Scalapino, and S. R. White. “Conserving Approximations for Strongly Correlated Electron Systems: Bethe-Salpeter Equation and Dynamics for the Two-Dimensional Hubbard Model.” In: *Physical Review Letters* 62.8 (1989). DOI: [10.1103/PhysRevLett.62.961](https://doi.org/10.1103/PhysRevLett.62.961) (cit. on p. 21).
- [BW91] N. E. Bickers and S. R. White. “Conserving approximations for strongly fluctuating electron systems. II. Numerical results and parquet extension.” In: *Physical Review B* 43.10 (1991). DOI: [10.1103/PhysRevB.43.8044](https://doi.org/10.1103/PhysRevB.43.8044) (cit. on p. 21).
- [Cha+18] P. Chalupa, P. Gunacker, T. Schäfer, K. Held, and A. Toschi. “Divergences of the irreducible vertex functions in correlated metallic systems: Insights from the Anderson impurity model.” In: *Physical Review B* 97.24 (2018). DOI: [10.1103/PhysRevB.97.245136](https://doi.org/10.1103/PhysRevB.97.245136) (cit. on p. 119).
- [Cha+21] P. Chalupa, T. Schäfer, M. Reitner, D. Springer, S. Andergassen, and A. Toschi. “Fingerprints of the Local Moment Formation and its Kondo Screening in the Generalized Susceptibilities of Many-Electron Problems.” In: *Physical Review Letters* 126.5 (2021). DOI: [10.1103/PhysRevLett.126.056403](https://doi.org/10.1103/PhysRevLett.126.056403) (cit. on p. 119).
- [Cha+22] P. Chalupa-Gantner, F. B. Kugler, C. Hille, J. von Delft, S. Andergassen, and A. Toschi. “Fulfillment of sum rules and Ward identities in the multiloop functional renormalization group solution of the Anderson impurity model.” In: *Physical Review Research* 4.2 (2022). DOI: [10.1103/PhysRevResearch.4.023050](https://doi.org/10.1103/PhysRevResearch.4.023050) (cit. on pp. 28, 124).
- [Col15] P. Coleman. *Introduction to Many-Body Physics*. Cambridge University Press, 2015. DOI: [10.1017/CB09781139020916](https://doi.org/10.1017/CB09781139020916) (cit. on pp. 1, 2, 7).
- [Del22] J. von Delft. “The Physics of Quantum Impurity Models.” In: *Dynamical mean-field theory of correlated electrons*. Ed. by E. Pavarini, E. Koch, A. I. Lichtenstein, and D. Vollhardt. Schriften des Forschungszentrums Jülich, Reihe Modeling and Simulation Volume 12. Forschungszentrum Jülich, 2022 (cit. on p. 118).
- [Den+19] X. Deng, K. M. Stadler, K. Haule, A. Weichselbaum, J. von Delft, and G. Kotliar. “Signatures of Mottness and Hundness in archetypal correlated metals.” In: *Nature Communications* 10.1 (2019). DOI: [10.1038/s41467-019-10257-2](https://doi.org/10.1038/s41467-019-10257-2) (cit. on p. 121).
- [DHS03] A. Damascelli, Z. Hussain, and Z.-X. Shen. “Angle-resolved photoemission studies of the cuprate superconductors.” In: *Reviews of Modern Physics* 75.2 (2003). DOI: [10.1103/RevModPhys.75.473](https://doi.org/10.1103/RevModPhys.75.473) (cit. on p. 6).
- [DM64a] C. De Dominicis and P. C. Martin. “Stationary Entropy Principle and Renormalization in Normal and Superfluid Systems. I. Algebraic Formulation.” In: *Journal of Mathematical Physics* 5.1 (1964). DOI: [10.1063/1.1704062](https://doi.org/10.1063/1.1704062) (cit. on p. 21).
- [DM64b] C. De Dominicis and P. C. Martin. “Stationary Entropy Principle and Renormalization in Normal and Superfluid Systems. II. Diagrammatic Formulation.” In: *Journal of Mathematical Physics* 5.1 (1964). DOI: [10.1063/1.1704064](https://doi.org/10.1063/1.1704064) (cit. on p. 21).
- [DST57] I. T. Diatlov, V. V. Sudakov, and K. A. Ter-Martirosian. “Asymptotic Meson-Meson Scattering Theory.” In: *Soviet Phys. JETP* Vol: 5 (1957) (cit. on p. 21).

- [Dup+21] N. Dupuis, L. Canet, A. Eichhorn, W. Metzner, J. M. Pawłowski, M. Tissier, and N. Wschebor. “The nonperturbative functional renormalization group and its applications.” In: *Physics Reports*. The nonperturbative functional renormalization group and its applications 910 (2021). DOI: [10.1016/j.physrep.2021.01.001](https://doi.org/10.1016/j.physrep.2021.01.001) (cit. on p. 25).
- [Dys49] F. J. Dyson. “The S Matrix in Quantum Electrodynamics.” In: *Physical Review* 75.11 (1949). DOI: [10.1103/PhysRev.75.1736](https://doi.org/10.1103/PhysRev.75.1736) (cit. on pp. 17, 23).
- [Eck+23] C. J. Eckhardt, P. Kappl, A. Kauch, and K. Held. “A functional-analysis derivation of the parquet equation.” In: *SciPost Physics* 15.5 (2023). DOI: [10.21468/SciPostPhys.15.5.203](https://doi.org/10.21468/SciPostPhys.15.5.203) (cit. on p. 23).
- [Erp+23] A. Erpenbeck et al. “Tensor train continuous time solver for quantum impurity models.” In: *Physical Review B* 107.24 (2023). DOI: [10.1103/PhysRevB.107.245135](https://doi.org/10.1103/PhysRevB.107.245135) (cit. on p. 155).
- [Eßl+24] H. Eßl, M. Reitner, G. Sangiovanni, and A. Toschi. “General Shiba mapping for on-site four-point correlation functions.” In: *Physical Review Research* 6.3 (2024). DOI: [10.1103/PhysRevResearch.6.033061](https://doi.org/10.1103/PhysRevResearch.6.033061) (cit. on p. 119).
- [Fil+18] M. Filippone, C. P. Moca, A. Weichselbaum, J. von Delft, and C. Mora. “At which magnetic field, exactly, does the Kondo resonance begin to split? A Fermi liquid description of the low-energy properties of the Anderson model.” In: *Physical Review B* 98.7 (2018). DOI: [10.1103/PhysRevB.98.075404](https://doi.org/10.1103/PhysRevB.98.075404) (cit. on p. 121).
- [FMS09] A. Furrer, J. Mesot, and T. Strässle. *Neutron Scattering in Condensed Matter Physics*. World Scientific, 2009. DOI: [10.1142/4870](https://doi.org/10.1142/4870) (cit. on p. 4).
- [For18] D. Forster. *Hydrodynamic Fluctuations, Broken Symmetry, And Correlation Functions*. Boca Raton: CRC Press, 2018. 352 pp. DOI: [10.1201/9780429493683](https://doi.org/10.1201/9780429493683) (cit. on p. 2).
- [Fou+20] R. Fournier, L. Wang, O. V. Yazyev, and Q. Wu. “Artificial Neural Network Approach to the Analytic Continuation Problem.” In: *Physical Review Letters* 124.5 (2020). DOI: [10.1103/PhysRevLett.124.056401](https://doi.org/10.1103/PhysRevLett.124.056401) (cit. on p. 9).
- [Fra+22] K. Fraboulet, S. Heinzlmann, P. M. Bonetti, A. Al-Eryani, D. Vilardi, A. Toschi, and S. Andergassen. “Single-boson exchange functional renormalization group application to the two-dimensional Hubbard model at weak coupling.” In: *The European Physical Journal B* 95.12 (2022). DOI: [10.1140/epjb/s10051-022-00438-2](https://doi.org/10.1140/epjb/s10051-022-00438-2) (cit. on pp. 28, 80).
- [Fra+25] M. Frankenbach, A. Ge, M. Ritter, N. Ritz, and J. von Delft. “Compressing local vertex functions from MuNRG using tensor cross interpolation.” In: *to be published* (2025) (cit. on p. 156).
- [FYG21] J. Fei, C.-N. Yeh, and E. Gull. “Nevanlinna Analytical Continuation.” In: *Physical Review Letters* 126.5 (2021). DOI: [10.1103/PhysRevLett.126.056402](https://doi.org/10.1103/PhysRevLett.126.056402) (cit. on p. 9).
- [Ge+24] A. Ge, J. Halbinger, S.-S. B. Lee, J. von Delft, and F. B. Kugler. “Analytic Continuation of Multipoint Correlation Functions.” In: *Annalen der Physik* 536.7 (2024). DOI: [10.1002/andp.202300504](https://doi.org/10.1002/andp.202300504) (cit. on pp. 9, 19, 122).
- [Ge25] A. Ge. “Correlator-based approaches in real and imaginary frequencies.” PhD thesis. Ludwig-Maximilians-Universität München, 2025 (cit. on pp. 21, 28, 154).

- [Geo+96] A. Georges, G. Kotliar, W. Krauth, and M. J. Rozenberg. “Dynamical mean-field theory of strongly correlated fermion systems and the limit of infinite dimensions.” In: *Reviews of Modern Physics* 68.1 (1996). DOI: [10.1103/RevModPhys.68.13](https://doi.org/10.1103/RevModPhys.68.13) (cit. on pp. [121](#), [151](#), [152](#)).
- [Gie+22] M. Gievers, E. Walter, A. Ge, J. v. Delft, and F. B. Kugler. “Multiloop flow equations for single-boson exchange fRG.” In: *The European Physical Journal B* 95.7 (2022). DOI: [10.1140/epjb/s10051-022-00353-6](https://doi.org/10.1140/epjb/s10051-022-00353-6) (cit. on pp. [25](#), [80](#)).
- [Gie+25] M. Gievers, R. Schmidt, J. von Delft, and F. B. Kugler. “Subleading logarithmic behavior in the parquet formalism.” In: *Physical Review B* 111.8 (2025). DOI: [10.1103/PhysRevB.111.085151](https://doi.org/10.1103/PhysRevB.111.085151) (cit. on p. [80](#)).
- [GK92] A. Georges and G. Kotliar. “Hubbard model in infinite dimensions.” In: *Physical Review B* 45.12 (1992). DOI: [10.1103/PhysRevB.45.6479](https://doi.org/10.1103/PhysRevB.45.6479) (cit. on pp. [121](#), [151](#)).
- [Gun+16] O. Gunnarsson, T. Schäfer, J. P. F. LeBlanc, J. Merino, G. Sangiovanni, G. Rohringer, and A. Toschi. “Parquet decomposition calculations of the electronic self-energy.” In: *Physical Review B* 93.24 (2016). DOI: [10.1103/PhysRevB.93.245102](https://doi.org/10.1103/PhysRevB.93.245102) (cit. on p. [119](#)).
- [Haf+14] H. Hafermann, E. G. C. P. van Loon, M. I. Katsnelson, A. I. Lichtenstein, and O. Parcollet. “Collective charge excitations of strongly correlated electrons, vertex corrections, and gauge invariance.” In: *Physical Review B* 90.23 (2014). DOI: [10.1103/PhysRevB.90.235105](https://doi.org/10.1103/PhysRevB.90.235105) (cit. on p. [124](#)).
- [Hal24] J. J. Halbinger. “Imaginary- and real-frequency correlation functions in condensed matter physics.” PhD thesis. Ludwig-Maximilians-Universität München, 2024 (cit. on p. [122](#)).
- [Hal78a] F. D. M. Haldane. “Scaling Theory of the Asymmetric Anderson Model.” In: *Physical Review Letters* 40.6 (1978). DOI: [10.1103/PhysRevLett.40.416](https://doi.org/10.1103/PhysRevLett.40.416) (cit. on p. [121](#)).
- [Hal78b] F. D. M. Haldane. “Theory of the atomic limit of the Anderson model. I. Perturbation expansions re-examined.” In: *Journal of Physics C: Solid State Physics* 11.24 (1978). DOI: [10.1088/0022-3719/11/24/030](https://doi.org/10.1088/0022-3719/11/24/030) (cit. on p. [121](#)).
- [HBB34] W. J. de Haas, J. de Boer, and G. J. van den Berg. “The electrical resistance of gold, copper and lead at low temperatures.” In: *Physica* 1.7 (1934). DOI: [10.1016/S0031-8914\(34\)80310-2](https://doi.org/10.1016/S0031-8914(34)80310-2) (cit. on p. [118](#)).
- [Hed65] L. Hedin. “New method for calculating the one-particle Green’s function with application to the electron-gas problem.” In: *Physical Review* 139.3 (1965) (cit. on p. [80](#)).
- [Hel22] K. Held. “Beyond DMFT: Spin Fluctuations, Pseudogaps and Superconductivity.” In: *Dynamical mean-field theory of correlated electrons*. Ed. by E. Pavarini, E. Koch, A. I. Lichtenstein, D. Vollhardt, and Forschungszentrum Jülich. Schriften des Forschungszentrums Jülich Volume 12. Jülich: Forschungszentrum Jülich, 2022 (cit. on p. [153](#)).
- [Het+98] M. H. Hettler, A. N. Tahvildar-Zadeh, M. Jarrell, T. Pruschke, and H. R. Krishnamurthy. “Nonlocal dynamical correlations of strongly interacting electron systems.” In: *Physical Review B* 58.12 (1998). DOI: [10.1103/PhysRevB.58.R7475](https://doi.org/10.1103/PhysRevB.58.R7475) (cit. on p. [152](#)).

- [Hew93] A. C. Hewson. *The Kondo Problem to Heavy Fermions*. Cambridge Studies in Magnetism. Cambridge University Press, 1993. DOI: [10.1017/CB09780511470752](https://doi.org/10.1017/CB09780511470752) (cit. on p. 118).
- [Hey+17] J. Heyder, F. Bauer, D. Schimmel, and J. von Delft. “Derivation of Oguri’s linear conductance formula for interacting fermions within the Keldysh formalism.” In: *Physical Review B* 96.12 (2017). DOI: [10.1103/PhysRevB.96.125141](https://doi.org/10.1103/PhysRevB.96.125141) (cit. on p. 124).
- [HGL23] Z. Huang, E. Gull, and L. Lin. “Robust analytic continuation of Green’s functions via projection, pole estimation, and semidefinite relaxation.” In: *Physical Review B* 107.7 (2023). DOI: [10.1103/PhysRevB.107.075151](https://doi.org/10.1103/PhysRevB.107.075151) (cit. on p. 9).
- [HKT08] K. Held, A. A. Katanin, and A. Toschi. “Dynamical Vertex Approximation: An Introduction.” In: *Progress of Theoretical Physics Supplement* 176 (2008). DOI: [10.1143/PTPS.176.117](https://doi.org/10.1143/PTPS.176.117) (cit. on p. 153).
- [Hug57] N. M. Hugenholtz. “Perturbation theory of large quantum systems.” In: *Physica* 23.1 (1957). DOI: [10.1016/S0031-8914\(57\)92950-6](https://doi.org/10.1016/S0031-8914(57)92950-6) (cit. on p. 16).
- [Jak10] S. G. Jakobs. “Functional renormalization group studies of quantum transport through mesoscopic systems.” PhD thesis. RWTH Aachen, 2010. 205 pp. (cit. on pp. 15, 16, 21).
- [Jar92] M. Jarrell. “Hubbard model in infinite dimensions: A quantum Monte Carlo study.” In: *Physical Review Letters* 69.1 (1992). DOI: [10.1103/PhysRevLett.69.168](https://doi.org/10.1103/PhysRevLett.69.168) (cit. on pp. 121, 151).
- [JG96] M. Jarrell and J. E. Gubernatis. “Bayesian inference and the analytic continuation of imaginary-time quantum Monte Carlo data.” In: *Physics Reports* 269.3 (1996). DOI: [10.1016/0370-1573\(95\)00074-7](https://doi.org/10.1016/0370-1573(95)00074-7) (cit. on p. 9).
- [JKP17] V. Janiš, A. Kauch, and V. Pokorný. “Thermodynamically consistent description of criticality in models of correlated electrons.” In: *Physical Review B* 95.4 (2017). DOI: [10.1103/PhysRevB.95.045108](https://doi.org/10.1103/PhysRevB.95.045108) (cit. on p. 124).
- [JPS10] S. G. Jakobs, M. Pletyukhov, and H. Schoeller. “Properties of multi-particle Green’s and vertex functions within Keldysh formalism.” In: *Journal of Physics A: Mathematical and Theoretical* 43.10 (2010). DOI: [10.1088/1751-8113/43/10/103001](https://doi.org/10.1088/1751-8113/43/10/103001) (cit. on pp. 19, 21).
- [Kad18] L. P. Kadanoff. *Quantum Statistical Mechanics*. Boca Raton: CRC Press, 2018. 224 pp. DOI: [10.1201/9780429493218](https://doi.org/10.1201/9780429493218) (cit. on p. 11).
- [Käl52] G. Källén. “On the Definition of the Renormalization Constants in Quantum Electrodynamics.” In: *Helvetica Physica Acta* 25 (IV 1952). DOI: [10.5169/seals-112316](https://doi.org/10.5169/seals-112316) (cit. on p. 7).
- [Kat04] A. A. Katanin. “Fulfillment of Ward identities in the functional renormalization group approach.” In: *Physical Review B* 70.11 (2004). DOI: [10.1103/PhysRevB.70.115109](https://doi.org/10.1103/PhysRevB.70.115109) (cit. on pp. 27, 124).
- [Kat09] A. A. Katanin. “Two-loop functional renormalization group approach to the one- and two-dimensional Hubbard model.” In: *Physical Review B* 79.23 (2009). DOI: [10.1103/PhysRevB.79.235119](https://doi.org/10.1103/PhysRevB.79.235119) (cit. on p. 26).
- [KBS10] P. Kopietz, L. Bartosch, and F. Schütz. *Introduction to the Functional Renormalization Group*. Lecture Notes in Physics. Springer, 2010. DOI: [10.1007/978-3-642-05094-7](https://doi.org/10.1007/978-3-642-05094-7) (cit. on pp. 17, 25).

- [KD18a] F. B. Kugler and J. v. Delft. “Derivation of exact flow equations from the self-consistent parquet relations.” In: *New Journal of Physics* 20.12 (2018). DOI: [10.1088/1367-2630/aaf65f](https://doi.org/10.1088/1367-2630/aaf65f) (cit. on pp. 26–28, 124).
- [KD18b] F. B. Kugler and J. von Delft. “Multiloop functional renormalization group for general models.” In: *Physical Review B* 97.3 (2018). DOI: [10.1103/PhysRevB.97.035162](https://doi.org/10.1103/PhysRevB.97.035162) (cit. on pp. 26, 27).
- [KD18c] F. B. Kugler and J. von Delft. “Multiloop Functional Renormalization Group That Sums Up All Parquet Diagrams.” In: *Physical Review Letters* 120.5 (2018). DOI: [10.1103/PhysRevLett.120.057403](https://doi.org/10.1103/PhysRevLett.120.057403) (cit. on pp. 26, 27).
- [Kei+15] B. Keimer, S. A. Kivelson, M. R. Norman, S. Uchida, and J. Zaanen. “From quantum matter to high-temperature superconductivity in copper oxides.” In: *Nature* 518.7538 (2015). DOI: [10.1038/nature14165](https://doi.org/10.1038/nature14165) (cit. on p. 152).
- [Kel64] L. V. Keldysh. “Diagram technique for nonequilibrium processes.” In: *J. Exptl. Theoret. Phys. (U.S.S.R.)* 47 (1964). DOI: [10.1142/9789811279461_0007](https://doi.org/10.1142/9789811279461_0007) (cit. on pp. 11, 18).
- [Kho11] B. N. Khoromskij. “O(dlog N)-Quantics Approximation of N-d Tensors in High-Dimensional Numerical Modeling.” In: *Constructive Approximation* 34.2 (2011). DOI: [10.1007/s00365-011-9131-1](https://doi.org/10.1007/s00365-011-9131-1) (cit. on p. 154).
- [Kho18] B. N. Khoromskij. *Tensor Numerical Methods in Scientific Computing*. De Gruyter, 2018. DOI: [10.1515/9783110365917](https://doi.org/10.1515/9783110365917) (cit. on p. 154).
- [Khu90] A. Khurana. “Electrical conductivity in the infinite-dimensional Hubbard model.” In: *Physical Review Letters* 64.16 (1990). DOI: [10.1103/PhysRevLett.64.1990](https://doi.org/10.1103/PhysRevLett.64.1990) (cit. on p. 152).
- [Kie+22] D. Kiese, T. Müller, Y. Iqbal, R. Thomale, and S. Trebst. “Multiloop functional renormalization group approach to quantum spin systems.” In: *Physical Review Research* 4.2 (2022). DOI: [10.1103/PhysRevResearch.4.023185](https://doi.org/10.1103/PhysRevResearch.4.023185) (cit. on p. 28).
- [Kie+24] D. Kiese, N. Wentzell, I. Krivenko, O. Parcollet, K. Held, and F. Krien. *Embedded multi-boson exchange: A step beyond quantum cluster theories*. 2024. DOI: [10.48550/arXiv.2406.15629](https://doi.org/10.48550/arXiv.2406.15629) (cit. on p. 80).
- [KK22] F. B. Kugler and G. Kotliar. “Is the Orbital-Selective Mott Phase Stable against Interorbital Hopping?” In: *Physical Review Letters* 129.9 (2022). DOI: [10.1103/PhysRevLett.129.096403](https://doi.org/10.1103/PhysRevLett.129.096403) (cit. on p. 121).
- [KKH21] F. Krien, A. Kauch, and K. Held. “Tiling with triangles: parquet and $GW\gamma$ methods unified.” In: *Physical Review Research* 3.1 (2021). DOI: [10.1103/PhysRevResearch.3.013149](https://doi.org/10.1103/PhysRevResearch.3.013149) (cit. on p. 80).
- [KKK24] F. B. Kugler, C.-J. Kang, and G. Kotliar. “Low-energy perspective on two-orbital Hund metals and the case of LaNiO_2 .” In: *Physical Review B* 110.15 (2024). DOI: [10.1103/PhysRevB.110.155101](https://doi.org/10.1103/PhysRevB.110.155101) (cit. on p. 121).
- [KLD21] F. B. Kugler, S.-S. B. Lee, and J. von Delft. “Multipoint Correlation Functions: Spectral Representation and Numerical Evaluation.” In: *Physical Review X* 11.4 (2021). DOI: [10.1103/PhysRevX.11.041006](https://doi.org/10.1103/PhysRevX.11.041006) (cit. on p. 122).
- [KLR20] F. Krien, A. I. Lichtenstein, and G. Rohringer. “Fluctuation diagnostic of the nodal/antinodal dichotomy in the Hubbard model at weak coupling: A parquet dual fermion approach.” In: *Physical Review B* 102.23 (2020). DOI: [10.1103/PhysRevB.102.235133](https://doi.org/10.1103/PhysRevB.102.235133) (cit. on p. 80).

- [Kon64] J. Kondo. “Resistance Minimum in Dilute Magnetic Alloys.” In: *Progress of Theoretical Physics* 32.1 (1964). DOI: [10.1143/PTP.32.37](https://doi.org/10.1143/PTP.32.37) (cit. on pp. 118, 119).
- [Kop+10] P. Kopietz, L. Bartosch, L. Costa, A. Isidori, and A. Ferraz. “Ward identities for the Anderson impurity model: derivation via functional methods and the exact renormalization group.” In: *Journal of Physics A: Mathematical and Theoretical* 43.38 (2010). DOI: [10.1088/1751-8113/43/38/385004](https://doi.org/10.1088/1751-8113/43/38/385004) (cit. on p. 124).
- [Kot+01] G. Kotliar, S. Y. Savrasov, G. Pálsson, and G. Biroli. “Cellular Dynamical Mean Field Approach to Strongly Correlated Systems.” In: *Physical Review Letters* 87.18 (2001). DOI: [10.1103/PhysRevLett.87.186401](https://doi.org/10.1103/PhysRevLett.87.186401) (cit. on p. 152).
- [Kot+06] G. Kotliar, S. Y. Savrasov, K. Haule, V. S. Oudovenko, O. Parcollet, and C. A. Marianetti. “Electronic structure calculations with dynamical mean-field theory.” In: *Reviews of Modern Physics* 78.3 (2006). DOI: [10.1103/RevModPhys.78.865](https://doi.org/10.1103/RevModPhys.78.865) (cit. on p. 151).
- [Kri+17] F. Krien, E. G. C. P. van Loon, H. Hafermann, J. Otsuki, M. I. Katsnelson, and A. I. Lichtenstein. “Conservation in two-particle self-consistent extensions of dynamical mean-field theory.” In: *Physical Review B* 96.7 (2017). DOI: [10.1103/PhysRevB.96.075155](https://doi.org/10.1103/PhysRevB.96.075155) (cit. on p. 124).
- [Kri+20] F. Krien, A. Valli, P. Chalupa, M. Capone, A. I. Lichtenstein, and A. Toschi. “Boson-exchange parquet solver for dual fermions.” In: *Physical Review B* 102.19 (2020). DOI: [10.1103/PhysRevB.102.195131](https://doi.org/10.1103/PhysRevB.102.195131) (cit. on p. 80).
- [Kri18] F. Krien. “Conserving dynamical mean-field approaches to strongly correlated systems.” PhD thesis. Hamburg University, 2018 (cit. on p. 124).
- [Kri19] F. Krien. “Efficient evaluation of the polarization function in dynamical mean-field theory.” In: *Physical Review B* 99.23 (2019). DOI: [10.1103/PhysRevB.99.235106](https://doi.org/10.1103/PhysRevB.99.235106) (cit. on p. 79).
- [Kub57] R. Kubo. “Statistical-Mechanical Theory of Irreversible Processes. I. General Theory and Simple Applications to Magnetic and Conduction Problems.” In: *Journal of the Physical Society of Japan* 12.6 (1957). DOI: [10.1143/JPSJ.12.570](https://doi.org/10.1143/JPSJ.12.570) (cit. on pp. 2, 7, 19).
- [Kub66] R. Kubo. “The fluctuation-dissipation theorem.” In: *Reports on Progress in Physics* 29.1 (1966). DOI: [10.1088/0034-4885/29/1/306](https://doi.org/10.1088/0034-4885/29/1/306) (cit. on p. 2).
- [Kug+19] F. B. Kugler, S.-S. B. Lee, A. Weichselbaum, G. Kotliar, and J. von Delft. “Orbital differentiation in Hund metals.” In: *Physical Review B* 100.11 (2019). DOI: [10.1103/PhysRevB.100.115159](https://doi.org/10.1103/PhysRevB.100.115159) (cit. on p. 121).
- [Kug+20] F. B. Kugler, M. Zingl, H. U. R. Strand, S.-S. B. Lee, J. von Delft, and A. Georges. “Strongly Correlated Materials from a Numerical Renormalization Group Perspective: How the Fermi-Liquid State of Sr₂RuO₄ Emerges.” In: *Physical Review Letters* 124.1 (2020). DOI: [10.1103/PhysRevLett.124.016401](https://doi.org/10.1103/PhysRevLett.124.016401) (cit. on p. 121).
- [Kug19] F. Kugler. “Renormalization group approaches to strongly correlated electron systems.” PhD thesis. Ludwig-Maximilians-Universität München, 2019 (cit. on pp. 23, 26, 27, 153).

- [Kug22] F. B. Kugler. “Improved estimator for numerical renormalization group calculations of the self-energy.” In: *Physical Review B* 105.24 (2022). DOI: [10.1103/PhysRevB.105.245132](https://doi.org/10.1103/PhysRevB.105.245132) (cit. on pp. 122, 123).
- [Kus06] H. Kusunose. “Influence of Spatial Correlations in Strongly Correlated Electron Systems: Extension to Dynamical Mean Field Approximation.” In: *Journal of the Physical Society of Japan* 75.5 (2006). DOI: [10.1143/JPSJ.75.054713](https://doi.org/10.1143/JPSJ.75.054713) (cit. on p. 153).
- [KV19] F. Krien and A. Valli. “Parquetlike equations for the Hedin three-leg vertex.” In: *Physical Review B* 100.24 (2019). DOI: [10.1103/PhysRevB.100.245147](https://doi.org/10.1103/PhysRevB.100.245147) (cit. on p. 79).
- [KVC19] F. Krien, A. Valli, and M. Capone. “Single-boson exchange decomposition of the vertex function.” In: *Physical Review B* 100.15 (2019). DOI: [10.1103/PhysRevB.100.155149](https://doi.org/10.1103/PhysRevB.100.155149) (cit. on p. 79).
- [KWW80] H. R. Krishna-murthy, J. W. Wilkins, and K. G. Wilson. “Renormalization-group approach to the Anderson model of dilute magnetic alloys. I. Static properties for the symmetric case.” In: *Physical Review B* 21.3 (1980). DOI: [10.1103/PhysRevB.21.1003](https://doi.org/10.1103/PhysRevB.21.1003) (cit. on p. 121).
- [LAK54] L. D. Landau, A. A. Abrikosov, and I. M. Khalatnikov. “An asymptotic expression for the photon Green function in quantum electrodynamics.” In: *Dokl. Akad. Nauk SSSR* 95.6 (1954). Ed. by D. ter Haar. DOI: [10.1016/b978-0-08-010586-4.50085-7](https://doi.org/10.1016/b978-0-08-010586-4.50085-7) (cit. on p. 21).
- [LDW17] S.-S. B. Lee, J. von Delft, and A. Weichselbaum. “Doublon-Holon Origin of the Subpeaks at the Hubbard Band Edges.” In: *Physical Review Letters* 119.23 (2017). DOI: [10.1103/PhysRevLett.119.236402](https://doi.org/10.1103/PhysRevLett.119.236402) (cit. on p. 122).
- [Leh54] H. Lehmann. “Über Eigenschaften von Ausbreitungsfunktionen und Renormierungskonstanten quantisierter Felder.” de. In: *Il Nuovo Cimento (1943-1954)* 11.4 (1954). DOI: [10.1007/BF02783624](https://doi.org/10.1007/BF02783624) (cit. on p. 7).
- [Lih+24] J.-M. Lihm, J. Halbinger, J. Shim, J. von Delft, F. B. Kugler, and S.-S. B. Lee. “Symmetric improved estimators for multipoint vertex functions.” In: *Physical Review B* 109.12 (2024). DOI: [10.1103/PhysRevB.109.125138](https://doi.org/10.1103/PhysRevB.109.125138) (cit. on pp. 122, 123).
- [Lin24] M. Lindsey. *Multiscale interpolative construction of quantized tensor trains*. 2024. DOI: [10.48550/arXiv.2311.12554](https://doi.org/10.48550/arXiv.2311.12554) (cit. on p. 156).
- [LK00] A. I. Lichtenstein and M. I. Katsnelson. “Antiferromagnetism and d-wave superconductivity in cuprates: A cluster dynamical mean-field theory.” In: *Physical Review B* 62.14 (2000). DOI: [10.1103/PhysRevB.62.R9283](https://doi.org/10.1103/PhysRevB.62.R9283) (cit. on p. 152).
- [LKD21] S.-S. B. Lee, F. B. Kugler, and J. von Delft. “Computing Local Multipoint Correlators Using the Numerical Renormalization Group.” In: *Physical Review X* 11.4 (2021). DOI: [10.1103/PhysRevX.11.041007](https://doi.org/10.1103/PhysRevX.11.041007) (cit. on pp. 122, 123).
- [Lov84] S. W. Lovesey. *Theory of neutron scattering from condensed matter. Vol. 1. Nuclear scattering*. Oxford: Clarendon Press, 1984 (cit. on p. 4).
- [LW16] S.-S. B. Lee and A. Weichselbaum. “Adaptive broadening to improve spectral resolution in the numerical renormalization group.” In: *Physical Review B* 94.23 (2016). DOI: [10.1103/PhysRevB.94.235127](https://doi.org/10.1103/PhysRevB.94.235127) (cit. on p. 122).

- [Mai+05] T. Maier, M. Jarrell, T. Pruschke, and M. H. Hettler. “Quantum cluster theories.” In: *Reviews of Modern Physics* 77.3 (2005). DOI: [10.1103/RevModPhys.77.1027](https://doi.org/10.1103/RevModPhys.77.1027) (cit. on p. 152).
- [Mat55] T. Matsubara. “A New Approach to Quantum-Statistical Mechanics.” In: *Progress of Theoretical Physics* 14.4 (1955). DOI: [10.1143/PTP.14.351](https://doi.org/10.1143/PTP.14.351) (cit. on p. 7).
- [Mei+24] M. Meixner, H. Menke, M. Klett, S. Heinzlmann, S. Andergassen, P. Hansmann, and T. Schäfer. “Mott transition and pseudogap of the square-lattice Hubbard model: Results from center-focused cellular dynamical mean-field theory.” In: *SciPost Physics* 16.2 (2024). DOI: [10.21468/SciPostPhys.16.2.059](https://doi.org/10.21468/SciPostPhys.16.2.059) (cit. on p. 152).
- [Met+12] W. Metzner, M. Salmhofer, C. Honerkamp, V. Meden, and K. Schönhammer. “Functional renormalization group approach to correlated fermion systems.” In: *Reviews of Modern Physics* 84.1 (2012). DOI: [10.1103/RevModPhys.84.299](https://doi.org/10.1103/RevModPhys.84.299) (cit. on p. 25).
- [MH12] S. A. Maier and C. Honerkamp. “Effective three-particle interactions in low-energy models for multiband systems.” In: *Physical Review B* 85.6 (2012). DOI: [10.1103/PhysRevB.85.064520](https://doi.org/10.1103/PhysRevB.85.064520) (cit. on p. 26).
- [Mor+15] C. Mora, C. P. Moca, J. von Delft, and G. Zaránd. “Fermi-liquid theory for the single-impurity Anderson model.” In: *Physical Review B* 92.7 (2015). DOI: [10.1103/PhysRevB.92.075120](https://doi.org/10.1103/PhysRevB.92.075120) (cit. on p. 121).
- [Mor94] T. R. Morris. “The exact renormalization group and approximate solutions.” In: *International Journal of Modern Physics A* 09.14 (1994). DOI: [10.1142/S0217751X94000972](https://doi.org/10.1142/S0217751X94000972) (cit. on p. 25).
- [MS59] P. C. Martin and J. Schwinger. “Theory of Many-Particle Systems. I.” In: *Physical Review* 115.6 (1959). DOI: [10.1103/PhysRev.115.1342](https://doi.org/10.1103/PhysRev.115.1342) (cit. on pp. 7, 19).
- [MSW24] M. Murray, H. Shinaoka, and P. Werner. “Nonequilibrium diagrammatic many-body simulations with quantics tensor trains.” In: *Physical Review B* 109.16 (2024). DOI: [10.1103/PhysRevB.109.165135](https://doi.org/10.1103/PhysRevB.109.165135) (cit. on p. 156).
- [MV89] W. Metzner and D. Vollhardt. “Correlated Lattice Fermions in $d = \infty$ Dimensions.” In: *Physical Review Letters* 62.3 (1989). DOI: [10.1103/PhysRevLett.62.324](https://doi.org/10.1103/PhysRevLett.62.324) (cit. on p. 151).
- [MW66] N. D. Mermin and H. Wagner. “Absence of Ferromagnetism or Antiferromagnetism in One- or Two-Dimensional Isotropic Heisenberg Models.” In: *Physical Review Letters* 17.22 (1966). DOI: [10.1103/PhysRevLett.17.1133](https://doi.org/10.1103/PhysRevLett.17.1133) (cit. on pp. 26, 152).
- [NGR69] P. Nozières, J. Gavoret, and B. Roulet. “Singularities in the X-Ray Absorption and Emission of Metals. II. Self-Consistent Treatment of Divergences.” In: *Physical Review* 178.3 (1969). DOI: [10.1103/PhysRev.178.1084](https://doi.org/10.1103/PhysRev.178.1084) (cit. on p. 21).
- [NO19] J. W. Negele and H. Orland. *Quantum Many-particle Systems*. CRC Press, 2019. 476 pp. (cit. on pp. 7, 16, 17, 26).

- [Núñ+22] Y. Núñez Fernández, M. Jeannin, P. T. Dumitrescu, T. Kloss, J. Kaye, O. Parcollet, and X. Waintal. “Learning Feynman Diagrams with Tensor Trains.” In: *Physical Review X* 12.4 (2022). DOI: [10.1103/PhysRevX.12.041018](https://doi.org/10.1103/PhysRevX.12.041018) (cit. on p. 155).
- [Núñ+25] Y. Núñez Fernández et al. “Learning tensor networks with tensor cross interpolation: New algorithms and libraries.” In: *SciPost Physics* 18.3 (2025). DOI: [10.21468/SciPostPhys.18.3.104](https://doi.org/10.21468/SciPostPhys.18.3.104) (cit. on p. 155).
- [Ose09] I. V. Oseledets. “Approximation of matrices with logarithmic number of parameters.” In: *Doklady Mathematics* 80.2 (2009). DOI: [10.1134/S1064562409050056](https://doi.org/10.1134/S1064562409050056) (cit. on p. 154).
- [Ose11] I. V. Oseledets. “Tensor-Train Decomposition.” In: *SIAM Journal on Scientific Computing* 33.5 (2011). DOI: [10.1137/090752286](https://doi.org/10.1137/090752286) (cit. on p. 155).
- [OT10] I. Oseledets and E. Tyrtyshnikov. “TT-cross approximation for multidimensional arrays.” In: *Linear Algebra and its Applications* 432.1 (2010). DOI: [10.1016/j.laa.2009.07.024](https://doi.org/10.1016/j.laa.2009.07.024) (cit. on p. 155).
- [Ots+17] J. Otsuki, M. Ohzeki, H. Shinaoka, and K. Yoshimi. “Sparse modeling approach to analytical continuation of imaginary-time quantum Monte Carlo data.” In: *Physical Review E* 95.6 (2017). DOI: [10.1103/PhysRevE.95.061302](https://doi.org/10.1103/PhysRevE.95.061302) (cit. on p. 9).
- [Pad+25] H. Padma et al. *Beyond-Hubbard pairing in a cuprate ladder*. 2025. DOI: [10.48550/arXiv.2501.10287](https://doi.org/10.48550/arXiv.2501.10287) (cit. on p. 16).
- [Pat+25] M. Patricolo, M. Gievers, K. Fraboulet, A. Al-Eryani, S. Heinzelmann, P. Bonetti, A. Toschi, D. Vilaridi, and S. Andergassen. “Single-boson exchange formulation of the Schwinger-Dyson equation and its application to the functional renormalization group.” In: *SciPost Physics* 18.3 (2025). DOI: [10.21468/SciPostPhys.18.3.078](https://doi.org/10.21468/SciPostPhys.18.3.078) (cit. on p. 80).
- [PB05] T. Pruschke and R. Bulla. “Hund’s coupling and the metal-insulator transition in the two-band Hubbard model.” In: *The European Physical Journal B - Condensed Matter and Complex Systems* 44.2 (2005). DOI: [10.1140/epjb/e2005-00117-4](https://doi.org/10.1140/epjb/e2005-00117-4) (cit. on p. 121).
- [PPA06] R. Peters, T. Pruschke, and F. B. Anders. “Numerical renormalization group approach to Green’s functions for quantum impurity models.” In: *Physical Review B* 74.24 (2006). DOI: [10.1103/PhysRevB.74.245114](https://doi.org/10.1103/PhysRevB.74.245114) (cit. on p. 122).
- [RGN69] B. Roulet, J. Gavoret, and P. Nozières. “Singularities in the X-Ray Absorption and Emission of Metals. I. First-Order Parquet Calculation.” In: *Physical Review* 178.3 (1969). DOI: [10.1103/PhysRev.178.1072](https://doi.org/10.1103/PhysRev.178.1072) (cit. on p. 21).
- [Rit+22] M. K. Ritter, D. Kiese, T. Müller, F. B. Kugler, R. Thomale, S. Trebst, and J. von Delft. “Benchmark calculations of multiloop pseudofermion fRG.” In: *The European Physical Journal B* 95.7 (2022). DOI: [10.1140/epjb/s10051-022-00349-2](https://doi.org/10.1140/epjb/s10051-022-00349-2) (cit. on pp. 28, 55).
- [Rit+24] M. K. Ritter, Y. Núñez Fernández, M. Wallerberger, J. von Delft, H. Shinaoka, and X. Waintal. “Quantics Tensor Cross Interpolation for High-Resolution Parsimonious Representations of Multivariate Functions.” In: *Physical Review Letters* 132.5 (2024). DOI: [10.1103/PhysRevLett.132.056501](https://doi.org/10.1103/PhysRevLett.132.056501) (cit. on pp. 154, 155).

- [RKL08] A. N. Rubtsov, M. I. Katsnelson, and A. I. Lichtenstein. “Dual fermion approach to nonlocal correlations in the Hubbard model.” In: *Physical Review B* 77.3 (2008). DOI: [10.1103/PhysRevB.77.033101](https://doi.org/10.1103/PhysRevB.77.033101) (cit. on p. 153).
- [RKL12] A. N. Rubtsov, M. I. Katsnelson, and A. I. Lichtenstein. “Dual boson approach to collective excitations in correlated fermionic systems.” In: *Annals of Physics* 327.5 (2012). DOI: [10.1016/j.aop.2012.01.002](https://doi.org/10.1016/j.aop.2012.01.002) (cit. on p. 153).
- [Roh+18] G. Rohringer, H. Hafermann, A. Toschi, A. A. Katanin, A. E. Antipov, M. I. Katsnelson, A. I. Lichtenstein, A. N. Rubtsov, and K. Held. “Diagrammatic routes to nonlocal correlations beyond dynamical mean field theory.” In: *Reviews of Modern Physics* 90.2 (2018). DOI: [10.1103/RevModPhys.90.025003](https://doi.org/10.1103/RevModPhys.90.025003) (cit. on pp. 152, 153).
- [Roh+24] S. Rohshap, M. K. Ritter, H. Shinaoka, J. v. Delft, M. Wallerberger, and A. Kauch. *Two-particle calculations with quantum tensor trains – solving the parquet equations*. 2024. DOI: [10.48550/arXiv.2410.22975](https://doi.org/10.48550/arXiv.2410.22975) (cit. on pp. 154–156).
- [Roh13] G. Rohringer. “New routes towards a theoretical treatment of nonlocal electronic correlations.” PhD thesis. Technische Universität Wien, 2013. DOI: [10.34726/hss.2013.21498](https://doi.org/10.34726/hss.2013.21498) (cit. on p. 20).
- [RVT12] G. Rohringer, A. Valli, and A. Toschi. “Local electronic correlation at the two-particle level.” In: *Physical Review B* 86.12 (2012). DOI: [10.1103/PhysRevB.86.125114](https://doi.org/10.1103/PhysRevB.86.125114) (cit. on p. 20).
- [San98] A. W. Sandvik. “Stochastic method for analytic continuation of quantum Monte Carlo data.” In: *Physical Review B* 57.17 (1998). DOI: [10.1103/PhysRevB.57.10287](https://doi.org/10.1103/PhysRevB.57.10287) (cit. on p. 9).
- [SB51] E. E. Salpeter and H. A. Bethe. “A Relativistic Equation for Bound-State Problems.” In: *Physical Review* 84.6 (1951). DOI: [10.1103/PhysRev.84.1232](https://doi.org/10.1103/PhysRev.84.1232) (cit. on p. 22).
- [Sch+13] T. Schäfer, G. Rohringer, O. Gunnarsson, S. Ciuchi, G. Sangiovanni, and A. Toschi. “Divergent Precursors of the Mott-Hubbard Transition at the Two-Particle Level.” In: *Physical Review Letters* 110.24 (2013). DOI: [10.1103/PhysRevLett.110.246405](https://doi.org/10.1103/PhysRevLett.110.246405) (cit. on p. 119).
- [Sch+21] T. Schäfer et al. “Tracking the footprints of spin fluctuations: a MultiMethod, MultiMessenger study of the two-dimensional Hubbard model.” In: *Physical Review X* 11.1 (2021). DOI: [10.1103/PhysRevX.11.011058](https://doi.org/10.1103/PhysRevX.11.011058) (cit. on p. 152).
- [Sch+25] A. Scheie et al. *Cooper-Pair Localization in the Magnetic Dynamics of a Cuprate Ladder*. 2025. DOI: [10.48550/arXiv.2501.10296](https://doi.org/10.48550/arXiv.2501.10296) (cit. on p. 16).
- [Sch51] J. Schwinger. “On the Green’s functions of quantized fields. I.” In: *Proceedings of the National Academy of Sciences* 37.7 (1951). DOI: [10.1073/pnas.37.7.452](https://doi.org/10.1073/pnas.37.7.452) (cit. on p. 23).
- [Sch61] J. Schwinger. “Brownian Motion of a Quantum Oscillator.” In: *Journal of Mathematical Physics* 2.3 (1961). DOI: [10.1063/1.1703727](https://doi.org/10.1063/1.1703727) (cit. on pp. 11, 12).
- [SDS25] O. Sulyma, J. von Delft, and B. Schneider. In: *private communication* (2025) (cit. on p. 123).

- [Sha94] R. Shankar. “Renormalization-group approach to interacting fermions.” In: *Reviews of Modern Physics* 66.1 (1994). DOI: [10.1103/RevModPhys.66.129](https://doi.org/10.1103/RevModPhys.66.129) (cit. on p. 25).
- [Shi+17] H. Shinaoka, J. Otsuki, M. Ohzeki, and K. Yoshimi. “Compressing Green’s function using intermediate representation between imaginary-time and real-frequency domains.” In: *Physical Review B* 96.3 (2017). DOI: [10.1103/PhysRevB.96.035147](https://doi.org/10.1103/PhysRevB.96.035147) (cit. on p. 9).
- [Shi+23] H. Shinaoka, M. Wallerberger, Y. Murakami, K. Nogaki, R. Sakurai, P. Werner, and A. Kauch. “Multiscale Space-Time Ansatz for Correlation Functions of Quantum Systems Based on Quantics Tensor Trains.” In: *Physical Review X* 13.2 (2023). DOI: [10.1103/PhysRevX.13.021015](https://doi.org/10.1103/PhysRevX.13.021015) (cit. on p. 154).
- [Smi92] R. A. Smith. “Planar version of Baym-Kadanoff theory.” In: *Physical Review A* 46.8 (1992). DOI: [10.1103/PhysRevA.46.4586](https://doi.org/10.1103/PhysRevA.46.4586) (cit. on p. 124).
- [Spr+20] D. Springer, P. Chalupa, S. Ciuchi, G. Sangiovanni, and A. Toschi. “Interplay between local response and vertex divergences in many-fermion systems with on-site attraction.” In: *Physical Review B* 101.15 (2020). DOI: [10.1103/PhysRevB.101.155148](https://doi.org/10.1103/PhysRevB.101.155148) (cit. on p. 119).
- [Squ12] G. L. Squires. *Introduction to the Theory of Thermal Neutron Scattering*. 3rd ed. Cambridge: Cambridge University Press, 2012. DOI: [10.1017/CB09781139107808](https://doi.org/10.1017/CB09781139107808) (cit. on p. 4).
- [Śro+24] M. Środa, K. Inayoshi, H. Shinaoka, and P. Werner. *High-resolution nonequilibrium GW calculations based on quantics tensor trains*. 2024. DOI: [10.48550/arXiv.2412.14032](https://doi.org/10.48550/arXiv.2412.14032) (cit. on p. 156).
- [Sta+15] K. M. Stadler, Z. P. Yin, J. von Delft, G. Kotliar, and A. Weichselbaum. “Dynamical Mean-Field Theory Plus Numerical Renormalization-Group Study of Spin-Orbital Separation in a Three-Band Hund Metal.” In: *Physical Review Letters* 115.13 (2015). DOI: [10.1103/PhysRevLett.115.136401](https://doi.org/10.1103/PhysRevLett.115.136401) (cit. on p. 121).
- [Sta+19] K. M. Stadler, G. Kotliar, A. Weichselbaum, and J. von Delft. “Hundness versus Mottness in a three-band Hubbard–Hund model: On the origin of strong correlations in Hund metals.” In: *Annals of Physics* 405 (2019). DOI: [10.1016/j.aop.2018.10.017](https://doi.org/10.1016/j.aop.2018.10.017) (cit. on p. 121).
- [Sta+21] K. M. Stadler, G. Kotliar, S.-S. B. Lee, A. Weichselbaum, and J. von Delft. “Differentiating Hund from Mott physics in a three-band Hubbard-Hund model: Temperature dependence of spectral, transport, and thermodynamic properties.” In: *Physical Review B* 104.11 (2021). DOI: [10.1103/PhysRevB.104.115107](https://doi.org/10.1103/PhysRevB.104.115107) (cit. on p. 121).
- [STB04] D. Sénéchal, A.-M. Tremblay, and C. Bourbonnais, eds. *Theoretical Methods for Strongly Correlated Electrons*. CRM Series in Mathematical Physics. New York: Springer-Verlag, 2004. DOI: [10.1007/b97552](https://doi.org/10.1007/b97552) (cit. on p. 124).
- [Tag+19] A. Tagliavini, C. Hille, F. Kugler, S. Andergassen, A. Toschi, and C. Honerkamp. “Multiloop functional renormalization group for the two-dimensional Hubbard model: Loop convergence of the response functions.” In: *SciPost Physics* 6.1 (2019). DOI: [10.21468/SciPostPhys.6.1.009](https://doi.org/10.21468/SciPostPhys.6.1.009) (cit. on p. 28).
- [Tak57] Y. Takahashi. “On the generalized ward identity.” In: *Il Nuovo Cimento (1955-1965)* 6.2 (1957). DOI: [10.1007/BF02832514](https://doi.org/10.1007/BF02832514) (cit. on p. 123).

- [Tam+19] A. Tamai et al. “High-Resolution Photoemission on Sr_2RuO_4 Reveals Correlation-Enhanced Effective Spin-Orbit Coupling and Dominantly Local Self-Energies.” In: *Physical Review X* 9.2 (2019). DOI: [10.1103/PhysRevX.9.021048](https://doi.org/10.1103/PhysRevX.9.021048) (cit. on p. 6).
- [Tar+14] C. Taranto, S. Andergassen, J. Bauer, K. Held, A. Katanin, W. Metzner, G. Rohringer, and A. Toschi. “From Infinite to Two Dimensions through the Functional Renormalization Group.” In: *Physical Review Letters* 112.19 (2014). DOI: [10.1103/PhysRevLett.112.196402](https://doi.org/10.1103/PhysRevLett.112.196402) (cit. on p. 154).
- [Tho+20] J. Thoenniss, M. K. Ritter, F. B. Kugler, J. v. Delft, and M. Punk. *Multi-loop pseudofermion functional renormalization for quantum spin systems: Application to the spin-1/2 kagome Heisenberg model*. 2020. DOI: [10.48550/arXiv.2011.01268](https://doi.org/10.48550/arXiv.2011.01268) (cit. on p. 28).
- [TKH07] A. Toschi, A. A. Katanin, and K. Held. “Dynamical vertex approximation: A step beyond dynamical mean-field theory.” In: *Physical Review B* 75.4 (2007). DOI: [10.1103/PhysRevB.75.045118](https://doi.org/10.1103/PhysRevB.75.045118) (cit. on p. 153).
- [TSS25] H. Takahashi, R. Sakurai, and H. Shinaoka. “Compactness of quantics tensor train representations of local imaginary-time propagators.” In: *SciPost Physics* 18.1 (2025). DOI: [10.21468/SciPostPhys.18.1.007](https://doi.org/10.21468/SciPostPhys.18.1.007) (cit. on pp. 155, 156).
- [TW83] A. Tsvetick and P. Wiegmann. “Exact results in the theory of magnetic alloys.” In: *Advances in Physics* 32.4 (1983). DOI: [10.1080/00018738300101581](https://doi.org/10.1080/00018738300101581) (cit. on p. 121).
- [Vig+17] S. Vig et al. “Measurement of the dynamic charge response of materials using low-energy, momentum-resolved electron energy-loss spectroscopy (M-EELS).” In: *SciPost Physics* 3.4 (2017). DOI: [10.21468/SciPostPhys.3.4.026](https://doi.org/10.21468/SciPostPhys.3.4.026) (cit. on p. 5).
- [VTM19] D. Vilaridi, C. Taranto, and W. Metzner. “Antiferromagnetic and d -wave pairing correlations in the strongly interacting two-dimensional Hubbard model from the functional renormalization group.” In: *Physical Review B* 99.10 (2019). DOI: [10.1103/PhysRevB.99.104501](https://doi.org/10.1103/PhysRevB.99.104501) (cit. on pp. 117, 154).
- [Wal22] E. Walter. “Real-frequency dynamics of quantum impurity models studied with fRG, NRG, CFT.” PhD thesis. Ludwig-Maximilians-Universität München, 2022 (cit. on pp. 15, 16, 21, 24, 28, 55, 124).
- [War50] J. C. Ward. “An Identity in Quantum Electrodynamics.” In: *Physical Review* 78.2 (1950). DOI: [10.1103/PhysRev.78.182](https://doi.org/10.1103/PhysRev.78.182) (cit. on p. 123).
- [WD07] A. Weichselbaum and J. von Delft. “Sum-Rule Conserving Spectral Functions from the Numerical Renormalization Group.” In: *Physical Review Letters* 99.7 (2007). DOI: [10.1103/PhysRevLett.99.076402](https://doi.org/10.1103/PhysRevLett.99.076402) (cit. on p. 122).
- [Wei12a] A. Weichselbaum. “Non-abelian symmetries in tensor networks: A quantum symmetry space approach.” In: *Annals of Physics* 327.12 (2012). DOI: [10.1016/j.aop.2012.07.009](https://doi.org/10.1016/j.aop.2012.07.009) (cit. on p. 122).
- [Wei12b] A. Weichselbaum. “Tensor networks and the numerical renormalization group.” In: *Physical Review B* 86.24 (2012). DOI: [10.1103/PhysRevB.86.245124](https://doi.org/10.1103/PhysRevB.86.245124) (cit. on p. 122).

- [Wei20] A. Weichselbaum. “X-symbols for non-Abelian symmetries in tensor networks.” In: *Physical Review Research* 2.2 (2020). DOI: [10.1103/PhysRevResearch.2.023385](https://doi.org/10.1103/PhysRevResearch.2.023385) (cit. on p. 122).
- [Wen+15] N. Wentzell, C. Taranto, A. Katanin, A. Toschi, and S. Andergassen. “Correlated starting points for the functional renormalization group.” In: *Physical Review B* 91.4 (2015). DOI: [10.1103/PhysRevB.91.045120](https://doi.org/10.1103/PhysRevB.91.045120) (cit. on p. 154).
- [Wen+20] N. Wentzell, G. Li, A. Tagliavini, C. Taranto, G. Rohringer, K. Held, A. Toschi, and S. Andergassen. “High-frequency asymptotics of the vertex function: Diagrammatic parametrization and algorithmic implementation.” In: *Physical Review B* 102.8 (2020). DOI: [10.1103/PhysRevB.102.085106](https://doi.org/10.1103/PhysRevB.102.085106) (cit. on p. 24).
- [Wet93] C. Wetterich. “Exact evolution equation for the effective potential.” In: *Physics Letters B* 301.1 (1993). DOI: [10.1016/0370-2693\(93\)90726-X](https://doi.org/10.1016/0370-2693(93)90726-X) (cit. on p. 25).
- [WH02] E. Wang and U. Heinz. “Generalized fluctuation-dissipation theorem for nonlinear response functions.” In: *Physical Review D* 66.2 (2002). DOI: [10.1103/PhysRevD.66.025008](https://doi.org/10.1103/PhysRevD.66.025008) (cit. on p. 19).
- [Wic50] G. C. Wick. “The Evaluation of the Collision Matrix.” In: *Physical Review* 80.2 (1950). DOI: [10.1103/PhysRev.80.268](https://doi.org/10.1103/PhysRev.80.268) (cit. on p. 14).
- [Wil75] K. G. Wilson. “The renormalization group: Critical phenomena and the Kondo problem.” In: *Reviews of Modern Physics* 47.4 (1975). DOI: [10.1103/RevModPhys.47.773](https://doi.org/10.1103/RevModPhys.47.773) (cit. on pp. 25, 119, 121).
- [YL22] E. Ye and N. F. G. Loureiro. “Quantum-inspired method for solving the Vlasov-Poisson equations.” In: *Physical Review E* 106.3 (2022). DOI: [10.1103/PhysRevE.106.035208](https://doi.org/10.1103/PhysRevE.106.035208) (cit. on p. 155).
- [ZG24] L. Zhang and E. Gull. “Minimal pole representation and controlled analytic continuation of Matsubara response functions.” In: *Physical Review B* 110.3 (2024). DOI: [10.1103/PhysRevB.110.035154](https://doi.org/10.1103/PhysRevB.110.035154) (cit. on p. 9).
- [ZYG24] L. Zhang, Y. Yu, and E. Gull. “Minimal pole representation and analytic continuation of matrix-valued correlation functions.” In: *Physical Review B* 110.23 (2024). DOI: [10.1103/PhysRevB.110.235131](https://doi.org/10.1103/PhysRevB.110.235131) (cit. on p. 9).

